Investigating the capacity of locked nucleic acid mixmer antisense oligonucleotides to inhibit viral replication

Inaugural-Dissertation

zur Erlangung des Doktorgrades
der Mathematisch-Naturwissenschaftlichen Fakultät
der Heinrich-Heine-Universität Düsseldorf

vorgelegt von

Philipp Niklas Ostermann

aus Unna

Düsseldorf, Juli 2022

aus dem Institut für Virologie

der Heinrich-Heine-Universität Düsseldorf

Gedruckt mit der Genehmigung der
Mathematisch-Naturwissenschaftlichen Fakultät der
Heinrich-Heine-Universität Düsseldorf

Berichterstatter:

1. Prof. Dr. rer. nat. Heiner Schaal

2. Prof. Dr. rer. nat. Michael Feldbrügge

Tag der mündlichen Prüfung: 20.10.2022

„Alice laughed. 'There's no use trying,' she said. 'One can't believe impossible things.'

I daresay you haven't had much practice,' said the Queen. 'When I was your age, I always did it for half-an-hour a day. Why, sometimes I've believed as many as six impossible things before breakfast. There goes the shawl again!"

- Lewis Carroll

Abstract

Efficacious antiviral agents are still rare and typically only available against viral diseases of high public interest. Therefore, finding novel antiviral agents or antiviral strategies remains a high priority. Antisense oligonucleotides (ASOs) can be used for a variety of applications, including molecular diagnostics, as tools for basic research or for therapeutic applications. Thanks to improved chemical modifications and better characterization of their functions, more therapeutic ASOs are now being tested in clinical trials with some already approved. However, there are still vast knowledge gaps concerning general ASO function, for instance, their efficacy in different cell types or ASO-induced effects on target RNA with respect to the rates of cytoplasmic and nuclear activity. Despite such gaps, a previous study indicated the capacity of locked nucleic acid mixmer-modified antisense oligonucleotides (LNA mixmers) to inhibit HIV-1 replication in cell culture. To investigate whether such LNA mixmers can also interfere with RNA viruses replicating in the cytoplasm, this thesis investigates whether unassisted LNA mixmer delivery can inhibit replication of SARS-CoV-2. To do this, infectious SARS-CoV-2 was first isolated from a naso-/oropharyngeal swab specimen to establish a valid infection model. The delivered anti-SARS-CoV-2 LNA mixmers, however, failed to inhibit viral replication in subsequent infection experiments. To exclude that induction of double membrane vesicles is a reason for the unexpected failure of LNA mixmer activity against SARS-CoV-2, LNA mixmer-mediated inhibition was tested against Hazara virus. Hazara virus is considered a surrogate model for the highly lethal Crimean-Congo hemorrhagic fever virus, and it has not been described to induce double membrane vesicles. Since there was no antiviral LNA mixmer activity against this second RNA virus, which also replicates in the cytoplasm, a possible high susceptibility of splicing regulatory elements, which were targeted while successfully inhibiting HIV-1 replication, was analyzed using the nuclear replicating Influenza A virus. However, even the LNA mixmers against Influenza A virus did not exhibit any observable antiviral activity. Besides their diverse replication mechanisms, however, the analyzed viruses also differ in their host cells. By analyzing HIV-1 inhibition in different cell models, it became apparent that T-cells are particularly susceptible to ASO activity compared to other cell types. This key finding might thus explain the apparent lack of antiviral LNA mixmer activity against SARS-CoV-2, Hazara virus and Influenza A virus, all of which do not replicate in T-cells.

Zusammenfassung

Wirksame antivirale Mittel stehen meist nur für Viruserkrankungen von großem öffentlichen Interesse zur Verfügung. Daher hat generell die Suche nach neuen antiviralen Wirkstoffen weiterhin hohe Priorität. Antisense Oligonukleotide (ASOs) können für eine Vielzahl von Anwendungen eingesetzt werden. Zum Beispiel für die Diagnostik, als Werkzeuge für die Grundlagenforschung oder für therapeutische Anwendungen. Dank verbesserter chemischer Modifikationen und einer besseren Charakterisierung ihrer Funktionen werden immer mehr therapeutische ASOs in klinischen Studien getestet. Von diesen sind einige sogar bereits zugelassen worden. Allerdings gibt es immer noch große Wissenslücken in Bezug auf die Funktion von ASOs. Vor allem bezüglich ihrer Aktivität im Zytoplasma und Zellkern oder ihrer Wirksamkeit in verschiedenen Zelltypen. Trotz dieser Wissenslücken konnte eine frühere Studie die Eignung von Locked Nucleic Acid Mixmer modifizierten Antisense Oligonukleotiden (LNA Mixmere) für die Hemmung der HIV-1 Replikation in Zellkultur nachweisen. Um herauszufinden, ob LNA Mixmere auch die Replikation von RNA Viren, die im Zytoplasma replizieren, hemmen können, wurden hier als erstes LNA Mixmere gegen SARS-CoV-2 untersucht. Hierfür wurde zunächst infektiöses SARS-CoV-2 aus einem Rachenabstrich isoliert. Dadurch konnte ein valides Infektionsmodell in der Zellkultur etabliert werden. Die anti-SARS-CoV-2 LNA Mixmere konnten jedoch in anschließenden Infektionsexperimenten die SARS-CoV-2 Replikation nicht hemmen. Um auszuschließen, dass die Induktion doppelmembran-haltiger Strukturen ein Grund für das unerwartete Fehlen einer antiviralen Aktivität der LNA Mixmere gegen SARS CoV-2 war, wurde eine LNA Mixmer-vermittelte Inhibition gegen das Hazara Virus untersucht. Von diesem Virus, welches häufig als nicht-pathogenes Ersatzmodell für das Krim-Kongo hämorrhagische Fieber Virus eingesetzt wird, ist nämlich nicht beschrieben, dass es solche doppelmembran-haltigen Strukturen während der Infektion induziert. Da auch gegen dieses zweite im Zytoplasma replizierende RNA Virus keine antivirale LNA Mixmer Aktivität nachgewiesen werden konnte, wurde als nächstes eine mögliche hohe Anfälligkeit von spleißregulatorischen Elementen, die bei erfolgreicher LNA Mixmer-vermittelten Hemmung der HIV-1 Replikation eine Rolle spielten, analysiert. Da sowohl SARS-CoV-2 als auch das Hazara Virus als im Zytoplasma replizierende Viren keine spleißregulatorischen Elementen besitzen, wurde das im Zellkern replizierende Influenza A Virus verwendet. Allerdings zeigten auch die LNA Mixmere dieses RNA Virus keine antivirale Aktivität. Neben ihren unterschiedlichen Replikationsmechanismen unterscheiden sich die hier untersuchten RNA Viren jedoch auch in ihren Wirtszellen. Bei der Analyse der HIV-1 Hemmung in verschiedenen Zellmodellen stellte sich heraus, dass T-Zellen im Vergleich zu anderen Zelltypen besonders empfänglich für LNA Mixmer Aktivität sind. Diese wichtige Erkenntnis könnte daher das Fehlen einer antiviralen Aktivität gegen SARS-CoV-2, das Hazara Virus und das Influenza A Virus erklären, die alle nicht in T-Zellen replizieren.

Acknowledgments

Content

1   Introduction

Efficacious antiviral agents are still rare and available for the most part only against viral disease of high public concern. Given the huge variety of viral diseases together with the continuous emergence of novel viral pathogens, there is still an urgent need for novel antiviral agents and therapy strategies.

In this context, a preceding study suggested the suitability of chemically-modified antisense oligonucleotides, which were designed to bind viral RNA, to inhibit HIV-1 replication (1).

This thesis aims at investigating the potential of such *locked nucleic acid mixmer antisense oligonucleotides* (LNA mixmers) to approach inhibition also of other viruses to find a new way in the fight against viral disease.

Throughout this thesis, usage of LNA mixmers was pursued to interfere with SARS-CoV-2, Hazara virus (a Crimean-Congo hemorrhagic fever virus surrogate model) and Influenza A virus replication. Moreover, to expand the earlier work, additional target sites within the HIV-1 genome were analyzed to better understand LNA mixmer-mediated inhibition of HIV-1.

1.1   Antivirals

While bacteria could initially be brought under control since the discovery of antibiotics in the 1920s, treatment of viral infections was restricted to supportive medication for a much longer time.

Massive screening programs for antiviral drugs in the 1960s and '70s yielded only minor success (2). At that time, antiviral therapy was considered virtually impossible, because viruses do not have their own metabolism. However, the nucleoside analogue Acyclovir, which is used to treat herpes simplex virus (HSV) infection, is one notable exception as its approval in the early 1980s showed that antiviral activity can be achieved (3).

Following the discovery of HIV-1 as the cause of AIDS in the 1980s, efforts were made worldwide to develop other antiviral agents that could not only interfere with its viral life cycle *in vitro* but also inhibit viral replication after administration to infected individuals (2).

In this context, introduction of the antiretroviral therapy (ART) regimen is often considered the most important breakthrough in the fight against AIDS. However, some may regard the nucleoside analogue Zidovudine (azidothymidine [AZT]), approved by the United States Food and Drug administration (FDA) in 1987, as the biggest step forward in antiretroviral therapy,

because it was the first drug administered to AIDS patients that inhibited HIV-1 replication and lowered symptoms (2, 4).

Based on this success, additional antiviral therapy strategies were introduced over time also addressing other viral diseases (5, 6). Given some huge pitfalls and limitations of the currently available antiviral therapy options, however, there remains an urgent need for new antiviral therapies and compounds.

Small molecule inhibitors

Of the various therapeutic options, the use of small molecule inhibitors is the most common. This class of antivirals allows a more or less specific interference with certain steps of the viral life cycle. This is possible by binding of small molecule inhibitor compounds to viral enzymes that have no or only very distantly related human homologues.

As mentioned before, also herpes simplex virus (HSV) infections can be treated using the small molecular inhibitor named acyclovir. Acyclovir is a nucleoside analogue. It is first converted into acyclovir monophosphate specifically by the HSV thymidine kinase (2, 3). Hence, it has the additional advantage that it is almost exclusively activated in virus-infected cells. Afterwards, it is converted by host cell kinases to acyclovir triphosphate. Acyclovir monophosphate as well as its triphosphate form are both inhibitors of the HSV DNA-dependent DNA polymerase (2, 3).

However, the search for such small molecule inhibitors is difficult. First, screening for compounds that specifically bind viral target enzymes but not potential cellular homologues is an enormous and cost-intensive effort. Therefore, such small molecule inhibitors exist primarily for viruses of high public concern, such as HSV, HIV-1 or hepatitis B virus (2).

Furthermore, the success rate of such screening approaches is limited by a low number of virus-specific proteins and a high viral mutation rate, both with respect especially to RNA viruses. Hence, this thesis focuses on an alternative therapy approach in the context of RNA viruses.

Monoclonal antibodies and plasma therapy

In addition to small molecule inhibitors, the use of monoclonal antibodies (mAbs) or plasma therapy may be pursued to treat viral infections. Both antiviral therapy options are based on passive immunization (7-9).

However, there are still only few mAbs approved by the regulatory authorities (7). This is likely explained by the possibility of side-effects, restricted bioavailability and with the emergence of escape mutants (10-13).

Administration of convalescent plasma is not a recent idea and indeed showed promising results in animal studies against different viruses (14, 15). Its efficacy in the real world, however, is questionable (16, 17). Hence, plasma therapy remains a rather experimental therapy approach that may be beneficial only under certain circumstances (18).

Antisense oligonucleotides

Antisense oligonucleotides (ASOs) are single-stranded oligonucleotides with a typical length of up to 30 nucleotides. The first ASO-based therapeutic agent approved by the FDA was also the first antiviral ASO that was granted approval by a responsible health authority (19). The drug Fomivirsen, a 21 nucleotide-long, phosphorothioate-modified ASO (see below), is applied intraocularly to treat cytomegalovirus (CMV) retinitis in immunocompromised patients (20).

Fomivirsen in no longer available because safer and more efficient alternatives exist today. In addition, it remains the only approved antiviral ASO to date. However, its history has been a major step forward in the field of therapeutic ASOs.

1.2   LNA mixmer-modified antisense oligonucleotides

The idea behind antisense oligonucleotides (ASOs) as therapeutic compounds came up decades ago and led Stephenson and Zamecnik eventually to the first proof-of-principle of ASOs as potential therapeutics in 1978 (21). Their work showing inhibition of Rous Sarcoma Virus replication by using single-stranded DNA oligonucleotides complementary to specific Rous Sarcoma RNA genome sequences was followed by many more studies describing opportunities for ASOs to treat various diseases (reviewed in (22)). Nevertheless, safety issues and a low bioavailability *in vivo* rapidly diminished the high hopes that were based on the promising results in cell culture systems.

Throughout the years, these issues were addressed by the introduction of chemical modifications. These chemical modifications achieved a reduction in side-effects and toxicities, and on the other hand increased serum stability, exo- and endonuclease resistance, and their bioavailability *in vivo* (25, 26). Overall, these modifications led to the current state in which numerous ASOs are tested in clinical trials and with a handful already approved by the respective authorities (reviewed in (27)).

For example, there are now three candidate drugs for treatment of viral infections that already completed phase II clinical trials (ClinicalTrials.gov Identifiers: NCT02508090, NCT02981602 and NCT03020745). The drug *miravirsen*, which is used to treat Hepatitis C virus infection, was the first of these and, importantly, it shares its locked nucleic acid mixmer-modification (LNA mixmer) with those ASOs used in this work (28).

1.2.1 Chemical modifications

Today, there is a vast diversity of chemical modifications used to improve or direct ASO function (reviewed in (27)). Likewise, the ASOs used throughout this thesis were chemically modified. ASO chemical modifications may be grouped into conjugated molecules (not shown), backbone, base and 2' ribose modifications (Fig. 1.1).
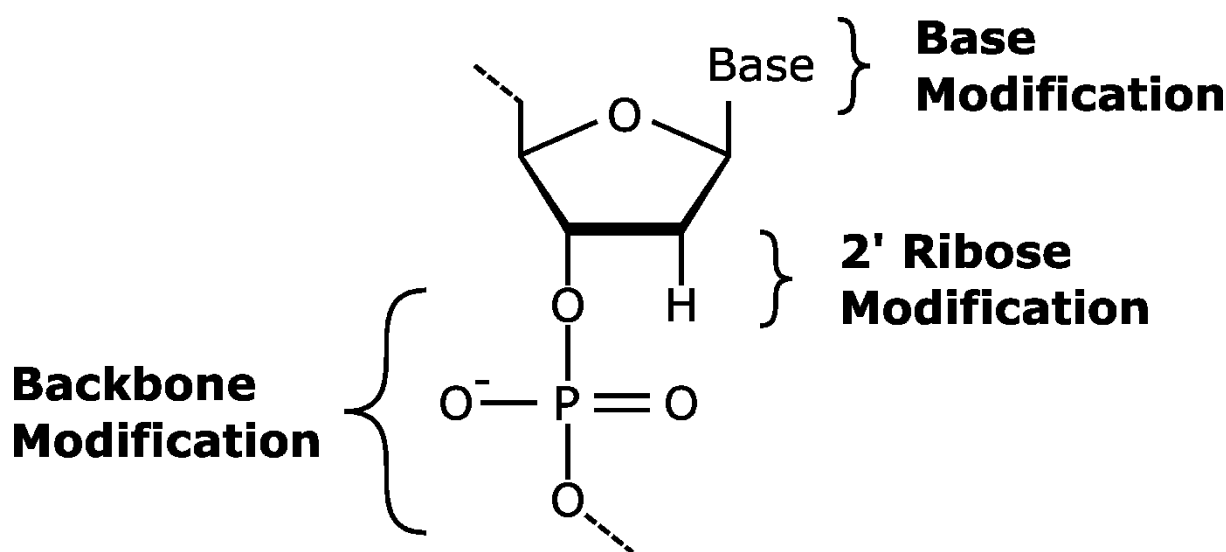
Fig. 1.1 Chemical modifications of antisense oligonucleotides. Chemical modifications used to improve and direct antisense oligonucleotide (ASO) function may be grouped into backbone, base and 2' ribose modifications. These modifications may affect every single nucleic acid moiety throughout an ASO. Also, small molecules may be attached to ASOs to enhance and direct cellular uptake. This is, however, not shown, because usually one such small molecule is attached to a whole ASO molecule.

Conjugated molecules

The attachment of certain molecules to ASOs may be pursued to reach a certain level of cell type or tissue specificity after systemic administration. Additionally, this may also contribute to a higher cellular uptake in the targeted cells (25).

One example in this context is the conjugation of N-Acetylgalactosamine (GalNAc). GalNAc is bound by cellular asialoglycoprotein receptors (29). These receptors are expressed in a high level on hepatocytes (30). Hence, attachment of GalNAc to ASOs leads to an efficient uptake in hepatocytes (31, 32). However, overall, only few such conjugates are described, with GalNAc being the most promising, that reliably allow targeting of specific cell types (25).

Backbone modifications

With respect to backbone modifications, phosphorodiamidate morpholino oligonucleotides (PMOs), which harbour methylenemorpholine rings instead of ribose sugars and phosphorodiamidate linkages substituting the natural phosphodiester bonds, provide one interesting example (26, 27). Due to their chemical structure, they are supposedly not susceptible to enzymatic degradation (33).

The ASOs used within this thesis, however, harbour the phosphorothioate (PS) modification. This modification is based on the exchange of one of the non-bridging oxygen atoms in the natural phosphodiester bond by a sulphur atom (Fig. 1.2 **A**, **B**) (26).

PS-ASOs exhibit an increased resistance to nucleases and furthermore, have a higher binding affinity for proteins (26). This higher affinity to proteins has some huge advantages.

For instance, the binding of PS-ASOs to serum proteins increases their serum half-time, which presumably leads to a higher bioavailability in the human body (34).

Secondly, PS-ASOs were shown to enter cells via natural pathways like endocytosis. This characteristic renders transfection or carrier reagent-free application possible (35). This means that clinical administration does not rely on the use, for example, of nanoparticles.

Importantly, transfection reagent-based application is still often used in cell culture experiments, because it increases the ASO efficacy (36). To analyse ASO-exerted effects that may be expected after clinical administration, however, transfection reagent-free application (also referred to as unassisted delivery) is indispensable, since many factors may influence ASO activity after this so-called *free uptake* (see below).
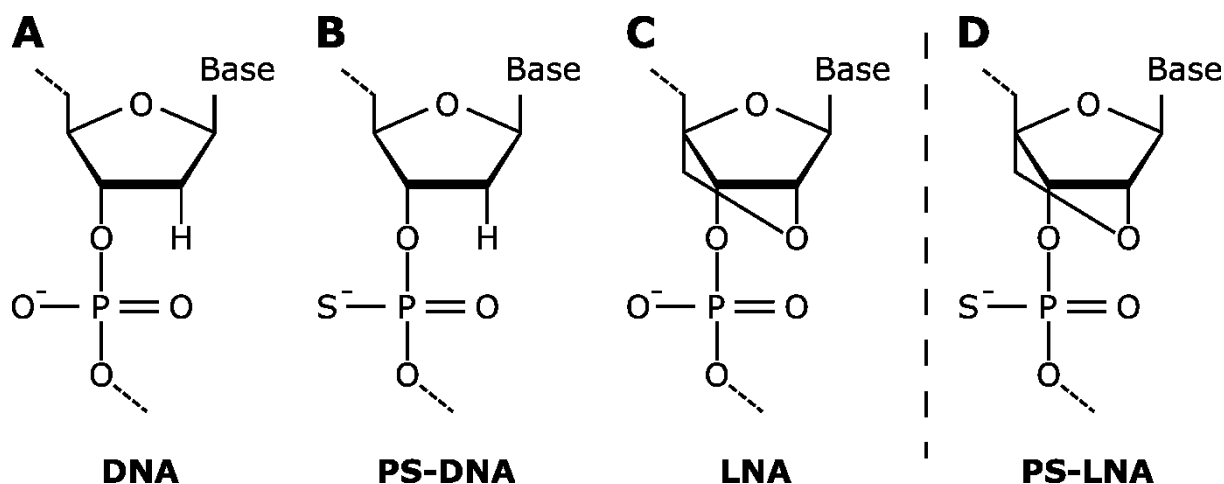
Fig. 1.2 Phosphorothioate locked nucleic acid-modified antisense oligonucleotides. (**A**, **B**) The phosphorothioate (PS) backbone modification relies on substituting one non-bridging oxygen atom in the DNA phosphodiester bond by a sulphur atom. (**C**) The 2' ribose locked nucleic acid (LNA) modification is based on a methylene bridge connecting the 2' oxygen and the 4' carbon atom. (**D**) State-of-the-art ASOs make use of the PS backbone modification and additionally one of the available 2' ribose modifications like the LNA modification.

To date, many of the ASOs that are currently tested in clinical trials make us of this PS backbone modification (27).

Base modifications

The most common base modification is the use of 5-methylcytosines. This modification was shown to enhance base pairing, this way increasing the binding affinity of 5-methylcytosine containing ASOs to complementary RNA (37).

2' ribose modifications

The perhaps most diverse group of ASO modifications encompass the 2' ribose modifications. Again, these modifications aim at increasing serum half-life, nuclease resistance and binding affinity to complementary RNA, while decreasing side-effects (26).

Chemical modifications at the 2' position of the ribose moiety include, for instance, the 2'-O-methyl (2'-OMe), the 2'-O-methoxyethyl (2'-MOE) or the locked nucleic acid (LNA) modification. While the 2'-OMe and 2'-MOE modifications are based on adding a methylene or methoxyethylen group to the 2' -oxygen atom, respectively, the LNA modification is the integration of a stable methylene bridge connecting the 2'-oxygen and the 4' carbon atom (Fig. 1.2 **C**).

All of these 2' ribose modifications were shown to have advantages and disadvantages. This is why there are so many different ASO types currently investigated in cell culture-based systems, but also in clinical trials (27).

The aim of this thesis was to analyse the potential of LNA-modified ASOs to inhibit RNA virus and retrovirus replication. This specific 2' modification leads to a higher target RNA affinity compared to 2'-MOE modification as well as an increased nuclease resistance presumably by mediating a constrained ribose configuration (38, 39).

Importantly, such 2' ribose modifications are generally used in addition to the previously described PS backbone modification (Fig. 1.2 **D**). This combination allows transfection or carrier-free administration while also increasing serum and intracellular half-life as well as the binding affinity to complementary RNA.

1.2.2 ASO function

In addition to the chemical modification of ASOs, other factors have been shown to influence ASO function. Some are well-described and used to control or enhance ASO activity. However, there are still factors that puzzle the scientific community and are, hence the subject of intensive research.

Gapmer and Mixmer design

One major factor, which influences ASO-exerted function and that has been well-defined over the years is the specific pattern of 2' ribose-modified nucleotides within an ASO. As mentioned above, many of the state-of-the-art ASOs, like the LNA mixmers tested during this thesis, are fully modified with respect to their backbone (27). This modification enables free cellular uptake. Within the cells, however, the specific pattern of 2'ribose-modified nucleotides may determine their way of action (26).

In this context, ASOs are currently divided into so-called *gapmer* and *mixmer* ASOs (40). Like siRNA, ASOs in gapmer design are used to achieve knockdown of target RNA (41). This is possible by making use of a central stretch of 5 – 10 2' ribose-unmodified nucleotides (Fig. 1.3 **A**) (26, 41). After binding to its complementary RNA, the gapmer ASO-RNA duplex may be bound by cellular RNase H and this central stretch allows cleavage of the ASO-bound RNA (41). Here, 2'ribose-modified nucleotides at the 5' and 3' ends, respectively, are used to increase nuclease resistance and half-life of the ASO itself, while the central stretch of 2' ribose-unmodified nucleotides is necessary for gapmer ASO-mediated RNA cleavage.

A

RNase H

Gapmer ASO
5' LLLLnnnnnnnLLLL 3'

Target RNA
3' ‖‖‖‖ ▭▭▭▭▭▭▭▭▭▭ ‖‖‖‖ 5'

B

RNA binding protein

Mixmer ASO
5' LLnnLnLnnLnnLnLL 3'

Target RNA
3' ‖‖‖‖ ▭▭▭▭▭▭▭▭▭▭ ‖‖‖‖ 5'
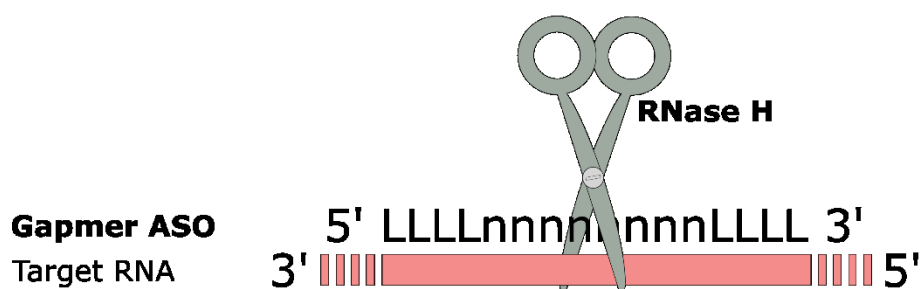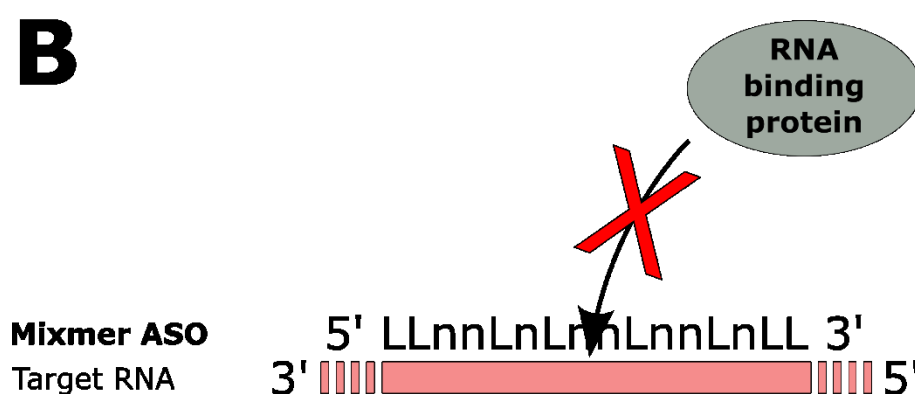
Fig. 1.3 Exerted functions of antisense oligonucleotides in gapmer and mixmer design. (A) A central stretch of 2' ribose-unmodified nucleotides (n) allows cellular RNase H-mediated cleavage of gapmer ASO-bound RNA. Flanking this central stretch with 2' ribose-modified nucleotides (L) is responsible to nevertheless make use of the higher binding affinity and nuclease resistance exerted by 2' ribose-modified nucleotides. **(B)** Mixmer ASOs lack this central stretch of 2' ribose-unmodified nucleotides. Mixmer ASOs may be used as steric blocks to prevent the binding of certain proteins to the target RNA.

The alternative to gapmer ASOs are ASOs in mixmer design. These mixmer ASOs do not harbor a central stretch of 2' ribose-unmodified nucleotides (40). Since 2' ribose-modified nucleotides prevent RNase H cleavage of ASO-bound target RNA, application of mixmer ASOs does not lead to a directed RNA knockdown (40). More importantly, however, since they lack this central stretch of 2' ribose-unmodified nucleotides, mixmer ASOs were shown to have a higher serum half-life than gapmer ASOs (42). Hence, this thesis aimed at investigating the potential only of mixmer ASOs (LNA mixmers) to inhibit viral replication.

The positions of 2' ribose-modified nucleotides within mixmer ASOs may be selected randomly. However, the specific pattern of 2' ribose-modified and -unmodified nucleotides supposedly influences ASO activity (43). Hence, companies like Qiagen for instance, use in-house algorithms to distribute the 2' ribose-modified nucleotides to certain positions within

the mixmer ASO. Unfortunately, to protect these underlying algorithms, there is no information about which nucleotides within an ASOs harbor the desired 2' ribose modification when ordering mixmer ASOs from these companies.

While mixmer ASOs do not allow RNase H-dependent cleavage of complementary RNA, the mere binding of mixmer ASOs to RNA transcripts prevents additional binding of RNA binding proteins (Fig. 1.3 **B**) (26). This way, important *cis*-acting RNA regulatory elements can be masked to interfere with cellular processes like pre-mRNA splicing (44).

For example, the FDA-approved ASO Nusinersen (Spinraza) masks a splicing regulatory element (SRE) in intron 7 of the human survival of motor neuron 2 (*SMN2*) gene (45, 46). It is suggested that this ASO-mediated masking prevents splicing regulatory proteins (SRPs) heterogeneous nuclear ribonuclear proteins (hnRNP) A1 and A2 from binding to the *SMN2* pre-mRNA (45, 47). Since hnRNPA1 and A2 supposedly inhibit usage of the *SMN2* exon 7 splice acceptor, ASO-mediated masking of this specific SRE consequently leads to a higher rate of *SMN2* exon 7 inclusion into processed *SMN2* mRNA (45, 47). Inclusion of *SMN2* exon 7 is necessary for the generation of full-length SMN2 protein during translation (45).

Overall, this specific characteristic of LNA mixmers to mask *cis*-acting regulatory elements will be made use of while aiming at the inhibition of pathogenic RNA viruses.

Productive and non-productive pathway

Importantly, PS-modified ASOs, like the LNA mixmers used throughout this thesis, can enter cells without the use of transfection reagents (35). It is suggested that due to the high protein binding affinity of the PS backbone, PS-ASOs are endocytosed together with ASO-bound protein (48). Once in the endosomal compartment, two pathways, a *productive* and a *non-productive* pathway exist that determine ASO activity (reviewed in (46)).

Both pathways are not well-understood. Research into ASO activity only since recently started to illuminate participating proteins and other factors that may influence the rates at which these two pathways are used ((49-52) and reviewed in (48)).

The productive pathway is believed to start with ASOs escaping the cellular endosomal compartment during endosomal maturation and/or lysosome formation (46). In the cytoplasm, the applied ASOs may bind their target RNA to exert their proposed functions (41, 48). Furthermore, these cytoplasmic ASOs have the chance to be transported into the nucleus, most likely also via a RAN-mediated nuclear import pathway (46). Within the nucleus, ASOs have again the chance to bind their target RNA to exert their respective functions (46).

Importantly, while only a minor part of ASOs participate in this so-called productive pathway, the majority of administered ASOs remain within the endosomal compartment where they cannot reach their target RNA (46). Despite having a higher resistance to exo- and endonucleases compared to unmodified ASOs, even the PS- and 2' ribose-modified ASOs will be degraded overtime never exerting their pursued function. To overcome this non-productive pathway constitutes one of the biggest challenges in ASO-related research.

With viruses that are likewise taken up via endocytosis, targeting viral RNA by administration of PS-modified ASOs may reveal a yet underestimated potential since it might allow increased binding by endocytosed ASOs to their viral target RNA.

1.3   Severe Acute Respiratory Syndrome-related Coronavirus type 2

Given its only recent emergence together with its high infectivity and at the time not well understood clinical manifestations, the first virus that was sought to be approached by LNA mixmer-mediated inhibition during this thesis was SARS-CoV-2.

1.3.1   SARS-CoV-2 epidemiology

After Severe Acute Respiratory Syndrome-related Coronavirus (SARS-CoV) and Middle East Respiratory Syndrome-related Coronavirus (MERS-CoV), Severe Acute Respiratory Syndrome-related Coronavirus type 2 (SARS-CoV-2) is the third coronavirus to emerge in the 21th century (53-55). Unlike its two predecessors, however, SARS-CoV-2 became pandemic within only few months having caused to date 300 million infections worldwide (56). Moreover, as the causative agent of coronavirus disease 2019 (COVID-19), its global distribution has led to over 5 million deaths (57).

In this context, as part of this thesis, it could be shown that early commercial serology tests lacked sensitivity compared to an established in-house neutralization and immunofluorescence test (58). Therefore, especially during the beginning of this pandemic, it was suggested that the SARS-CoV-2 prevalence was even higher than determined alone from the confirmed cases (58).

A major breakthrough in containing the current pandemic was the introduction of SARS-CoV-2 vaccines one year after the first confirmed SARS-CoV-2 infections (59-62).

However, the emergence of SARS-CoV-2 variants of concern (VOCs), characterized by higher replication rates, increased infectivity, or immune evasion capabilities, soon dampened the initial success by steadily increasing numbers of breakthrough infections (63-66).

For example, neutralization of the most recent Omicron variant by sera has been shown to be reduced after immunization compared to neutralization of an early pandemic strain or even the previously encountered beta and delta variants (67).

In addition to bypassing the immune system through mutations in the viral spike protein to reduce recognition by antibodies, a recent study has also shown that the alpha variant better suppresses innate immune responses in respiratory cells compared to previous viral isolates (68). This revealed yet another mechanism of how these VOCs enhance replication.

In conjunction with these findings and due to the impaired immune response to SARS-CoV-2 vaccination in individuals of advanced age or under immunosuppression dissecting possible interference points for antivirals remains of paramount importance (69, 70).

2.3.2   Pathogenesis – Coronavirus disease 2019

SARS-CoV-2 is the causative agent of coronavirus disease 2019 (COVID-2019) (54). COVID-19 primarily is a lung disease accompanied by symptoms like coughing, sore throat, fever, fatigue or headache (54, 55, 71). A variety of symptoms like diarrhea, cardiac complications and encephalitis revealed, moreover, that COVID-19 afflicts tissues and organs beyond the respiratory tract (71, 72).

Interestingly, especially with respect to the usefulness of ASOs in CNS disease (46, 73), with symptoms like dizziness, impaired consciousness, ataxia and seizures, central nervous system (CNS) involvement in COVID-19 was early on observed during the SARS-CoV-2 pandemic (74-76).

Additionally, an increasing number of people was found to suffer from COVID-19-associated long-term sequelae (77-79). These long-term sequelae may include abnormal breathing, fatigue, abdominal pain, or cognitive symptoms (77-79). Due to the relative high incidence of such symptoms that can persist weeks to months after infection, the term post- or long-COVID-19 was coined.

Consistent with this, a retrospective cohort study analyzing neurologic and psychiatric outcomes six months after infection found higher rates of cognitive symptoms such as encephalitis, dementia, or insomnia in the cohort infected with SARS-CoV-2 compared to control groups infected with influenza and other respiratory viruses (80).

1.3.3 SARS-CoV-2 molecular biology

To give an overview of the viral sequences targeted by the designed LNA mixmers, this chapter briefly summarizes the main aspects of SARS-CoV-2 replication.

SARS-CoV-2 virion structure

The SARS-CoV-2 virion consists of a lipid bilayer envelope containing the viral (+)ssRNA genome (Fig. 1.4) (81). This genome is packaged in a dense nucleocapsid structure composed of viral nucleoproteins (82, 83). The viral lipid bilayer envelope harbors viral membrane and envelope protein (82). Furthermore, SARS-CoV-2 spike glycoprotein is integrated into the viral envelope (82). Binding of this spike glycoprotein to the specific SARS-CoV-2 receptors is essential for viral entry (84). Due to mutations in the viral spike protein, over time different SARS-CoV-2 variants emerged that lowered the initial success from vaccination and mAbs (12, 63, 66). Hence, targeting of other viral components, like conserved RNA regions with LNA mixmers may be of advantage.
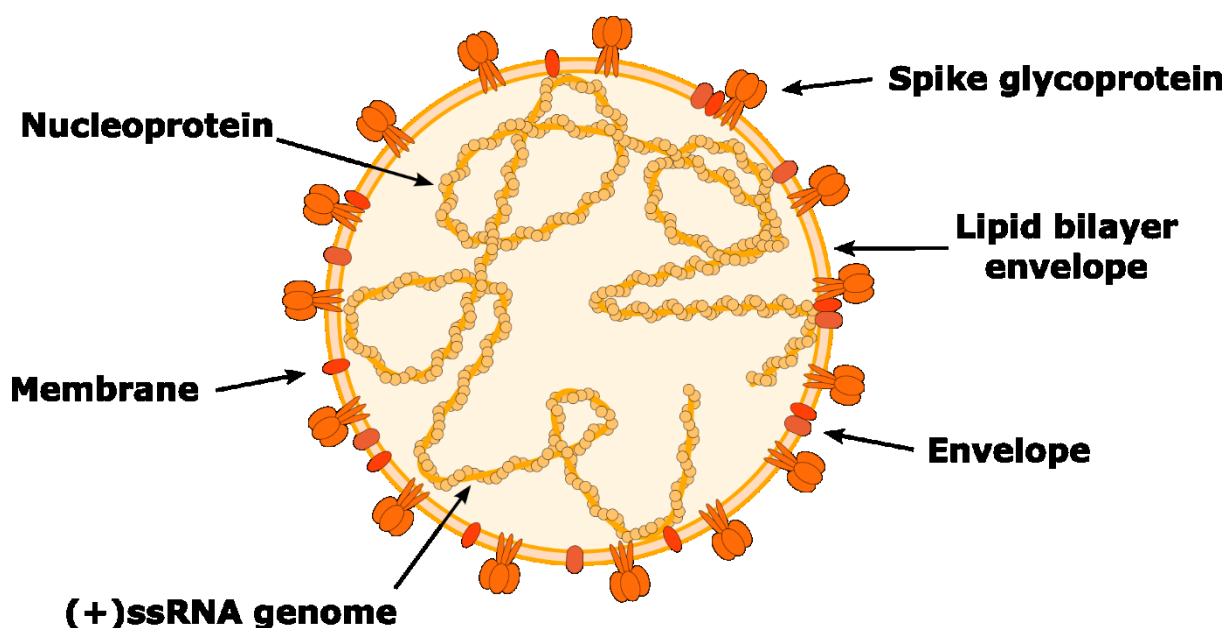
Fig. 1.4 SARS-CoV-2 virion. The SARS-CoV-2 particle or *virion* consists of a cellular membrane-derived lipid bilayer envelope containing the viral (+)ssRNA genome. The SARS-CoV-2 genome is packaged in a nucleocapsid made up by viral nucleoprotein. The SARS-CoV-2 spike glycoprotein, envelope protein and membrane protein are located within the viral lipid bilayer envelope. The viral spike glycoprotein protrudes from the virion.

SARS-CoV-2 replication

Attachment to SARS-CoV-2 target cells is mediated by the SARS-CoV-2 spike glycoprotein that protrudes from the viral envelope and binds to one of SARS-CoV-2's cellular receptors (Fig. 1.5, Attachment) (84, 85). Early during the pandemic, angiotensin-converting enzyme 2 (ACE2) was shown to act as primary receptor for SARS-CoV-2 (85). However, cellular membrane proteins asialoglycoprotein receptor 1 (ASGR1) and kringle domain-containing transmembrane protein 1 (KREMEN1) were recently also shown to function as *bona fide* entry receptors for SARS-CoV-2 (86).
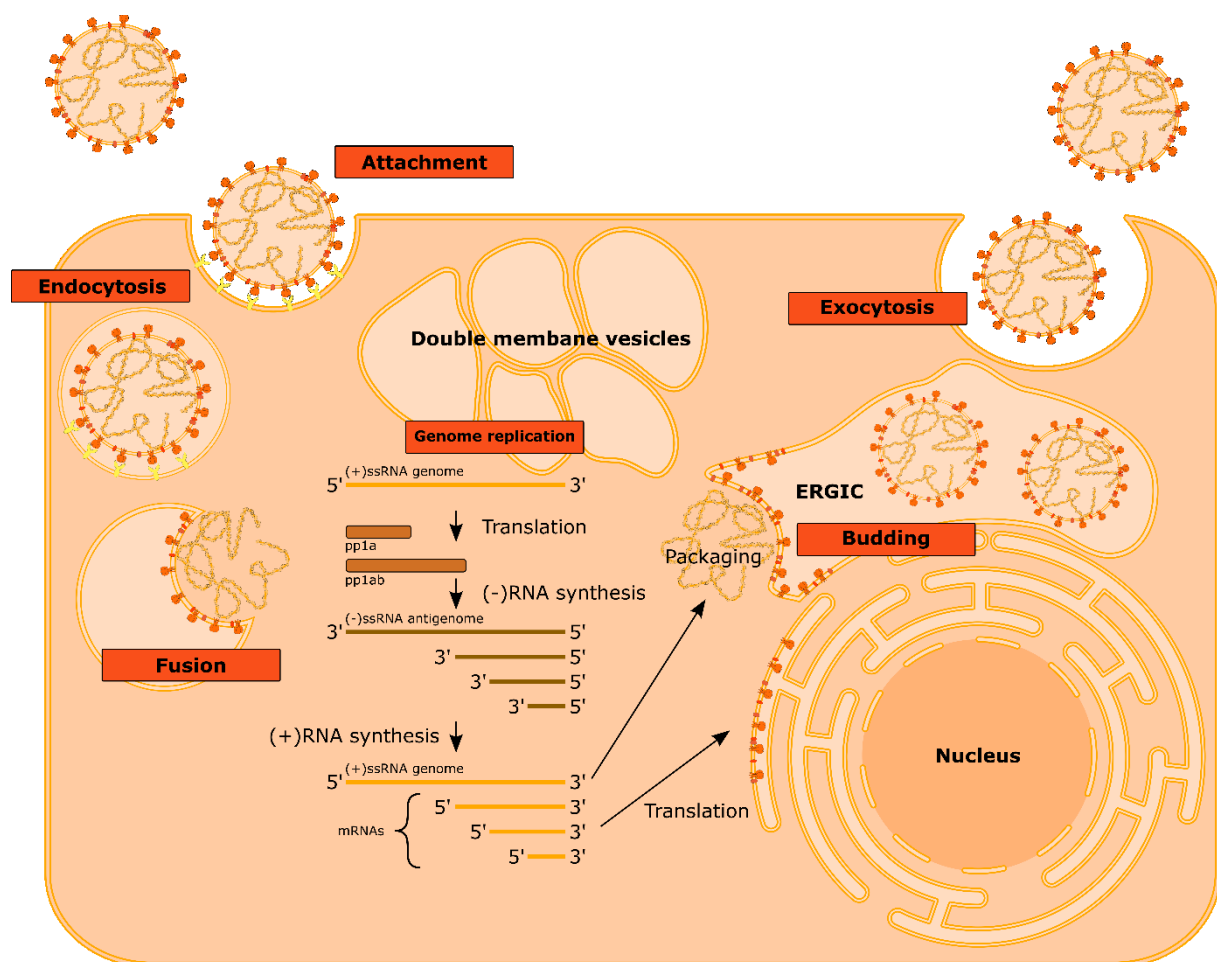
Fig. 1.5 SARS-CoV-2 replication cycle. Attachment of the SARS-CoV-2 virion to the cellular surface by binding of viral spike glycoprotein to one of SARS-CoV-2's receptors induces endocytosis. The viral genome is released into the cytoplasm after pH-dependent membrane fusion within the endosomal pathway. Membrane fusion may also occur at the plasma membrane. The exact site of membrane fusion is suggested to depend on the specific cellular protease that induces membrane fusion by cleavage of the SARS-CoV-2 spike glycoprotein. Genome replication is considered to take place under induction of so-called double membrane vesicles to supposedly protect the viral RNA from innate immunity sensors. Translation of the already capped (+)ssRNA genome results in the generation of viral precursor protein pp1a and via a programmed -1 ribosomal frameshift in pp1ab. Autoproteolytic cleavage of pp1a and pp1ab allows formation of the SARS-CoV-2 RNA-dependend RNA

polymerase or *replicase* complex. This complex generates a *nested* set of (-)ssRNA from the (+)ssRNA genome by discontinuous transcription (See Fig. 1.14). Viral mRNAs and the (+)ssRNA genome are generated by transcription of their (-)ssRNA equivalents. SARS-CoV-2 particles are formed by budding into a so-called ER-Golgi intermediate compartment (ERGIC). Viral egress is via the exocytosis.

Importantly, different cell types were shown to be susceptible to SARS-CoV-2 infection (87-89). This could be due to the broad expression of these receptors throughout the human body (86, 90). Interestingly, the work performed during this thesis showed that also neurons within human 3D-brain organoids are susceptible to SARS-CoV-2, although only to a lesser extent (91). Here, the broad tissue distribution of ASOs may be beneficial in the fight against SARS-CoV-2 (92).

Binding of viral spike glycoprotein to one of the viral receptors mediates endocytosis of the viral particle (Fig. 1.5, Endocytosis) (85). Viral spike glycoprotein is cleaved by cellular proteases in a process called priming (85, 93). This step seems to be primarily induced by cellular transmembrane protease serine 2 (TMPRSS2) (85). In addition to TMRPSS2, other proteases, such as cathepsins L, were shown to be able to prime the SARS-CoV-2 spike glycoprotein (93). Priming of the viral spike, i.e., cleavage of the glycoprotein, is a prerequisite for infectivity, as it is necessary for mediating fusion of the viral membrane with the endosomal membrane (Fig. 1.5, Fusion) (94). This way, the SARS-CoV-2 genome is ultimately released into the cytoplasm (for review about SARS-CoV-2 entry see (84)).

Infection with SARS-CoV-2 induces the formation of so-called double membrane vesicles that are suggested to protect the viral (+)ssRNA genome from innate immunity (Fig. 1.5, Double membrane vesicles) (83, 95, 96). Direct translation of the (+)ssRNA genome results in viral precursor protein pp1a and via a programmed -1 ribosomal frameshift also in pp1ab (Fig. 1.5, Genome replication) (97). Autoproteolytic cleavage by viral proteases generates different viral non-structural proteins (nsps) (97). One main function of these nsps is to form the SARS-CoV-2 RNA-dependent RNA polymerase (RdRp) complex (97). RdRp complex-dependent d*iscontinuous* transcription of the (+)ssRNA genome produces a set of *nested* (-)ssRNA transcripts (97). The term nested describes the fact that these (-)ssRNAs are all produced by transcription from the 3'end of the viral (+)ssRNA genome. Due to a potential template-switch during transcription, these (-)ssRNA are of different lengths (see below).

Importantly, the coronavirus RdRp or replicase complex exhibits a proof-reading function that enables the virus to replicate its 30 kb genome without compromising viral fitness by excessive accumulation of point mutations (82, 97). The point mutations, which nonetheless occur, result in the various variants that circulate in the population, as mentioned earlier.

Subsequent RdRp-dependent transcription of the nested (-)ssRNA products allows generation of all necessary viral mRNAs (97). The full-length (+)ssRNA genome is hereby generated from the full-length (-)ssRNA antigenome (97).

SARS-CoV-2 particle formation is via budding into the so-called ER-Golgi intermediate compartment (ERGIC) (Fig. 1.5, ERGIC) (2). Viral egress was shown to occur via the secretory pathway by exocytosis (Fig. 1.5, Exocytosis) (98, 99).

SARS-CoV-2 (-)ssRNA synthesis

During this thesis, two different viral regulatory sequences were targeted by LNA mixmer application. To understand the underlying idea, the coronavirus (-)ssRNA synthesis, which occurs via discontinuous transcription is described.

Discontinuous transcription is dependent on so-called transcription regulating sequences (TRS), which consist of a core consensus sequence (Fig. 1.6, upper panel) (82). These TRS are located upstream of almost every viral ORF (100). Importantly, one viral TRS is located within the SARS-CoV-2 5' *leader* sequence (100). This TRS is coined TRS-L, whereas all downstream TRS are referred to as TRS-B, with B for *body* (Fig. 1.6, upper panel) (100). To approach inhibition of SARS-CoV-2 replication, one LNA mixmer was designed to mask this TRS-L, which should abrogate (-)ssRNA synthesis.

Another prerequisite for (-)ssRNA synthesis is the binding of certain proteins or protein complexes to the 5' and 3' end of the (+)ssRNA genome, respectively (Fig. 1.6, lower panel) (82, 100). Due to its novelty, SARS-CoV-2 genome binding proteins are not well-studied yet. In the context of other coronaviruses, however, binding of hnRNPs to the genomic 3' end was shown to be important for viral replication (101-105). Hence, another anti-SARS-CoV-2 LNA mixmer was employed to disturb binding of hnRNPs to the SARS-CoV-2 genomic RNA within its 3' end.
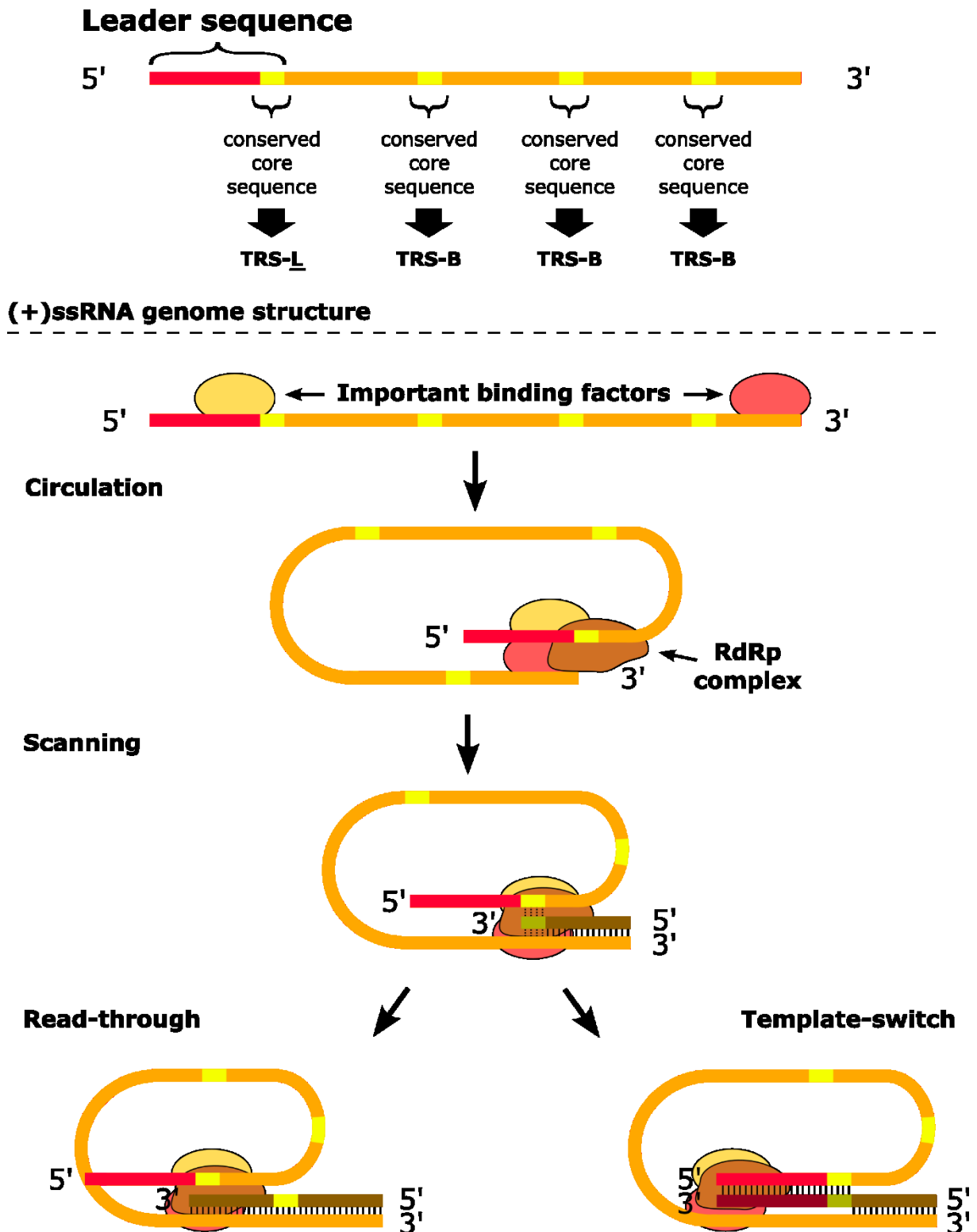
Fig. 1.6 SARS-CoV-2 (-)ssRNA synthesis. (Upper panel) The SARS-CoV-2 (+)ssRNA genome contains a 5' end leader sequence that protects viral RNA from viral non-structural protein 1 (nsp1)-induced endonucleolytic cleavage. A so-called *core consensus sequence* (CCS) is found throughout the viral genome upstream of almost all viral open reading frames (ORFs). These CCS are referred to as coronavirus transcription-regulating sequences (TRS). The TRS within the 5' leader sequence is coined the TRS-L and downstream TRS as TRS-B with B for *body*. (Lower panel) The binding of specific proteins to the 5' and 3' end of the coronavirus genome induces RNA template circulation. Synthesis of (-)ssRNA by the coronavirus RNA-dependent RNA polymerase (RdRp) complex starts at

the 3' end of the viral (+)ssRNA genome. During (-)ssRNA synthesis, base scanning at the conserved TRS-B may result in a template-switch to the TRS-L, which leads to the transcription directly of the coronavirus genomic 5' end and is termed a *discontinuous* transcription. Read-through events at the TRS-B are responsible for the generation of all necessary (-)ssRNA transcripts including the full-length coronavirus (-)ssRNA antigenome (Modified after (100)).

Interaction of the described proteins or protein complexes leads to a circulation of the viral genome (Fig. 1.6, Circulation) (100).

Synthesis of the viral (-)ssRNA starts by recruiting the RdRp complex to the 3' end of the viral genome (Fig. 1.6) (100). While transcribing the (+)ssRNA genome, potential base pairing of the newly synthesized TRS-B within the nascent (-)ssRNA strand with the TRS-L of the (+)ssRNA genome leader sequence may lead to a template-switch of the RdRp complex and hence, a discontinuous transcription (Fig. 1.6, Scanning and Template-switch) (100).

Read-though events during (-)ssRNA synthesis are important to allow generation of all (-)ssRNA and therefore also of all viral (+)ssRNA/mRNA species (Fig. 1.6, Read-Through) (100).

Due to the positioning of the TRS-B upstream of viral ORFs, discontinuous transcription is responsible that (+)ssRNA synthesis from the different (-)ssRNA templates produces all necessary viral mRNA transcripts (100).

Although the (-)ssRNA strand synthesis of (+)ssRNA viruses seems to offer a promising target site for LNA mixmer-mediated interference, the induction of double membranous structures throughout the cytoplasm commonly observed during (+)ssRNA virus infection, like here described for the SARS-CoV-2-induced DMVs, may hamper LNA mixmer activity. Therefore, in this work, possible antiviral activity of LNA mixmers is also tested in the context of (-)ssRNA virus infection, where such intracellular morphological changes are not as pronounced or not present at all.

Here, Hazara virus was used as a surrogate model for the also enveloped nairoviruses (order: *Bunyavirales*), a virus family that also includes the highly lethal Crimean-Congo hemorrhagic fever virus. Viral entry of nairoviruses is dependent on endocytosis, like in the case of coronaviruses (106). Moreover, the nairovirus genome is exclusively replicated in the cytoplasm (106). Therefore, investigating a possible interference with Hazara virus replication by LNA mixmers was sought to be a genuine approach to elucidate potential differences in antiviral LNA mixmer acitivity with respect to (+)ssRNA and (-)ssRNA viruses.

1.4   Hazara virus

1.4.1   Hazara virus as surrogate model for Crimean-Congo hemorrhagic fever virus

The most well-known member of the nairoviruses is without doubt Crimean-Congo hemorrhagic fever virus (CCHFV). First recognized in the 1940s, CCHFV is a tick-borne nairovirus with an estimated case fatality rate of up to 40 % during some outbreaks (WHO) (107). Besides being transmitted via tick bites, it can be transmitted via contact to animal tissue or blood due to its transmission cycle in livestock (108, 109).

After an incubation period of usually 1 to 3 days, symptoms of Crimean-Congo hemorrhagic fever (CCHF) that may occur are fever, myalgia, dizziness, vomiting, diarrhea, confusion, rash and sometimes hepatitis or disturbed kidney functions (WHO) (107).

Since there are still no specific antiviral drugs or licensed vaccines available that were evaluated with a positive outcome by clinical trials, treatment of CCHF remains primarily supportive (107). Together with its potential to cause outbreaks, the WHO, therefore lists CCHF as one of the diseases that are prioritized within the WHO's research and development blueprint (Fig. 1.7).

Overall, therefore, research into novel antiviral agents to tackle CCHF is important. Hence, this thesis aims to provide first evidence if LNA mixmers may be used to inhibit its replication. Here, it has to be mentioned that CCFHV is classified a risk group-4 pathogen. Hence, research into its molecular biology and specific antivirals is restricted to biosafety level-4 facilities, which may be partially responsible for the still vast knowledge gaps regarding its replication cycle and the lack of specific antivirals.

To overcome the necessity of biosafety level-4 conditions, CCHFV's close relative Hazara virus (HAZV) may be used to, nevertheless, obtain insights into the nairovirus replication cycle. HAZV belongs to the same genus as CCHFV, but is not known to cause human disease. Therefore, it is classified only a risk group-2 pathogen.

Hence, this thesis made used of HAZV as a commonly used surrogate model for CCHFV to test the ability of LNA mixmers to inhibit nairovirus replication after unassisted delivery to infected cells.

WHO's priority diseases for epidemic preparedness

- COVID-19

- **Crimean-Congo haemorrhagic fever**

- Ebola virus disease and Marburg virus disease

- Lassa fever

- Nipah and henipaviral diseases

- Middle East respiratory syndrome coronavirus (MERS-CoV) and Severe Acute Respiratory Syndrome (SARS)

- Rift Valley fever

- Zika

- "Disease X"*

*Disease X represents the potential threat that a yet unknown pathogen or a pathogen that is not yet known to cause human disease will cause a serious epidemic in the future

Fig. 1.7 World Health Organization's list of diseases with highest priority regarding research and development in public health emergency contexts. The World Health Organization (WHO) lists diseases that pose the highest threat to the public health based on their epidemic potential. These diseases are given priority with respect to the WHO's research and development (R&D) blueprint.

1.4.2   Nairovirus molecular biology

Due to the not well-studied replication cycle of nairoviruses, this chapter therefore illustrates its key aspects, which may become important for LNA mixmer design and function.

Nairovirus virion structure

Hazara virus (HAZV) and CCHFV are members of the *Nairoviridae* virus family. The nairovirus virion contains three genomic segments (L, M and S segment), which are encapsidated by viral nucleocapsid protein (Np) (106). Viral Np protein is previously translated from viral S segment mRNA (Fig. 1.8) (106). Together with the L segment-encoded viral L protein, an RNA-

dependent RNA polymerase (RdRp), the encapsidated RNA segments form ribonucleoprotein complexes (RNPs) (106). Since the 5' and 3' terminal ends of each genomic segment exhibit a high complementarity, these RNPs form so-called *panhandle* or *quasicircular* structures (109). This high complementarity is considered to play a role in promoter activity and may therefore serve as promising LNA mixmer target site (110-112).
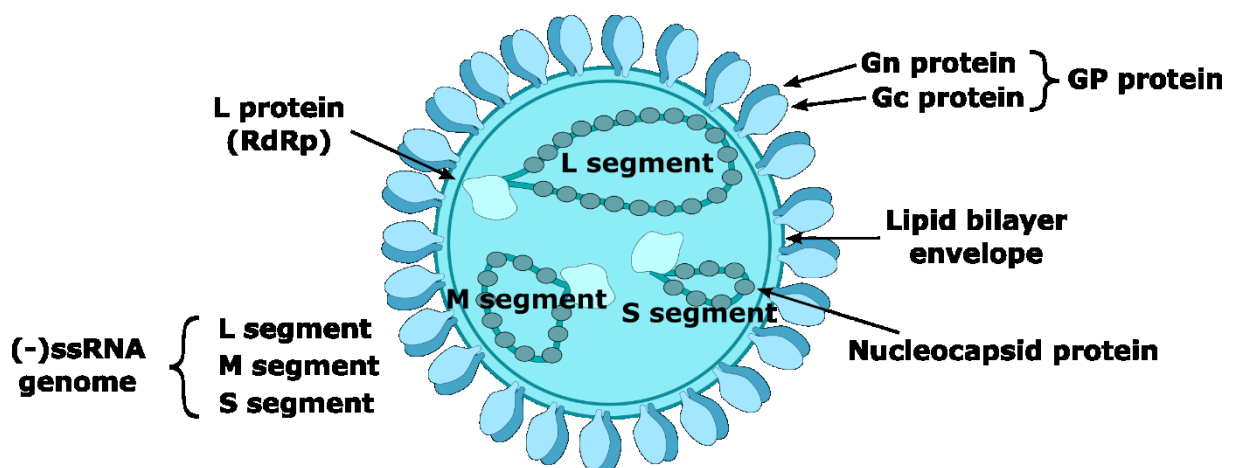
Fig. 1.8 Nairovirus virion. The Nairovirus virion contains the three (-)ssRNA genomic segments L, M and S that form ribonucleoprotein complexes together with viral nucleocapsid protein and viral L protein, which is an RNA-dependent RNA polymerase (RdRp). The tri-segmented genome is surrounded by a viral lipid bilayer envelope containing viral glycoprotein (GP) Gn and Gc.

The genomic RNPs are shielded from the environment by a lipid bilayer envelope (106). This envelope contains viral Gn and Gc protein, which are produced by proteolytic cleavage of the M Segment-encoded glycoprotein precursor (GPC) (106). These two proteins form a heterodimer and function as viral glycoprotein (GP) (106).

Nairovirus replication

Nairovirus replication starts by binding of the viral Gn-Gc heterodimer to the cellular surface (Fig. 1.9, Attachment) (113). Knowledge about specific viral receptors is lacking. However, DC-SIGN and nucleolin were identified to promote CCHFV entry (109, 114).

Like SARS-CoV-2 particles, nairovirus particles are subsequently endocytosed, which, again, may render the viral RNA more susceptible to simultaneously endocytosed LNA mixmer compared to cellular RNA (Fig. 1.9, Endocytosis) (106). Membrane fusion occurs within the endosomal pathway, which leads to the release of the genomic RNP complexes into the cytoplasm, is pH-dependent (Fig. 1.9, Fusion) (106).
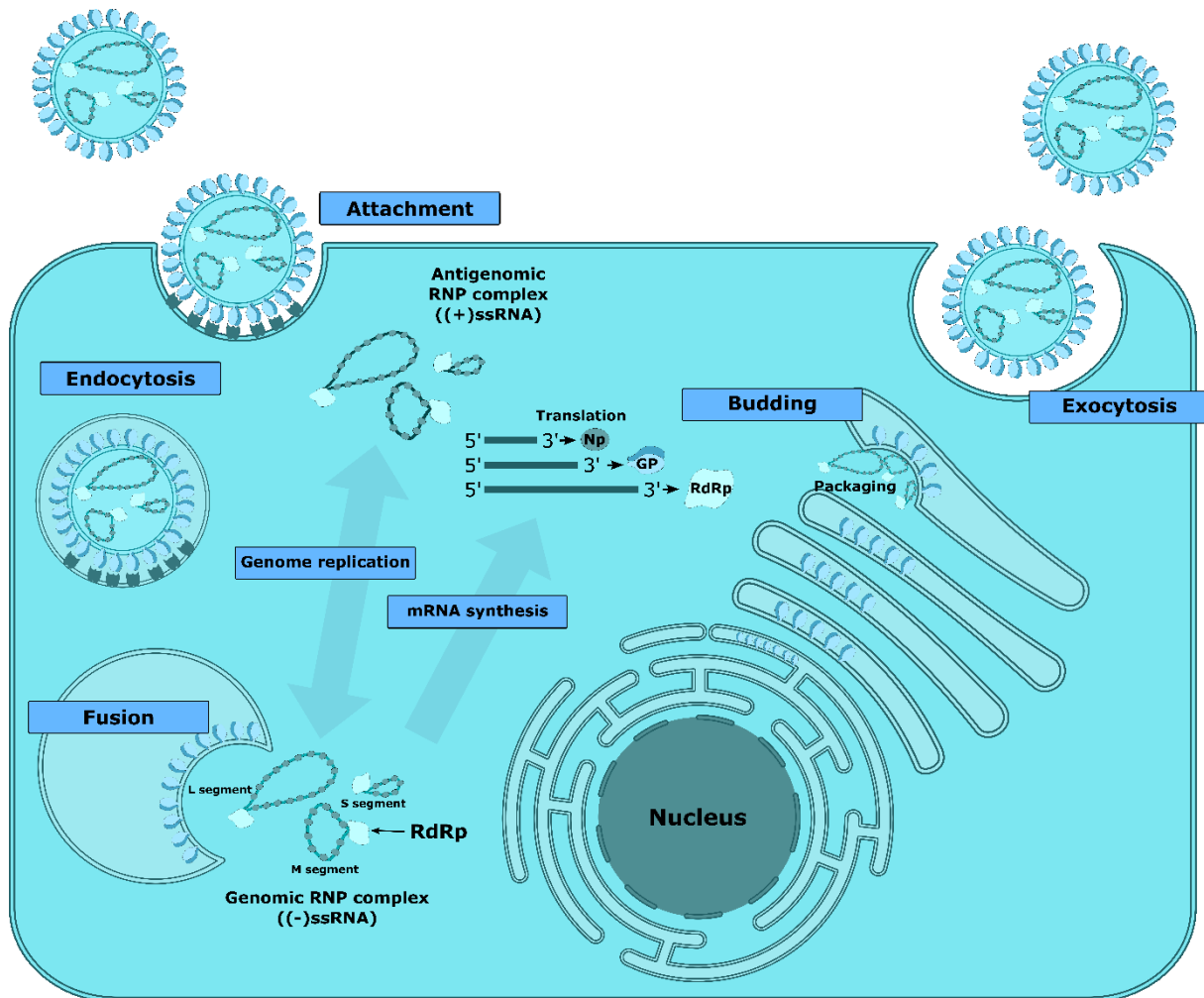
Fig. 1.9 Nairovirus replication cycle. After viral Gn-Gc heterodimer-dependent attachment to a susceptible host cell, viral particles are taken up via endocytosis. Membrane fusion occurs within the endosomal pathway. This way, the genomic (-)ssRNA segments are released into the cytoplasm. Viral RNA-dependent RNA polymerase-dependent transcription of the genomic (-)ssRNA segments generates viral mRNA and antigenomic (+)ssRNA. Viral mRNA codes for the RdRp, viral glycoprotein precursor (GPC) and nucleocapsid protein (Np). The GPC is cleaved into Gn and Gc, which are transported to the endoplasmic reticulum and form the viral glycoprotein (GP) complex. Formation of new nairovirus particles occurs at the Golgi by packaging of the genomic (-)ssRNA segments and budding into the cellular endomembrane system. The release of newly formed viral particles is via exocytosis.

Viral RdRp-dependent transcription of genomic (-)ssRNA produces viral mRNA that is translated into the different viral proteins (Fig. 1.9, mRNA synthesis) (106). Transcription is hereby further dependent on complementary regions within the 5' and 3' terminal non-translated regions of each genomic segment (106, 112). Hence, these complementary regions that also contribute to the before-mentioned panhandle structure, may be referred to as promoter elements (PEs) (112).

The L Segment codes for the viral RdRp, whereas the M Segment codes for the GPC, which is cleaved by host cell proteases into the N-terminal Gn and the C-terminal Gc (106). Due to contained signal peptides, Gn and Gc are transported to the endoplasmic reticulum (106). The S segment codes for viral nucleocapsid protein (Np) (106).

Besides viral mRNA, transcription of genomic (-)ssRNA produces so-called antigenomic (+)ssRNA. Antigenomic (+)ssRNA is a necessary intermediate product during replication of the viral genomic (-)ssRNA segments (Fig. 1.9, Genome replication) (106).

Packaging of the genomic (-)ssRNA segments into newly formed viral particles occurs at the Golgi apparatus during budding of newly formed viral particles into the cellular endomembrane system (Fig. 1.9, Budding) (106). Viral particles are released from the host cell via exocytosis (Fig. 1.9, Exocytosis) (106).

Overall, the work with the *Nairoviridae* member HAZV will perfectly complement the here performed study on the potential of LNA mixmers to inhibit cytoplasmic RNA virus replication. While including SARS-CoV-2 and HAZV, a direct comparison of antiviral LNA mixmer activity against cytoplasmic (+)ssRNA and (-)ssRNA viruses is possible.

Given the profound inhibition of HIV-1 that was previously shown for LNA mixmers targeting the two viral splicing regulatory elements (SREs) G_{I3}-2 and ESE_{tat} in infected T-cell lines and primary T-cells, this thesis, furthermore, aims to elucidate whether SREs provide highly accessible sites for LNA mixmer binding, which ultimately results in inhibition of viral replication (1).

Having with HIV-1 a first model virus against which antiviral LNA mixmers were already published, in this context, the activity of LNA mixmers against Influenza A virus will be analyzed.

Influenza viruses, unlike corona- and nairoviruses, have to import their genomic RNA into the nucleus where pre-mRNA splicing of viral transcripts is required to produce all viral gene products (106). In this respect, Influenza viruses are closer to the retroviruses including HIV-1. Since the previous study showing LNA mixmer-mediated inhibition of HIV-1 targeted two of HIV-1 SREs, it was suggested that Influenza A virus will present another promising candidate virus, which may be susceptible to LNA mixmer-mediated inhibition when targeting viral SREs (1).

However, in contrast to retroviruses, Influenza viruses do not integrate their genome into the host genome, but replicate their genomic segments independently of the host DNA (106). Hence, given the still vast knowledge gaps regarding to nuclear ASO activity (see above), testing LNA mixmers against Influenza virus will provide important information on how

different replication cycles, with respect to genome polarity and place of genome replication, may influence LNA mixmer activity.

1.5 Influenza A virus

1.5.1 Influenza A virus epidemiology

Influenza disease, which is generally referred to as *the flu*, is primarily caused by Influenza A and B virus infection (115). By predominantly affecting the respiratory tract, transmission is via virus containing droplets (116).

In countries with temperate climates, seasonal Influenza epidemics commonly occur. Annually, Influenza viruses cause an estimated 1 billion cases worldwide, of which 3 to 5 million are severe cases and 290,000 to 650,000 result in influenza-related death (WHO).

Due to their segmented genomes, Influenza virus co-infection may lead to reassortment of genomic segments (117). To distinguish this additional driver of virus evolution from *genetic drift*, which is based on the appearance of point mutations, the occurrence of such reassortment events is referred to as *genetic shift* (117).

These reassortment events, which are only observed within the four Influenza genera (Influenza A, B, C and D virus), can lead to the emergence of novel Influenza types with the potential to spread around the world (106, 118, 119).

1.5.2 Pathogenesis – Influenza disease

After an incubation period of about 2 days, Influenza (flu disease) is typically accompanied by fever, cough, headache, muscle and joint point. Without treatment, most infected individuals usually recover within a week (WHO) (115).

However, IAV infection may result in severe disease, which is responsible for the observed 290,000 to 650,000 Influenza-related deaths per year (115). According to the WHO, individuals that are at greater risk of severe disease are pregnant women, young children, people of old age, individuals that suffer from chronic medical conditions and, of course, those under immunosuppression (WHO).

Of the different compounds available to treat Influenza, only the neuraminidase inhibitors are commonly used nowadays (120). However, administration may have to occur within 24 to 48

hours post-infection to show beneficial effects (Pers. comm. with Dr. Ortwin Adams, Institute of Virology, University Hospital Düsseldorf). Furthermore, even if administered in time, there is still conflicting data about the usefulness of these anti-Influenza virus drugs (120).

Hence, novel antiviral agents against Influenza are of great need to reduce the total number of related deaths each year and to curb future pandemics.

1.5.3 IAV molecular biology

IAV virion structure

Influenza A viruses harbor eight different genomic (-)ssRNA segments, which are encapsidated in a nucleocapsid (Fig. 1.10) (121). This nucleocapsid is formed by viral nucleocapsid protein (NP) binding to the viral RNA (122). In addition to viral NP, an IAV RdRp complex consisting of viral PB1 (polymerase basic protein 1), PB2 (polymerase basic protein 2) and PA (polymerase acidic protein) binds to each genomic segment (106). Hence, the genomic segments are present as RNP complexes within the virions (122).
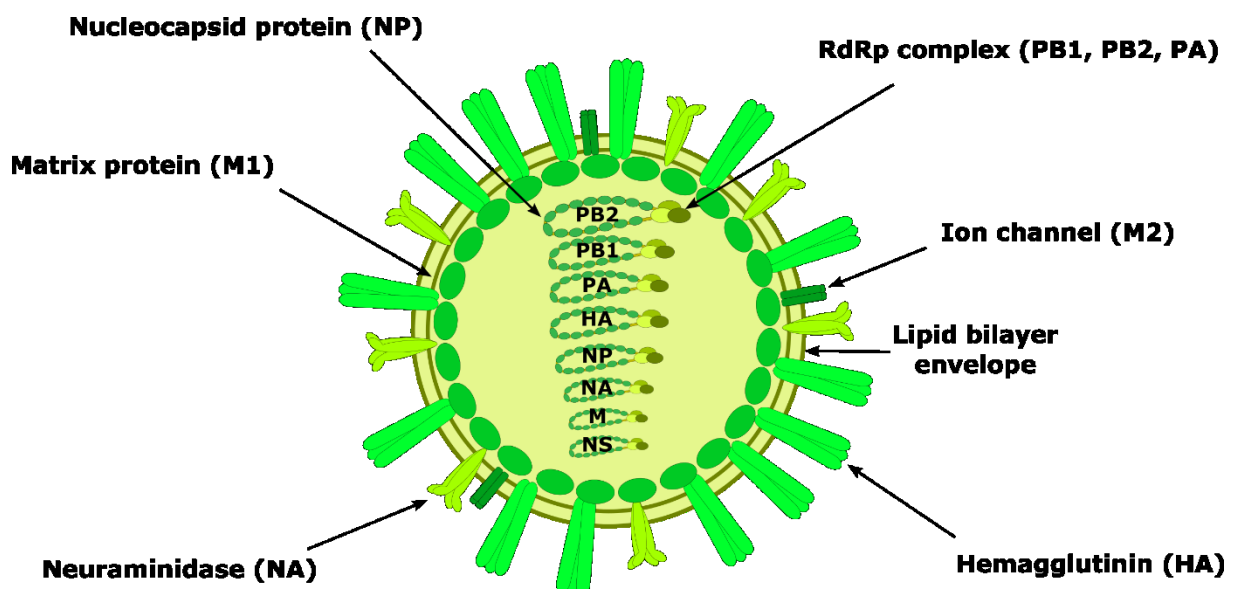
Fig. 1.10 Influenza A virus virion structure. The Influenza A virus (IAV) particle or virion contains the eight genomic (-)ssRNA segments (PB2, PB1, PA, HA, NP, NA, M, NS), which are bound by viral nucleocapsid protein (NP) and the viral RNA-dependent RNA polymerase (RdRp) complex together forming RNP structures. The IAV virion further consists of a lipid bilayer envelope containing viral neuraminidase (NA), hemagglutinin (HA) and the M2 ion channel. A layer of IAV matrix protein (M1) lines the inner side of the viral envelope.

Like nairovirus (-)ssRNA genomic segments, IAV genomic segments form quasicircular panhandle structures that are observable via electron microscopy (106).

The genomic RNP complexes are surrounded by a lipid bilayer envelope derived from the cellular plasma membrane (106). This viral envelope contains trimeric IAV hemagglutinin (HA) as well as tetrameric neuraminidase (NA) and M2 protein (113, 123).

The inner surface of the viral envelope is lined by IAV matrix protein (M1) (124).

IAV replication

The Influenza A virus replication cycle starts by binding of the trimeric HA protein to sialic acid containing cellular proteins or lipids presented on the cellular surface (Fig. 1.8, Attachment) (123).

Afterwards, IAV particles are endocytosed, which is similar to the entry of SARS-CoV-2, HAZV, and HIV-1 (Fig. 1.11. Endocytosis). Within the endosomal pathway, the multifunctional M2 protein serves as ion channel to acidify the interior of the virion (125). This contributes to the dissociation of the viral RNP complexes from the viral particle, which later on facilitates the release of the viral RNP complexes into the cytoplasm (125).

After trafficking within the endosomal pathway, the low pH finally triggers membrane fusion by inducing a structural change within the viral HA protein (Fig. 1.11, Fusion) (125). This, way the viral RNP complexes are released into the cytoplasm, where anti-IAV LNA mixmers may already bind viral target RNA.

Nuclear localization signals (NLS) within IAV PB1, PB2, PA and NP allow the viral RNP complexes to be actively transported into the nucleus. Nuclear import is an essential step during IAV replication (2).

Within the nucleus, the viral RdRp complex generates viral mRNA from the genomic (-)ssRNA segments (126).

Hereby, splicing of IAV M and NS segment-derived pre-mRNA is necessary to later produce all IAV proteins after nuclear mRNA export (127).

Besides viral mRNA, the genomic (-)ssRNA, also referred to as vRNA, is transcribed into antigenomic (+)ssRNA, which is also referred to as cRNA (106). IAV replicates its genome by transcribing the generated antigenomic (+)ssRNA back into the (-)ssRNA segments (Fig. 1.11, Genome replication) (106).

In the meantime, the majority of IAV protein is transported into the nucleus to participate in processes like mRNA synthesis, genome replication or the nuclear export of newly generated viral (-)ssRNA genomes (Fig. 1.11) (2).
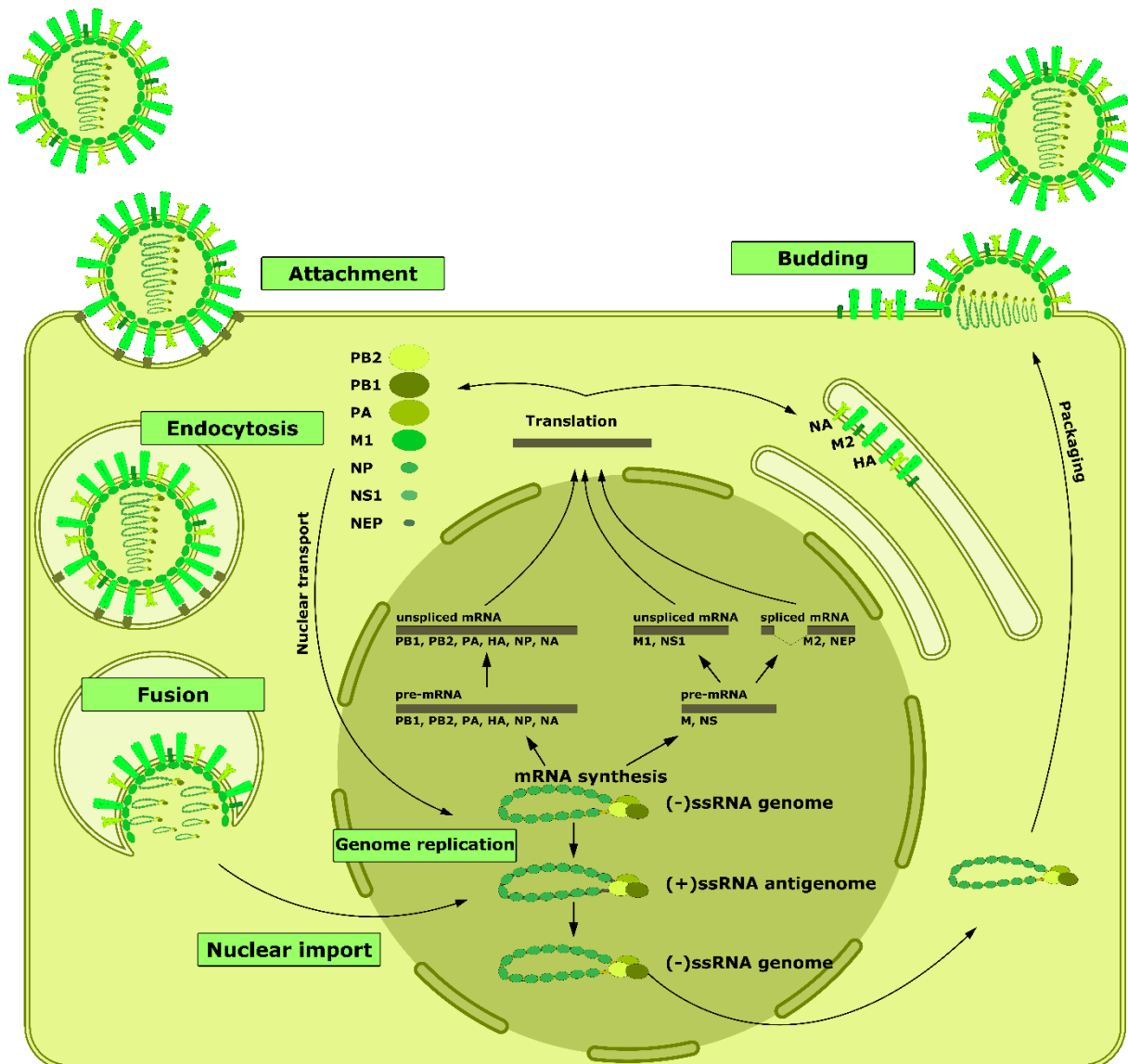
Fig. 1.11 Influenza A virus replication cycle. Attachment of viral particles to susceptible cells is via binding of viral hemagglutinin (HA) to sialic acid-containing proteins and lipids on the cell surface. After endocytosis, pH-dependent membrane fusion releases the eight viral genomic (-)ssRNA segments into the cytoplasm. Nuclear localization signals within Influenza A virus (IAV) PB1, PB2, PA and NP, which are bound to the viral genome segments, leads to nuclear import. Transcription of the IAV genomic segments leads to the generation of viral mRNA and antigenomic (+)ssRNA as intermediate for genome replication. The IAV M and NS pre-mRNA is spliced to generate unspliced and spliced mRNA species. Transcription of the antigenomic (+)ssRNA results in new (-)ssRNA genomic segments that are transported into the cytoplasm. Translation of the different IAV mRNA species in the cytoplasm produces the viral proteins PB1, PB2, PA, M1, PA, NP, NS1 and NEP which all have to capacity for nuclear import. Viral NA, M2 and HA are processed in the Golgi before being transported to the plasma membrane. Budding of IAV particles finally occurs at the plasma membrane.

The current model for nuclear export of the IAV genomic (-)ssRNA suggests that viral M1 protein binds to the genomic RNP complex and viral nuclear export protein (NEP) simultaneously binds to viral M1 protein. IAV NEP then interacts with cellular CRM1 to achieve nuclear export of the RNP complex (106).

While most of the viral proteins are transported into the nucleus, IAV NA, M2 and HA are processed in the Golgi and afterwards transported to the plasma membrane (Fig. 1.11) (106).

Budding of IAV particles occurs via outward curvature of the cellular plasma membrane (Fig. 1.11, Budding) (106). Incorporation of the viral RNP complexes into off-budding particles is most likely mediated by binding of the viral RNP complexes to M1 protein, which further binds the cytoplasmic tails of viral glycoproteins (106).

Here, different models were suggested to explain the packaging of all eight IAV genomic (-)ssRNA segments into a single virion (106). Recent evidence supposes that non-uniform binding of viral NP to each segment is involved that allows RNA-RNA interaction between individual (-)ssRNA segments to occur at NP-free RNA sites (106).

At a final step before release of IAV particles is possible, IAV NA protein cleaves sialic acid molecules from the cell surface that would otherwise retain the viral particles to the plasma membrane by binding to IAV HA protein present on each viral particle (106). Importantly, the viral NA protein also cleaves of sialic acid from the glycosylated IAV proteins. This step is necessary to prevent aggregation of free virions (106).

After the work with SARS-CoV-2, HAZV and IAV will advance our understanding of how LNA mixmers may be used to inhibit viral replication, this thesis aims at understanding LNA mixmer activity in different virus-infected cell lines. Given the already obtained knowledge on the profound antiviral activity of the published anti-HIV-1 LNA mixmers together with the still limited living standards of the 37 million HIV-1 infected individuals, this thesis investigated the use of one of these anti-HIV-1 LNA mixmers in different HIV-1 target cell lines with relevance to the clinical picture of HIV-1 infection (1).

Furthermore, based on the knowledge on LNA mixmer function obtained throughout this thesis, additional viral target sites for LNA mixmer administration were elaborated.

1.6   Human Immunodeficiency Virus Type 1

1.6.1   Human Immunodeficiency Virus epidemiology

More than 37 million people were living with an HIV infection in 2020, according to the World Health Organization (WHO) (Fig. 1.12). This number corresponds to approx. 0.5 % of the world population. For 2020 alone, a total of 1.5 million new infections with HIV were estimated. The number of deaths due to HIV-1-related causes was estimated to be 680,000 for 2020 (WHO). As a consequence, HIV infection remains one of the top 10 causes of death in low-income countries (WHO, 2019).

In Germany, an estimated 1 in 1000 people were living with an HIV infection in 2020 (Fig. 1.12) (Robert Koch Institut). The Robert Koch Institut (RKI) estimates that approx. 91,400 people lived with an HIV infection in Germany that year. Of these 91,400 presumed infections, more than 9,500 were undiagnosed.

Data of 2020	Worldwide[a]	Germany[b]
People living with HIV		
total	37 mio	91,400
per population [%]	0.48	0.11
New HIV infections	1.5 mio	2,600
HIV-related deaths	680,000	380

[a]WHO 2020, [b]RKI 2020

Fig. 1.12 HIV epidemiology. HIV infections worldwide and within Germany based on the 2020 data from the World Health Organization (WHO) and the Robert Koch Institute (RKI), respectively. The number of people living with HIV per population was calculated based on the respective population in 2020. Shown is an HIV-1 particle and the world map.

1.6.2 Pathogenesis – Acquired Immune Deficiency Syndrome

During the acute phase of HIV-1 infection, which is typically 2 to 4 weeks after infection, people may suffer from flu-like symptoms (e.g., fever, chills, swollen lymph nodes or night sweats) (113) (Centers for Disease Control and Prevention (CDC)). Following the acute phase, HIV-1 infection becomes latent (113). During this time, the viral load begins to slowly increase again while the number of CD4$^+$ T-cells decreases (113).

At the actual stage of acquired immune deficiency syndrome (AIDS), the immune system is so severely damaged that infected individuals often suffer from a variety of opportunistic infections to which they may then succumb (113).

1.6.3 Antiretroviral therapy

Although over the years many different vaccine candidates were tested in clinical trials, there are still no vaccines available to date that reliably prevent HIV-1 infection (128). Further, there is still no common sterile cure for HIV-1 infection. This is especially due to the stable integration of the viral provirus into the host genome and the persistence of HIV-1 in so-called viral reservoirs (129).

However, research into the complex HIV-1 replication cycle rendered treatment of HIV-1-infected individuals possible (113). To treat HIV-1-infected individuals, therapeutic compounds are nowadays available that interfere with different steps of HIV-1 replication (113). Administration of these compounds as part of *highly active antiretroviral therapy* (HAART), also known as *combined antiretroviral therapy* (cART), is able to completely prevent progression from mere HIV-1 infection the potential fatal state of AIDS (113).

State-of-the-art antiretroviral compounds may be divided into different classes according to the step of HIV-1 replication that is inhibited (113, 130). These classes are typically referred to as the entry inhibitors (A), reverse transcriptase inhibitors (B), integrase inhibitors (C), protease inhibitors (D) and capsid inhibitors (E) (Fig 1.13).

Overall, HAART made it possible to reduce viral titers below the limit of detection in treated patients (113). It further prevents progression of HIV-1 infection to the stage of AIDS allowing infected individuals to live a normal life span (131). However, as things stand today, antiretroviral therapy must be taken for the rest of the patient's life (132).

Therefore, considerable problems are to be expected over time with regard to compliance and long-term toxicities (133, 134). In this context, the various side effects and the possible

emergence of (multi-)resistant HIV-1 strains in particular pose a serious problem (135, 136). Hence, research into novel therapy approaches in urgently warranted.
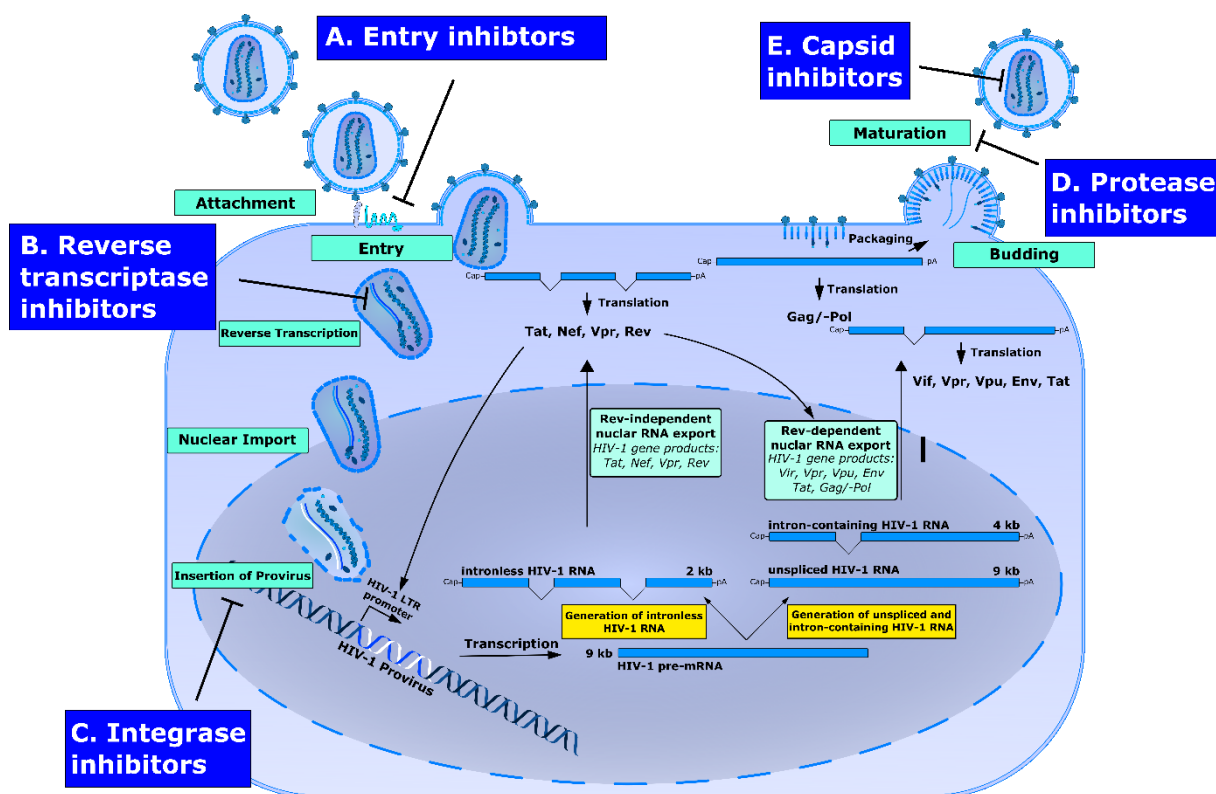
Fig. 1.13 Interference points of antiretroviral therapy against HIV-1 infection. Schematic showing the HIV-1 replication cycle as in Fig. 1.15, but with interference points for current antiretroviral therapeutics. Inhibition of HIV-1 replication can occur at the stage of viral entry (A), reverse transcription (B), integration of the viral DNA into the host genome (C), during maturation by disturbing protease activity (D) or since only recently by interfering with viral capsid formation (E). As the first of its kind, the capsid inhibitor Lenacapavir is still tested in clinical trials, but already showed promising results as the first long-acting antiretroviral drug.

Given their long serum half-life together with their broad tissue distribution, which may render even the viral reservoirs throughout the body accessible, ASOs may offer a very promising addition to the current HAART repertoire.

1.6.4 HIV-1 molecular biology

HIV-1 virion structure

The enveloped HIV-1 virion contains two copies of the viral (+)ssRNA genome (Fig. 1.14) (137). These two RNA molecules are bound by viral nucleocapsid protein (NC or p7) (137). Each RNA

molecule forms a dense nucleocapsid structure with bound NC (137). The nucleocapsid is surrounded by the viral capsid, which is made up by HIV-1 capsid protein (CA or p24) (137). The viral capsid is surrounded by HIV-1 matrix protein (MA or p17) (137). The viral matrix protein forms an inner layer to the viral envelope and in this way stabilize the virion (113). Structural proteins p7, p24 and p17 derive from the same viral precursor protein (Pr55^{Gag}) that is translated from the HIV-1 Gag open reading frame (ORF) (137). During particle formation, HIV-1 Pr55^{Gag} makes up the inner layer of the virion and is cleaved by the HIV-1 protease during or after budding from the cellular membrane (137). This step is part of a process called virus *maturation* (see below).
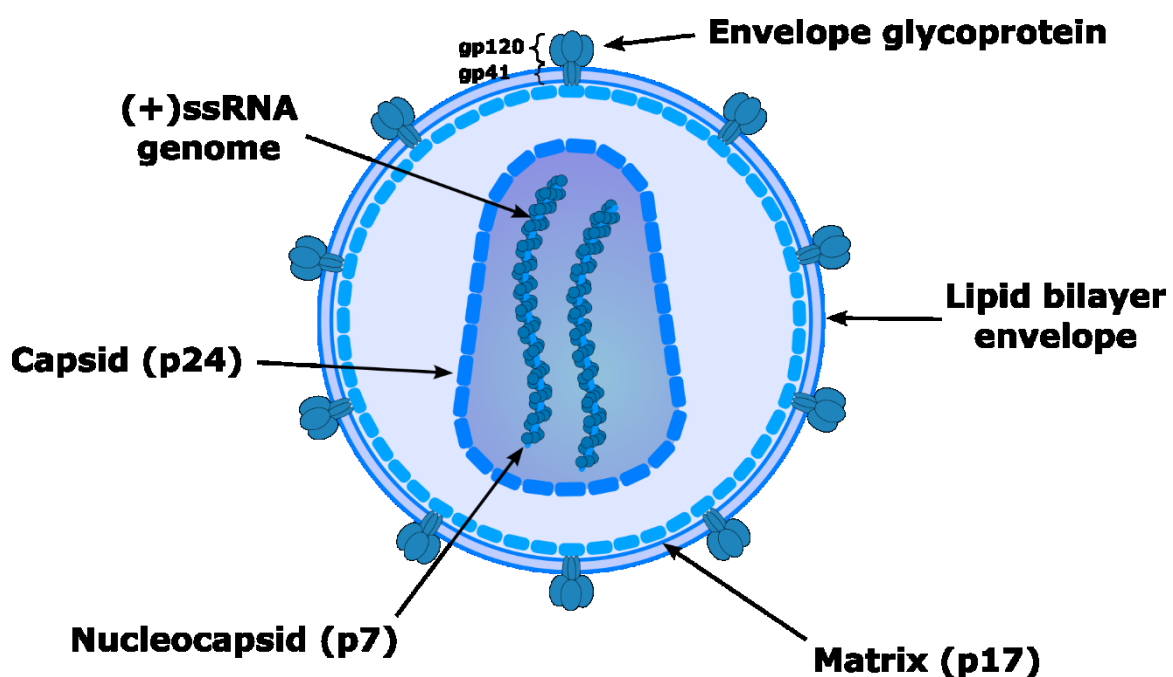
Fig. 1.14 HIV-1 virion. The HIV-1 particle or *virion* consists of a cellular membrane-derived lipid bilayer envelope harbouring HIV-1 envelope glycoproteins. The HIV-1 envelope glycoprotein consists of three heterodimers each made up by a gp41 and a gp120 subunit. HIV-1 matrix (p17) proteins form an inner layer to the viral lipid bilayer envelope. Two molecules of the single-stranded, positive sense HIV-1 RNA genome are densely packed within a nucleocapsid. The nucleocapsid is surrounded by the viral capsid structure. The virion further contains viral proteins that are necessary to complete the viral life cycle after infection of new cells, but that are not shown here.

The HIV-1 envelope glycoprotein (Env) is found throughout the viral lipid bilayer envelope (Fig. 1.14) (137). Viral Env is produced from the viral gp160 precursor protein that is cleaved by cellular furin or furin-like proteases into the C-terminal gp120 and the N-terminal gp41 viral proteins (137, 138). The gp120 and gp41 proteins form a heterodimer, which then forms the Env homotrimer to make up for the viral glycoprotein (138). Here, the three gp41 subunits form the transmembrane domain whereas the gp120 subunits are located on the outer

surface of the viral membrane (137). Binding of gp120 to cellular CD4 is important for virus *attachment* and triggers viral *entry* into new cells (see below) (113).

In addition to binding CD4, the viral Env glycoprotein binds either CXCR4 or CCR5, which serve as so-called co-receptors (113). Here, especially the V3 loop within the gp120 protein is a major determinant (139). Importantly, HIV-1 is able to infect different cell types. Hence, if aiming at inhibition of viral replication, LNA mixmer-exerted activity must be analyzed in the different target cells (113).

The HIV-1 replication cycle

The HIV-1 replication cycle begins with binding of the gp120 receptor binding domain to cellular CD4 (Fig. 1.15, Attachment) (138). Conformational changes of gp120 after interaction with CD4 then also lead to binding of the gp120 V3 loop region with one of HIV-1's co-receptors, CXCR4 or CCR5 (113, 138). Binding of gp120 to CD4 and either CXCR4 or CCR4 mediates insertion of the gp41 fusion peptide (Env amino acids 512 – 527 of HXB2 HIV-1 reference genome) into the host cell membrane by yet another conformational rearrangement (113, 138). This eventually triggers the fusion of the viral envelope with the host cell membrane (138).

This fusion allows the HIV-1 capsid to enter the cytoplasm directly at the plasma membrane (Fig. 1.15, Entry) (138). The viral capsid, which still contains the two copies of the HIV-1 (+)ssRNA genome, is transported into the nucleus by exploiting the cellular cytoskeleton (140). It was very recently shown that still intact viral capsids can be transported through nuclear pores (Fig. 1.15, Nuclear import) (141).

On its way into the nucleus, the viral (+)ssRNA genome is *reverse-transcribed* into a double-stranded DNA molecule by the HIV-1 reverse transcriptase (RT) enzyme (Fig. 1.15, Reverse Transcription) (137). The viral RT is translated from the Pol ORF within the unspliced HIV-1 Gag/-Pol mRNA and was packed beforehand into newly formed viral particles (Fig. 1.15) (137).

In addition to the HIV-1 RT, the HIV-1 Gag/-Pol mRNA also encodes HIV-1 structural proteins p17, p24 and p7 (see above) via the Gag ORF as well as HIV-1 enzymatic viral gene products integrase (IN) and protease (Pro) also via the Pol ORF (137). The HIV-1 Gag-Pol precursor protein is thereby generated through a programmed -1 ribosomal frameshift that occurs during translation of the HIV-1 Gag/-Pol transcript (137).

Upon completion of reverse transcription of the HIV-1 RNA genome, viral integrase mediates stable integration of the now double-stranded viral DNA into the host cell genome (137). From this point on, the integrated HIV-1 genome is referred to as the viral *provirus* (Fig. 1.15, Insertion of Provirus) (137) .
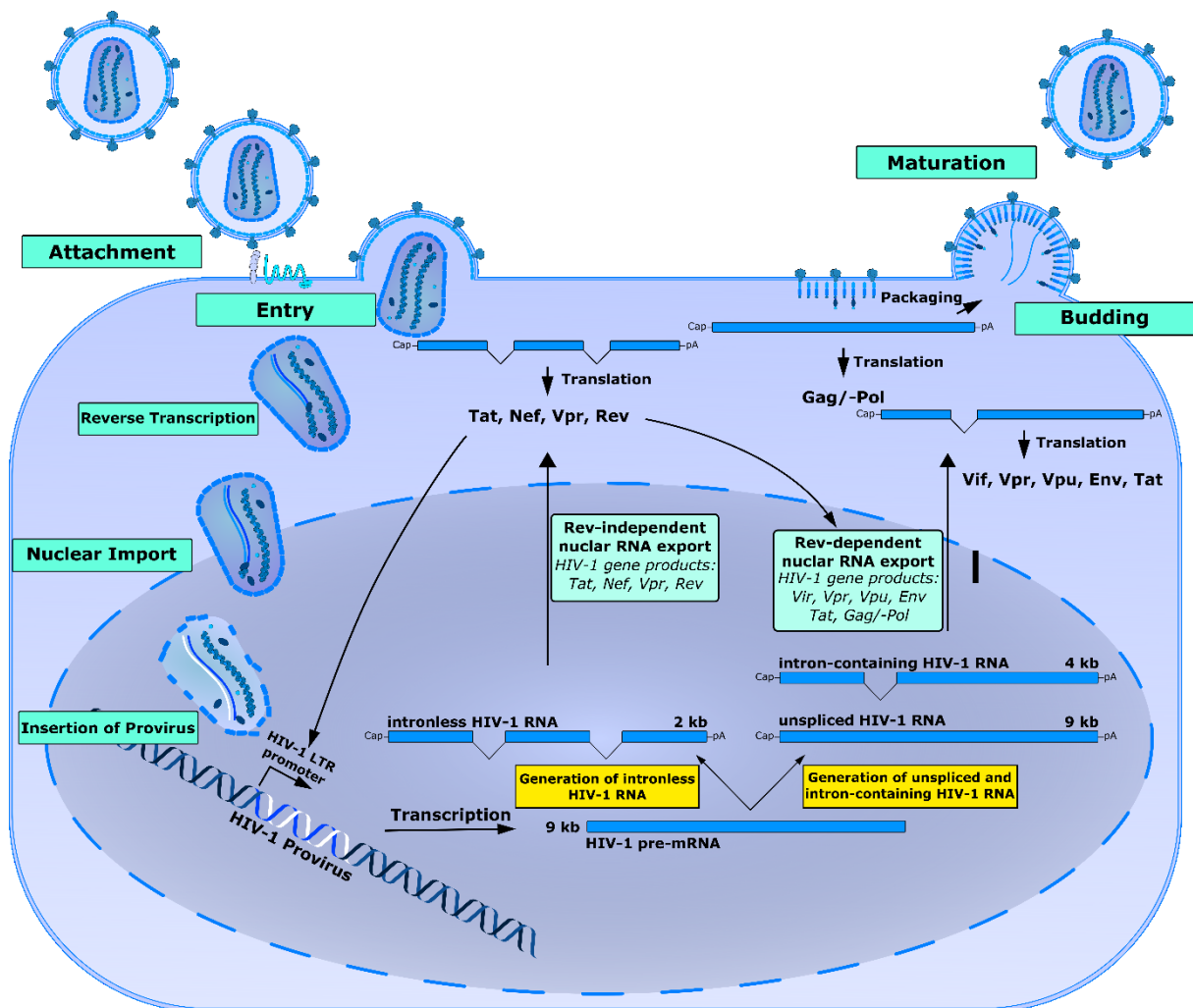
Fig. 1.15 HIV-1 replication cycle. After attachment to the cellular membrane by binding of HIV-1 Env to viral receptor CD4, viral entry is dependent on co-receptor-mediated membrane fusion. Reverse transcription of the HIV-1 RNA genome occurs while the viral capsid is transported into the nucleus. After nuclear import, the now double-stranded HIV-1 DNA is stably inserted into the host genome as HIV-1 provirus. Expression of the viral pre-mRNA is under control of the HIV-1 long terminal repeat (LTR) promoter. From this HIV-1 pre-mRNA, intronless (2kb class), intron-containing (4 kb) and unspliced HIV-1 RNA (9kb) is generated. Nuclear RNA export of the intronless viral transcripts is mediated through cellular mechanisms and results in HIV-1 gene products Tat, Nef, Vpr and Rev. HIV-1 Tat translocates back into the nucleus and enhances HIV-1 LTR promoter activity by binding to a downstream located RNA secondary structure. HIV-1 Rev is also transported into the nucleus, where it binds to the HIV-1 Rev response element (RRE, not shown), and mediates nuclear RNA export of the intron-containing and unspliced HIV-1 RNA transcripts. This leads to the expression of additional viral gene products Vif, Vpu and Env translated from the intron-containing transcripts and HIV-1 Gag/-Pol from the unspliced transcript. HIV-1 unspliced RNA furthermore serves as viral genome and therefore is packaged into newly formed viral particles that budd-off from the cellular membrane. HIV-1 Gag, Gag-Pol and Env gene products were previously transported to the cellular membrane and are also present within or on the viral particles. HIV-1 protease-mediated cleavage of viral precursor proteins leads to the maturation of HIV-1 virions.

HIV-1 long terminal repeat (LTR) promoter-induced transcription of proviral DNA results in the generation of a single viral pre-mRNA species (142). This viral pre-mRNA is processed into the

HIV-1 intronless RNA transcripts of the 2kb RNA class, the intron-containing HIV-1 transcripts of the 4kb class and the unspliced HIV-1 transcript, which is also referred to as the viral 9 kb RNA (Fig. 1.15, yellow boxes) (142).

Intronless viral transcripts are exported from the nucleus via cellular export mechanisms (143). Once in the cytoplasm, the HIV-1 2 kb RNA is translated into viral gene products Tat, Nef, Vpr and Rev (144).

HIV-1 Tat, the *trans-activator of transcription*, is a regulatory protein of approx. 15 kDa, which contains a nuclear location signal (NLS) (137). Hence, HIV-1 Tat translocates into the nucleus where it binds the viral *trans*-activating response element (TAR) at the 5' end of nascent HIV-1 RNA transcripts (137). Binding of HIV-1 Tat to the TAR secondary structure enhances HIV-1 RNA transcription (Fig. 1.15, Tat) (145).

Meanwhile, also HIV-1 Rev shuttles into the nucleus (143). Here, Rev binds to the HIV-1 Rev response element (RRE), which is located exclusively in the intron-containing and unspliced HIV-1 RNA transcripts. This way, Rev mediates nuclear export of these otherwise nuclear-retained viral RNA transcript species (Fig. 1.15, Rev) (see below).

HIV-1 intron-containing RNA codes for the additional viral proteins Vif, Vpu and viral glycoprotein Env (142). The unspliced HIV-1 RNA encodes viral gene products Gag and Gag-Pol while also serving as viral genome (137). Importantly, the viral matrix protein, which is located at the N-terminus of the Gag ($Pr55^{Gag}$) and Gag-Pol precursor protein, is myristoylated (137). Hence, both HIV-1 precursor proteins stick into the plasma membrane after cytoplasmic trafficking (Fig. 1.15, upper right corner) (137, 146).

Binding of the $Pr55^{Gag}$ C-terminal nucleocapsid protein to the HIV-1 *psi* packaging signal (ψ) in *trans* is responsible for packaging of the viral genome into newly formed particles (Fig. 1.15, Packaging) (144).

Finally, budding from the plasma membrane is possible by exploiting the cellular ESCRT machinery (Fig. 1.15, Budding) (146, 147). After budding, virion maturation takes place by HIV-1 protease-mediated cleavage of viral precursor proteins $Pr55^{Gag}$ and Gag-Pol (Fig. 1.15, Maturation) (137).

HIV-1 splicing

During HIV-1 infection, transcription of the proviral DNA by the host transcription machinery results in a single viral pre-mRNA species (137). This pre-mRNA is either spliced to generate viral transcripts of the 2 and 4 kb HIV-1 RNA class or processed without splicing to produce the HIV-1 9 kb RNA (Fig. 1.16) (142).
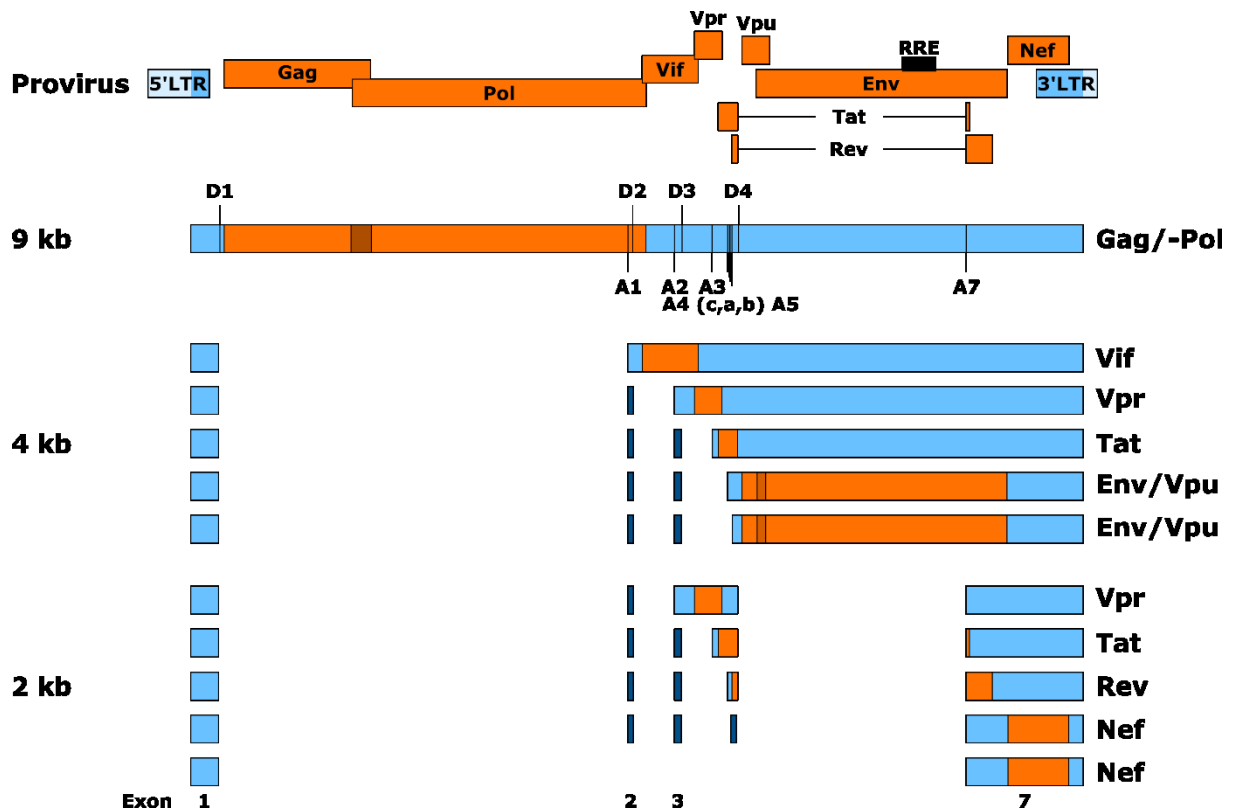
Fig. 1.16 HIV-1 splicing pattern. The HIV-1 provirus including viral open reading frames (ORFs; orange) encompassed by long terminal repeats (LTRs) is illustrated at the top of the sketch. Parts illustrated in light blue are only part of the provirus whereas blue indicates regions transcribed into viral RNA. The unspliced viral RNA (9 kb class) codes for Gag and Gag-Pol gene products and servs as viral genome. Splice donor (D1 –D4) and splice acceptor sites (A1 – A7) that are important for the generation of major HIV-1 RNA transcripts are indicated. Balanced splicing of the viral pre-mRNA results in the intron-containing viral transcripts of the 4 kb class (middle panel) and the intron-less viral transcripts of the 2 kb class (lower panel). The intron-containing RNA transcripts (4 kb class) codes for viral gene products Vif, Vpr, Tat, Env and Vpu. The intron-less 2 kb transcripts code for HIV-1 Vpr, Tat, Rev and Nef. The position of the HIV-1 Rev response element (RRE) is shown only at the HIV-1 provirus, but is present also within the 9 kb and 4 kb viral RNA transcripts. HIV-1 exons 1, 2, 3 and 7 are designated according to the general HIV-1 literature.

Generation of all intronless 2 kb and intron-containing 4 kb RNA transcripts requires excessive, but balanced alternative splicing (142). Hence, this step is highly regulated by at least four splice donor sites and eight splice acceptor sites in combination with numerous splicing regulatory elements (SREs) (Fig. 1.16) (142). In that way, more than 50 different viral mRNA transcript species are produced (148).

The generation of different viral splice variants by removal of specific regions within the HIV-1 pre-mRNA is essential to ensure that the translational start codon of each viral ORF (orange) is at least once the first after the eukaryotic 5'-cap structure (Fig. 1.16). This way, all HIV-1 ORFs will be translated. Of note, translation of the viral Pol ORF is due to the previously

described programmed -1 ribosomal frameshift and translation of the viral Env ORF is by leaky scanning of the upstream Vpu translational start codon (Fig. 1.16) (137, 149).

Since the discovery of HIV-1 in the early 1980s, mutational analysis provided important insights into its different viral regulatory RNA sequences. Along this line, also a huge diversity of HIV-1 SREs were identified that are located throughout the viral genome (142, 150-159).

For instance, Widera et al. identified a so-called G-run SRE within the viral Vpr ORF (153). A G-run SRE constitutes a specific DGGGD pentamer motif with D being adenine, cytosine or guanine (160). This specific G-run was coined G_{I3}-2, as it is the second G-run pentamer motif within HIV-1 intron 3. HIV-1 intron 3 is located between viral splice donor site 3 and splice acceptor site 3 (Fig. 1.16). The G_{I3}-2 SRE was shown to recruit members of the splicing regulatory protein hnRNP F/H family, this way, contributing to the balanced viral splicing (44, 153).

Mutational inactivation of the G_{I3}-2 resulted in aberrant viral splicing that was characterized, for example, by a decreased HIV-1 Tat1 RNA level, whereas the viral Vpr3 transcript level was increased during infection (44). In the same study, masking the G_{I3}-2 by LNA mixmer transfection resulted in the same disturbed viral splicing pattern, which substantiated its importance and moreover, provided evidence that LNA mixmer-mediated masking of SREs may inhibit HIV-1 replication (44).

HIV-1 Rev-mediated nuclear RNA export

Nuclear export of HIV-1 intron-containing and unspliced RNA is dependent on binding of viral Rev protein to the HIV-1 Rev response element (RRE) (Fig. 1.17) (143). The RRE is a complex RNA secondary structure of approx. 350 nucleotides located within the viral Env gene at positions 7710 - 8061 of the HIV-1 HXB2 reference genome (Fig. 1.17, black bar) (143, 161).

In the absence of Rev protein, so-called *cis*-repressive sequences (CRS) recruit cellular nuclear retention factors that occupy the viral transcripts in *trans* and supposedly actively prevent nuclear RNA export (Fig. 1.17, red circles) (162). The exact identity of these proteins is not well-studied, but there are presumably a whole set of these nuclear retention factors that bind to the HIV-1 RNA CRS including also some members of the hnRNP family (162). The CRS are removed from the intronless HIV-1 transcripts, this way allowing nuclear export of the HIV-1 2 kb RNA class via cellular mechanisms as described before (162).
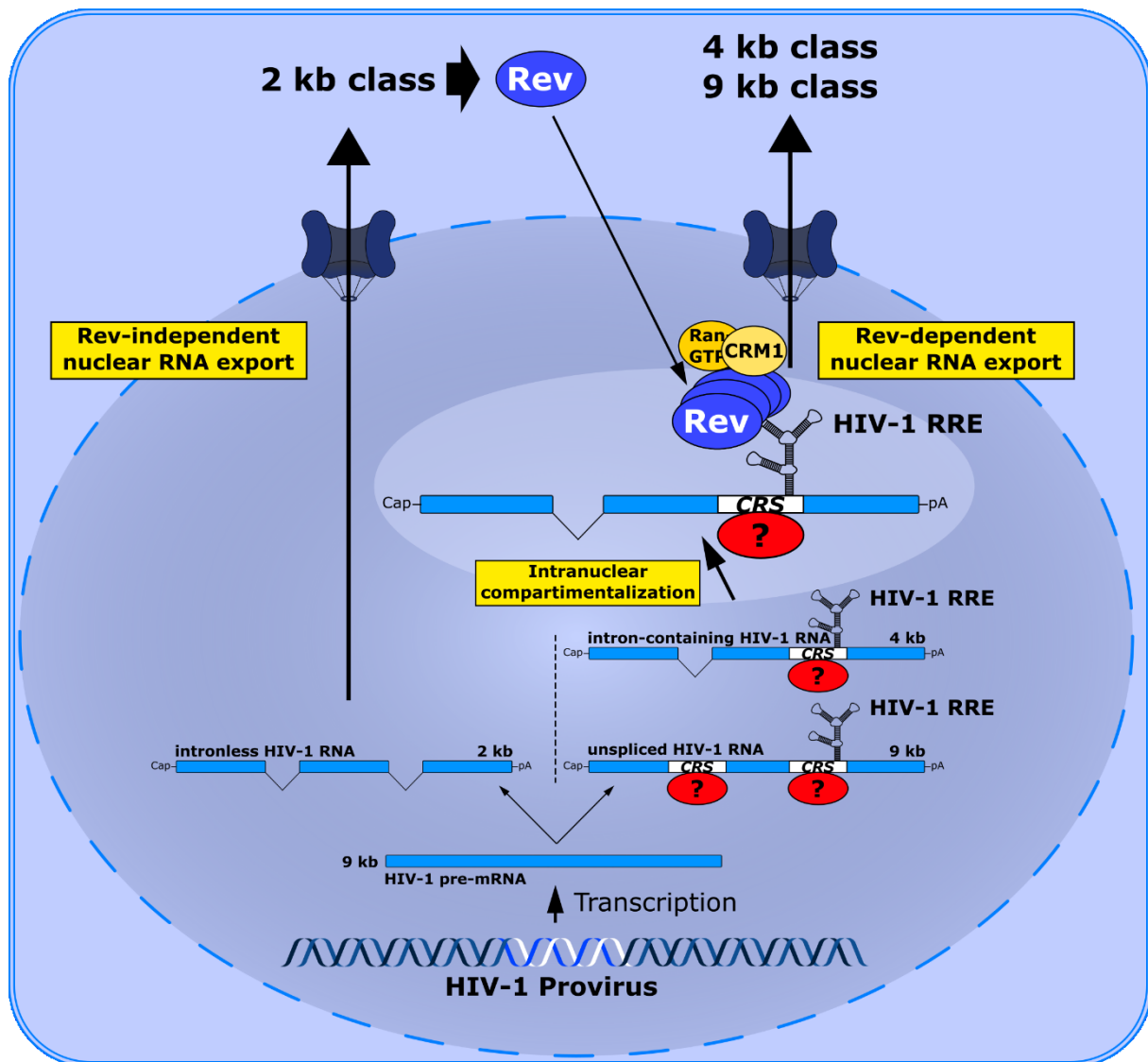
Fig. 1.17 HIV-1 Rev-mediated nuclear RNA export. After generation of the HIV-1 intronless, intron-containing and unspliced viral RNA transcripts, first, only the intronless transcripts are exported from the nucleus via the cellular export machinery (left side). The intron-containing and unspliced HIV-1 RNA transcripts are retained within the nucleus presumably via active retention by binding of nuclear proteins (red) to so-called *cis*-repressive sequences (CRS), which are removed from the intronless transcripts during splicing. Nuclear export of the intronless RNA transcripts results in the generation of viral gene products including HIV-1 Rev (blue). HIV-1 Rev contains a nuclear location signal (not shown) that mediates nuclear import. In the meantime, the running hypothesis suggests that intron-containing and unspliced viral RNA are transported to nuclear domains where these transcripts are more accessible to viral Rev. After shuttling into the nucleus, HIV-1 Rev binds specifically to the stem loop IIb (SLIIB; not shown) within the viral rev response element (RRE), which is a complex RNA secondary structure. After initial binding to the SLIIb, the RRE scaffold mediates oligomerization of Rev. HIV-1 Rev serves as an adapter protein that recruits the cellular export factor CRM1 (Exportin 1 or XPO1) (light yellow) and Ran-GTP (yellow), finally allowing nuclear export also of the HIV-1 intron-containing and unspliced RNA transcripts.

Importantly, HIV-1 Rev protein contains a nuclear localization signal (NLS), which is responsible for nuclear Rev import (163). Nevertheless, intranuclear trafficking of the intron-containing and unspliced HIV-1 RNA to nuclear compartments that are accessible to Rev, mediated by at least some of the CRS-binding nuclear retention factors, is suggested to be crucial for Rev-mediated export as well (Fig. 1.17) (162). As part of this thesis, HIV-1 CRS discovery and function concomitant possible bioinformatic-based prediction of viral and cellular CRS were summarized in a comprehensive literature review (162).

After nuclear import, Rev binds with high affinity to RRE's stem loop IIb (143). However, specific binding of a Rev monomer to this stem loop structure is not sufficient for full export activity (143). Here, after initial binding of a Rev protein to the SLIIb, the complex RRE scaffold contributes to oligomerization of Rev across the RRE (Fig. 1.17) (143).

To finally achieve nuclear export of HIV-1 intron-containing und unspliced RNA, the C-terminal nuclear export signal (NES) of viral Rev interacts with cellular CRM1 (Exportin 1 (XPO1)) and Ran-GTP (143). This assembly is responsible for the subsequent nuclear export of the Rev-RRE complex (Fig. 1.17).

With the ability of LNA mixmers to interfere with RNA secondary structure formation, the HIV-1 RNA nuclear export with its dependence on the viral RRE may be an additional target site for LNA mixmer-mediated inhibition of viral replication.

Overall, this thesis investigates the potential of LNA mixmers to inhibit viral replication after unassisted delivery. For this, antiviral LNA mixmer activity during cytoplasmic (+)ssRNA virus (SARS-CoV-2), cytoplasmic (-)ssRNA (HAZV), nuclear (-)ssRNA (IAV) and retroviral replication (HIV-1) is analyzed. This way, the overall ability of LNA mixmers to interfere with viral processing can be tested and possible factors that influence LNA mixmer activity may be revealed.

2　Material & Methods

2.1　Material

2.1.1　Cell culture materials

A. Cell lines

Cell line	Accession number
ARPE-19	CVCL_0145
CaCo-2	CVCL_0025
HEK293T	CVCL_0063
HeLa	CVCL_0030
Jurkat	CVCL_0065
PM1	CVCL_9472
THP-1	CVCL_0006
TZM-bl	CVCL_B478
Vero	CVCL_0059

B. Viruses

Virus	Strain/Isolate/Clone	Accession number Reference/Reference
Hazara virus	JC280	NC_038709 - 11
HIV-1	NL4-3	(pNL4-3) AF324493 (164)
HIV-1	NL-918 +g15	(139)
Influenza A virus	A/California/07/2009	NC_026431 - 38
Influenza A virus	A/Brisbane/02/2018	EPI_ISL_406712
SARS-CoV-2	NRW-42	EPI_ISL_425126 (91)

C. Cell culture media and reagents

Product	Company	Catalog number
Blasticidin	Thermo Fisher Scientific	R210-01 (Gibco)
Bovine serum albumin	Thermo Fisher Scientific	15260037

Dulbecco's Modified Eagle Medium (DMEM)	Thermo Fisher Scientific	11995065
Fetal calf serum (FCS)	PAN Biotech	P30-3031
Iscove's Modified Dulbecco's Medium (IMDM)	Thermo Fisher Scientific	21980065
Opti-MEM™	Thermo Fisher Scientific	11058021
Penicillin/streptomycin solution	Thermo Fisher Scientific	11548876
Phosphate buffered saline (PBS)	Thermo Fisher Scientific	14190144
RPMI medium (RPMI)	Thermo Fisher Scientific	11875101
TPCK Trypsin	Sigma-Aldrich	4352157
Trypan blue	Thermo Fisher Scientific	15250061
Trypsin/EDTA solution	Thermo Fisher Scientific	25300054

D. Transfection reagents

Product	Company	Catalog number
Lipofectamine 2000	Thermo Fisher Scientific	11668030
Polyethylenimine (PEI)	Sigma-Aldrich	408727
TransIT-LT1	Mirus	MIR 2305 / 731-0028

2.1.2 Plasmid cloning

A. Reagents, chemicals, enzymes, bacteria and material

Product	Company	Catalog number
AllPrep DNA/RNA/Protein Mini Kit	Qiagen	80004
Competent DH5α *E. coli*	NEB	C2987H
dNTPs [10 mM]	Qiagen	201901
DSMO	Finnzymes	F-515
Ethidium bromide solution	Carl Roth	HP47.1
Expand high fidelity PCR buffer (10x)	Roche	11759167001
Expand high fidelity PCR system	Roche	11732650001
Gel extraction kit	Qiagen	28706
LB-Agar	Invitrogen	22700025
LB-Medium	Carl Roth	X964.2

Midi Plasmid DNA preparation kit	Qiagen	12143
Monarch® PCR & DNA Cleanup Kit	NEB	T1030L
NEB® 10-β competent *E. coli*	NEB	C3019H
T4 ligase	NEB	M0202L
T4 ligation buffer (10x)	NEB	B0202S
Tris-borate-EDTA (10x)	Sigma-Aldrich	T4415-4L

B. Restriction enzymes and buffer

Product	Company	Catalog number
CutSmart (10x)	NEB	B6004
KpnI-HF	NEB	R3142
NheI-HF	NEB	R3131
PacI	NEB	R0547
PmeI	NEB	R0560

2.1.3 Oligonucleotides

Primer	Sequence (5' --> 3')	Application
#0640	CAATACTACTTCTTGTGGGTTGG	PCR
#0732	CTAGTGTCCATTCATTGTAT	PCR
#1544	CTTGAAAGCGAAAGTAAAGC	PCR
#3387	TTGCTCAATGCCACAGCCAT	PCR
#3388	TTTGACCACTTGCCACCCAT	PCR
#3395	GGCGACTGGGACAGCA	PCR
#3396	CCTGTCTACTTGCCACAC	PCR
#3397	CGGCGACTGAATCTGCTAT	PCR
#3398	CCTAACACTAGGCAAAGGTG	PCR
#3631	CGGCGACTGAATTGGGTG	PCR
#3632	TGGATGCTTCCAGGGCTC	PCR
#4801	AACAACTGCTGTTTATCCAT	PCR
#4907	CTGTGCCCAGTGGTGCT	PCR
#4908	GACCTGAAGAACTCGGAGG	PCR
#6338	ATGCTTAATTAAGGCGCCCGAACAGG	Cloning of pWPI_Vpr3_BSD
#6339	ATGCGTTTAAACGGCTTCCACTCCTGCCC	Cloning of pWPI_Vpr3_BSD
#6638	ACTAATCAGGCATGAAAACAGAATG	PCR

#6639	TGGAGCTAGGATGAGTCC	PCR
#6743	AGTCGGTACCGCAGTAACGCCATTTTGCAAG	Cloning of pSFFVU3-RL-betaGlobin-WT-SV40-FLref
#6744	AGTCGCTAGCCTGTCGGAGGACTGGC	Cloning of pSFFVU3-RL-betaGlobin-WT-SV40-FLref
#6750	GCTTTTGTCATGAAACAAACTTG	PCR
#6751	GAGATGCCTAAGGCTTG	PCR
#6752	CCATAGCAGATGCCTTG	PCR
#CENPJfwd	TGGAAGAGAGCAGAAGCCATA	PCR
#CENPJrev	TTCGAGTTCCATTGGGAAAC	PCR
#IRES-F	ACTACGGGCTGCAGGAATTC	PCR
#IRES-R	CGTGTTTTTCAAAGGAAAACCACG	PCR
#MT-CO1f	CTCTTCGTCTGATCCGTCCT	PCR
#MT-CO1r	ATCCTACCAGGCTTCGGAAT	PCR

2.1.3 Antisense oligonucleotides

All LNA mixmers were purchased from Qiagen.

LNA mixmer	5'Label	Sequence	Target	Design ID	Cat. No.
CENPJ DownS	-	GGATCTTCGAGGTGGA	CENPJ	YCO0239949	339407
CENPJ SA	-	GGATTGCCTATTAGAA	CENPJ	YCO0198392	339407
CENPJ UpS	-	AATAAAATTGTCAAGA	CENPJ	YCO0239950	339407
Hazara virus	-	AACGATATCTTTGAGA	HAZV	YCO0200594	339407
HIV-1 G_{I3}-2	FAM/-	TATGGCTCCCTCTGTG	HIV-1	YCO0073444	339407
HIV-1 SLIIb	-	TCATTGACGCTGCGCC	HIV-1	164619	500150*
Influenza A virus LNA #1	FAM	TCCCATTCGCTTCTGG	IAV	YCO0207968	339407
Influenza A virus LNA #2	FAM	TGAATCGCTGCATCTG	IAV	YCO0207968	339407

| SARS-CoV-2 #1 | - | GTTTAGAGAACAGATC | SARS-CoV-2 | YCO0197768 | 339407 |
| SARS-CoV-2 #2 | - | AATTTTACACATTAGG | SARS-CoV-2 | YCO0197769 | 339407 |

*The SLIIb LNA mixmer was purchased from Exiqon, but is now available from Qiagen.

2.1.4 Plasmids

Name	Origin
pcRev	Research group Schaal, Institute of Virology, University Hospital Düsseldorf
pLTR-RL-betaGlobin-WT-SV40-FLref	Kindly provided by Dr. Walotka (Research group Schaal, Institute of Virology, University Hospital Düsseldorf)
pSFFVU3-RL-betaGlobin-WT-SV40-FLref	pLTR-RL-betaGlobin-WT-SV40-FLref
pSV 9G8 SD1 TIA1 delvpuenv-eGFP D36GpA	Research group Schaal, Institute of Virology, University Hospital Düsseldorf
puc2CL7EGwo Vpr3	Master Thesis of Philipp Ostermann (Research group Schaal, Institute of Virology, University Hospital Düsseldorf)
pWPI_Vpr3_BSD	pWPI_BSD (kindly provided by Dr. Walker, Institute of Virology, University Hospital Düsseldorf)

2.1.5 RNA extraction

Product	Company	Catalog number
Aqueous Phenol	Carl Roth	A980.3
AVL buffer	Qiagen	19073

Chloroform	Merck	102445
Direct-zol RNA Miniprep	Zymo Research	R2050
Ethanol	Merck	107017
Isoamyl alcohol	Merck	100979
Isopropanol	VWR	20842330
β-mercaptoethanol	Sigma	M3148

2.1.6   cDNA synthesis

Product	Company	Catalog number
5x First strand buffer	Invitrogen	Y02321
DNase I recombinant	Roche	4716728001
DTT	Invitrogen	Y00147
Oligo(dT) primer	Roche	10814270001
RNAsin	Promega	N2515
Superscript III reverse transcriptase	Invitrogen	18080085

2.1.7   Reverse transcription-PCR analysis

Product	Company	Catalog number
Ammonium persulfate	Merck	1.01201.0500
AmpliTaq DNA polymerase	Applied Biosystems	N8080166
AmpliTaq DNA polymerase buffer (10x)	Applied Biosystems	100020475
Polyacrylamide (30 % solution)	Carl Roth	3029.1
TEMED	Carl Roth	2367.3

2.1.8   Reverse transcription-quantitative PCR analysis

Product	Company	Catalog number
PrecisionPLUS qPCR Master Mix	Primer Design	PPLUS-CL
TaqMan Fast Virus 1-step Master Mix	Thermo Fisher Scientific	4444432

2.1.9   SARS-CoV-2 Immune fluorescence staining

Product	Company	Catalog number
Goat-anti-human IgG FITC	Life technologies	H10001C
Methanol	VWR	20903.368

2.1.10 Luciferase assay

Product	Company	Catalog number
2x Lysis-Juice	PJK GmbH	102515
Beetle-juice Luciferase assay Firefly	PJK GmbH	102511
Nunc flat white bottom 96-well plate	Thermo Fisher Scientific	136101
Renilla-juice Luciferase assay	PJK GmbH	102531

2.1.11 Laboratory instruments and software

Product	Company
ABI Fast 7500	Applied Biosystems
Biometra Thermocycler Tprofessional TRIO PCR	Analytic Jena
Cell Discoverer 7	Zeiss
Fiji Win64	Ref (Schindelin et al 2012)
Geneious 10.0.9	Biomatters Ltd.
GraphPad Prism 8	GraphPad
H7100 TEM	Hitachi
i-control 1.12 software	Tecan
Inkscape 1.1	Inkscape
Morada camera	EMSIS GmbH
NanoDropTm 2000	Thermo Fisher Scientific
Nikon DS-Fi3	Nikon
Nikon Eclipse Ts2	Nikon
NIS-Elements BR 5.21.03	Nikon
Platform Rocker, PMR-30 (Grant)	VWR

Roche Capillaries LightCycler 1.5	Roche
Tecan Infinite 200 reader	Tecan
ZEN 3.5 (blue edition)	Zeiss

2.2 Methods

2.2.1 Cultivation of mammalian cells

Adherent cells

ARPE-19, CaCo-2, HEK293T, HeLa, TZM-bl and Vero cells were cultured as adherent cells. Adherent cells were cultured in T75 cell culture flasks with Dulbecco's Modified Eagle Medium (DMEM) and passaged by trypsinization. Cell culture medium was supplemented with 10 % fetal calf serum (FCS) and 1 % penicillin/streptomycin solution. Cell culture medium of CaCo-2 cells additionally contained 1 % non-essential amino acids. Vero cells were cultured with only 2 % FCS. For trypsinization, the cell monolayer was washed twice with 10 ml phosphate-buffered saline (PBS) and subsequently rinsed with 2 ml trypsin-EDTA solution. After an incubation of up to 10 min, the cells were collected in 10 ml fresh cell culture medium. The cell suspension was diluted and transferred into new T75 cell culture flasks.

All cell lines were incubated at 37°C and 5 % CO_2 in a humidified cell culture incubator.

Suspension cells

PM1, Jurkat and THP-1 cells were cultured in suspension. Suspension cells were cultured in T75 cell culture flasks using RPMI medium (RPMI). The T75 cell culture flasks were stored in an upright position. Cell culture medium was supplemented with 10 % FCS and 1 % penicillin/streptomycin solution. To passage suspension cells, the respective cells were resuspended and a small volume of the resulting cell suspension transferred into new flasks already containing fresh medium.

All cell lines were incubated at 37°C and 5 % CO_2 in a humidified cell culture incubator.

Sanger sequencing of cellular DNA regions of interest

Whole-cell DNA was extracted using the AllPrep® DNA/RNA/Protein Mini Kit (Qiagen) following the manufacturer's manual. Whole-cell DNA was then used as template for a subsequent cloning PCR using a high-fidelity PCR polymerase system to amplify the DNA

region of interest (see below).). A 5 µl aliquot of the resulting 50 µl PCR samples were analyzed via DNA gel electrophoresis using a simple 1 % agarose gel (see below). The PCR products within the remaining 45 µl of the cloning PCR samples were purified using the New England Biolabs Monarch PCR & DNA clean up kit. The PCR products were eluted in 15 µl water and 2 µl of the respective forward DNA primer (10 µM) were added. These samples were sent to Eurofins Genomics for Sanger sequencing service. The obtained .ABI files were analyzed using the Geneious software.

2.2.2   Transfection of mammalian cells

Mirus LT-1 transfection reagent

The Mirus LT-1 reagent was used to transfect cells with plasmid DNA. To transfect cells with the Mirus LT-1 reagent, first, the LT-1 reagent was pre-incubated with serum-free and antibiotic-free cell culture medium in a total volume of 100 µl for 5 min at room temperature (RT). The used amount of the LT-1 reagent was two times the amount of transfected plasmid DNA in µl. After this 5 min incubation step, the LT-1 reagent containing medium was mixed with the desired amount of plasmid DNA and incubated for another 15 min at RT. Afterwards, the transfection mix was pipetted to cell that were seeded one day prior to transfection. During this work, $2.5x10^5$ cells were seeded into a standard 6-well plate for transfection with Mirus LT-1 reagent.

Lipofectamine 2000 transfection reagent

The Lipofectamine 2000 reagent was used to co-transfect cells with plasmid DNA and LNA mixmers or to transfect cells with LNA mixmers only. To transfect cells, first, 2 µl of the Lipofectamine 2000 reagent were incubated with 250 µl Opti-MEM cell culture medium for 5 min at RT. In the meantime, the desired amount of plasmid DNA and LNA mixmer were mixed with 250 µl Opti-MEM cell culture medium. After the 5 min incubation step, the transfection reagent containing medium was mixed with the plasmid DNA/LNA mixmer containing medium. This mixture was incubated for 20 min at RT.

Cells that were to be transfected were seeded one day prior to the transfection into standard well plates. Just before the 20 min incubation period was over, the medium was removed from the cells and 500 µl Opti-MEM cell culture medium was added to each well. The transfection mix was added onto these 500 µl once the 20 min incubation was over.

After 4 hours of incubation at 37°C, the cells were washed twice with PBS and fresh Opti-MEM medium, now containing 5 % FCS, was added to the cells.

During this work, either $2.5x10^5$ cells were seeded into a standard 6-well plate or $5x10^4$ cells were seeded into a 24-well plate for transfection with Lipofectamine 2000 reagent.

Polyethylenimine

The transfection reagent polyethylenimine (PEI) was used to generate lentiviral vectors and HIV -1 virus stocks. For this, 10 µl PEI stock solution (100 mg/ml) were first diluted 1:100 in serum-free DMEM (c_{end} 1 mg/mL). The PEI working solution was prepared by mixing 675 µl diluted PEI solution (c_{end} 1 mg/mL) with 14.325 ml serum-free DMEM.

Mix 500 µl of this PEI working solution with the desired amount of plasmid DNA, usually 9 µg DNA in total. This mixture is incubated for 30 min at RT. Afterwards, this DNA/PEI mixture is added to the cells.

2.2.3 Lentiviral transduction

Generation of lentiviral vectors

To generate lentiviral vectors, $6.5x10^6$ HEK293T cells were seeded into a gelatin-coated (0.1 %) T175 cell culture flask. The next day, the HEK293T cells were transfected with 3 µg envelope plasmid (pz-VSV-G), 3 µg packaging plasmid (pCD NL-BH) and 3 µg of the respective transfer vector (2nd generation lentiviral vector system) using PEI transfection reagent. The following day, the cell culture medium was removed, and the cells were incubated for 24 h in 15 ml IMDM. Viral vectors were harvested by first centrifuging the cell culture supernatant at 500 x*g* for 10 min with subsequent aliquoting of the viral vector containing supernatant and storage at -80°C.

Transduction of mammalian cells for the generation of stable cell lines

To generate stable cell lines, $1.5x10^6$ cells were collected by centrifugation. The cells were resuspended in 500 µl lentiviral vector stock and centrifuged for 30 min at 100 x*g*. After centrifugation, the cells were incubated in a total 4 ml cell culture medium in T25 cell culture flasks.

Selection of antibiotic-resistant cells

To select antibiotic-resistant cells, the cells were first washed with warm PBS. Fresh cell culture medium containing the respective selection antibiotic in a concentration of 1 µg/ml was added to the cells. Within the first 3 days after transduction, the cells were washed, and fresh selection medium was added on a daily basis. As soon as only single cells survived the selection process and small islets formed, the cells were trypsinized and seeded into a new T25 cell culture flask.

2.2.4 SARS-CoV-2

Inoculation of cells with naso-/oropharyngeal swab specimen

The first day, 2.5×10^5 Vero cells were seeded into a T25 cell culture flask. To inoculate cells, 200 µl of the SARS-CoV-2 containing naso-/oropharyngeal swab specimen were centrifuged at 3000 xg for 1 min and the resulting supernatant mixed with 800 µl maintenance medium (DMEM with 2 % FCS and 1 % P/S). The cells were incubated for 1 h with this 1 ml inoculum on a laboratory shaker at 37°C in a cell culture incubator. After this 1 h incubation, 4 ml maintenance medium were added to the cells.

Generation of SARS-CoV-2 stocks

To generate SARS-CoV-2 stocks, either inoculated Vero cells or newly infected Vero cells were incubated for 4 to 7 days at 37°C in a cell culture supernatant. The SARS-CoV-2 containing supernatant was harvested by centrifugation at 500 *xg* for 10 min and aliquoting of the resulting supernatant. SARS-CoV-2 stocks were stored at -80°C.

SARS-CoV-2 virus stock titer determination

The SARS-CoV-2 virus stock titer was determined by a standard endpoint dilution assay based on the appearance of SARS-CoV-2-induced cytopathic effects in Vero cells. A total of 5×10^3 Vero cells were seeded into a 96-well plate (cell plate) per well. The next day, the SARS-CoV-2 stock was diluted successively in 8 replicates in another 96-well plate (virus plate). For this, 180 µl cell culture medium were filled into each well of a 96-well plate and 20 µl virus stock was added to the wells of the first column. Successive transfer of 20 µl from column to column then resulted in the desired 1:10 dilutions. Afterwards, the cell culture medium was removed from the Vero cells, and 100 µl fresh medium was added into each well. Subsequently, 100 µl from the virus plate wells were added into the respective wells of the cell plate. At 4 days post-

infection (dpi), the wells were checked for the appearance of virus-induced CPE by microscopic inspection.

The viral titer as tissue culture infectious dose$_{50}$/ml (TCID$_{50}$/ml) was determined as:

$$TCID50/ml = \frac{D_s^{(N/R+0.5)} D_0 \times 1,000}{D_s \times V}$$

D_s = Dilution factor of successive dilutions; N = Total number of wells showing CPE; R = replicates per dilution; D_0 = Dilution factor of first dilution; V = Volume per well in µl.

To estimate the number of infectious particles in the virus stock in plaque forming units/ml (PFU/ml), the Poisson distribution was applied. Meaning, the viral titer in TCID$_{50}$/ml was taken times 0.7.

SARS-CoV-2-specific RT-qPCR

Per sample, 100 µl cell culture supernatant was harvested and inactivated, first by incubation with 400 µl AVL buffer (Qiagen) for 10 min at RT and then by addition of 400 µl 100 % ethanol. RNA was extracted from 200 µl using the EZ1 Virus Mini Kit v2. (Qiagen). The 60 µl eluate was subject to in-house RT-qPCR performed by the diagnostics department of the Institute of Virology at the University Hospital Düsseldorf according to the diagnostic SARS-CoV-2 E gene RT-qPCR method described (165) with minor modifications as in (91).

SARS-CoV-2 immunofluorescence test

The SARS-CoV-2 immunofluorescence test (IFT) was performed by collecting SARS-CoV-2-infected cells via centrifugation. The infected cells were resuspended in in PBS and 10 µl of this cell suspension was transferred to microscopic slides. After letting the PBS dry, the cells were fixed with ice-cold Methanol. Afterwards, the cells were washed with PBS. The IFT performed during this thesis was conducted as means of a diagnostic test (Institute of Virology, University Hospital Düsseldorf). Hence, the fixed cells were incubated with anonymous SARS-CoV-2 convalescent serum diluted 1:40 in PBS with 5 % FCS for 1 h at RT. After three washing steps with PBS, the cells were incubated with a goat anti-human IgG FITC conjugate for 1 h at RT and protected from light. The microscopic slides were washed up to six time with PBS and evaluated with a fluorescence microscope.

Transmission electron microscopy

Transmission electron microscopy (TEM) of SARS-CoV-2-infected Vero cells was conducted in collaboration with Dr. Ann-Kathrin Bergmann (Head of core facility electron microscopy, University Hospital Düsseldorf). 2.5×10^5 Vero cells were seeded into the wells of a 6-well plate. The next day, Vero cells were infected virus SARS-CoV-2 at an MOI of 0.5. At 8 hours post-infection (hpi), cells were washed with OBS and fixed in TEM fixation solution (4 % paraformaldehyde, 2.4 % glutaraldehyde in 0.1 M cacodylate buffer, pH 7.3) for 2 h at RT. Per condition, three wells were combined to obtain one TEM sample. TEM sample preparation was performed at the core facility electron microscopy of the University Hospital Düsseldorf. TEM analysis was performed using the Hitachi-H700 TEM at 100 kV equipped with Morada camera.

SARS-CoV-2 infection and anti-SARS-CoV-2 LNA mixmer treatment

At total of 5×10^3 Vero cells were seeded into the wells of a 96-well plate. The following day, virus stock was added to the cells to infect them with SARS-CoV-2 at an MOI of 0.01. At 1 hpi, the cells were washed with PBS and then treated with 200 µL fresh medium containing the LNA mixmers for 3 days.

2.2.5 Hazara virus

Experiments involving Hazara virus (HAZV) were performed in collaboration with Dr. Vanessa Monteil in the lab of Prof. Dr. Ali Mirazimi (Department of Laboratory Medicine, Karolinska Institutet, Solna, Sweden).

Hazara virus infections

For HAZV infection experiments, either 5×10^5 CaCo-2 cells were seeded into a 6-well plate or 10^5 CaCo-2 cells were seeded into a 24-well plate. The following day, the medium was removed, and the cells were infected with the depicted MOIs using HAZV strain JC280 in a low volume (700 µl in 6-wells and 200 µl in 24-wells) of infection medium (DMEM with only 2 % FCS). At 1 hpi, the cells were washed with PBS and then incubated in infection medium containing the depicted concentrations of the LNA mixmers, for up to 48 h.

Hazara virus-specific RT-qPCR

Hazara virus-specific RT-qPCR analysis was performed by first isolating viral and cellular RNA from the cell monolayers using the Direct-zol RNA Miniprep kit. For this, the cells were washed three times with cold PBS and lysed with 250 µl Trizol. A total of 200 µl Trizol was transferred into centrifugation tubes and mixed with 200 µl ethanol (100 %). RNA was extracted following the manufacturer's protocol of the Direct-zol RNA Miniprep kit. The extracted RNA was collected in 50 µl water.

The subsequent RT-qPCR was performed on a Roche Capillaries LightCycler using the TaqMan Fast Virus 1-step Master Mix. RT-qPCR analysis was conducted by normalizing HAZV N segment RNA levels (Fwd: CAAGGCAAGCATTGCACAAC, Rev: GCTTTCTCTCACCCCTTTTAGGA, Probe: FAM-TGAAGGATGGGTCAAAGA-MGB) to cellular RNase P RNA levels (Fwd: AGATTTGGACCTGCGAGCG, Rev: GAGCGGCTGTCTCCACAAGT, Probe: FAM-TTCTGACCTGAAGGCTCTGCGCG-MGB) following the $2^{-\Delta ct}$ method (166).

2.2.6 Influenza A virus

Influenza A virus infections

Influenza A virus (IAV) infections were conducted in collaboration with Dr. Ralf Grutza (Research group of Prof. Timm, Institute of Virology, University Hospital Düsseldorf). For infection experiments, $5x10^4$ CaCo-2 cells were seeded into the wells of a 24-well plate. The next day, the cells were washed with PBS and IAV stock (A/California/07/2009 or A/Brisbane/02/2018 kindly provided by Dr. Ralf Grutza, Research group Timm, Institute of Virology, University Hospital Düsseldorf) diluted 1:1 with IAV infection medium (2 ml DMEM plus 50 µl BSA stock and 2 µl TPCK trypsin stock) was added to the cells with 200 µl per well. After 1 h at 37°C with slight shaking of the plate every 10 min, the cells were washed with PBS and 500 µl infection medium now containing the LNA mixmers were added to each well.

Influenza A virus-specific RT-qPCR

RNA was extracted from 200 µl cell culture supernatant by using the EZ1 Virus Mini Kit v2. (Qiagen). The 60 µl eluate was subject to in-house RT-qPCR performed by the diagnostics department of the Institute of Virology at the University Hospital Düsseldorf.

2.2.7 HIV-1

Generation of HIV-1 stocks

To generate HIV-1 virus stocks, $6.5x10^6$ HEK293T cells were seeded into a gelatin-coated (0.1 %) T175 cell culture flask. The next day, the HEK293T cells were transfected with 9 μg HIV-1 proviral plasmid pNL4-3 or the pNL4-3 derivate pNL-918 +g15 using PEI transfection reagent. The following day, the cell culture medium was removed, and the cells were incubated for 24 h in 15 ml IMDM. HIV-1 viral particles were harvested by first centrifuging the cell culture supernatant at 500 x*g* for 10 min with subsequent aliquoting of the HIV-1 containing supernatant and storage at -80°C.

HIV-1 virus stock titer determination

A Fixation solution

Component	Final concentration
25 % glutaraldehyde	0.25 %
37 % formaldehyde	0.8 %
PBS	

B Staining solution

Component	Final concentration
$K_3[Fe(CN)_6]$ [400 mM]	4 mM
$K_4[Fe(CN)_6]$ [400 mM]	4 mM
$MgCl_2$ [200 nM]	2 mM
X-Gal in dimethylformamide [20 mg/ml]	0.4 mg/ml
PBS	

HIV-1 viral titers were determined by endpoint dilution assay using the HeLa cell line-derived HIV-1 reporter cell line TZM-bl with subsequent β-galactosidase staining. A total of $6x10^3$ TZM-bl cells were seeded into a 96-well plate (cell plate) per well. The next day, the HIV-1 stock was diluted 1:10 and 350 μl of this virus stock dilution were pipetted into each well of the first column of a 96-deep well plate (virus plate). The remaining wells were filled with 220 μl cell culture medium. The diluted virus stock within the first column was now diluted in 8 replicates

by transfer of always 110 µl into the wells of the next column to obtain serial dilutions of 1:3. Afterwards, the cell culture medium was removed from the cell plate, and the empty wells were filled with 200 µl of the different virus dilutions. At 2 dpi, the cells were washed with 200 µl cold PBS and fixed in 100 µl fixation solution (see above, A) for 10 min at 4°C. The fixation solution was removed and after one washing step with cold PBS, the cells were stained with 100 µl staining solution (see above, B) at 37°C. After 4 h, the cell plates were analyzed by microscopic inspection. Wells that showed blue-stained (β-galactosidase-positive) cells, were counted as infected.

The viral titer as tissue culture infectious dose$_{50}$/ml (TCID$_{50}$/ml) was determined as:

$$TCID50/ml = \frac{D_s^{(N/R+0.5)}D_0 \times 1,000}{D_s \times V}$$

D_s = Dilution factor of successive dilutions; N = Total number of wells showing blue-stained cells; R = replicates per dilution; D_0 = Dilution factor of first dilution; V = Volume per well in µl.

To estimate the number of infectious particles in the HIV-1 virus stock in plaque forming units/ml (PFU/ml), the Poisson distribution was applied. Meaning, the viral titer in TCID$_{50}$/ml was taken times 0.7.

HIV-1 infections

To infect T-cells with HIV-1, 10^6 cells were incubated with the amount of HIV-1 virus stock that corresponds to the desired MOI in about 1 ml infection medium (RPMI with 5 % FCS) in a 15 ml centrifugation tube. After 6 h at 37°C, the cells were washed with PBS by centrifugation at 500 x*g* for 3 min. Afterwards, the cells were transferred into T25 cell culture flasks and incubated in 1 infection medium. At this point, the LNA mixmers were added to the infection medium

HIV-1 infection of TZM-bl cells was performed by seeding of 2.5x10^5 cells into a 6-well plate the first day. After 24 h, the cells were infected in 1 ml infection medium (DMEM with 5 % FCS) containing the amount of HIV-1 virus stock that corresponds to the desired MOI. At 6 hpi, the cells were washed with PBS and incubated in 2 ml infection medium. At this point, the LNA mixmers were added to the medium.

Before infection of monocyte-like THP-1 cells with HIV-1, the THP-1 cells were stimulated with phorbol 12-myristate 13-acetate (PMA). For this, 5x105 cells were transferred into 6-wells and after 30 to 45 min, PMA was added to the cells in a concentration of 2 ng/ml. After 4 days, the cells were washed with PBS and infected with HIV-1, likewise the TZM-bl cells.

HIV-1-specific RT-qPCR

To conduct HIV-1-specific RT-qPCR analysis, first, total RNA was extracted from HIV-1-infected cells (see below). Afterwards, cDNA was synthesized from the RNA using an oligo(dT) primer (see below). For RT-qPCR analysis, the cDNA was diluted 1:10 in water and 2 µl of the diluted cDNA were mixed with 10 µl 2x SYBR green Master Mix, 1 µl forward primer (10 µM), 1 µl reverse primer (10 µM) and 6 µl water. The HIV-1-specific RT-qPCR was performed on the Roche Capillaries LightCycler platform and samples were run in technical triplicates. RT-qPCR analysis was conducted by normalizing the RNA level of interest following the $2^{-\Delta ct}$ method (166).

2.2.8   RNA extraction

A Solution D

Component	Final concentration
Guanidinium thiocyanate	4 M
Sodium citrate [1 M]	25 mM
Sarcosyl [10 %]	0.5 %
β-mercaptoethanol	100 mM

H_2O

Cells were washed with cold PBS either by centrifugation (suspension cells) or within the cell culture vessels (adherent cells). Afterwards, cells were lysed with 500 µl Solution D (see above A). Total RNA was extracted by phenol-chloroform extraction. For this, cell lysates were, first, mixed with 7.2 µl β-mercaptoethanol, 50 µl sodium acetate (2 M, pH 4) and 500 µl phenol. A total of 103 µl of a chloroform-isoamyl alcohol solution (Ratio 24:1) were added and the samples were vortexed for 15 sec each. After a 10 min incubation on ice, the samples were centrifuged for at least 20 min at 4°C. Subsequently, 400 µl of the RNA containing upper (aqueous) phase were mixed with 400 µl isopropanol (100 %) and incubated for at least 2 h at -20°C to precipitate the RNA. The RNA samples were then centrifuged at approx. 11,000 x*g* for 20 min. The resulting RNA pellets were washed twice with 70 % Ethanol and resuspended in 10 µl H_2O. RNA concentrations were determined using the NanoDrop^{Tm} spectrophotometer platform.

2.2.9 RT-PCR analysis

cDNA synthesis

Master mix A

Component	Amount per sample	Final concentration
Oligo d(T) primer [7.5 µM]	0.5 µl	0.375 µM
dNTPs [10 mM]	0.5 µl	500 µM
H_2O	0.5 µl	-

Master mix B

Component	Amount per sample	Final concentration
5x First strand buffer	2 µl	1x
DTT [0.1 M]	0.5 µl	5 mM
RNAsin [U/µl]	0.5 µl	2 U/µl
Superscript III [200 U/µl]	0.5 µl	10 U/µl

A total of 500 ng to 2.5 µg of RNA were used for subsequent cDNA synthesis. First, the different RNA samples were all set to a volume of 10 µl. Then, these samples were incubated at 70°C for 5 min. Afterwards, 5 µl of the samples were mixed with 1.5 µl of master mix A and incubated at 65°C for 5 min. After this incubation step, the samples for briefly put on ice. Then, the 6.5 µl samples were mixed with 3.5 µl of master mix B and first incubated for 60 min at 50°C and then for 15 min at 72°C.

RT-PCR

Master mix C

Component	Amount per sample	Final concentration
10x AmpliTaq buffer	1.25 µl	1x
dNTPs [10 mM]	0.25 µl	200 µM
Fwd primer [10 µM]	0.25 µl	200 nM
Rev primer [10 µM]	0.25 µl	200 nM
AmpliTaq Polymerase [5 U/µl]	0.0625 µl	0.025 U/µl

H_2O	9.44 µl	-

For RT-PCR analysis, 1 µl of the generated cDNA was mixed with master mix C in a PCR reaction tube (see above). The RT-PCR samples were placed in a PCR thermocycler and were subjected to the following protocol:

RT-PCR program

Step	Temperature [°C]	Time [mm:ss]	Cycles
Initial denaturation	95	03:00	1
Denaturation	95	00:30	
Annealing	54 – 56[a]	01:00	18 - 33
Elongation	72	00:30 per kb	
Final elongation	72	10:00	1
Hold	16	∞	-

[a]The annealing temperature was 5°C below the melting temperature of the used primers

Polyacrylamide DNA gel electrophoresis

The RT-PCR products were mixed with 3 µl DNA loading dye (10 % glycerol, 6x Tris-borate-EDTA, bromophenol blue) and subjected to DNA gel electrophoresis using a 10 % polyacrylamide gel (see below). The gel electrophoresis was run at 35 mA. Afterwards, the polyacrylamide gel was incubated in 1x tris-borate-EDTA containing 0.41 µg/ml ethidium bromide. RT-PCR products were analyzed using an INTAS UV transilluminator.

Polyacrylamide gel (10 %)

Component	Volume per gel (approx. 30 ml)	Final concentration
H_2O	13.8 ml	-
Polyacrylamide solution [30 %]	10.0 ml	10 %
5x Tris-borate-EDTA	6.0 ml	1x
Ammonium persulfate [10 %]	420 µl	0.14 %
TEMED	21 µl	0.07 %

Sanger sequencing of RT-PCR products

To sequence RT-PCR products, the respective gel bands were excised from the polyacrylamide gel using a sterile scalpel and transferred into 1.5 ml centrifugation tubes. The gel fragments were incubated in 100 µl polyacrylamide gel extraction solution (0.5 M NH_4Ac, 10 mM MgAc, 1 mM EDTA, 0.1 % SDS) for 30 min at 50°C. To extract the DNA, the gel fragments were pelleted, and the supernatant was mixed with 300 µl buffer QG of the Qiagen DNA gel extraction kit. Afterwards, the samples were mixed with 100 µl isopropanol. The DNA was extracted via the column-based Qiagen DNA gel extraction kit following the manufacturer's protocol. The DNA was eluted in 30 µl water. To obtain enough DNA material for Sanger sequencing, the purified RT-PCR products were re-amplified by subjecting 2 µl of the DNA eluate to a high-fidelity DNA polymerase-based cloning PCR using the same primer pair as for the RT-PCR (see below). A 5 µl aliquot of the resulting 50 µl PCR samples were analyzed via DNA gel electrophoresis using a simple 1 % agarose gel (see below). The PCR products within the remaining 45 µl of the cloning PCR samples was purified using the New England Biolabs Monarch PCR & DNA clean up kit. The PCR products were eluted in 15 µl water and 2 µl of the respective forward DNA primer (10 µM) were added. These samples were sent to Eurofins Genomics for Sanger sequencing service. The obtained .ABI files were analyzed using the Geneious software.

2.2.10 Luciferase assay

The luciferase assay was performed on a Tecan Infinite 200 reader. First, each well was washed with PBS and scraped into 1x Lysis Juice diluted in water. Renilla and Firefly substrate reagent were prepared according to the manufacturer's instruction manual. Each sample was run in technical quadruplets. For this, 20 µl of the samples were transferred into the wells of a Nunc flat white bottom 96-well plate. The infinite reader was operated via the i-control 1.12 software. The infinite reader was first primed with 1 ml of the Renilla and Firefly substrate reagents, respectively. Afterwards, 100 µl of the respective substrate reagent was injected automatically into each well with 200 µl/sec and with a refill speed with 100 µl/sec. The luminescence of each sample was determined.

2.2.11 XC contrast staining

The XC contrast staining was performed by removing the cell culture medium from the cells and subsequent incubation with the XC staining solution (1 % methylene blue, 1 % acetic acid,

0.34 % carbol-fuchsin (w/v) in methanol) at RT for 5 min. Afterwards, the XC staining solution was discarded and the cells were washed several times with PBS.

2.2.12 Live cell imaging

To conduct live cell imaging, 5×10^4 TZM-bl cells were seeded into the wells of a 24-well plate. The next day, the cells were transfected using 2 µl Lipofectamine 2000 transfection reagent with 50 nM LNA mixmer and a total of 500 ng plasmid DNA (250 ng + 250 ng in co-transfection). At 5 hours pos-transfection, the plates were incubated at 37°C and 5 % CO_2 and imaged using the Cell Discoverer 7 (Zeiss). The obtained CZI files were processed using the ZEN 3.5 (blue edition) software.

2.2.13 Plasmid restriction cloning

Backbone digestion

To generate the desired plasmids, first, the backbone/vector was prepared by restriction enzyme digestion using the New England Biolabs Restriction Enzyme Platform. A total of 4 µg plasmid were digested in a volume of 20 µl containing 1 µl of the selected restriction enzymes, 2 µl 10x CutSmart buffer and water at 37°C for 1 h. The digested plasmid was analyzed by agarose gel electrophoresis using a 0.5 – 1% agarose gel that was prepared with 1x tris-borate-EDTA and approx. 0.4 µg/ml ethidium bromide. Undigested plasmid and plasmid digested with the used restriction enzymes in individual conditions served as control for restriction enzyme-mediated cleavage. The gel electrophoresis was run at 75 mA and analyzed under UV light with a wavelength of 366 nm.

Insert preparation

The respective DNA inserts for the restriction cloning were prepared by PCR-dependent insertion of specific restriction enzyme recognition sites. For this, either 2 µl of a plasmid containing the desired insert sequence or 2 µl cDNA served as template for a high-fidelity DNA polymerase-based cloning PCR (see below). For PCR products exceeding 2 kb, the cloning PCR mix may have been supplemented with 2 % DMSO. The same PCR program was pursued as for the RT-PCR (see above) with the only exception that the cloning PCR was run for 36 cycles.

Cloning PCR mix (50 µl)

Component	Amount per sample	Final concentration
10x Expand High Fidelity PCR System buffer	5 µl	1x
dNTPs [10 mM]	1 µl	200 µM
Fwd primer [10 µM]	1 µl	200 nM
Rev primer [10 µM]	1 µl	200 nM
Expand High Fidelity PCR System [3.5 U/µl]	0.5 µl	0.035 U/µl
Template	2 µl	-
H_2O	39.5 µl	-

Following cloning PCR, 5 µl of the 50 µl PCR mix were analyzed via agarose gel electrophoresis. The PCR products within the remaining 45 µl of the cloning PCR samples were purified using the New England Biolabs Monarch PCR & DNA clean up kit. The DNA was eluted in 16 µl water and mixed with 2 µl 10x CutSmart buffer and the same restriction enzymes used for the backbone digestion. After an 1 h incubation at 37°C, the now cleaved DNA was again purified using the New England Biolabs Monarch PCR & DNA clean up kit.

Ligation

The backbone and insert were ligated by mixing both in a molar ratio of 1:3 in a volume of 20 µl containing 2 µl T4 ligase buffer, 1 µl T4 ligase and water. This mixture was incubated at RT for approx. 30 min or at 16°C overnight.

Transformation of competent bacteria

Chemically competent *E. coli* was transformed using 1 to 5 µl of the ligation mix. For this, the desired amount of the ligation mix was carefully pipetted to the bacteria aliquots. After a 30 min incubation on ice, the samples were subjected to a 30 sec heat-shock at 42°C. Afterwards, the bacteria were recovered on ice for 5 min. After addition of 900 µl LB medium (10 g/L bactotrypton, 5 g/L yeast extraction and 10 g/L NaCl in water at pH 7.5), the bacteria were incubated at 37°C for 90 min. Subsequently, the 100 to 200 µl of the bacteria samples were plated onto ampicillin (100 µg/ml) containing LB agar plates. These plates were incubated at 37°C for 24 h.

Analytic plasmid preparation (Mini)

To screen for bacterial clones harboring the desired plasmid, single colonies were picked with a sterile pipette tip and transferred into 5 ml LB medium containing ampicillin (100 µg/ml). After 18 h of incubation at 37°C, the 2 ml of the bacteria cultures were pelleted by centrifugation at approx. 20,000 x*g* and resuspended in 300 µl buffer 1 (50 mM Tris-HCl, 10 mM EDTA, 400 µg/ml RNase A in water at pH 7.5). The bacterial cells were lysed by adding 300 µl of buffer 2 (0.2 M NaOH, 1 % SDS in water) and incubation for 5 min at RT. The lysis reaction as stopped by addition of 300 µl buffer 3 (3 M Kac in water at pH 5.5). Cell debris was removed by centrifugation a approx. 18,000 x*g* for 15 min. The resulting supernatants were mixed with 600 µl isopropanol and centrifuged at 4°C for 30 min again at 18,000 x*g*. The pelleted plasmid DNA was washed with 70 % ethanol (200 µl), air-dried for 5 to 15 min at RT and resuspended in 50 µl water. To analyze the obtained plasmid DNA, approx. 300 ng were digested using selected restriction enzymes and subsequently analyzed by agarose gel electrophoresis. To validate this analysis on nucleotide level, 1.5 µg of the plasmid DNA was sent to Eurofins Genomics for Sanger sequencing.

Plasmid stock preparation (Midi)

To generate plasmid DNA stocks, the remaining 3 ml of the bacteria cultures were added to 100 ml LB medium containing ampicillin (100 µg/ml) and incubated overnight at 37°C. The bacterial cells were pelleted at approx. 3,000 x*g* and resuspended in buffer P1 of the Qiagen Midi preparation kit. The plasmid DNA was purified using the Qiagen Midi preparation kit by following the manufacturer's manual. The eluted plasmid DNA was mixed with 3.5 ml isopropanol and centrifuged at 15,000 x*g*. The plasmid DNA pellet was washed once with 2 ml 70 % ethanol and air-dried. The pellet was resuspended in 100 to 300 µl Tris-EDTA buffer (pH 8.0).

3   Results

Antisense oligonucleotides (ASO) are used for a variety of applications, like molecular diagnostics (24), as tools for basic research (44) or for therapeutic applications (73).

In the context of therapeutic application, especially the work of the last few decades resulted in an increasing number of chemically-modified antisense oligonucleotides tested in clinical trials with a handful now approved by the U.S Food and Drug Administration (FDA) (27). Since every chemical modification has advantages and disadvantages, there is no single best choice leading to the huge diversity of ASO types currently investigated (27). Furthermore, given the still small number of specific antiviral agents available to date, there is great interest in antiviral ASOs.

In a previous study, so-called locked nucleic acid (LNA)-modified ASOs in mixmer design (LNA mixmers) were tested against HIV-1 infection to explore their potential antiviral activity (1). Those 16-mer LNA mixmers targeting the HIV-1 splicing regulatory elements G_{I3}-2 and ESE_{tat} were shown to abrogate viral replication already in a low molecular range, after transfection reagent-free (unassisted) delivery (1). The unassisted – also termed gymnotic - delivery is an application method, which is made possible by the employed phosphorothioate (PS) backbone, and which circumvents transfection reagent-caused bias on ASO function, but reduces their overall efficacy (35).

To investigate the mechanism underlying the observed inhibition of HIV-1 replication, viral RNA transcript levels were examined in a transfection-based reporter system. Interestingly, LNA mixmer transfection was shown to affect HIV-1 splicing, most likely by masking the targeted splicing regulatory elements on the viral pre-mRNA, whereas unassisted LNA mixmer delivery indicated induced degradation of LNA mixmer-bound transcripts (1). This conclusion was substantiated by the observation that fluorescein-labeled LNA mixmers displayed a nuclear localization after transfection compared to a predominant cytoplasmic distribution after unassisted delivery (1).

Importantly, while demonstrating profound inhibition of viral replication, this study suggested that LNA mixmer application without the use of transfection reagents, may have affected cytoplasmic RNA rather than nuclear RNA in the employed setting.

Since the unassisted delivery method of ASOs is considered to mimic the natural or free uptake as it would occur after therapeutic application, LNA mixmers may, therefore, be of use also against viruses that replicate exclusively in the cytoplasm.

Hence, based on the preceding work on anti-HIV-1 LNA mixmers, the aim of this thesis was to explore the potential of LNA mixmers to inhibit viral replication particularly of RNA viruses,

replicating in the cytoplasm, such as the recently emerged severe acute respiratory coronavirus 2 (SARS-CoV-2).

3.1 Unassisted LNA mixmer delivery does not interfere with SARS-CoV-2 replication

3.1.1 Generation of the infectious SARS-CoV-2 NRW-42 isolate by inoculation of Vero cells with a naso-/oropharyngeal swab specimen

With the recent emergence of SARS-CoV-2, a virus that was not well understood at the time, but was already characterized by a high infection rate and the potential to cause severe disease, the first goal of this thesis was to investigate whether LNA mixmers may also be used to inhibit SARS-CoV-2 replication (54).

Therefore, the first step was to generate an infectious SARS-CoV-2 isolate to afterwards analyze the antiviral activity of anti-SARS-CoV-2 LNA mixmers. To accomplish isolation of SARS-CoV-2 in cell culture, Vero cells were incubated with naso-/oropharyngeal swab specimen obtained from SARS-CoV-2-infected individuals in a combined effort with Dr. Lisa Müller (Institute of Virology, University Hospital Düsseldorf). To check for successful inoculation, cell culture supernatants were monitored for SARS-CoV-2 RNA, and the Vero cell monolayers were observed for the appearance of virus-induced cytopathic effects (CPE) on a daily basis (Fig. 3.1 **A**).
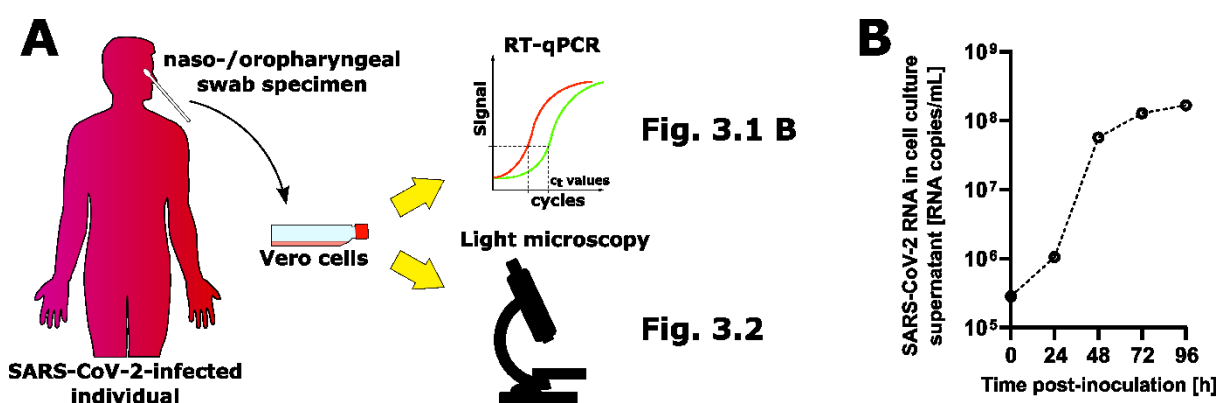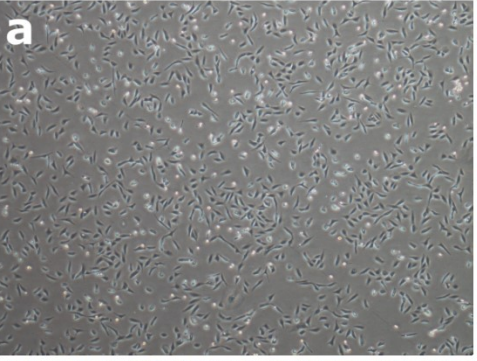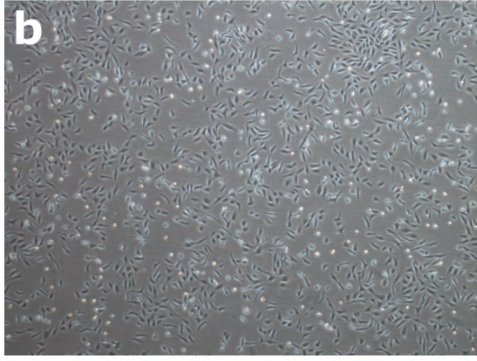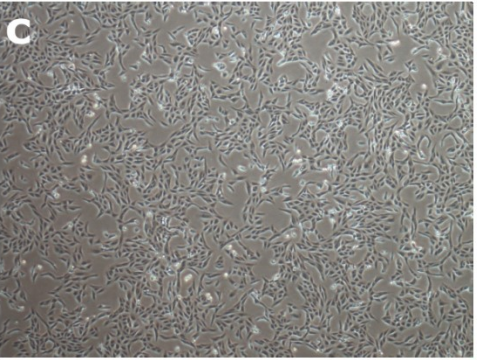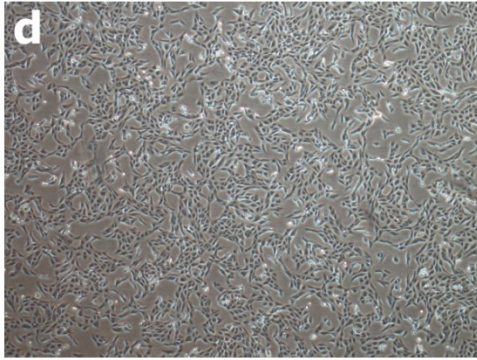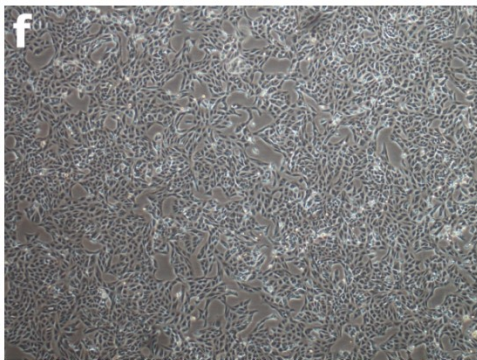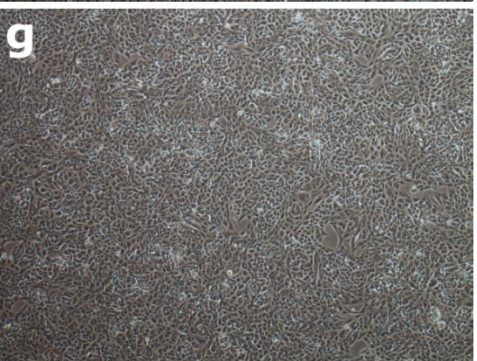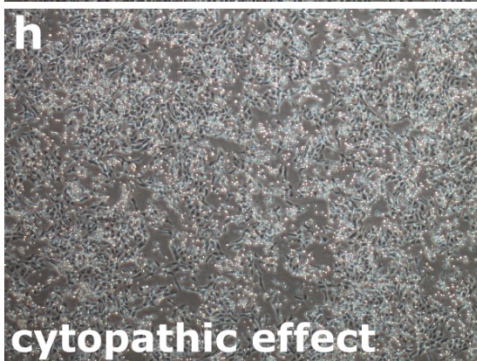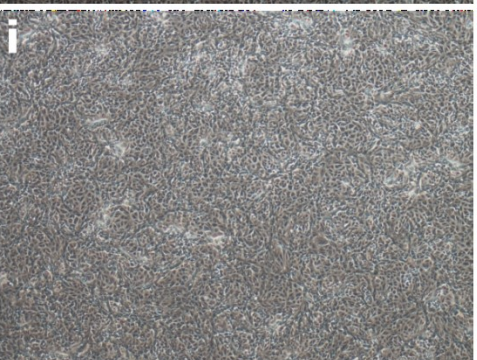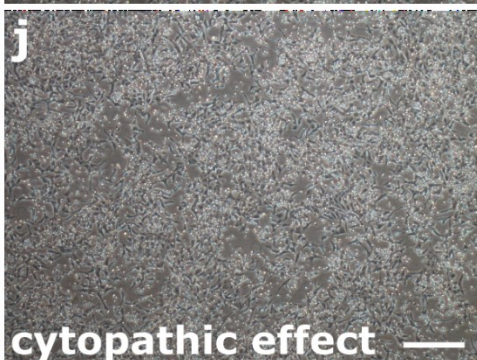
Fig. 3.1 Inoculation of Vero cells with a naso-/oropharyngeal swab specimen from a SARS-CoV-2-infected individual results in increase of SARS-CoV-2 RNA in the cell culture supernatant over time. (**A**) Schematic showing the initial work flow to generate an infectious SARS-CoV-2 isolate with monitoring of viral RNA in the cell culture supernatant via RT-qPCR and possible virus-induced cytopathic effects via light microscopy. (**B**) Monitoring of SARS-CoV-2 RNA via RT-qPCR over a period of 96 hours post-inoculation.

After inoculation with a swab specimen, RT-qPCR analysis revealed a strong increase in SARS-CoV-2 RNA over the course of three days post-inoculation in the Vero cell culture supernatant (Fig. 3.1 **B**) (91).

In addition to the observed increase in SARS-CoV-2 RNA, light microscopic analysis showed that the inoculated Vero cells began to detach from the cell culture flask at 3 days post-inoculation (Fig. 3.2 h, j) as it was described in other studies after SARS-CoV-2 infection (167, 168). Together, these observations were the first evidence for successful cell culture inoculation with SARS-CoV-2 and hinted towards the appearance of a virus-induced CPE in the employed Vero cells after 3 days post-infection (dpi).

		Control	Inoculated

Time post-inoculation

0 h

a

b

24 h

c

d

48 h

e

f

72 h

g

h

cytopathic effect

96 h

i

j

cytopathic effect

cytopathic effect

Fig. 3.2 Inoculation of Vero cells with a naso-/oropharyngeal swab specimen from a SARS-CoV-2-infected individual results in a putative virus-induced cytopathic effect 72 hours post-inoculation. Light microscopic imaging to monitor Vero cell monolayer after inoculation with a naso-/oropharyngeal swab specimen from a SARS-CoV-2-infected individual over a period of 96 hours post-inoculation. Untreated Vero cells served as control. Scale bar is 100 μm.

In a next step, the presence of SARS-CoV-2 antigens within the inoculated Vero cells was analyzed via immune fluorescence staining using SARS-CoV-2 convalescent serum to exclude a potential cross-reaction during the performed RT-qPCR. As expected, staining of the inoculated cells with SARS-CoV-2 convalescent serum and a FITC-conjugated secondary antibody resulted in a strong fluorescent signal, which was completely lacking in the control cells. This signal was also lacking after using a control serum obtained from an individual without present or past infection with SARS-CoV-2 (Fig. 3.3). Hence, the conducted experiment substantiated a successful inoculation of Vero cells with SARS-CoV-2.
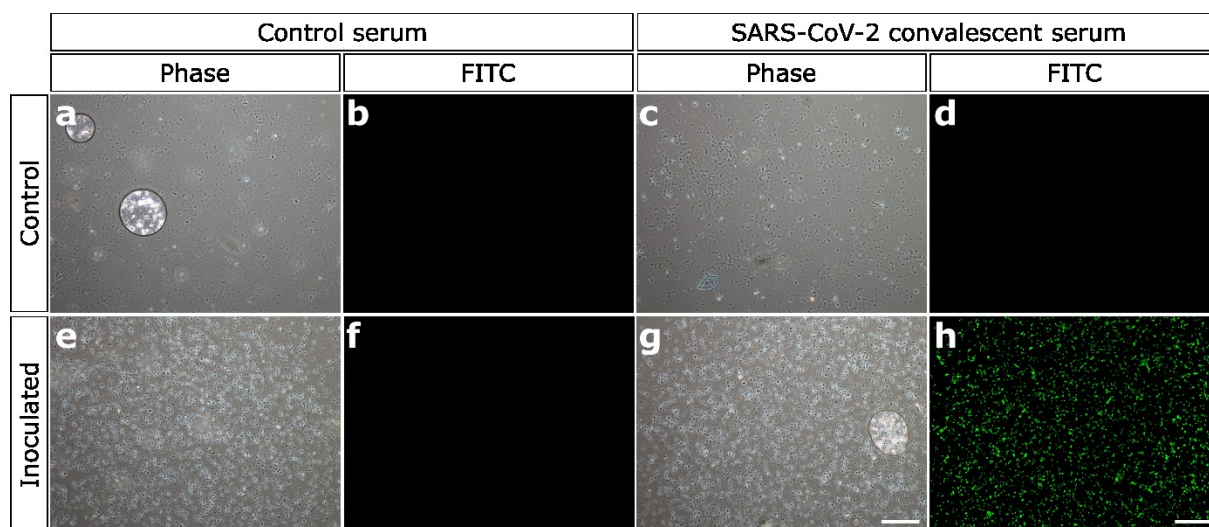
Fig. 3.3 Immune fluorescence staining with SARS-CoV-2 convalescent serum indicates the presence of SARS-CoV-2 antigens in the inoculated Vero cells. Microscopic imaging of Vero cells inoculated with a naso-/oropharyngeal swab specimen from a SARS-CoV-2-infected individual after immune fluorescence staining with SARS-CoV-2 convalescent serum. Untreated Vero cells and serum from an individual without known present or past infection with SARS-CoV-2 served as controls. Scale bar is 100 μm.

So far, however, only SARS-CoV-2 RNA and antigens were detected as indirect evidence for proper SARS-CoV-2 production in the inoculated cells. To also test for the generation of infectious SARS-CoV-2 particles, supernatant from the initially inoculated Vero cells was transferred to new Vero cells at 4 dpi and in two dilutions (Fig. 3.4 **A**).

Again, there was a strong increase in SARS-CoV-2 RNA in cell culture supernatant over the course of three days similar to what was observed after the preceding initial inoculation with

the naso-/oropharyngeal swab specimen (Fig. 3.4 **B**). Of note, infection with the lower dilution resulted in a higher SARS-CoV-2 RNA yield at 3 and 4 dpi, which may be explained by premature cell lysis induced by the higher viral load of the 10^{-2} dilution (2).
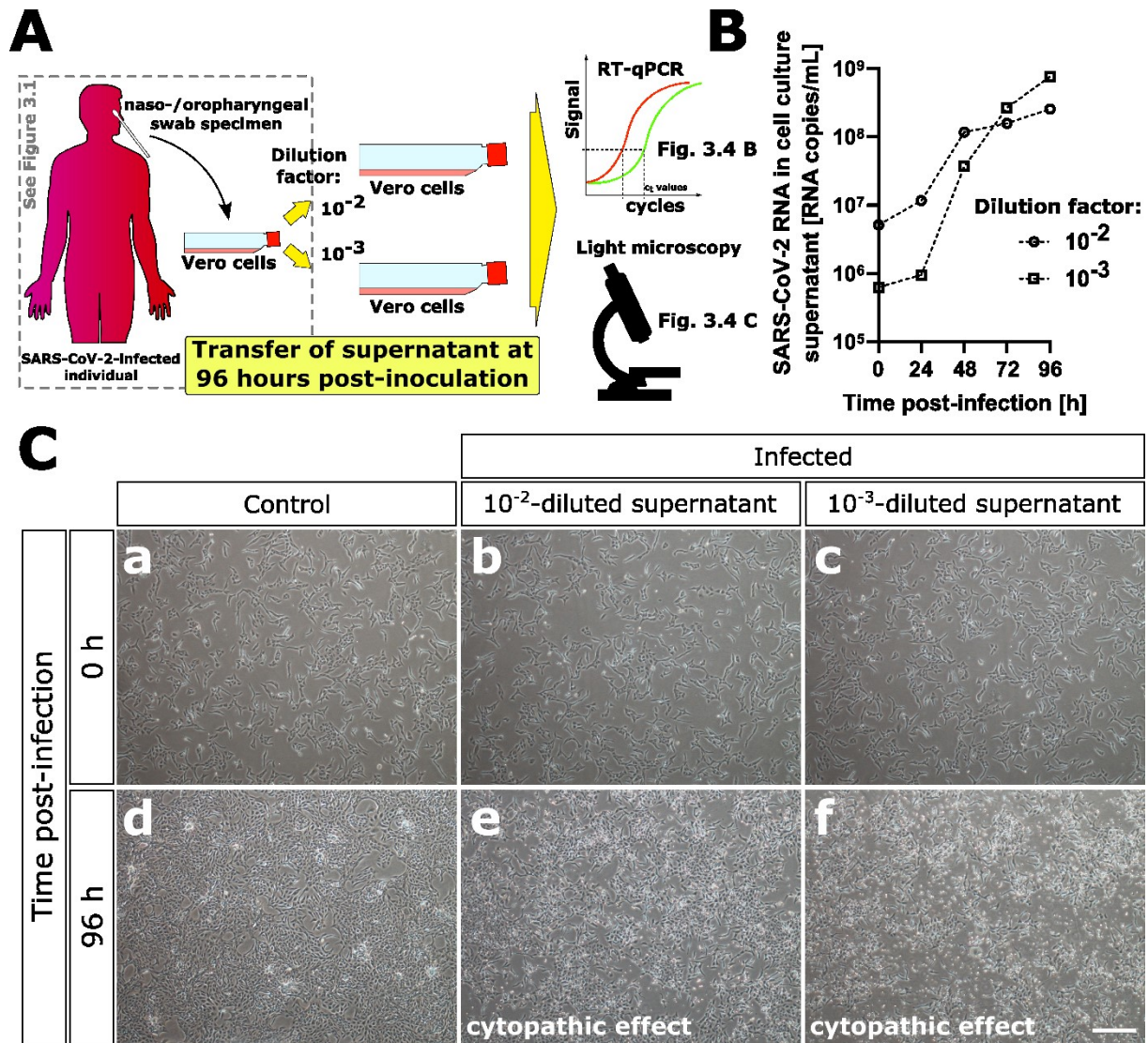
Fig. 3.4 Transfer of diluted cell culture supernatant from the inoculated Vero cells to new Vero cells hints towards the presence of infectious SARS-CoV-2. (**A**) Schematic illustrating the experimental work flow to show the presence of infectious SARS-CoV-2 in the cell culture system by transfer of diluted cell culture supernatant to new Vero cells and continuous monitoring of viral RNA in the cell culture supernatant via RT-qPCR and possible virus-induced cytopathic effects via light microscopy. (**B**) Monitoring of SARS-CoV-2 RNA in the cell culture supernatant of Vero cells treated with diluted cell culture supernatant (dilutions of 10^{-2} and 10^{-3}) obtained from the initially inoculated Vero cells via RT-qPCR over a period of 96 hours post-infection. (**C**) Light microscopic imaging at 96 hours post-infection to check for the presence of virus-induced cytopathic effects in Vero cells treated with diluted cell culture supernatant (dilutions of 10^{-2} and 10^{-3}) obtained from the initially inoculated Vero cells. Untreated Vero cells served as control. Scale bar is 100 μm.

In line with the increase in SARS-CoV-2 RNA, light microscopic analysis revealed the same CPE at 4 dpi that appeared also after inoculation with the swab specimen, overall demonstrating

the presence of infectious SARS-CoV-2 within the Vero cell culture supernatant of the initially inoculated Vero cells (Fig. 3.4 **C**).

Before analyzing the antiviral activity of anti-SARS-CoV-2 LNA mixmers in infected Vero cells, a SARS-CoV-2 stock was generated by infection of new Vero cells with the now designated SARS-CoV-2 *NRW-42* isolate. The designation NRW-42 was selected, because the same swab specimen that was used to generate this cell culture isolate was also part of a retrospective analysis of local SARS-CoV-2 outbreaks. As part of this parallel study, this specific swab specimen was coined NRW-42 (169). Next, the viral titer of this NRW-42 stock was determined by performance of an end point dilution assay based on the appearance of the virus-induced CPE.

Furthermore, generation of intact SARS-CoV-2 particles after infection with the SARS-CoV-2 NRW-42 isolate was also analyzed via transmission electron microscopy in collaboration with Dr. Ann Kathrin Bergmann (Electron microscopy core facility of the University Hospital Düsseldorf, Heinrich Heine University Düsseldorf).

Transmission electron microscopic (TEM) analysis was performed by infecting Vero cells at a multiplicity of infection (MOI) of 0.5 with subsequent fixation at 8 hours post-infection (hpi). This analysis revealed intact viral particles on the outside of the cellular membrane (Fig. 3.5 a, black arrowheads) as well as within double membrane vesicles within infected cells (Fig. 3.5 b, white dotted line), which corresponded to the coronavirus replication cycle (2). Images taken under approx. 80,000-fold magnification clearly showed the viral envelope (black arrow) and indicated the viral spike protein on the outer surface of the viral particles (Fig. 3.5 c, d). Hence, it was concluded that this cell culture system with the SARS-CoV-2 NRW-42 isolate, isolated and grown here is suitable for SARS-CoV-2 replication studies.
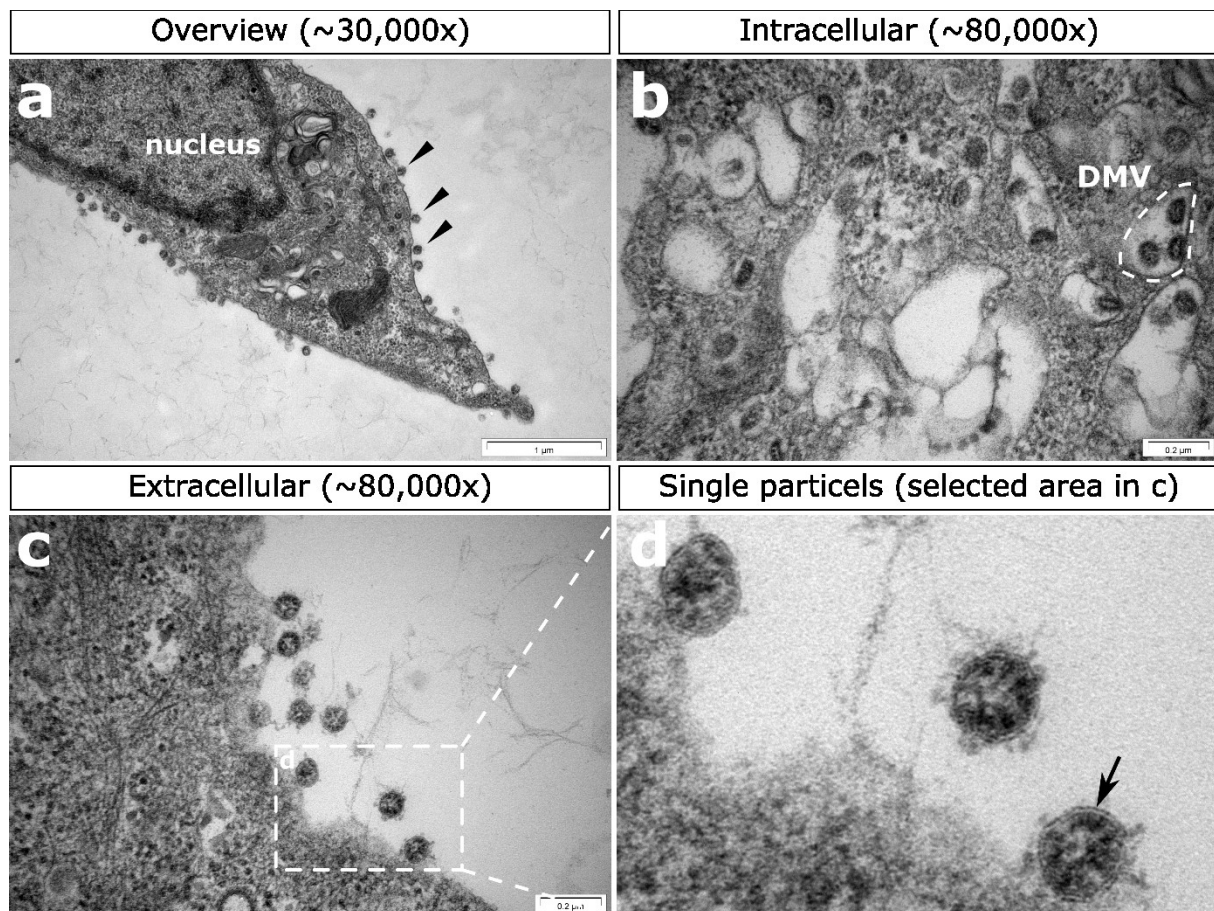
Fig. 3.5 Transmission electron microscopic analysis of SARS-CoV-2-infected Vero cells demonstrates the presence of intact SARS-CoV-2 particles. Transmission electron microscopic analysis of Vero cells infected with SARS-CoV-2 NRW-42 isolate at an MOI of 0.5 at 8 hours post-infection. Black arrowheads in (a) point to SARS-CoV-2 particles at the outer surface of the cellular membrane. The white dotted line in (b) indicates a double membrane vesicle (DMV) containing three SARS-CoV-2 particles. The section indicated with a white dotted line in (c) is shown enlarged in (d). The black arrow in (d) points to the viral envelope.

After analysis of the replication cycle by transmission electron microscopy, whole-genome sequencing in collaboration with Dr. Andreas Walker (Institute of Virology, University Hospital Düsseldorf, Heinrich Heine University Düsseldorf) was performed to dissect possible nucleotide substitutions of the NRW-42 isolate with reference to the original SARS-CoV-2 Wuhan-Hu-1 isolate also with respect to the later design of anti-SARS-CoV-2 LNA mixmers (see below). The whole-genome sequencing performed revealed only six nucleotide substitutions compared with the SARS-CoV-2 Wuhan-Hu-1 reference genome (NC_045512) (See Table 3.1) (54). Out of these mutations, so far only the designated D614G mutation, which is caused by the A>G mutation at nucleotide position 23,403, was shown to impact viral replication. This mutation was found to increase the binding affinity of the SARS-CoV-2 spike glycoprotein to human ACE-2, this way boosting viral infectivity (170, 171). Since the D614G genotype quickly

became the predominant genotype at the time, the here generated NRW-42 isolate was considered a good representative isolate of the circulating SARS-CoV-2 strains to conduct infection experiments with (171). Of note, no cell culture adaption by mutations was observed as revealed by comparison of the NRW-42 cell culture isolate sequence with the NRW-42 swab specimen sequence.

Tab 3.1 Whole-genome sequence analysis revealed six nucleotide exchanges between isolates SARS-CoV-2 NRW-42 and Wuhan-Hu-1.

Isolate	Location	Nucleotide position in SARS-CoV-2 Wuhan-Hu-1					
		241	1059	3037	14408	23403	25563
Wuhan-Hu-1 (NC_045512)	Wuhan, China	C	C	C	C	A	G
NRW-42 (EPI_ISL_425126)	Düsseldorf, Germany	T	T	T	T	G	T
RNA Motif or ORF	-	5' UTR	Orf1ab	Orf1ab	Orf1ab	S	Orf3a
Amino acid substitution	-	-	Thr>Ile	Phe>Phe	Pro>Leu	Asp>Gly	Gln>His

C = Cytosine; A = Adenine; G = Guanine; T = Thymine; ORF = open reading frame; UTR = Untranslated region; S = SARS-CoV-2 Spike protein

In summary, inoculation of Vero cells with a naso-/oropharyngeal swab specimen from an SARS-CoV-2-infected individual allowed generation of an early infectious SARS-CoV-2 cell culture isolate, designated the SARS-CoV-2 NRW-42 isolate, which has only six nucleotide substitutions compared to the SARS-CoV-2 Wuhan-Hu-1 reference genome and can be used to model SARS-CoV-2 infection in cell culture.

3.1.2 Targeting two sequence motifs located at the 5' and 3' untranslated region of the SARS-CoV-2 RNA genome by unassisted LNA mixmer delivery does not inhibit viral replication

With the exact sequence of the SARS-CoV-2 NRW-42 isolate known, it was now possible to specifically target vial sequences with LNA mixmers (Fig. 3.6 **B**). In the preceding study that showed LNA mixmer-mediated inhibition of HIV-1 replication, the two viral splicing regulatory elements (SREs) G_{I3}-2 and ESE_{tat} were targeted by unassisted delivery of the designed 16-mer LNA mixmers (1). In contrast to HIV-1, SARS-CoV-2 is not dependent on splicing and moreover,

replication of its RNA genome occurs exclusively in the cytoplasm (82). Therefore, instead of SREs, the conserved core sequence of SARS-CoV-2 within the coronavirus leader sequence in the viral 5'-untranslated region (UTR) and a 3'-UTR region rich in hnRNP sites were chosen as the target sequence to inhibit SARS-CoV-2 replication (Fig. 3.6).
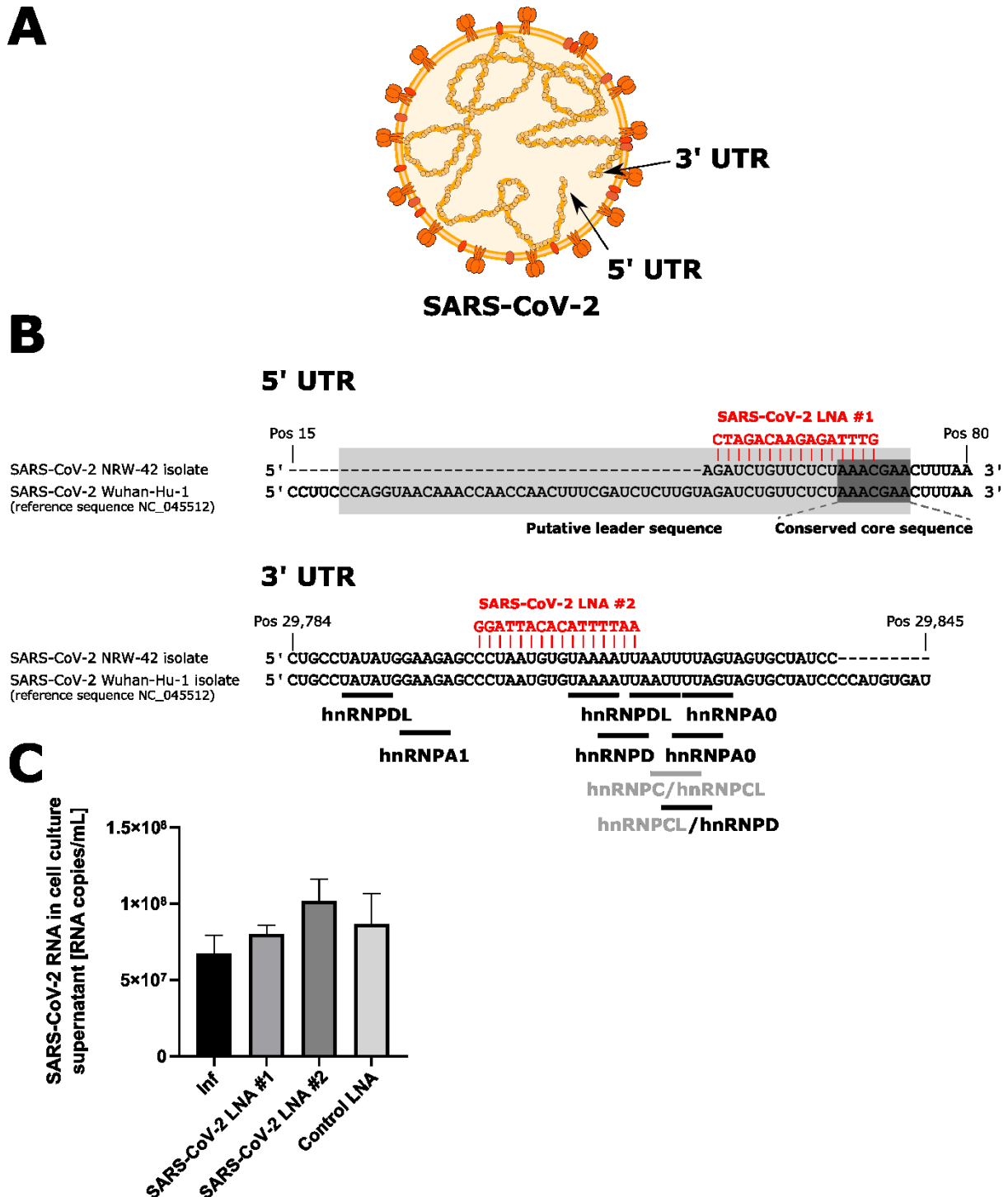
Fig. 3.6 Unassisted delivery of SARS-CoV-2 specific LNA mixmers does not interfere with viral replication. (**A**) Schematic illustrating a SARS-CoV-2 particle containing the 29,903 nucleotide long viral RNA genome with its 5' and 3' untranslated regions (UTRs). (**B**) Overview of the two SARS-CoV-2 specific LNA mixmer target sequences

located at the viral 5' UTR (upper panel) and the 3'UTR (lower panel). The SARS-CoV-2 NRW-42 isolate sequence (GISAID: EPI_ISL_425126) is shown aligned to the SARS-CoV-2 Wuhan-1 reference sequence (NC_045512). The genomic sequences from nucleotide positions 15 to 80 (5'UTR) and 29,784 to 29,845 (3'UTR) are shown. The anti-SARS-CoV-2 LNA #1 binds to the SARS-CoV-2 *conserved core sequence* RNA motif within the putative SARS-CoV-2 leader sequence (82). The anti-SARS-CoV-2 LNA #2 binds to a sequence rich in hnRNP binding sites with suggested function in coronavirus replication (101-103). Known binding site pentamer motifs for different hnRNPs are indicated (103, 172). Exclusively nuclear-located hnRNPs are shown in light grey (173). (**C**) Quantification of SARS-CoV-2 RNA within cell culture supernatant at 72 hours post-infection via RT-qPCR analysis. Vero cells were infected with SARS-CoV-2 NRW-42 isolate at an MOI of 0.01. Cells were washed with PBS at 1 hour post-infection and LNA mixmers were added to the new medium in a final conc. of 3 µM. Data presented as mean +SD (n = 3).

The conserved core sequence within the SARS-CoV-2 5'UTR is essential for coronavirus replication, because it allows the generation of nested RNA products containing the coronavirus leader sequence during negative strand RNA synthesis (Fig. 3.6 **B**) (100).

Given that the anti-HIV-1 LNA mixmer in the preceding study with the most profound antiviral activity turned out to be the anti-G_{I3}-2 LNA mixmer, the other anti-SARS-CoV-2 LNA mixmer was designed to mask hnRNP binding sites. Importantly, hnRNP binding within the 3'UTR of the coronavirus genome is crucial for replication (Fig. 3.6 **B**) (101-103, 105).

To test the antiviral potential of these two anti-SARS-CoV-2 LNA mixmers, Vero cells were infected with SARS-CoV-2 NRW-42. After one hour, cells were washed and treated with 3 µM either one of the LNA mixmers for 72 hours. Surprisingly, however, subsequent quantification of viral RNA in the cell culture supernatants did not detect LNA-mediated reduction of viral replication (Fig. 3.6 **C**).

Based on this result, it was questioned whether the anti-SARS-CoV-2 LNA mixmers might fail to reach their viral target transcripts after unassisted delivery to infected cells, for two reasons. First, it was previously suggested that unassisted anti-HIV-1 LNA mixmer delivery robustly degrades target RNA levels, which would lead to reduced SARS-CoV-2 RNA levels both by directed degradation and replication inhibition, but this was obviously not observed here (1). Secondly, given the importance of the targeted SARS-CoV-2 RNA motifs, especially of the core consensus sequence within the 5'UTR, for viral replication, mere binding of the LNA mixmers should theoretically already disturb viral replication.

Indeed, endosomal entrapment of endocytosed LNA mixmers is a huge pitfall of ASO application that is currently widely investigated (46). Here, the characteristic replication mechanisms of (+)ssRNA viruses, including coronaviruses, which involves the formation of microenvironments within double membrane vesicles, observed also via the here performed TEM analysis (Fig. 3.5 b) and that protect the viral genome from detection by innate immunity,

may contribute to complete insulation of viral RNA from the applied LNA mixmers. This would render ASO application for coronavirus inhibition futile.

3.2 Unassisted delivery of an LNA mixmer targeting the 5' ends of Hazara virus L and S segment does not inhibit viral replication

Hazara virus is a negative strand RNA virus that belongs to the *Nairoviridae* of the order *Bunyavirales*. Classified a risk group 2 pathogen, it is often used as a surrogate model for its close relative Crimean Congo hemorrhagic fever virus (CCHFV), which is a serious public health threat in over 30 countries worldwide with case fatality rates up to 40 % and hence, classified a risk group 4 pathogen (WHO).

In contrast to coronaviruses, the cytoplasmic (-)ssRNA nairoviruses were neither shown to induce such drastic reshaping of cellular membranes nor to use double membrane vesicles for genome replication. Therefore, to test whether the failure to inhibit SARS-CoV-2 replication was specifically related to reshaping of cellular membranes and/or the double membrane compartmentalization, unassisted LNA mixmer delivery was used to approach inhibition of the Hazara virus replication.

The Hazara virus RNA genome consists of three segments (L, M and S) that form so-called panhandle structures due to the high complementarity of their 3' and 5' termini (Fig. 3.1 **A**) (106). This complementarity is suggested necessary for bunyaviral RNA promoter acitivty and hence, for the generation of viral antigenomic RNA during replication (110-112).

Following the same approach as for LNA-mixmer-based inhibition of SARS-CoV-2 replication, the designed anti-Hazara virus LNA mixmer targeted this important RNA pan handle structure to ensure that inhibition of viral replication by mere LNA mixmer binding is possible.

Further, due to the high conservation of the Hazara virus RNA termini, it was possible to design one LNA mixmer that targets the promoter elements within the 5' end of the viral S as well as of the L segment (Fig. 3.7 **A**, right panel).

To test the antiviral activity of the designed anti-Hazara virus LNA mixmer in a collaboration with Dr. Vanessa Monteil (Department of Laboratory Medicine, Karolinska Institute, Solna, Sweden), CaCo-2 cells were infected with Hazara virus (Strain JC280) at an MOI of 0.1. After one hour, cells were washed and treated with the anti-Hazara virus LNA mixmer in increasing concentrations for 48 hours. RT-qPCR analysis was then performed to compare viral replication between anti-Hazara virus LNA mixmer treated cells and non-treated cells. In this pilot experiment, no antiviral activity of the designed anti-Hazara virus LNA mixmer was observed, indicating that failure of inhibition of SARS-CoV-2 replication was most likely not

related to reshaping of cellular membranes and/or the double membrane compartmentalization (Fig. 3.7 **B**).
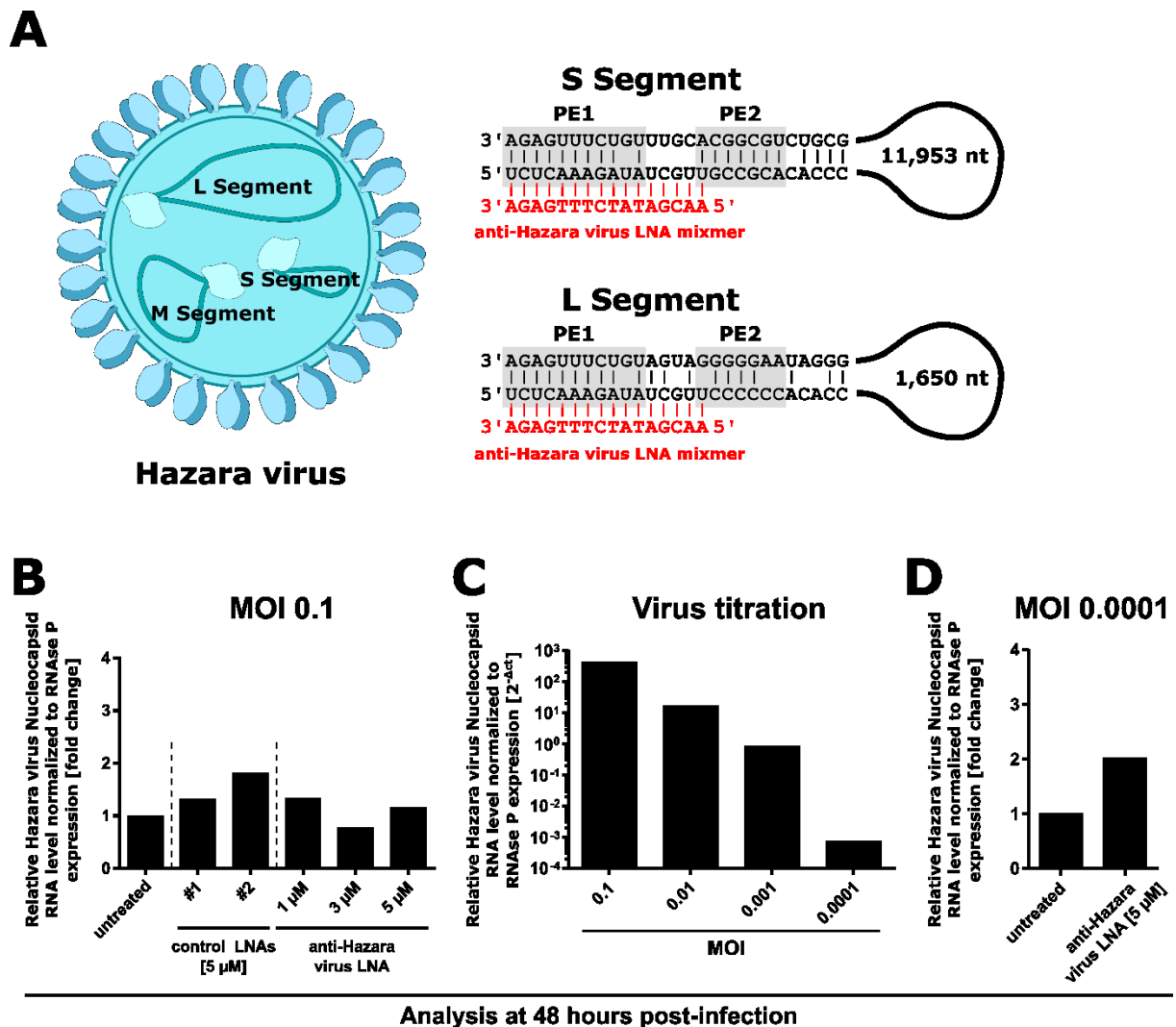
Fig. 3.7 Unassisted delivery of an LNA mixmer targeting the 5' ends of Hazara virus L and S segment does not inhibit viral replication. (**A**) Schematic illustrating a Hazara virus particle containing the three viral genomic RNA segments (left panel). The terminal 5' and 3' sequences of segments S and L are shown as the suggested double-stranded panhandle structure (right panel) (111). The designed anti-Hazara virus LNA mixmer (red) binds to the 5' ends of both segments. The conserved promoter elements (PE) 1 and 2 are shaded in grey. (**B**) Quantification of Hazara virus RNA from cell lysate at 48 hours post-infection via RT-qPCR analysis presented as fold change to untreated control cells. CaCo-2 cells were infected with Hazara virus (Strain JC280) at an MOI of 0.1. Cells were washed with PBS at 1 hour post-infection and LNA mixmers were added to the new medium in the depicted final conc. (n = 1). (**C**) Quantification of Hazara virus RNA from cell lysate at 48 hours post-infection via RT-qPCR analysis. CaCo-2 cells were infected with Hazara virus (Strain JC280) at the depicted MOIs (n = 1). (**D**) Quantification of Hazara virus RNA from cell lysate at 48 hours post-infection via RT-qPCR analysis presented as fold change to untreated control cells. CaCo-2 cells were infected with Hazara virus (Strain JC280) at an MOI of 0.0001. Cells were washed with PBS at 1 hour post-infection and the anti-Hazara virus LNA mixmer was added to the new medium at a final conc. of 5 µM (n = 1).

Nevertheless, to be able to detect even a minor antiviral effect of the anti-Hazara virus LNA mixmer, viral titration was performed to determine the lowest possible MOI that would allow analysis of viral replication via RT-qPCR and thus increase the sensitivity for the anti-Hazara virus LNA mixmer assay. Infection of CaCo-2 cells at decreasing MOIs from 0.1 to 0.0001 showed that an MOI as low as 0.0001 is still sufficient to analyze viral replication via RT-qPCR (Fig. 3.7 **C**).

Therefore, during the next experiment, CaCo-2 cells were infected with Hazara virus at an MOI of 0.0001 before unassisted delivery of the anti-Hazara virus LNA mixmer. Nonetheless, no antiviral acitivity could be observed for this LNA mixmer (Fig. 3.7 **D**).

In summary, the performed experiments investigating the potential of the designed anti-Hazara virus LNA mixmer to inhibit Hazara virus replication could not show any antiviral activity. These results suggest that the formation of microenvironments within double membrane vesicles is most likely not the reason for failure of LNA mixmer-mediated inhibition of SARS-CoV-2 replication, at least not the sole cause.

With respect to the specific HIV-1 RNA sequences targeted in the preceding study of LNA mixmer-induced inhibition of HIV-1 replication, namely the viral SREs G_{I3}-2 and ESE_{tat}, and the apparent lack of such SREs in the genomes of SARS-CoV-2 and Hazara virus, the question remains whether the observed LNA mixmer-induced HV-1 RNA degradation after unassisted delivery underlies some sort of target sequence-specific effect or even one restricted to the specific HIV-1 replication cycle (1).

3.3 Unassisted delivery of LNA mixmers targeting splicing regulatory elements in the Influenza A virus M segment does not inhibit viral replication

In the previous experiments, no antiviral activity of LNA mixmers against SARS-CoV-2 and Hazara virus was observed. This implies that no induced target RNA degradation occurred in the cytoplasm after unassisted LNA mixmer delivery. Because such an LNA mixmer-induced degradation was so far only observed for anti-HIV-1 LNA mixmers, specifically targeting the two HIV-1 SREs G_{I3}-2 and ESE_{tat}, the question was addressed whether this observed degradation might be target sequence-specific (1).

IAV constitutes another RNA virus with high public health concern and for which cell culture infection assays are well-established. Since IAV also engages the nucleus for its replication and its RNA transcripts contain SREs like HIV-1, IAV was used as another candidate virus that may be susceptible to LNA mixmer-induced RNA degradation. With IAV, it was now investigated

whether LNA mixmer-induced target RNA degradation underlies a certain target sequence-specificity.

IAV is a negative strand RNA virus that belongs to the *Orthomyxoviridae.* Besides Influenza B virus, IAV is the main etiological agent of flu disease, together causing an estimated 1 billion cases worldwide every year, of which 3 to 5 million are severe cases and 290,000 to 650,000 result in influenza-related death (WHO).

Its viral genome is split into eight segments and their nuclear import is required for viral replication (106). This nuclear import of viral genomic RNA enables exploitation of the cellular splicing machinery, which allows an overall higher coding capacity of single viral transcripts.

With respect to IAV, the pre-mRNA derived from the M and NS segment is spliced to produce different proteins (106). The IAV M segment pre-mRNA, for instance, has the coding capacity to generate viral M1 and M2 protein. IAV M1 protein is produced from the unspliced viral M mRNA and M2 protein from an intronless transcript, which is generated by regulated usage of a splice donor site and splice acceptor site within the IAV M pre-mRNA (Fig. 3.8 **A**, **B**). Loss of IAV M1 or M2 protein drastically affects viral replication (174-178).

Since the two anti-HIV-1 LNA mixmers that were observed to degrade RNA targeted the two HIV-1 SREs G_{I3}-2 and ESE_{tat}, it was hypothesized that such SRE motifs in particular may present sequences that are vulnerable to LNA mixmer-induced degradation. Here, the IAV M segment pre-mRNA seemed to be a promising target transcript considering its balanced splicing during infection

A HEXplorer algorithm-based prediction analysis of the SRE landscape downstream of the IAV M segment splice acceptor site indeed showed the location of potential SREs by revealing two HEXplorer-positive regions (Fig. 3.8 **C**). Based on the RESCUE (Relative Enhancer and Silencer Classification by Unanimous Enrichment) sequence analysis approach underlying the HEXplorer algorithm, HEXplorer-positive sequences tend to correlate with SR protein binding sites. SR proteins represent one family of splicing regulatory proteins. In this context, importantly, Shih and Krug showed that the use of the IAV M splice acceptor site is supported by the binding of the SR protein SRSF1. Mapping of the SRSF1 binding site showed a strong overlap with the HEXplorer-positive regions, underlining the presence of viral SRE sites important for balanced splicing downstream of the IAV M splice acceptor site (Fig. 3.8 **C**, **D**) (179).

To address the question of whether the IAV M segment is susceptible to LNA mixmer-induced degradation, two anti-IAV LNA mixmers, one targeting the SRSF1 binding site and another targeting the second HEXplorer-predicted SR binding site immediately downstream of it were, therefore designed and for their putative anti-IAV activity tested (Fig. 3.8 **D**).
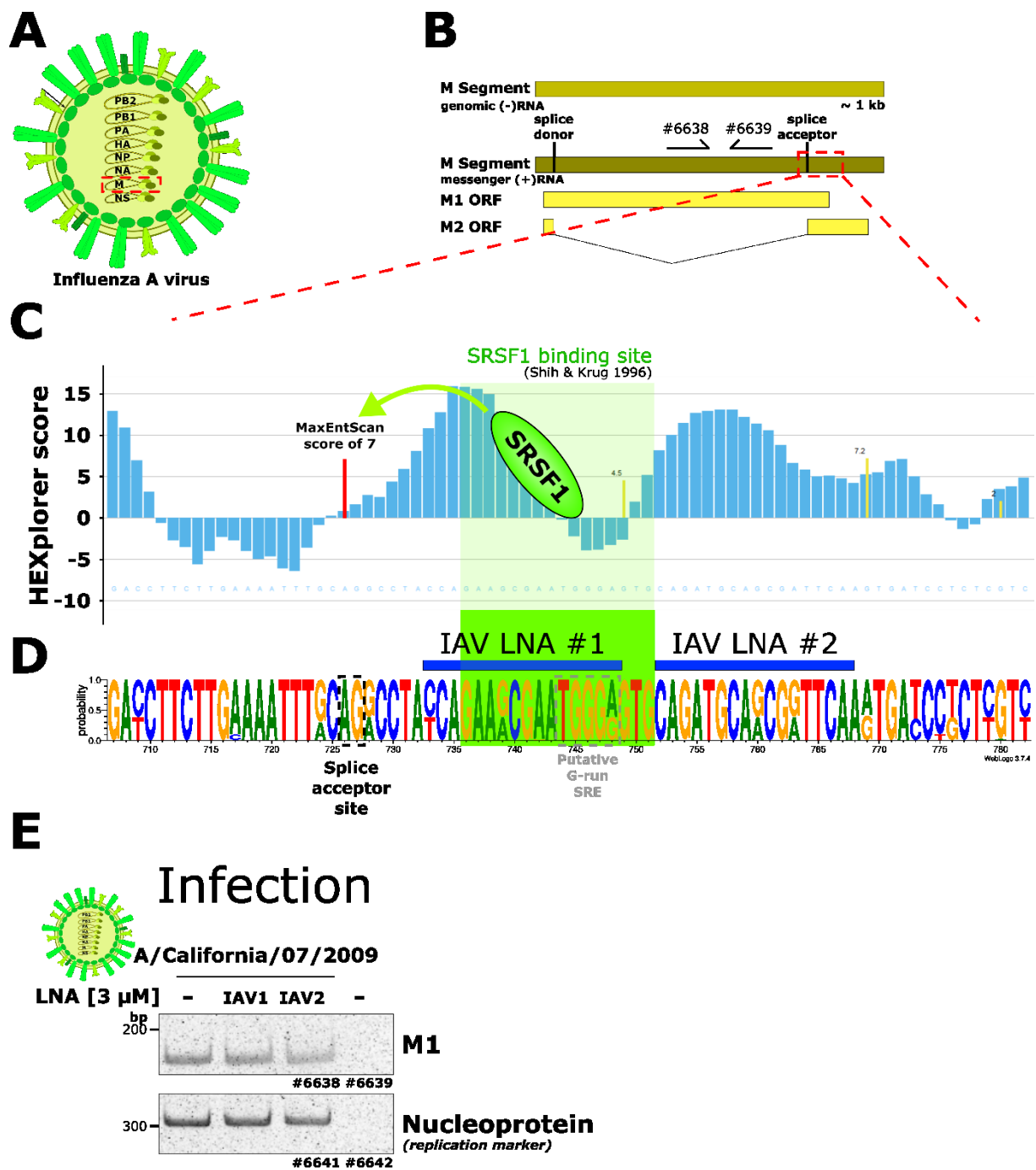
Fig. 3.8 Unassisted delivery of LNA mixmers targeting potential splicing regulatory elements in the Influenza A virus M Segment does not inhibit viral replication. (**A**) Schematic illustrating an Influenza A virus (IAV) particle containing the eight viral genomic RNA segments. (**B**) Schematic showing the genomic IAV negative strand M segment with complementary plus strand mRNA and the relative position of the two open reading frames (ORFs) coding for viral M1 and M2 protein, respectively. M2 protein derives from a spliced mRNA by usage of the indicated splice donor and splice acceptor site. (**C**) HEXplorer profile predicting the splicing regulatory element (SRE) landscape in the depicted IAV RNA region (180). Indicated is the position and MaxEntScan score of the annotated IAV M2 splice acceptor site (red bar) and positions and HBond scores of putative GT dinucleotide containing splice donor sites (yellow bars). (**D**) Sequence logo showing the probability of each base at the positions 707 to 782 of the IAV M Segment mRNA based on the 878 human IAV M Segment sequences collected

in 2020 and uploaded to the NCBI Influenza Virus Database (181). The positions of the splice acceptor site (AG dinucleotide in black dotted line) and a published SRSF1 binding site (green shaded) (179) are indicated. A putative G-run SRE motif (DGGGD) like shown in the HIV-1 genome is also marked (grey). Binding sites for the anti-IAV LNA mixmer #1 and #2 are indicated with a blue bar. Sequence logo created with WebLogo 3 (Version 3.7.4) (182). (**E**) Amount of unspliced Influenza A virus M1 transcript after infection of CaCo-2 cells with IAV and unassisted LNA mixmer delivery as analyzed via RT-PCR. Cells were infected with IAV strain A/California/07/2009 as described in the method section and washed with PBS at 1 hour post-infection. The indicated LNA mixmers were added to the new medium at a final conc. of 3 µM (n = 1). RT-PCR analysis of IAV nucleoprotein transcript served as replication marker.

LNA mixmer-induced degradation of the IAV M RNA by unassisted LNA mixmer delivery was analyzed by infecting CaCo-2 cells with the IAV A/California/07/2009 strain and subsequent treatment with the anti-IAV LNA mixmers. Unexpectedly, however, no decrease in viral M transcript was observed by RT-PCR analysis 48 hpi after unassisted delivery of both anti-IAV LNA mixmers suggesting lack of induced RNA degradation (Fig. 3.8 **E**, M1). Of note, the same was observed after infection with IAV A/Brisbane/02/2018 strain (data not shown). In agreement with the unexpected lack of LNA-induced RNA degradation, viral replication as analyzed by IAV nucleocapsid was also unaffected (Fig. 3.8 **E**, Nucleoprotein).

In summary, after unassisted delivery no LNA mixmer-induced degradation was detected in the context of IAV infection, although the targeted sequences exhibited many parallels to the LNA mixmer-targeted HIV-1 SREs that are susceptible to LNA mixmer-induced degradation.

Based on the obtained results so far, it was concluded that gaining an understanding behind the apparent HIV-1 RNA specificity of LNA mixmer-induced degradation is important to explain the failure of SARS-CoV-2, Hazara virus and IAV replication by unassisted LNA mixmer delivery. Therefore, as a next step to evaluate the antiviral capacity of LNA mixmers with this thesis, the mechanism underlying the observed LNA mixmer-induced degradation of HIV-1 RNA was investigated.

3.4 False positioning of PCR primer pairs can lead to misinterpretation of RT-PCR results after unassisted LNA mixmer delivery

3.4.1 Positions of HIV-1-specific primer pair binding sites relative to the G_{I3}-2 LNA mixmer binding site affect RT-PCR outcome

Unassisted delivery of LNA mixmers targeting SARS-CoV-2, Hazara virus and Influenza A virus RNA could not be shown to induce viral RNA degradation as previously observed for anti-HIV-1

LNA mixmers (1). To understand this supposed HIV-1 RNA specificity, the underlying pathway of LNA mixmer-induced RNA degradation should be characterized.

At first, G_{I3}-2 LNA mixmer-mediated target RNA degradation as observed in the preceding study should be verified while assessing its overall efficacy in parallel. The target region of the G_{I3}-2 LNA mixmer is located within HIV-1 Gag/-Pol, Vif and Vpr RNA transcripts while HIV-1 transcripts coding for Tat and Env, for instance, lack the G_{I3}-2 LNA mixmer target region (Fig. 3.9 **A**, vertical red dashed line).

To confirm G_{I3}-2 LNA mixmer-induced degradation and investigate its efficacy, T-cells were infected with the laboratory HIV-1 strain NL4-3 at an MOI of 0.005 and subsequently treated with increasing concentrations of the G_{I3}-2 LNA mixmer. At 24 hpi, total RNA was isolated and RT-PCR analysis was performed. The RT-PCR analysis was performed according to the experimental set-up used in Hillebrand et al., 2019, using a primer pair (#1544/#3632) that amplifies HIV-1 Tat, Vpr and Vif RNA. As expected, unassisted delivery of the anti-G_{I3}-2 LNA mixmer resulted in the absence of HIV-1 Vpr (Vpr3) and Vif RNA (Vif2), but did not affect HIV-1 Tat (Tat1-3) RNA levels (Fig. 3.9 **B**, a). Interestingly, treating the cells with an anti-G_{I3}-2 LNA concentration as low as 0.5 µM also resulted in the complete absence of HIV-1 Vpr and Vif RNA, a finding not addressed before (Fig. 3.9 **B**, a).

Hence, the conducted RT-PCR analysis confirmed efficient G_{I3}-2 LNA mixmer-mediated target RNA degradation during viral infection, which was previously suggested to cause the observed inhibition of HIV-1 replication.

Based on these results that already 0.5 µM of the G_{I3}-2 LNA mixmer is sufficient to completely degrade HIV-1 Vif and Vpr RNA after HIV-1 infection, the EC_{50} value of G_{I3}-2 LNA mixmer-mediated degradation was to be determined to explore on one hand the full potential of LNA mixmer-induced RNA degradation and on the other hand find working concentrations for subsequent experiments.
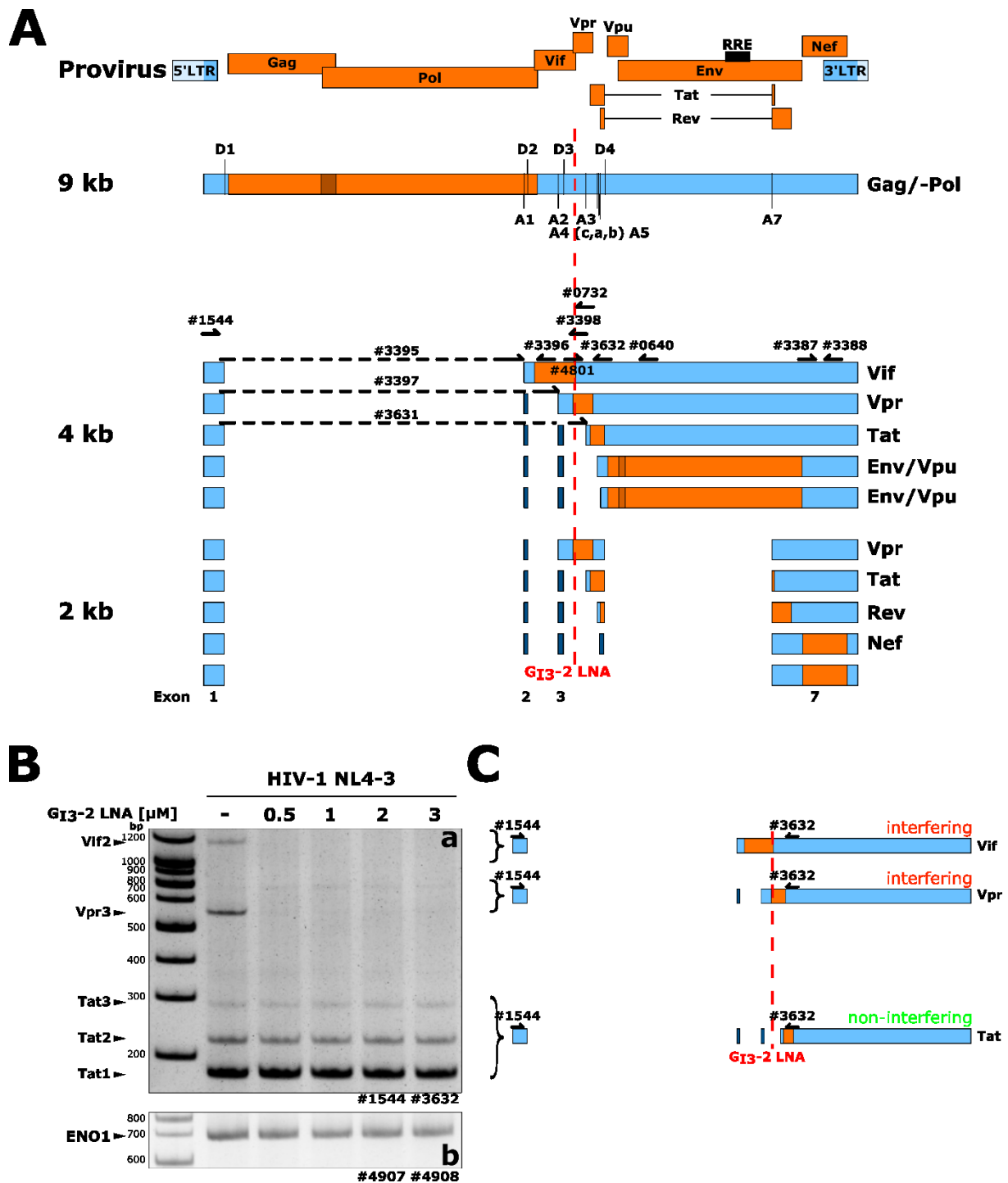
Fig. 3.9 RT-PCR analysis after unassisted G$_{I3}$-2 LNA mixmer delivery suggests LNA mixmer-mediated target RNA degradation already at concentration of 0.5 µM during HIV-1 infection. (**A**) Schematic of the HIV-1 genome with relative positions of viral long terminal repeats (LTRs), open reading frames (ORFs) (orange), the rev response element (RRE), splice donor sites (D1-D4), splice acceptor sites (A1-A7), primer binding sites as indicated by the tip of the arrows, respectively, and the G$_{I3}$-2 LNA mixmer binding site (red). HIV-1 transcripts can be summarized into the unspliced 9 kb, intron-containing 4 kb and the intronless 2 kb class. (**B**) Amount of specific HIV-1 transcripts after infection of Jurkat T-cells and unassisted G$_{I3}$-2 LNA mixmer delivery as analyzed via RT-PCR using the indicated primer pair (a) and with cellular ENO1 expression (b) as control (left panel). Cells were infected with HIV-1 laboratory strain NL4-3 at an MOI 0.005 and at 6 hours post-infection washed with PBS. The G$_{I3}$-2 LNA mixmer was added to the new medium at increasing concentrations (n = 3). Positions of the primer pair binding

sites relative to the G_{I3}-2 LNA mixmer binding site on the analyzed transcripts are shown (right panel). HIV-1 transcripts containing the G_{I3}-2 LNA mixmer binding sequence within their amplified region of interest during RT-PCR are depicted as interfering (red) and HIV-1 transcripts with their amplified region of interest not containing the specific G_{I3}-2 LNA mixmer binding site as non-interfering (green).

To determine the EC_{50} value, HIV-1 RNA transcript variant-specific RT-qPCR analysis was pursued to separately quantify levels of viral transcript variants. Given the complex architecture of HIV-1 splicing events with overlapping sequences between different viral transcripts, so-called exon junction primers were used. Following this approach, G_{I3}-2 LNA mixmer-mediated degradation specifically of the HIV-1 Vpr3 transcript variant with an exon junction primer (#3397) and the reverse primer #3398, should be analyzed (Fig. 3.9 **A**). To account for different infection rates between samples in RT-qPCR analysis, an HIV-1 RNA transcript unaffected by the anti-G_{I3}-2 LNA mixmer-induced degradation was used for normalization (housekeeper). Here, an HIV-1 Tat1 transcript variant-specific primer pair (#3631 #3632) was used to normalize HIV-1 Vpr3 RNA levels to HIV-1 Tat1 transcript variant levels (Fig. 3.9 **A**).

Usage at first of the described HIV-1 Tat1-specific primer pair (#3631/#3632) for RT-PCR analysis confirmed the observation that HIV-1 Tat transcript levels remain unaffected by unassisted anti-G_{I3}-2 LNA mixmer delivery (Fig. 3.10 a). The absence of additional PCR bands after the conducted RT-PCR analysis additionally confirmed the specificity of the used Tat1 transcript variant-specific primer pair #3631/#3632 (data not shown).
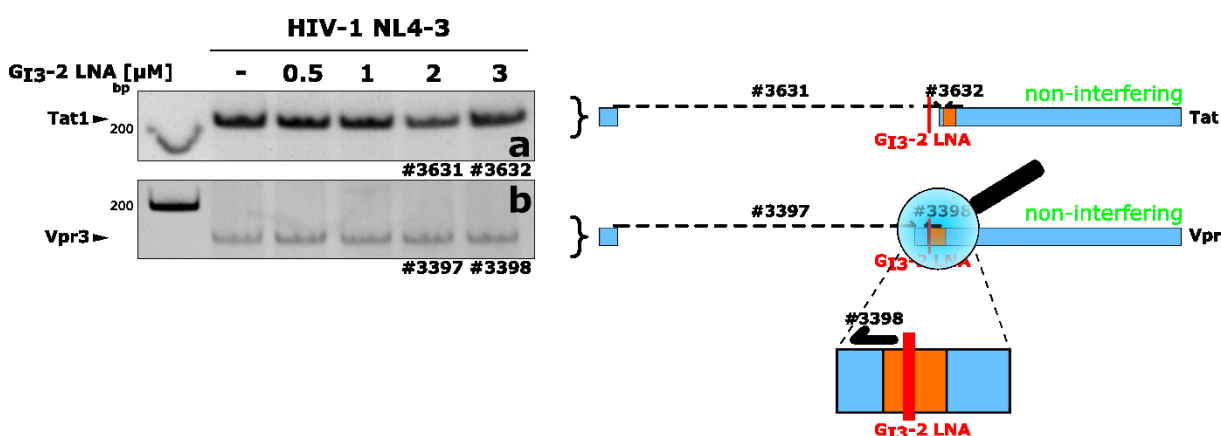
Fig. 3.10 An HIV-1 Vpr3 transcript-specific primer pair suggests that non-detectability of LNA mixmer-targeted HIV-1 RNA transcripts by RT-PCR analysis is dependent on the position of the employed primer pair. Amount of specific HIV-1 transcript variants Tat1 (a) and Vpr3 (b) after infection of Jurkat T-cells and unassisted G_{I3}-2 LNA mixmer delivery as analyzed via RT-PCR using the indicated primer pairs (left panel). Cells were infected with HIV-1 laboratory strain NL4-3 at an MOI 0.005 and at 6 hours post-infection washed with PBS. The G_{I3}-2 LNA mixmer was added to the new medium at increasing concentrations (n = 3). Positions of the primer pair binding sites relative to the G_{I3}-2 LNA mixmer binding site on the analyzed transcripts are shown (right panel). HIV-1

transcripts containing the G_{I3}-2 LNA mixmer binding sequence within their amplified region of interest during RT-PCR are depicted as interfering (red) and HIV-1 transcripts with their amplified region of interest not containing the specific G_{I3}-2 LNA mixmer binding site as non-interfering (green).

Completely unexpected, however, the performed HIV-1 Vpr3 transcript variant-specific RT-PCR analysis for the EC_{50} value determination using primer pair #3397/#3398 detected the same Vpr3 transcript level throughout all conditions irrespectively of the employed anti-G_{I3}-2 LNA mixmer concentration that was used to treat the infected cells (Fig. 3.10 b).

This observation was in complete contrast to the previously hypothesized G_{I3}-2 LNA mixmer-induced degradation of HIV 1 Vpr transcripts (Fig. 3.9 **B**, a). This result rather argues that the LNA-RNA duplex either does not dissociate during RNA purification but persists, thereby preventing cDNA synthesis, or that the LNA mixmers are also extracted during RNA isolation and ultimately interfere with PCR amplification.

To first exclude, however, that the selected PCR cycle number led to a saturation of amplified DNA, this way diminishing the expected difference in HIV-1 Vpr3 transcript levels, the HIV-1 Vpr3 transcript variant-specific RT-PCR analysis was repeated using different cycle numbers (21, 24 and 29 cylces). Nevertheless, neither of these analyses led to a difference in HIV-1 Vpr RNA levels (data not shown), which means that the non-detectability of the target RNA was obviously not due to LNA mixmer-induced RNA degradation but supposedly due to inhibition of the RT-PCR performed here.

To verify this hypothesis of co-extraction of LNA mixmers during RNA isolation, which may lead to an interference with either the cDNA synthesis or the subsequent PCR, RT-PCR analyses with additional primer pairs were performed. Analyzing simultaneously HIV-1 Vif, Vpr, Tat and Env RNA transcripts with primers #1544 and #0640, again, showed decreased Vpr3 and Vif2 transcript levels while Tat and Env RNA remained unaffected, as would be expected by an anti-G_{I3}-2 LNA mixmer-induced interference with the RT-PCR (Fig. 3.11, a).
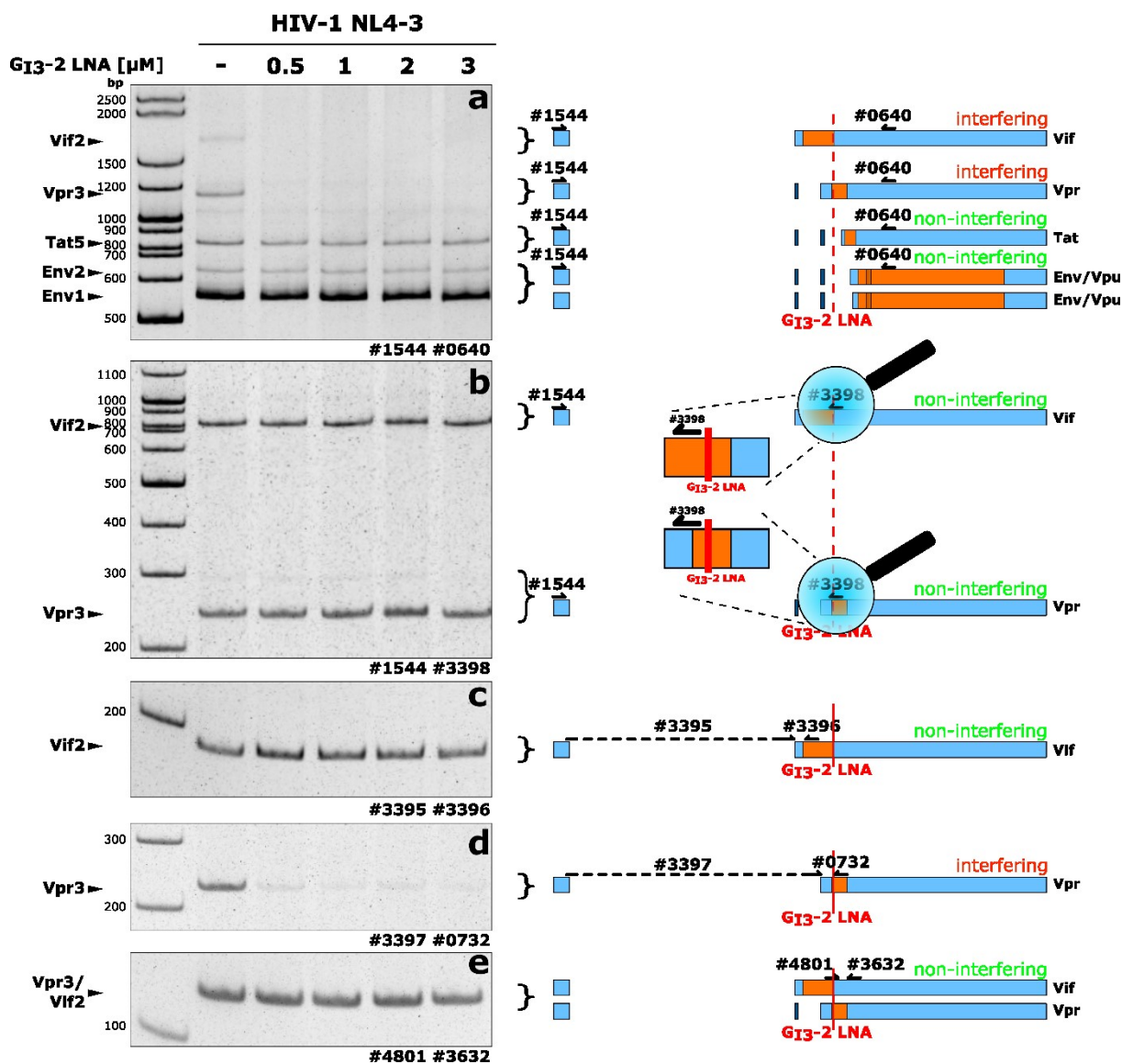
Fig. 3.11 Non-detectability of LNA mixmer-targeted HIV-1 RNA transcripts after RT-PCR due to relative position of the used primer pair. Amount of specific HIV-1 transcripts after infection of Jurkat T-cells and unassisted G_{I3}-2 LNA mixmer delivery as analyzed via RT-PCR using the indicated primer pairs (Left panel). Cells were infected with HIV-1 laboratory strain NL4-3 at an MOI 0.005 and at 6 hours post-infection washed with PBS. The G_{I3}-2 LNA mixmer was added to the new medium at increasing concentrations (n = 1). Positions of the primer pair binding sites relative to the G_{I3}-2 LNA mixmer binding site on the analyzed transcripts are shown (Right panel). HIV-1 transcripts containing the G_{I3}-2 LNA mixmer binding sequence within their amplified region of interest during RT-PCR are depicted as interfering (red) and HIV-1 transcripts with their amplified region of interest not containing the specific G_{I3}-2 LNA mixmer binding site as non-interfering (green).

As anticipated, amplification of Vif2 and Vpr3 RNA using primers #1544 and #3398 showed no sign of decreased RNA signals after unassisted anti-G_{I3}-2 LNA mixmer delivery (Fig. 3.11, b). Also, in line with the hypothesis of RT-PCR interference, amplification of Vif2 transcript variant RNA using primers #3395 and #3396 (Fig. 3.11, c) as well as of Vif2 and Vpr3 transcripts

together by using primers #4801 and #3632 (Fig. 3.11, e) detected the same transcript levels throughout the different experimental conditions irrespectively of prior G_{I3}-2 LNA mixmer treatment.

Amplification, again, of the HIV-1 Vpr3 transcript variant, but this time using the exon junction primer #3397 together with the reverse primer #0732, a primer pair that surrounds the G_{I3}-2 LNA mixmer binding site, resulted in non-detectability of Vpr3 RNA (Fig. 3.11, d).

Overall, the combined data obtained from the various RT-PCR analyses hinted towards the presence of G_{I3}-2 LNA mixmers within the RT-PCR samples after performed RNA isolation (Fig. 3.9, 3.10, 3.11). Interestingly, inhibition of cDNA synthesis, which precedes the PCR during RT-PCR analysis, seems unlikely. This is because if the LNA mixmers were already inhibiting oligo(dT)-primed cDNA synthesis, cDNA synthesis should stop at the G_{I3}-2 LNA mixmer binding site and no longer transcripts should be detectable via subsequent PCR. Such an inhibition would then lead to a lack of PCR signal for RNA regions that are located upstream of the G_{I3}-2 LNA mixmer binding site. Hence, the here performed RT-PCR analysis using primer pairs #3397/#3398 (Fig. 10, b), #1544/#3398 Fig. 3.11 b) and 3395/#3396 (Fig. 3.11 c) point rather to a subsequent LNA mixmer-mediated interference with the PCR amplification. Given the complex HIV-1 splicing pattern, however, which leads to such a variety of viral transcript variants, this conclusion of PCR interference was further analyzed in a simplified expression model.

3.4.2 Co-extraction of LNA mixmers after unassisted G_{I3}-2 LNA mixmer delivery results in the inhibition of the performed PCR rather than of the preceding cDNA synthesis during RT-PCR analysis

To confirm the conclusion that the co-extracted G_{I3}-2 LNA mixmer interferes only with the PCR amplification, but not with the cDNA synthesis during RT-PCR analysis, an artificial system based on HEK293T cells stably expressing an HIV-1 subgenomic transcript was established. This stable HEK293T cell line was generated by lentiviral vector transduction of HEK293T cells and subsequent selection for blasticidin resistant cells. Expression of the HIV-1 subgenomic reporter transcript containing an HIV-1 sequence region spanning viral exons 1, 3 and the first 177 nucleotides of the 291 nucleotide-long Vpr open reading frame is under control of the EF1α promoter (Fig. 3.12 **A**, upper panel).

This same transcript contains an internal ribosome entry site (IRES) responsible for expression of the downstream located blasticidin resistance gene. Since only one mRNA species is generated from this splice site-less transcription unit containing the specific G_{I3}-2 LNA mixmer binding site, it should be possible to amplify only this transcript isoform in the RT-PCR analyses

with different primer pairs. Therefore, it was used to specifically investigate the observed LNA mixmer-dependent inhibition of RT-PCR analysis.
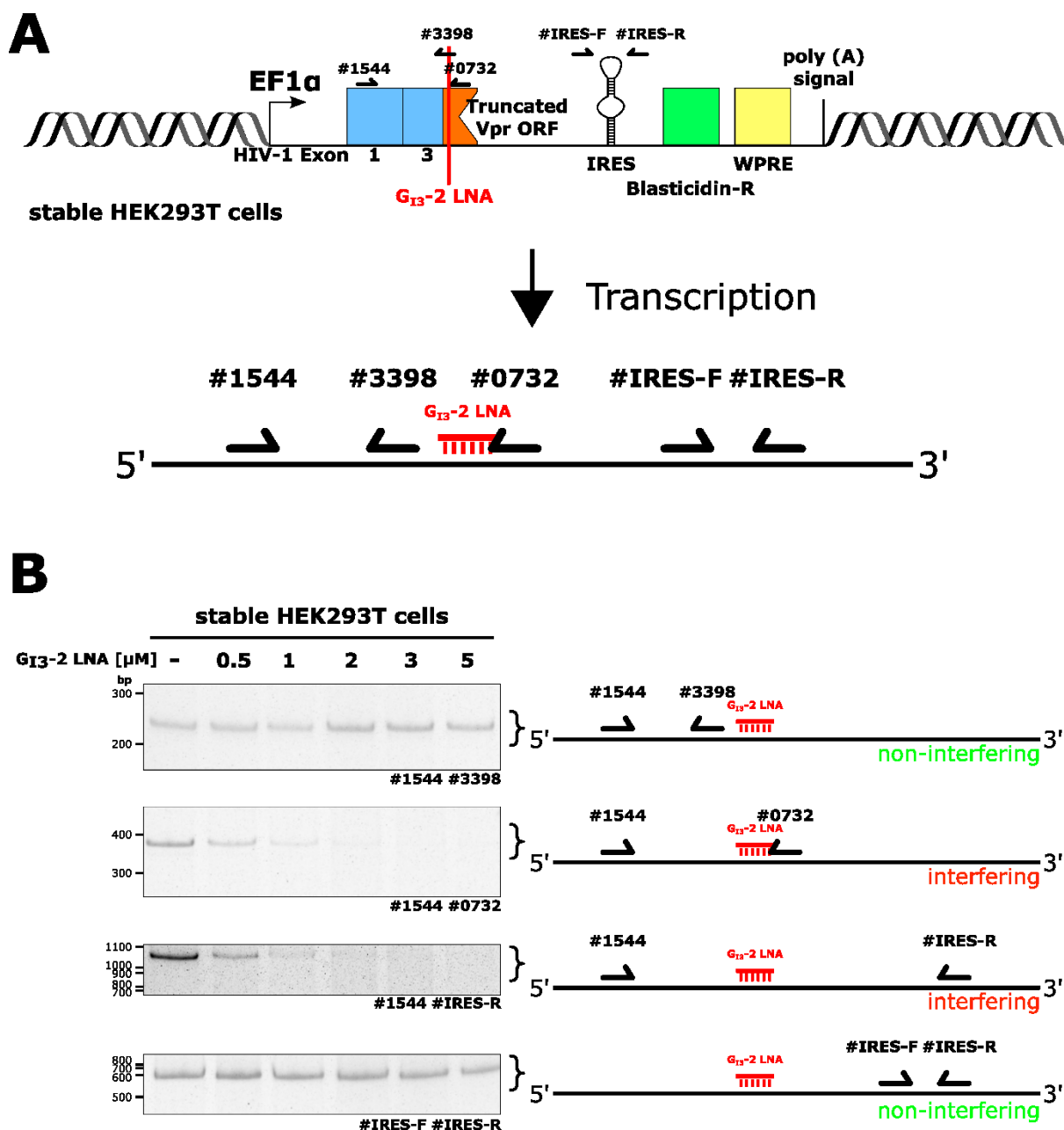
Fig. 3.12 Non-detectability of LNA mixmer-targeted HIV-1 RNA transcripts after RT-PCR analysis caused by LNA mixmer-mediated interference with the PCR amplification step. (**A**) Schematic of the transcriptional unit containing an HIV-1 subgenomic sequence with the G_{I3}-2 LNA mixmer binding site, an internal ribosomal entry site (IRES), the open reading frame from a blasticidin resistance gene (Blasticidin-R) and the woodchuck hepatitis virus post-transcriptional regulatory element (WPRE) that was stably inserted into HEK293T cells (Upper panel). Relative positions of primer binding sites (black arrows) and the G_{I3}-2 LNA mixmer binding site (red) are indicated. Expression under control of the EF1α promoter results in a bi-cistronic transcript which is illustrated below with the positions of the used primer binding sites (black arrows) relative to the G_{I3}-2 LNA mixmer binding site (red). (**B**) Amount of the generated transcript after unassisted G_{I3}-2 LNA mixmer delivery as analyzed via RT-PCR using

the indicated primer pairs (Left panel). The G_{I3}-2 LNA mixmer was added to the new medium at increasing concentrations (n = 1). Positions of the primer binding sites relative to the G_{I3}-2 LNA mixmer binding site on the analyzed transcript are shown for each RT-PCR (Right panel). RT-PCR products containing the G_{I3}-2 LNA mixmer binding sequence are depicted as interfering (red) and RT-PCR products not containing the specific G_{I3}-2 LNA mixmer binding site as non-interfering (green).

To test if the G_{I3}-2 LNA mixmer interferes with the cDNA synthesis or the subsequent PCR amplification, total RNA was isolated after unassisted G_{I3}-2 LNA mixmer delivery to the generated HEK293T cell line and RT-PCR analysis with different primer pairs was performed. The primers were selected based on the location of their binding sites relative to the G_{I3}-2 LNA mixmer binding site (Fig. 3.12 **A**, lower panel).

First, RT-PCR analyses using the primer pairs #1544/#0732 and #1544/#IRES-R that surround the G_{I3}-2 LNA mixmer binding site compared to the RT-PCR analysis performed with the #IRES-F/#IRES-R primer pair, which is located downstream of the G_{I3}-2 LNA mixmer binding site confirmed G_{I3}-2 LNA mixmer-mediated interference with the overall RT-PCR analysis (Fig. 3.12).

As expected based on the various RT-PCR analyses performed before, also by using the #1544/3398 primer pair that amplifies a region upstream of the G_{I3}-2 LNA mixmer, the reporter RNA could be detected. Here, the observed expression level was again comparable in all experimental conditions irrespective on how much G_{I3}-2 LNA mixmer was used to treat the cells beforehand (Fig. 3.12).

Together with the first round of experiments, this shows that the G_{I3}-2 LNA mixmer remains in the samples after nucleic acid extraction, here somehow not abrogating the cDNA synthesis, but rather only the subsequent PCR amplification.

However, so far only the non-detectability of G_{I3}-2 LNA mixmer-targeted RNA during RT-PCR analysis was used as indication for LNA mixmer-mediated PCR interference. To further confirm the presence of LNA mixmers in the PCR samples, fluorescein (FAM)-labeled LNA mixmers were used in subsequent experiments.

3.4.3 A FAM-label indicates the presence of LNA mixmers in the PCR mix after unassisted delivery

As a first approach to verify the presence of FAM-labeled LNA mixmers within total RNA preparations, detection via the NanoDrop^{TM} spectrophotometer platform was pursued. This

detection method should the absorbance of low volume samples can be easily determined at distinct wavelengths.

To initially confirm that the presence of FAM-labeled LNA mixmers within samples can be investigated via this platform, absorbance of a FAM-labeled G_{I3}-2 LNA mixmer at 488 nm was analyzed in samples of decreasing FAM-G_{I3}-2 LNA mixmer concentrations. The same concentrations of the non-FAM-labeled G_{I3}-2 LNA mixmer served as controls.

Here, it was shown that this method clearly detected the presence of the FAM-label within the samples of 100 µM to 1 µM as shown by the does-dependent decrease in absorbance together with the significant lower absorbance values in samples containing the non-FAM-labeled G_{I3}-2 LNA mixmer at 5 µM and 1 µM (Fig. 3.13 **A**). Of note, absorbance values of 0.03 and 0.035 at wavelength 546 and 555 for the 100 µM FAM-G_{I3}-2 LNA mixmer sample, respectively, underlined detection specifically of the FAM-label via the NanoDrop™ spectrophotometer (data not shown).
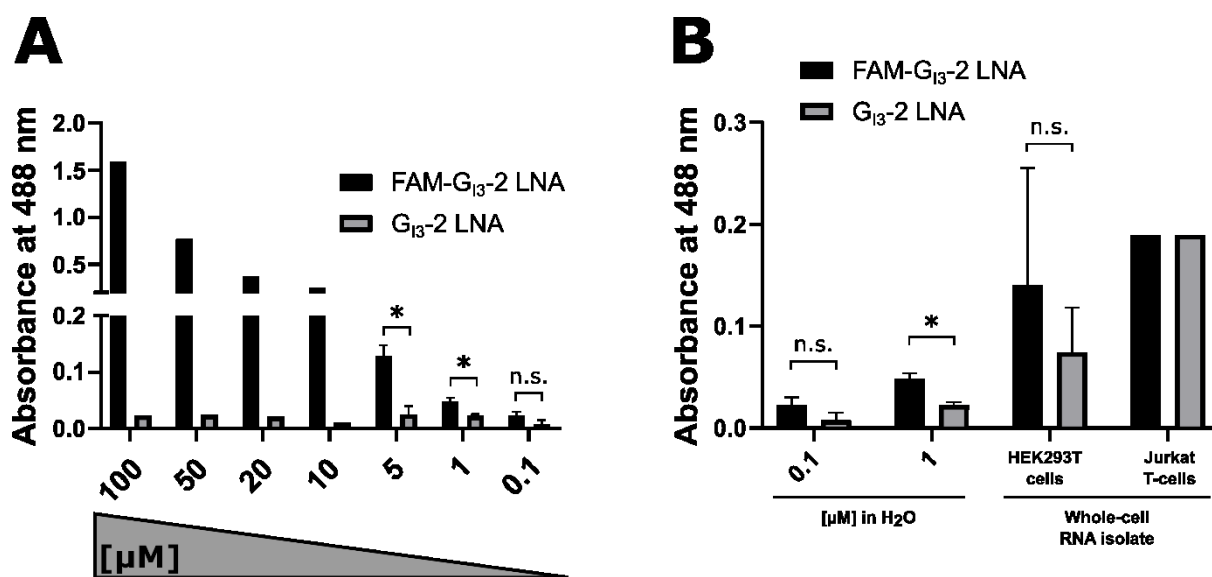
Fig. 3.13 High absorbance-background in whole-cell RNA preparations does not allow detection of FAM-labeled LNA mixmers via a NanoDrop™ spectrophotometer at low concentrations. (**A**) Absorbance values of decreasing concentrations of a FAM-labeled G_{I3}-2 LNA mixmer and a non-FAM-labeled G_{I3}-2 LNA mixmer. Absorbance of LNA mixmer concentrations 5 µM, 1 µM and 0.1 µM was tested in three replicates (n = 3). Data presented as mean +SD. Statistical significance analyzed by multiple t-tests following the False Discovery Rate (FDR) approach (Two-stage step-up method of Benjamini, Krieger and Yekutieli). *p < 0.05. (**B**) Absorbance of HEK293T and Jurkat T-cell whole-cell RNA isolates 24 hours after unassisted (FAM-labeled) G_{I3}-2 LNA mixmer delivery analyzed with a NanoDrop™ spectrophotometer at 488 nm (n = 3 for HEK293T cells; n = 1 for Jurkat T-cells). Absorbance values of 0.1 µM and 1 µM (FAM-labeled) G_{I3}-2 LNA mixmer in H_2O form (**A**) are illustrated for comparison. Data presented as mean +SD. Statistical significance analyzed by unpaired, two-tailed t-test. *p < 0.05.

Given the non-significant difference between absorbance values coming from the 0.1 µM FAM-G_{I3}-2 and non-FAM G_{I3}-2 LNA mixmer samples, the lower detection limit via this NanoDrop™ spectrophotometer platform was suggested to lie between 1 µM and 0.1 µM FAM-G_{I3}-2 LNA mixmers.

After verifying the NanoDrop™ system for the detection of the FAM-G_{I3}-2 LNA mixmer, it was tested whether the FAM-G_{I3}-2 LNA mixmer can be detected after unassisted delivery to cells and subsequent RNA isolation. Therefore, HEK293T and Jurkat T-cells were treated either with the FAM- or non-FAM-labeled G_{I3}-2 LNA mixmer at 3 µM, which is the maximum concentration used for the previously performed HIV-1 infection experiment and that showed profound interference with the conducted RT-PCR analysis. Total RNA was isolated at 24 hours post-treatment and the absorbance of the generated whole-cell RNA isolates at 488 nm was determined.

Comparison of the HEK293T cells samples did not reveal a significant difference in their absorbance after three independent biological replicates (Fig. 3.13 **B**). Further, testing the Jurkat T-cell whole-cell RNA preparations in one replicate obtained the same absorbance level of 0.190 at 488 nm for the FAM-G_{I3}-2 LNA mixmer Jurkat and the non-FAM-G_{I3}-2 LNA mixmer Jurkat sample, respectively (Fig. 3.13 **B**).

The background absorbance in the whole-cell RNA preparations was obviously higher than the lower detection limit of the NanoDrop™ spectrophotometer platform (Fig. 3.13 **B**). Hence, it was suggested that the lack of different absorbance values after unassisted LNA mixmer delivery derived from the high background absorbance and not from missing FAM-LNA mixmer in those samples.

Overall, the NanoDrop™ spectrophotometer system was found unsuitable for the detection of FAM-labeled LNA mixmers in whole-cell RNA preparations due to a high background absorbance in these samples.

Therefore, in a second FAM-label-based approach to confirm the presence of LNA mixmer within PCR samples after nucleic acid extraction, an RT-qPCR light cycler platform was used. RT-qPCR light cycler typically measures absorbance to quantify DNA products during PCR. Hence, their output is a relative value indicating the amount of PCR product. However, they are more sensitive to fluorescence signals compared to the previously used NanoDrop™ spectrophotometer system.

This approach based on the specific interference with the fluorescence signal that is typically derived only from the used PCR probe, by the present FAM-labeled LNA mixmers. It was suggested that this additional fluorescent signal from the FAM-LNA mixmer, which is at the same wavelength as the signal from the PCR probe during the employed setting, will lead to a

misinterpretation of the amount of transcripts within the samples by the RT-qPCR light cycler system (Fig. 3.14 **A**).
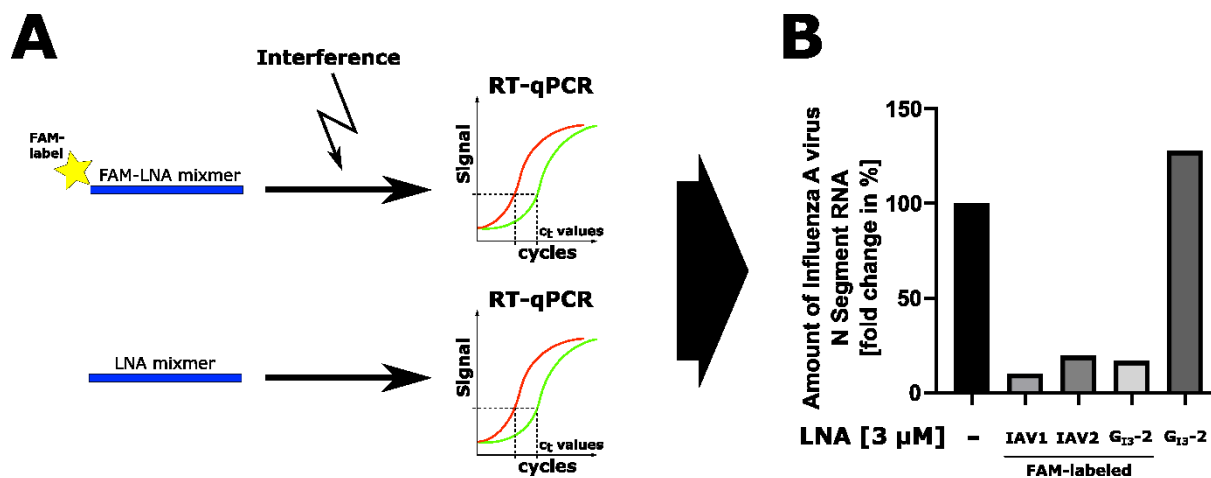
Fig. 3.14 Interference with RT-qPCR analysis by prior unassisted FAM-labeled LNA mixmer delivery further indicates their co-extraction with cellular RNA. (A) Schematic illustrating the interference caused only by FAM-labeled LNA mixmers during RT-qPCR analysis. **(B)** Quantification of Influenza A virus N Segment RNA within cell culture supernatant of CaCo-2 cells at 48 hours post-infection with Influenza A virus via RT-qPCR analysis. Cells were infected with IAV strain A/California/07/2009 and washed with PBS at 1 hour post-infection. The indicated LNA mixmers were added to the new medium at a final conc. of 3 µM (n = 1).

Since it was shown during this thesis that the two anti-IAV LNA mixmers had no impact on IAV nucleocapsid RNA levels in the employed setting, IAV nucleocapsid RNA levels were analyzed for this RT-qPCR light cycler-based approach after IAV infection of CaCo-2 cells (Fig. 3.8 **E**). This setting, therefore, provides a suitable model system to analyze a possible FAM-label-mediated interference. In addition to the FAM-labeled anti-IAV LNA mixmers, the IAV-infected CaCo-2 cells were treated with either the FAM-labeled G_{I3}-2 LNA mixmer or the non-FAM-labeled G_{I3}-2 LNA mixmer. Both LNA mixmers target the same HIV-1 sequence and hence, should not affect the IAV nucleocapsid RNA level.

As expected, treatment with the non-FAM-G_{I3}-2 LNA mixmer resulted in an interpreted amount of IAV N segment that was comparable to the amount in the untreated control via the performed RT-qPCR analysis (Fig. 3.14 **B**).

Prior treatment with either of the two anti-IAV FAM-labeled LNA mixmers (IAV1, IAV2) resulted in an interpreted lower level of IAV N segment RNA (Fig. 3.14 **B**). Because both anti-IAV LNA mixmers were previously shown by RT-PCR analysis not to reduce IAV N segment levels (Fig. 3.8 **E**), it was suggested that interference with the fluorescence signal from the RT-

qPCR-specific IAV N segment probe was caused by residual FAM-labeled LNA mixmers in the RNA samples.

This conclusion was substantiated by the observation that treatment with the FAM-G$_{I3}$-2 LNA mixmer likewise supposedly decreased IAV N RNA levels, although treatment with the non-FAM-labeled G$_{I3}$-2 LNA mixmer did not.

In summary, performance of the IAV N segment-specific RT-qPCR provided additional evidence for the presence of (FAM)-LNA mixmers within PCR samples after conducted nucleic acid extraction.

Altogether, the combined data collected here indicates that not the suggested targeted RNA degradation, but LNA mixmer-mediated PCR interference is the cause for the non-detectability of the investigated HIV-1 transcripts after unassisted LNA mixmer delivery (1). Moreover, due to the detection of the presumably degraded Vpr and Vif transcripts after unassisted G$_{I3}$-2 LNA mixmer delivery to HIV-1 infected T-cells by simply exchanging the employed primer pairs for RT-PCR analysis, it was argued whether LNA mixmer-mediated target RNA degradation occurs at all. The absence of such an LNA mixmer-mediated RNA degradation would start also to illuminate the previous results that failed to show an inhibition of SARS-CoV-2, Hazara virus and IAV replication after unassisted LNA mixmer delivery.

Interestingly though, profound inhibition of HIV-1 replication after unassisted G$_{I3}$-2 LNA mixmer delivery was indisputably demonstrated by showing decreased HIV-1 p24 levels via western blot analysis as well as decreased levels of the three HIV-1 RNA classes (2, 4 and 9 kb) via northern blot analysis at 6 dpi (1). This observation brings up the question what causes inhibition of HIV-1 replication after unassisted G$_{I3}$-2 LNA mixmer delivery if not targeted RNA degradation.

3.5 Unassisted G$_{I3}$-2 LNA mixmer delivery inhibits HIV-1 replication via induced splice switching

3.5.1 Unassisted G$_{I3}$-2 LNA mixmer delivery leads to the same HIV-1 Tat1/Vpr3 ratio as observed after mutational analysis and LNA mixmer transfection

Given that the data collected so far contradicts an LNA mixmer-induced degradation, but unassisted anti-HIV-1 G$_{I3}$-2 LNA mixmer delivery, nevertheless, was shown to profoundly inhibit HIV-1 replication, the underlying mechanism was analyzed.

In the preceding study, transfection-based delivery of the G_{I3}-2 and ESE$_{tat}$ LNA mixmer was observed to affect viral splicing by masking of HIV-1 SREs. Hence, the first suggestion was that perhaps interference with viral splicing may contribute to the LNA mixmer-induced inhibition of HIV-1 replication also after unassisted delivery.

Since LNA mixmer-induced inhibition of HIV-1 replication after unassisted delivery was analyzed at 6 dpi as the earliest time-point during the preceding study, it should initially be tested when this LNA mixmer-mediated inhibition can first be observed. The here gathered information is essential to obtain insights into the underlying mechanism in subsequent experiments.

For the analysis of time-dependent HIV-1 inhibition, an HIV-1 exon 7-specific RT-qPCR was performed. The used primer pair allowed amplification of total HIV-1 RNA, because HIV-1 exon 7 is contained within each viral transcript variant (Fig. 3.9 **A**). Hence, HIV-1 exon 7 RT-qPCR analysis represents one of the most sensitive methods to investigate HIV-1 replication.

To see at which time-point unassisted LNA mixmer delivery results in a reduced level in viral RNA, PM1 T-cells were infected with the HIV-1 laboratory strain NL4-3. At 6 hpi, the cells were washed and treated with the G_{I3}-2 LNA mixmer for a duration of 3 dpi. The G_{I3}-2 LNA mixmer was, again, selected over the ESE$_{tat}$ LNA mixmer due to its stronger antiviral activity observed (1). Each day, one sample of the G_{I3}-2 LNA mixmer and untreated control cells, respectively, was harvested for RT-qPCR analysis. Although after three independent biological replicates, the HIV-1 RNA was significantly reduced in the G_{I3}-2 LNA mixmer-treated cells compared to the control cells only at 3 dpi, the conducted analysis hinted towards a G_{I3}-2 LNA mixmer-mediated inhibitory effect already at 2 dpi (Fig. 3.15). Therefore, it was concluded that the G_{I3}-2 LNA mixmer exerts its antiviral effect after unassisted delivery already during the course of 3 dpi.

Based on the suggested effect on HIV-1 splicing after unassisted G_{I3}-2 LNA mixmer delivery, the role of the HIV-1 G_{I3}-2 SRE for the generation of viral splice variants was considered.

During its initial identification and characterization, Widera and co-workers substituted the second guanine of the G-run pentamer motif DGGGD (With D being G, A or T) within HIV-1 NL4-3 genome (44). Infection with the G_{I3}-2-mutated HIV-1 resulted in a reduced level of HIV-1 Tat1 concomitant a higher level of HIV-1 Vpr3 as shown by RT-PCR analysis (44).
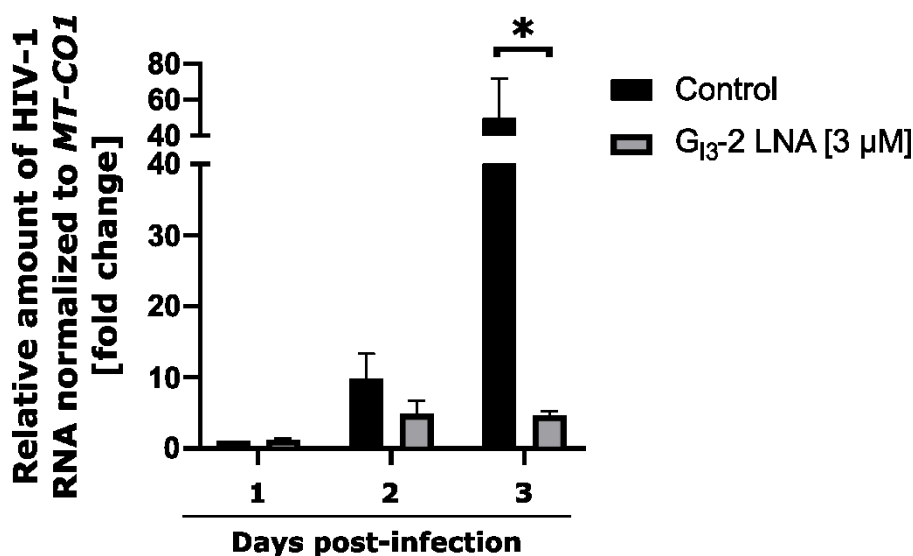
Fig. 3.15 Unassisted G$_{I3}$-2 LNA mixmer delivery inhibits viral replication already over the course of 3 days post-infection. Quantification of HIV-1 RNA isolated from HIV-1 infected PM1 T-cells over the course of three days post-infection via RT-qPCR analysis using HIV-1 exon 7 specific primers #3387 and #3388 and normalized to cellular *MT-CO1* expression. Cells were infected with HIV-1 laboratory strain NL4-3 at an MOI 0.005 and at 6 hours post-infection washed with PBS. The G$_{I3}$-2 LNA mixmer was added to the new medium at a final conc. of 3 µM. Untreated cells served as control. Data presented as mean +SD (n = 3). Statistical significance analyzed by multiple t tests following the False Discovery Rate (FDR) approach (Two-stage step-up method of Benjamini, Krieger and Yekutieli). *p < 0.05.

To illustrate this result for better comparison during subsequent steps, the band intensities of Tat1 and Vpr3 on the polyacrylamide gel generated in the described study were analyzed and the ratio of Tat1 to Vpr3 was determined. This densiometric analysis of Tat1 and Vpr RT-PCR products showed a clearly decreased Tat1/Vpr3 ratio after infection with G$_{I3}$-2-mutated HIV-1 compared to infection with wild-type NL4-3 HIV-1 at 2 dpi (Fig. 3.16 **A**) (44).

This decreased Tat1/Vpr3 ratio as the result of mutational G$_{I3}$-2 inactivation was confirmed via co-transfection of HeLa cells with HIV-1 proviral plasmid pNL4-3 together with the G$_{I3}$-2 LNA mixmer (1). Again, RT-PCR-based densiometric analysis of Tat1 and Vpr3 depicted the decreased Tat1/Vpr3 ratio also after LNA mixmer transfection-mediated G$_{I3}$-2 inactivation (Fig. 3.16 **B**) (1).

Based on additional experiments performed by Widera et al., members of the hnRNP F/H family were found to bind the G$_{I3}$-2 SRE. Further, it was shown that LNA mixmer transfection-mediated masking of the G$_{I3}$-2 leads to the observed reduction of the HIV-1 Tat1/Vpr3 RNA transcript ratio by preventing hnRNP F/H binding (Fig. 3.16 **C**) (44).

Hence, according to the hypothesis that induced splice switching is the cause for the demonstrated inhibition of HIV-1 replication also after unassisted G$_{I3}$-2 LNA mixmer delivery,

Tat1 and Vpr3-specific RT-qPCR analysis should reveal the same reduced Tat1/Vpr3 ratio in this context.

A **Mutational analysis (Widera et al., 2014)**

B **LNA transfection (Hillebrand et al., 2019)**

C

D **Unassisted (gymnotic) LNA delivery**
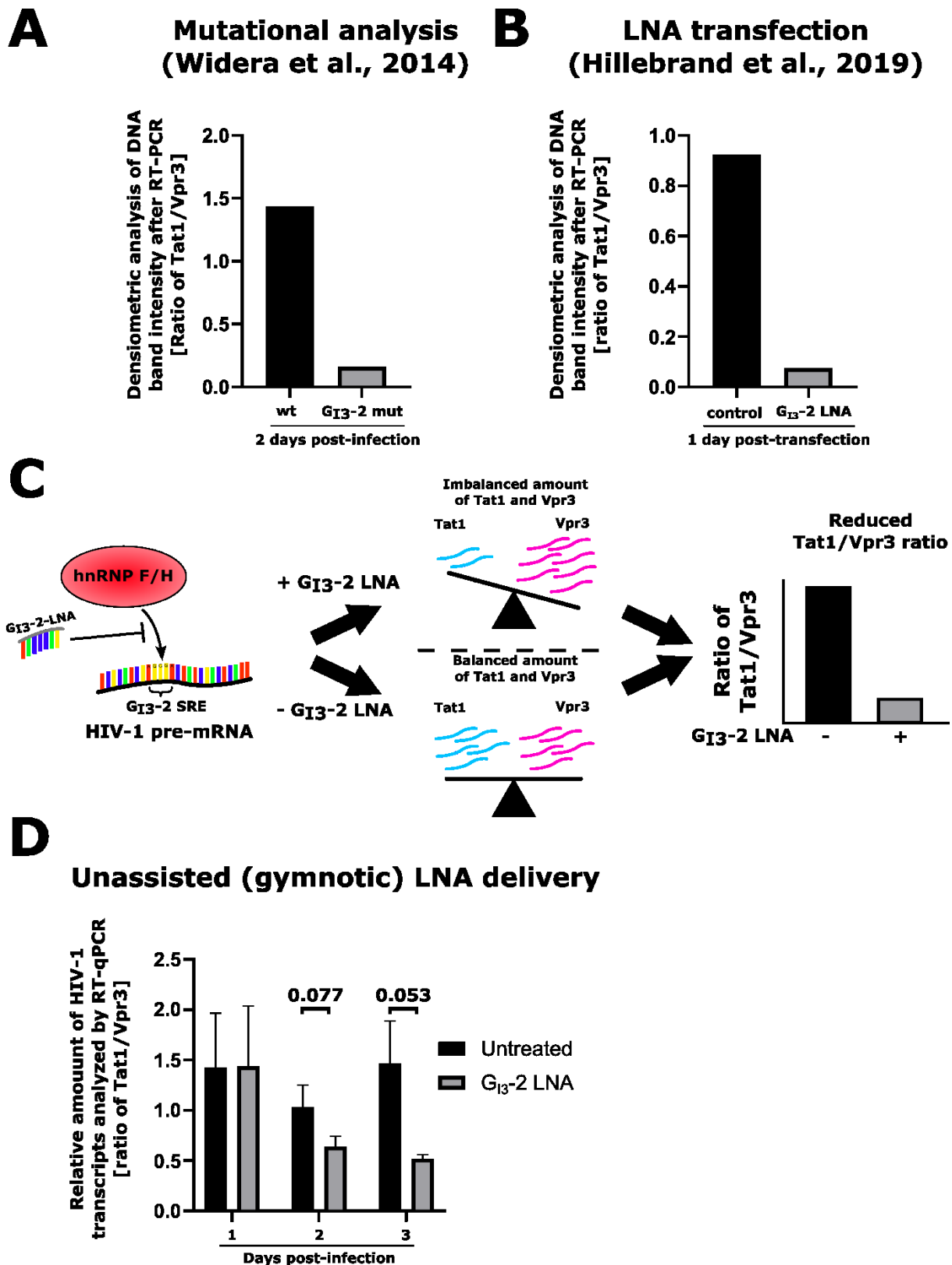
Fig. 3.16 HIV-1 Tat1 and Vpr3 transcript variant-specific RT-qPCR analyses after unassisted G$_{I3}$-2 LNA mixmer delivery hinted towards a comparable reduced Tat1/Vpr3 ratio as observed after mutational analysis and LNA mixmer transfection. (**A**) Ratio of HIV-1 Tat1 to Vpr3 transcript determined by densiometric analysis of DNA band intensity from RT-PCR analysis after mutational analysis of the HIV-1 G$_{I3}$-2 splicing regulatory element (SRE) in HIV-1 proviral plasmid pNL4-3 as published in (44). (**B**) Ratio of HIV-1 Tat1 to Vpr3 transcript determined by densiometric analysis of DNA band intensity from RT-PCR analysis after G$_{I3}$-2 LNA mixmer and HIV-1 proviral plasmid pNL4-3 co-transfection of HeLa cells as published in (1). (**C**) Schematic describing the suggested mechanism underlying G$_{I3}$-2 LNA mixmer-induced splice switching by prevention of hnRNP F/H binding through masking of the HIV-1 G$_{I3}$-2 SRE (44). (**D**) Ratio of HIV-1 Tat1 to Vpr3 transcript in HIV-1-infected PM1 T-cells over the course of three days post-infection determined by transcript specific RT-qPCR (Tat1: #3631, #3632; Vpr3: #3397, #3398). Cells were infected with HIV-1 laboratory strain NL4-3 at an MOI 0.005 and at 6 hours post-infection washed with PBS. The G$_{I3}$-2 LNA mixmer was added to the new medium at a final conc. of 3 µM. Untreated cells served as control. Data presented as mean +SD (n = 3). Statistical significance analyzed by multiple t tests following the False Discovery Rate (FDR) approach (Two-stage step-up method of Benjamini, Krieger and Yekutieli). *$p < 0.05$.

These HIV-1 Tat1 and Vp3 transcript-specific RT-qPCR analyses were previously shown not to be affected by the presence of the G$_{I3}$-2 LNA mixmer within the PCR samples (Fig. 3.10). Therefore, this approach will allow a valid analysis of Vpr3 and Tat1 transcript levels also after unassisted G$_{I3}$-2 LNA delivery.

As now expected, unassisted G$_{I3}$-2 LNA mixmer delivery after HIV-1 NL4-3 infection of T-cells suggested a trend towards comparable decreased Tat1/Vpr3 ratio over the course of 3 dpi (Fig. 3.16 **D**).

Although this effect did not reach significance after three independent biological replicates, the results hinted towards a G$_{I3}$-2 LNA mixmer-exerted effect on viral splicing also after unassisted delivery.

However, given the complex replication cycle of HIV-1 including the viral Tat protein-induced increase in HIV-1 LTR promoter activity together with the overall bias from re-infection during the three day time period, a simplified reporter system was established in a subsequent step. This reporter system should allow Tat- and re-infection-independent analysis of G$_{I3}$-2 LNA mixmer-induced splice switching.

3.5.2 Unassisted G$_{I3}$-2 LNA mixmer delivery affects HIV-1 transcript levels in lentiviral vector-transduced PM1 T-cells by induced splice switching

By conducting HIV-1 Tat1 and Vpr3 transcript-specific RT-qPCR analyses, the previous experiment suggested that unassisted G$_{I3}$-2 LNA mixmer delivery after HIV-1 infection indeed might disturb viral splicing by masking the G$_{I3}$-2 SRE during pre-mRNA processing. Potential bias from Tat-induced promoter activity and re-infection, however, might have influenced the obtained results.

Hence in the following, a replication-incompetent, HIV-1 Tat-independent lentiviral vector system was aimed to establish to confirm the hypothesized G$_{I3}$-2 LNA mixmer-mediated splice switching after unassisted delivery.

For this, HIV-1 RNA-derived cDNA encoding Vpr3 was inserted into a transfer plasmid that belongs to a second generation lentiviral vector system (Fig. 3.17 **A**, **B**). Subsequent transduction of susceptible cells results in the expression of parts of the actual HIV-1 pre-mRNA containing the G$_{I3}$-2 LNA mixmer binding site.

This pre-mRNA has the capacity to be processed into splice variants coding for the additional viral proteins Tat and Rev (Fig. 3.17 **C**). Here, the employed construct was selected to especially generate the transcripts from an assumed Tat-independent transcription unit whose processing may be influenced by the G$_{I3}$-2 LNA mixmer the same way as after unassisted delivery to HIV-1 NL4-3-infected T-cells.

Overall, a reduced Tat/Vpr ratio, meaning a decreased Tat, but an increased Vpr level was expected also after unassisted G$_{I3}$-2 LNA mixmer delivery to the lentiviral vector-transduced cells.

To test this, PM1 T-cells were transduced with the generated lentiviral particles, and after a subsequent washing step, treated with the G$_{I3}$-2 LNA mixmer for up to three days. Each day, one control and one G$_{I3}$-2 LNA mixmer-treated sample was harvested for RT-qPCR analyses.

Surprisingly, the ratio between the generated Tat transcript and the generated Vpr transcript was not significantly reduced by unassisted G$_{I3}$-2 LNA mixmer delivery over the course of 3 days post-transduction (dpt) (Fig. 3.18 **A**). Here, if at all, the RT-qPCR analysis after unassisted G$_{I3}$-2 LNA mixmer only hinted towards a scarce decrease in the Tat1/Vpr3 ratio.

Hence, this lentiviral vector-based experiment failed to reproduce the G$_{I3}$-2 LNA mixmer-mediated decrease in the HIV-1 Tat/Vpr ratio as suggested after infection with HIV-1 NL4-3. In addition, by simply analyzing the Tat/Vpr ratio, on the first glance, no G$_{I3}$-2 LNA mixmer-induced effect was observed.

Fig. 3.17 Schematic describing generation and genome structure of the used lentiviral particles expressing the depicted HIV-1 subgenomic region. (A) Expression of the HIV-1 9 kb class RNA from viral provirus may result in the generation of intron-containing Vpr RNA transcript (Vpr3). RNA isolation with subsequent cDNA synthesis and RT-PCR after HIV-1 proviral plasmid pNL4-3 transfection allowed insertion of the Vpr3 cDNA into a transfer vector **(B)** used for lentiviral particle production. **(B)** Schematic of the generated puc2CL7EGwo Vpr3 transfer vector used for lentiviral particle production. SFFV: spleen focus forming virus. LTR: long terminal repeat. Ψ: RNA packaging signal **(C)** Schematic overview of possible splice products after expression of the Vpr cDNA in transduced cells. **(A, C)** Overviews with open reading frames (ORFs) (orange), the rev response element (RRE), splice donor sites (D1-D4), splice acceptor sites (A1-A7) and the G_{I3}-2 LNA mixmer binding site (red).

By conducting RT-qPCR analysis with the HIV-1 exon 7-specific primer pair (#3387/#3388), however, unassisted G$_{I3}$-2 LNA mixmer delivery was found to increase the overall total amount of HIV-1 RNA derived from the lentiviral vector-derived construct at 1 dpt (Fig. 3.18 **F**).
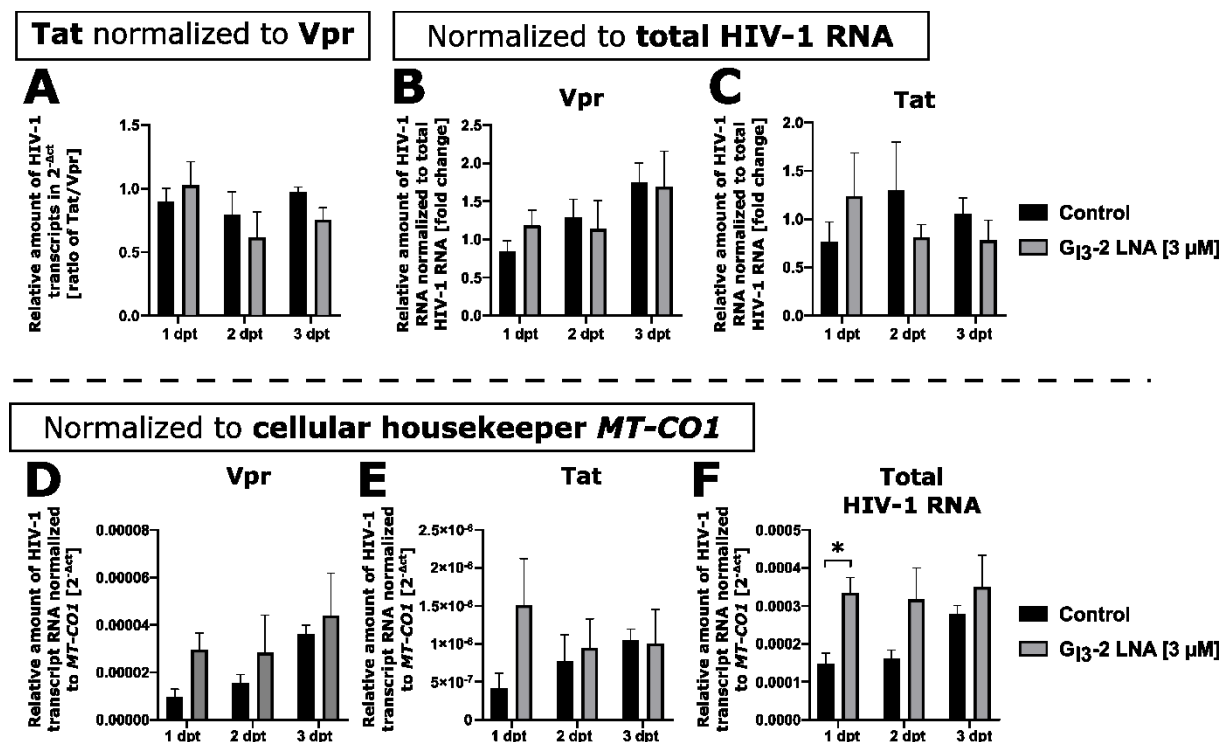
Fig. 3.18 Unassisted G$_{I3}$-2 LNA mixmer delivery affects HIV-1 transcript levels in lentiviral vector-transduced PM1 T cells. (A - F) Quantification of HIV-1 RNA transcripts isolated from lentiviral vector-transduced PM1 T-cells over the course of three days post-transduction via RT-qPCR analysis (Vpr: #3397, #3398; Tat: #6658, #3632; Total HIV-1 RNA: #3387, #3388). **(A)** Ratio of HIV-1 Tat to Vpr transcript. **(B, C)** Normalized to total HIV-1 RNA. **(D – F)** Normalized to cellular *MT-CO1* expression. **(A - F)** Cells were transduced with lentiviral vector LV-Vpr3 as described in the method section and at 6 hours post-transduction washed with PBS. The G$_{I3}$-2 LNA mixmer was added to the new medium at a final conc. of 3 μM. Untreated cells served as control. Data presented as mean +SD (n = 3). Statistical significance analyzed by multiple t tests following the False Discovery Rate (FDR) approach (Two-stage step-up method of Benjamini, Krieger and Yekutieli). *$p < 0.05$.

This observation was comparable also after normalizing to two other cellular housekeepers, actin and glyceraldehyde 3-phosphate dehydrogenase (GAPDH) (data not shown).

Here, it was concluded that unassisted G$_{I3}$-2 LNA mixmer delivery somehow increases the overall expression rate of the lentiviral construct. The most likely cause for this was suggested to be that, contrary to the initial assumption, SFFV U3 promoter acitivity can be enhanced by Tat. Further, unassisted G$_{I3}$-2 LNA mixmer delivery may increase Tat and Vpr transcripts, thereby not changing the previously analyzed Tat/Vpr ratio. Together, an increased Tat level

and a Tat-enhanced SFFV U3 promoter may explain the overall higher amount of HIV-1 RNA found after unassisted G_{I3}-2 LNA mixmer delivery.

As expected, normalizing the Vpr and Tat RNA levels to total HIV-1 RNA hinted towards a slightly increased relative level of Tat and Vpr after unassisted G_{I3}-2 LNA mixmer delivery at 1 dpt (Fig. 3.18 **B** and **C**).

Now, a possible enhancement of SFFV U3 promoter acitivity by HIV-1 was analyzed. To test if HIV-1 Tat enhances SFFV U3 promoter activity, the SFFV U3 promoter was cloned into a dual luciferase reporter obtained from Dr. Lara Walotka (Institute of Virology, University Hospital Düsseldorf, Heinrich Heine University Düsseldorf), in which firefly expression, which is used for normalization, is under control of the SV40 promoter. Expression of the renilla luciferase was brought under control of the SFFV U3 promoter (Fig. 3.19 **A**, lower panel).

As a positive control for HIV-1 Tat-mediated enhancement of promoter activity, the same reporter plasmid, but with renilla luciferase expression under control of the HIV-1 LTR promoter, was used (Fig. 3.19 **A**, upper panel).

Co-transfection of Hela cells with the HIV-1 LTR-containing control dual luciferase reporter together with either a control plasmid (pXGH5) or the HIV-1 Tat expression vector pcTat, first of all, showed HIV-1 Tat-mediated enhancement of HIV-1 LTR promoter activity, this way confirming the validity of this experimental setting (Fig. 3.19 **B**).

Interestingly, SFFV U3 promoter activity was indeed and in contrast to the original assumption, enhanced by HIV-1 Tat after all (Fig. 3.19 **B**). This enhancement was of course not nearly as strong as of the HIV LTR promoter.

However, even this slight Tat-dependent increase in SFFV U3 promoter acitivity together with the slight G_{I3}-2 LNA mixmer-mediated increase in Tat transcript indicated by RT-qPCR (Fig. 3.17 **C**) was suggested to be most likely responsible for the significantly increased total HIV-1 RNA observed after unassisted G_{I3}-2 LNA mixmer delivery (Fig. 3.17 **F**).
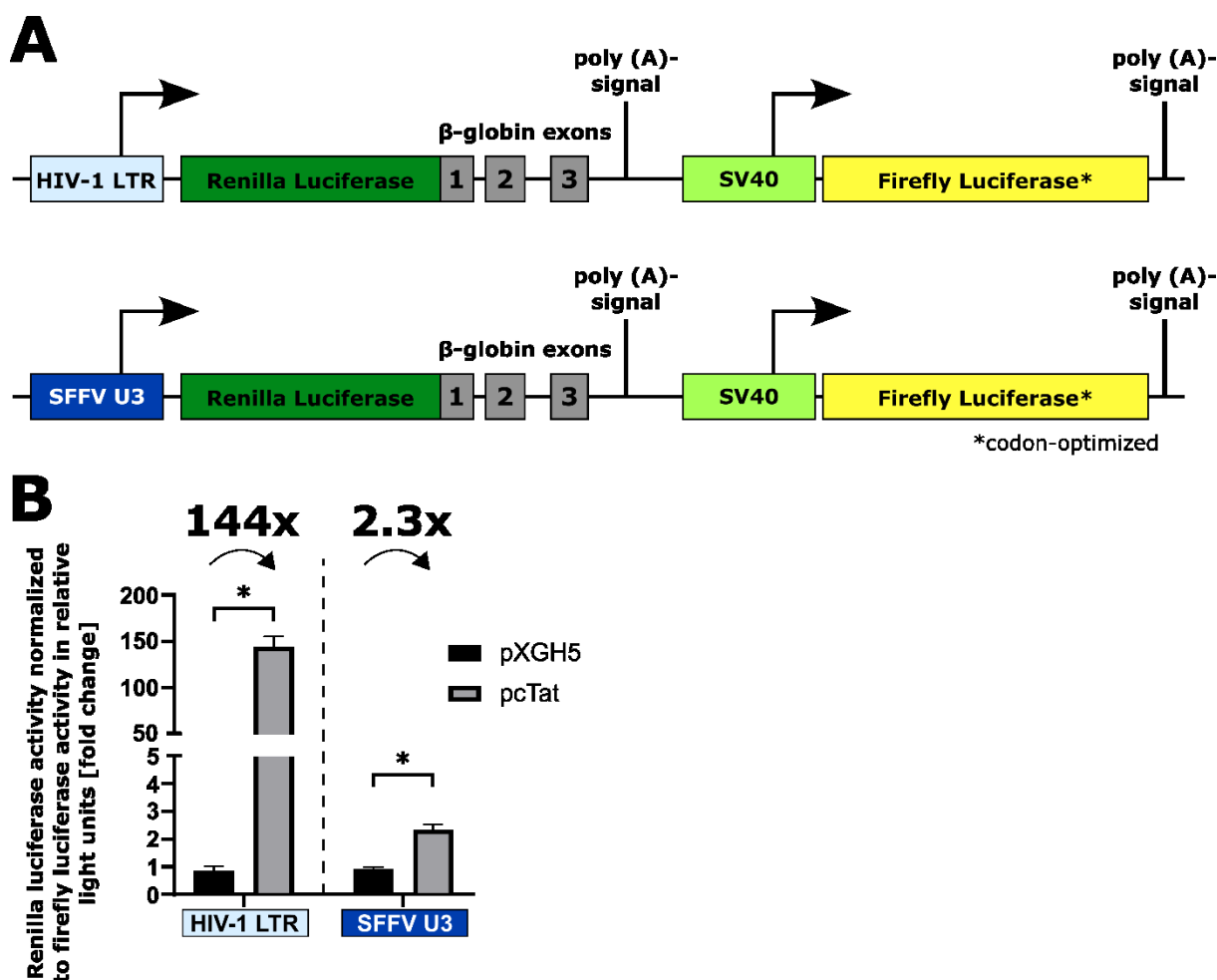
Fig. 3.19 HIV-1 Tat expression leads to enhanced SFFV U3 promoter acitivity. (A) Structure of the used dual luciferase reporter plasmids for the analysis of HIV-1 Tat-dependent enhancement of promoter activity. SFFV: spleen focus foaming virus. **(B)** Relative promoter activity determined by normalization of renilla luciferase activity to firefly luciferase activity shown as fold change to pXGH5 transfection control, respectively. pXGH5: human growth hormone (GH1) expression vector; pcTat: HIV-1 Tat expression vector. Data presented as mean +SD (n = 3). Statistical significance analyzed by unpaired, two-tailed t-test. *p < 0.05

In summary, this simplified viral pre-mRNA reporter model did not reflect the reduced HIV-1 Tat1/Vpr3 ratio as observed in the context of unassisted delivery to HIV-1-infected cells. Nevertheless, transcript variant-specific RT-qPCR analysis after unassisted G_{I3}-2 LNA mixmer delivery hinted towards an increase in both, Tat and Vpr transcript RNA.

Based on the data sets obtained during the preceding chapters, it was assumed that G_{I3}-2 LNA mixmer-mediated masking of the G_{I3}-2 SRE in this setting may cause this increase in HIV-1 transcripts Vpr and Tat. Following this assumption of induced splice-switching, however, another HIV-1 transcript must be eventually decreased after unassisted G_{I3}-2 LNA mixmer delivery.

Here, generation of HIV-1 Rev transcript variants was analyzed, because the splice acceptor sites (SA4c, SA4a and SA4c), which are used to produce viral Rev transcripts are downstream of the splice acceptor site (SA3) used to produce viral Tat transcript (Fig. 3.20 **A**). Hence, a G_{I3}-2 LNA mixmer-mediated masking of the G_{I3}-2 SRE may contribute to a higher usage of SA3 while decreasing SA4c, a and b usage.

In this setting HIV-1 Rev RNA derives from splicing of HIV-1 splice donor 3 (D3) to either splice acceptor A4c, A4a or A4b (Fig. 3.20 **A**). The three this way processed Rev transcripts were termed *Rev D3-A4c*, *Rev D3-A4a* and *Rev D3-A4b* in the following (Fig. 3.20 **A**).

To investigate a possible G_{I3}-2 LNA-mediated effect on the expression of these three Rev transcript variants, first, three exon junction primers were designed to allow Rev transcript variant-specific RT-qPCR (Fig. 3.20 **A**). RT-PCR analysis was performed to check whether usage of these three exon junction primers together with the same forward primer would result in the specific amplification of these Rev transcript variants.

Here, the conducted RT-PCR analysis revealed specific amplification of Rev D3-A4a and Rev D3-A4b, but not Rev D3-A4c (data not shown). Therefore, in the following, possible G_{I3}-2 LNA mixmer-mediated effects on Rev D3-A4a and Rev D3-A4b transcript variant levels were analyzed by RT-qPCR analysis.

Here, it was shown that unassisted G_{I3}-2 LNA mixmer delivery to the lentiviral vector-transduced PM1 T-cells indeed resulted in a reduced transcript level of Rev D3-A4a and Rev D3-A4b over the course of 3 dpt (Fig. 3.20 **B**, **C**). This observation confirmed the current assumption in that it hints towards G_{I3}-2 LNA mixmer-induced splice switching. In the context of this simplified reporter setting, however, the supposed masking of the G_{I3}-2 SRE leads to increased Tat and Vpr levels, but decreased Rev transcript variant levels.

As a consequence, this data, again, hinted towards a G_{I3}-2 LNA mixmer-mediated interference with viral pre-mRNA splicing.

In summary, with respect to the overall antiviral potential of LNA mixmers, the data sets collected in this work suggest that rather than induced degradation of target RNA, induced splice switching may be a reason for the observed inhibition of HIV-1 replication by unassisted LNA mixmer delivery.

This conclusion would then also explain the failure of LNA mixmer-mediated inhibition of SARS-CoV-2 and Hazara virus replication.

However, unassisted anti-IAV LNA mixmer delivery targeting IAV SRE sites, intriguingly, did not inhibit IAV replication in CaCo-2 cells (Fig. 3.8 **E**). Since up to this point, all experimental studies demonstrating HIV-1 inhibition by unassisted LNA mixmer delivery used T-cells, either like the PM1 T-cells used here (Fig. 3.15), or Jurkat and primary human T-cells as in the preceding work

(1), it was questioned whether there might also be some cell type specificity that restricts LNA mixmer-mediated effects after unassisted delivery.
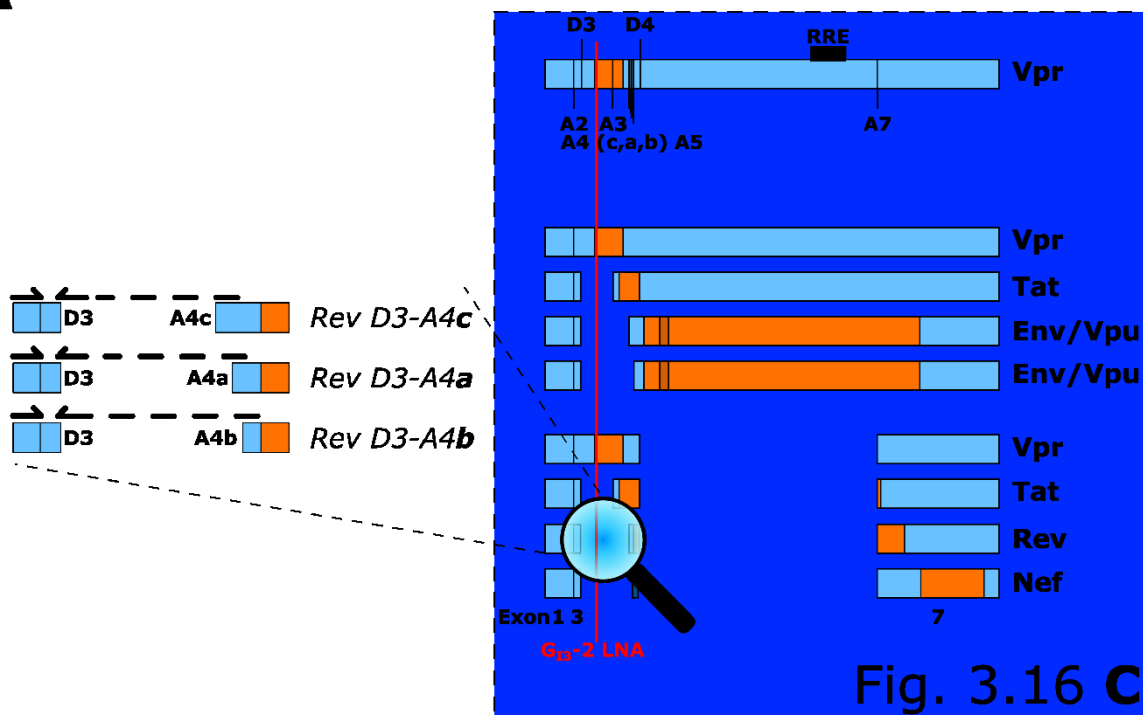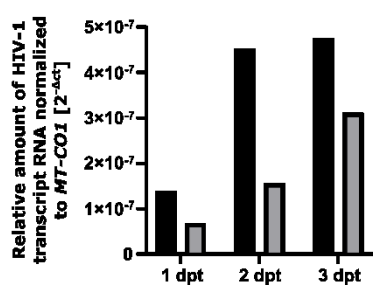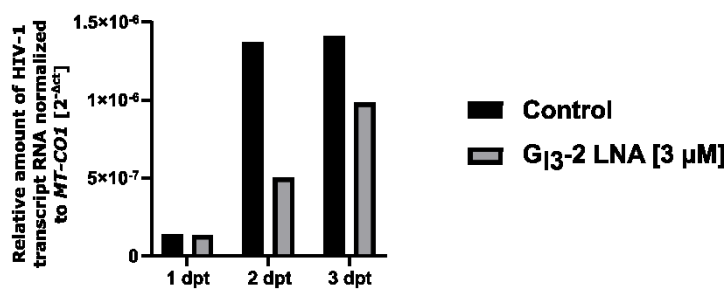
Fig. 3.20 Unassisted G_{I3}-2 LNA mixmer delivery affects HIV-1 Rev transcript levels in lentiviral vector-transduced PM1 T cells. (**A**) Schematic showing the three distinct HIV-1 splice acceptor sites A4c, A4a and A4b that can be used to generate HIV-1 Rev coding RNA transcript variants. Positions of the here used forward primer and the three different Rev specific exon junction primers are illustrated. (**B** – **C**) Quantification of HIV-1 Rev RNA transcripts isolated from lentiviral vector-transduced PM1 T-cells over the course of three days post-transduction via RT-qPCR analysis normalized to cellular *MT-CO1* expression (4a usage: #1544, #6751; 4b usage: #1544, #6752). Cells were transduced with lentiviral vector LV-Vpr3 as described in the method section and at 6 hours post-transduction washed with PBS. The G_{I3}-2 LNA mixmer was added to the new medium at a final conc. of 3 µM. Untreated cells served as control (n = 1).

3.6 Induced splice switching by unassisted LNA mixmer delivery is T-cell specific and seems to be limited to splicing regulatory elements

3.6.1 Inhibition of HIV-1 replication by unassisted G_{I3}-2 LNA mixmer delivery is restricted to T-cells

Based on the results obtained from the previous experiments, it was assumed that the anti-HIV-1 activity after unassisted G_{I3}-2 LNA mixmer delivery might be T-cell dependent.

Having with the G_{I3}-2 LNA mixmer an in-depth studied LNA mixmer with demonstrated antiviral HIV-1 activity in infected T-cells, this potential cell type specificity was sought to be analyzed in the context of G_{I3}-2 LNA mixmer-mediated HIV-1 inhibition in other cell types.

Therefore, to analyze the supposed T-cell specificity, the same experimental set-up was followed that showed profound inhibition of HIV-1 in T-cells at 3 dpi (Fig. 3.15), but now the monocyte-like THP-1 cells were infected with the R5-tropic HIV-1 NL4-3 derivate *NL-918 +g15* (139).

At 3 dpi, a time-point when unassisted G_{I3}-2 LNA mixmer delivery to the NL4-3-infected PM1 T-cells resulted in a significant and more than 10-fold decrease in HIV-1 RNA (Fig. 3.15), RT-qPCR analysis was performed to compare the amount of total HIV-1 RNA in the G_{I3}-2 treated to the untreated and control LNA mixmer-treated THP-1 cells.

Interestingly, after two independent infection experiments, no difference in total HIV-1 RNA was observed in the differently treated THP-1 cells at 3 dpi (Fig. 3.21 **A**). Therefore, this experiment provided first evidence that pointed towards a T-cell type specificity for LNA mixmer-exerted effects after unassisted delivery.

To collect more data that supports T-cell specificity, the HeLa cell-derived TZM-bl cell line was additionally used. This HIV-1 permissive cell line provided a third cell type to investigate G_{I3}-2 LNA mixmer-mediated HIV-1 inhibition. Although HeLa cells, as epithelial cells, are not susceptible to HIV-1 infection, this HeLa cell-derivate is permissive due to its expression of HIV-1 receptor CD4 and the two viral co-receptors CXCR4 and CCR5.

Hence, to analyze the assumed T-cell type specificity for LNA mixmer-exerted effects now in the context of these epithelial cells, TZM-bl cells were infected with HIV-1 NL4-3 and treated with the G_{I3}-2 LNA mixmer. Again, RT-qPCR analysis for total HIV-1 RNA was conducted at 3 dpi to check for a possible G_{I3}-2 LNA mixmer-mediated inhibition of HIV-1 replication.
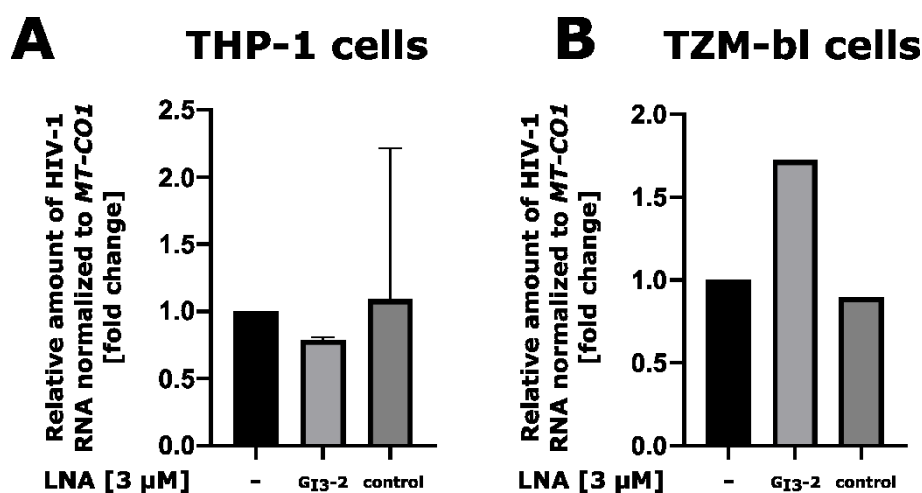
Fig. 3.21 Unassisted G$_{I3}$-2 LNA mixmer delivery does not inhibit HIV-1 replication in monocyte-like THP-1 cells and HeLa cell-derived TZM-bl cells. (**A** – **B**) Quantification of total HIV-1 RNA isolated from HIV-1 infected monocyte-like THP-1 and HeLa cell-derived TZM-bl cells at three days post-infection via RT-qPCR analysis using HIV-1 exon 7 specific primers #3387 and #3388 and normalized to cellular *MT-CO1* expression. (**A**) PMA-stimulated THP-1 cells were infected with the M-tropic HIV-1 laboratory strain NL4-3-derivate NL-918 +g15 (139) at an MOI 0.005 and at 6 hours post-infection washed with PBS (n = 2). (**B**) TZM-bl cells were infected with the HIV-1 laboratory strain NL4-3 at an MOI 0.005 and at 6 hours post-infection washed with PBS (n = 1). The G$_{I3}$-2 LNA mixmer was added to the new medium at a final conc. of 3 µM. Untreated and control LNA mixmer-treated cells served as control. (**A**) Data presented as mean +SD.

The obtained results showed that even in the permissive TZM-bl cells, the G$_{I3}$-2-LNA mixmer did not affect HIV-1 replication after unassisted delivery (Fig. 3.21 **B**).

Altogether, the performed experiments suggested that the antiviral activity of LNA mixmers after unassisted delivery depends on the cell type treated. Here, T-cells were shown to have a capability that allows efficient LNA mixmer-induced effects after unassisted delivery. However, until now only the cell type-specific activity of the anti-HIV-1 G$_{I3}$-2 LNA mixmer was investigated.

With the primary goal of this PhD thesis to explore the overall potential of LNA mixmers as antivirals, the question, therefore, remained whether this HIV-1-specific observation is a general phenomenon in the context of unassisted LNA mixmer delivery.

3.6.2 Induced splice switching of cellular gene *CENPJ* by unassisted LNA mixmer delivery is restricted to T-cells

Based on the results obtained so far, it was suggested that LNA mixmer-exerted acitivity after unassisted delivery may be restricted to certain cell types. In particular, LNA mixmer-exerted effects after unassisted delivery were to this point only observed in T-cells.

However, only LNA mixmers targeting HIV-1 sequences were analyzed. Hence, it is unknown whether this cell type-dependence is influenced by HIV-1 infection.

To test whether this T-cell type specificity accounts for LNA mixmer-exerted activity in general, a cellular gene targeted in T-cells by additional LNA mixmers was examined in the following.

As reporter gene, the human Centromere protein J gene (*CENPJ*) was selected. Here, Al-Dosari et al. identified a Seckel Syndrome-causing G>C substitution of the exon 12 splice acceptor site AG dinucleotide within *CENPJ*, which leads to the skipping not only of exon 12 during pre-mRNA processing, but leads to the generation of *CENPJ* transcripts missing exon 11 and 12, as well as transcripts missing exon 11, 12 and 13 (Fig. 3.22) (183).

A

#CENPJfwd

Exons →

| 10 | 3,242 bp | 11 | 3,645 bp | 12 | 219 bp | 13 | 812 bp | 14 |

225 bp | | 85 bp | | 65 bp | | 111 bp | | 141 bp

#CENPJrev ←

CENPJ UpS LNA   CENPJ DownS LNA
CENPJ SA LNA

Pos
42,225 TAAAATTTTCAATTAAATATTAAATCTAACTCTTGACAATTTTATTCTAATAGGCAATCCACCTCGAAGATCCAAGTCTGCACCTCCTCGTGATTTAG 42,322

Pos

Exon 12

Centromere protein J (CENPJ)
NCBI RefSeq: NG_009165
ENSEMBL: ENSG00000151849

B

Healthy

| 10 | 11 | 12 | 13 | 14 |

Splicing →

| 10 | 11 | 12 | 13 | 14 |
consecutive splicing

Seckel syndrome

| 10 | 11 | 12 | 13 | 14 |

G>C in splice acceptor site

Splicing →

10	11	X	13	14
10	X	X	13	14
10	X	X	X	14
exon skipping

(Al-Dosari et al., 2010)

Fig. 3.22 Schematic showing the region affected by the Seckel syndrome causing splice acceptor site mutation of exon 12 within the Centromere protein J (*CENPJ*) gene. (A) Overview of the region spanning exon 11 to 14 of the Centromere protein J (*CENPJ*) gene (Upper panel). Primer binding sites are indicated with black arrows. Sequence between nucleotide positions (pos) 42,225 and 42,322 is depicted with the splice acceptor site of exon 12 (red) and LNA mixmer binding sites (blue bars) (Lower panel). **(B)** Schematic illustrating the different splicing outcomes in the context of *CENPJ* pre-mRNA from healthy individuals or individuals harboring the indicated Seckel syndrome causing splice acceptor site mutation (G>C) as published in (183).

Due to the different exon skipping events observed, it was suggested that LNA mixmer-mediated interference with the *CENPJ* exon 12 splice acceptor site usage would offer a promising model system to investigate the presumed T-cell type specificity of LNA mixmer-mediated effects after unassisted delivery.

Before any LNA mixmers could be designed, the region surrounding the *CENPJ* exon 12 splice acceptor site was sequenced in Jurkat T-cells and in the commonly used human retinal pigment epithelium (RPE) cell line.

Sanger sequencing revealed the same nucleotide sequence in the Jurkat and RPE cells, which is also identical to the *CENPJ* reference sequence (NCBI RefSeq: NG_009165 and ENSEMBL: ENSG00000151849) (Fig. 3.23 **A**).

To investigate now the previously observed T-cell type specificity also in the context of an LNA mixmer targeting a cellular gene, thus independent of HIV-1 infection, three LNA mixmers were designed.

The three LNA mixmers were designed to mask either the exon 12 splice acceptor site AG dinucleotide directly (CENPJ **SA** LNA) or to mask sequences that encompass the AG dinucleotide (CENPJ **UpS** and **DownS** LNA), which may therefore also interfere with exon 12 SA usage (Fig. 3.23 **A**).

Subsequently, RPE and Jurkat T-cells were treated separately with these three anti-CENPJ LNA mixmer to test for the occurrence of induced splice switching.

As expected, unassisted delivery of the three anti-CENPJ LNA mixmers to RPEs and Jurkat T-cells led to the expected pattern of CENPJ splice variants only in the used T-cells, but not in the RPE cells (3.23 **B**). Sanger sequencing of the respective PCR products confirmed induced splice switching by identifying the same aberrant CENPJ splice products as observed in individuals harboring the exon 12 splice acceptor site AG dinucleotide mutation (data not shown).

Interestingly, only treatment with the anti-CENPJ LNA mixmer binding to the sequence downstream of the exon 12 splice acceptor site AG dinucleotide (CENPJ **DownS** LNA) induced splice switching after unassisted delivery. Importantly, a transfection control experiment demonstrated that all three anti-CENPJ LNA mixmer induce the same splice switching after transfection-based delivery to the RPE cells (data not shown).
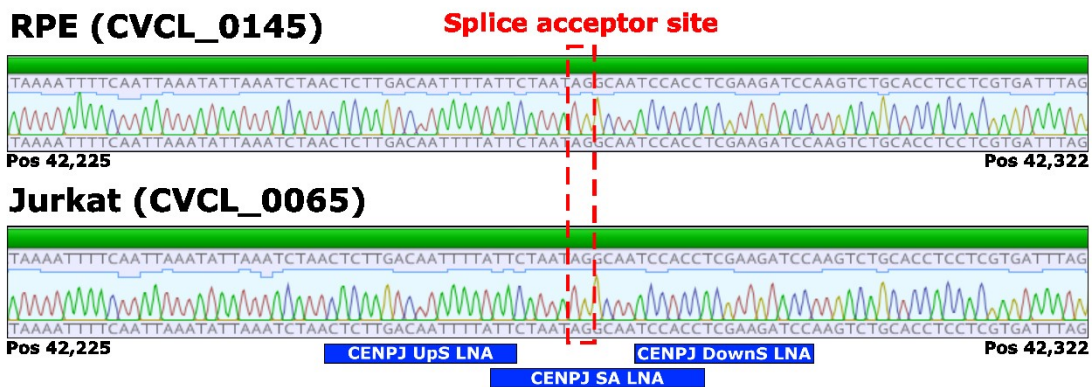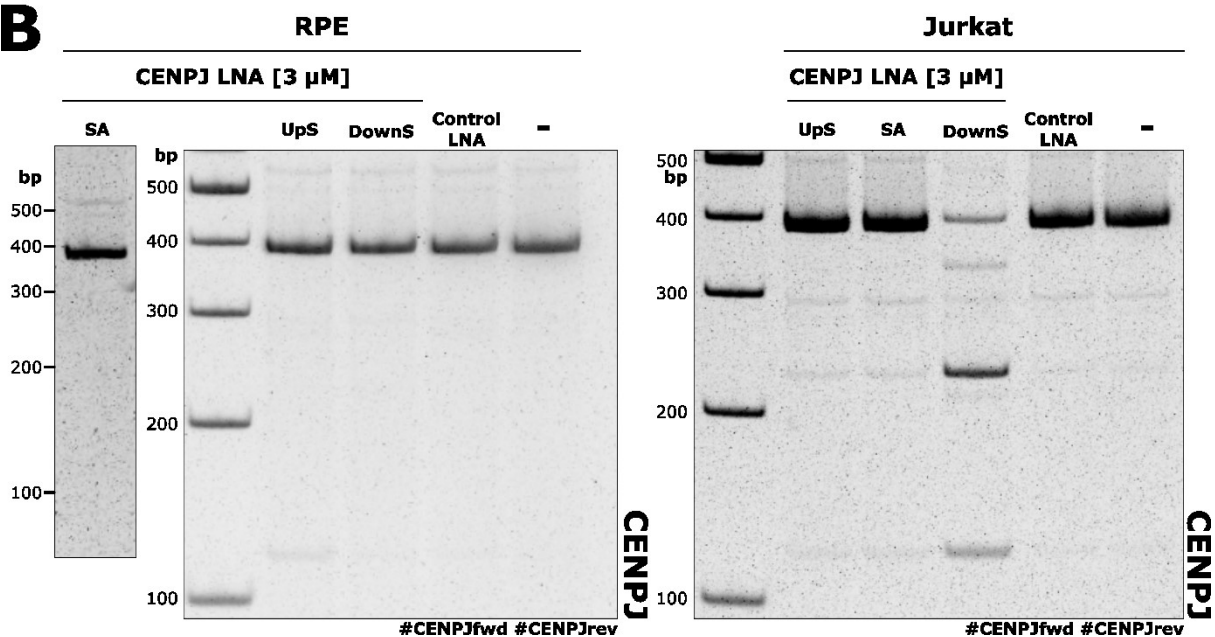
Fig. 3.23 Induced splice switching of the *CENPJ* pre-mRNA after unassisted LNA mixmer occurs in Jurkat T-cells and not in RPE cells. (**A**) Sanger-sequencing of the nucleotides between positions (pos) 42,225 and 42,322 of the *CENPJ* gene in RPE cells (ARPE-19 cell line) and Jurkat T-cells with the exact positions of the exon 12 splice acceptor site (red) and the used LNA mixmers (blue bars). (**B**) Amount of the different splice products generated from *CENPJ* pre-mRNA after unassisted LNA mixmer delivery to ARPE-19 cells (Left panel) and Jurkat T-cells (Right panel) as analyzed by RT-PCR 24 hours post-treatment. Untreated and control LNA mixmer-treated cells served as control.

Considering unpublished data by Dr. Frank Hillebrand (Institute of Virology, University Hospital Düsseldorf, Heinrich Heine University Düsseldorf) showing the inability of an LNA mixmer targeting the HIV-1 splice donor 4 to inhibit HIV-1 replication after unassisted delivery to T-cells, it was argued whether a yet unknown cellular mechanism may disrupt binding of LNA mixmers to splice sites.

In summary, this data set extended the observation that LNA mixmer-mediated splice switching after unassisted delivery is restricted to T-cells also in an HIV-1-independent setting involving an LNA mixmer targeting a cellular gene.

Overall, it was suggested that regarding the antiviral potential of LNA mixmers, so far T-cells remain the only, but a very promising target cell type.

In addition to this presumed characteristic of T-cells, the obtained results together with the unpublished data by Dr. Frank Hillebrand implied that targeting splice sites directly with LNA mixmers is somehow prevented by yet unknown mechanisms. In this, context the CENPJ DownS LNA perhaps interfered with binding of a splicing regulatory protein by masking an important SRE site, likewise the anti-HIV-1 G_{I3}-2 or ESE_{tat} LNA mixmers (1).

3.7 The HIV-1 Rev response element provides an additional target for LNA mixmer-mediated interference with viral replication

3.7.1 SLIIb LNA transfection reveals the HIV-1 Rev response element as a promising target for LNA mixmer-mediated interference with viral replication

Viruses, especially RNA viruses like HIV-1, exhibit high mutations rates. Therefore, inhibiting viral replication with LNA mixmers most likely requires the combined use of several LNA mixmers targeting different viral regions. Previous experiments implied that if targeted, splice sites do not allow LNA mixmer-mediated inhibition of viral replication, narrowing the repertoire of potentially used viral target sequences. To therefore expand the arsenal of potential antiviral LNA mixmers and with this further dissecting the overall potential of LNA mixmers to inhibit viral replication, the following experiments approached HIV-1 inhibition by aiming at the viral Rev response element (RRE).

The RRE is an RNA export element that enables a regulated nuclear export of intron-containing and unspliced HIV-1 RNA that is otherwise trapped in the nucleus via a presumed active retention through *cis*-repressive RNA elements (162). Hence, its function is essential for viral replication. Binding of HIV-1 Rev protein in *trans* to the RRE stem loop IIb sequence is a prerequisite for its function and leads to nuclear RNA export via simultaneous binding to cellular adapter proteins (143).

After showing that G_{I3}-2 LNA mixmer-induced splice switching, which takes place in the nucleus, rather than induced target RNA degradation that was suggested to occur in the cytoplasm is responsible for the observed inhibition of HIV-1 replication, targeting the RRE

stem loop IIb sequence seemed to be another promising approach to ultimately abrogate viral replication.

First of all, to analyze a possible interference with HIV-1 nuclear RNA export by LNA mixmer-mediated masking of the viral RRE SLIIb sequence, an HIV-1 Env-based reporter was used. This HIV-1 Env-based reporter plasmid expresses a pre-mRNA containing an open reading frame (ORF) that codes for an HIV-1 Env-eGFP fusion protein (Fig. 3.24). The 5' end of this ORF is encompassed by HIV-1 splice donor 1 and HIV-1 splice acceptor 7, but also contains the HIV-1 RRE. Hence, protein expression of the HIV-1 Env-eGFP fusion protein is only possible after HIV-1 Rev is co-expressed and binds to the RRE SLIIb sequence, this way mediating nuclear export of the unspliced RNA harboring the Env-eGFP fusion ORF. In the absence of Rev or if Rev binding to the SLIIb sequence is prevented, only nuclear export of a spliced RNA product generated by HIV-1 splice donor 1 and splice acceptor 7 usage is possible. Due to an additional translational start codon directly preceding the actual eGFP coding sequence, this splice product also leads to the expression of eGFP protein. By using the CD4, CXCR4 and CCR5 expressing TZM-bl cells for this experiment, nuclear export of the unspliced Env-eGFP transcript ultimately leads to the generation of multinucleated cells, so-called syncytia, by HIV-1 Env-induced membrane fusion between neighboring cells.

TZM-bl cells were co-transfected with the HIV-1 Env-based reporter plasmid, the HIV-1 Rev expression vector pcRev and either the designed SLIIb LNA mixmer, a control LNA mixmer or without an LNA mixmer. At day 1 post-transfection, a contrast staining was performed to better analyze the HIV-1 Env-induced cell fusion rate based on the size of induced syncytia and the number of nuclei per syncytium.

Light microscopic analysis clearly showed that co-transfection with the SLIIb LNA mixmer led to the generation of syncytia that were smaller in size compared to the syncytia observed in the two control conditions (Fig. 3.25 **A**). In the control wells that were not transfected with an LNA mixmer, but only the HIV-1 Env-eGFP expression and pcRev, some syncytia even began to detach from the bottom surface due to their size, which was not observed in the SLIIb LNA mixmer-transfected wells at all (Fig. 3.25 **A**, a, red arrowhead).
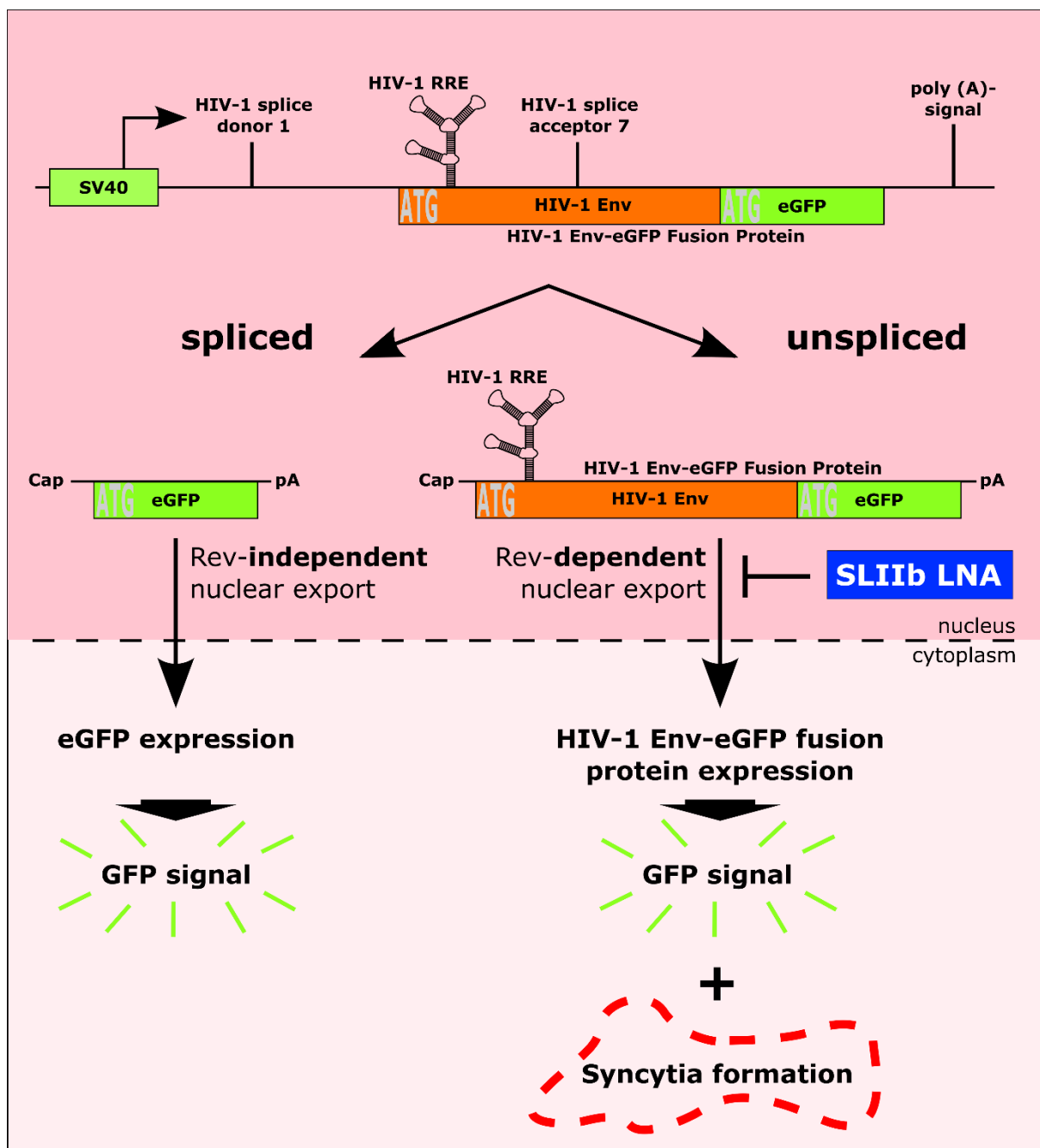
Fig. 3.24 Schematic describing the used HIV-1 Env-eGFP-based reporter to analyze SLIIb LNA mixmer-mediated inhibition of Env expression. Expression of the HIV-1 Env-eGFP pre-mRNA results in spliced mRNA with the coding capacity for eGFP (green) and unspliced mRNA with coding capacity for the HIV-1 Env-eGFP fusion protein (orange). Nuclear export of the spliced product is HIV-1 Rev-independent and nuclear export of the unspliced transcript containing the HIV-1 rev response element (RRE) is Rev-dependent. Binding of the SLIIb LNA mixmer to the RRE should prevent nuclear export of the unspliced transcript. Translation of the spliced transcript results in GFP signal and of the unspliced transcript in GFP signal plus syncytia formation in HIV-1 receptor expressing cells.

Quantifying cellular fusion rates between the conditions via counting the nuclei per syncytium in three independent biological replicates confirmed this initial observation by revealing a

significant lower fusion rate of the SLIIb LNA mixmer-transfected cells compared to in the two control cells (Fig. 3.25 **B**).

A
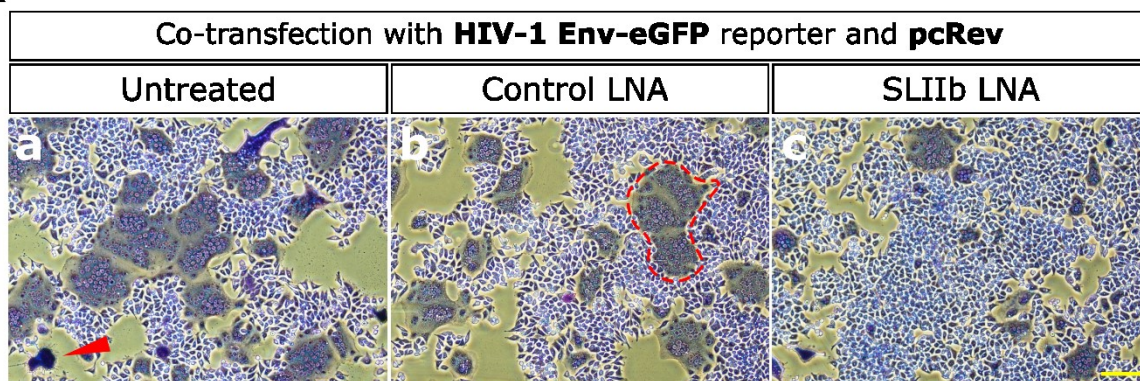
B
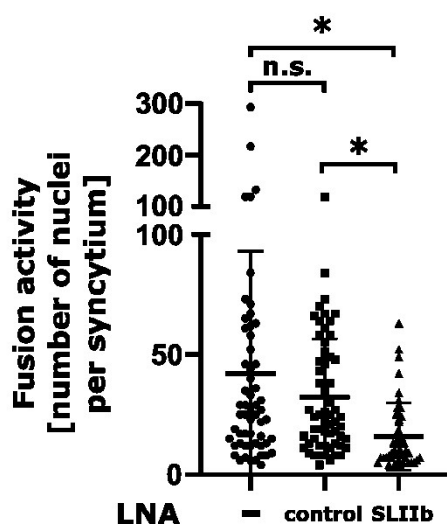
Fig. 3.25 SLIIb LNA mixmer-mediated inhibition of Env expression after transfection. (**A**) Light microscopic imaging after contrast staining shows SLIIb LNA mixmer-mediated inhibition of HIV-1 Env-eGFP fusion protein expression in TZM-bl cells co-transfected with the HIV-1 Env-eGFP reporter and the HIV-1 Rev expression vector pcRev based on the smaller observed average size of the induced syncytia. Exemplary sections are shown from one biological replicate. TZM-bl cells not transfected with an LNA mixmer or co-transfected with a control LNA mixmer served as control. One exemplary syncytium is indicated (red-dotted line). A red arrowhead points to a syncytium already partially detached from the cell culture vessel. Scale bar is 100 µm. (**B**) Quantification of the HIV-1 Env-eGFP-induced fusion rate of co-transfected TZM-bl cells in (**A**) by determining the average number of nuclei per syncytium. Syncytia (n = 57 for without LNA, n = 59 for control LNA, n = 44 for SLIIb) were analyzed from three independent biological replicates (n = 3). Statistical significance analyzed by one-way ANOVA with Tukey's multiple comparison test. Data presented as individual data points plus mean ±SD. *p < 0.05.

Concluding from the lower fusion rate after SLIIb LNA mixmer transfection that a reduced Env expression occurred, this first reporter-based experiment suggested that masking of the RRE SLIIb sequence by the SLIIb LNA mixmer interfered with HIV-1 RRE-Rev-dependent nuclear RNA export.

As a control to exclude possible SLIIb LNA mixmer-induced off-target effects on cell viability or cell growth that may have contributed to the reduced fusion rate, Vero cells were co-transfected with a SARS-CoV-2 spike glycoprotein expression vector and again, the SLIIb LNA mixmer, a control LNA mixmer or no LNA mixmer. Given expression of the SARS-CoV-2 receptor angiotensin-converting enzyme 2 (ACE2) in Vero cells, expression of viral spike glycoprotein in these cells induces syncytia formation, like HIV-1 Env expression in TZM-bl cells. Here, no reduction in the fusion rate after SLIIb LNA mixmer co-transfection was observed, overall implying that the SLIIb LNA mixmer has no off-target effects that would somehow affect syncytia formation on its own (data not shown).

In addition to the light microscopic analysis after contrast staining at day 1 post-transfection, a live cell imaging experiment was performed to substantiate the lower cell fusion rate of SLIIb LNA mixmer-transfected cells. Again, TZM-bl cells were co-transfected with the HIV-1 Env-eGFP reporter, pcRev and this time only either the SLIIb LNA mixmer or the control LNA mixmer. Over the course of 19 hours post-transfection light microscopic images and images via the eGFP channel were taken in fixed time intervals.

Here depicted are exemplary images that were taken 1.5 hours apart and in-between 13 and 19 hours post-transfection (Fig. 3.26). During this one live cell imaging experiment, the number of eGFP-positive cells implied a comparable transfection efficiency in the two wells compared (Fig. 3.26, white arrows point towards some eGFP-positive cells). Overall, the data obtained underlined the lower fusion rate in SLIIb LNA mixmer-transfected cells as seen by the much smaller syncytia, which were most apparent at 17.5 hours post-transfection (Fig. 3.26, syncytia are indicated by a white-dotted line). Similar to what was observed before, the high fusion rate of the control cells led to the detachment of syncytia from the cell culture vessel surface at 19 hours post-transfection, which was not observed in the SLIIb LNA mixmer-transfected well (Fig. 3.26, white arrowhead).

Together, these experiments show that SLIIb LNA mixmer-transfection inhibits Env expression, which was suggested to be caused by interference with the Rev-dependent nuclear RNA export.
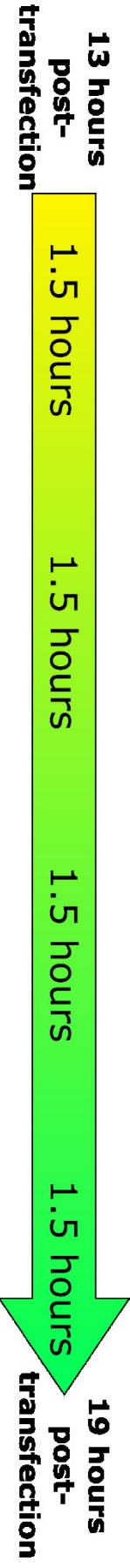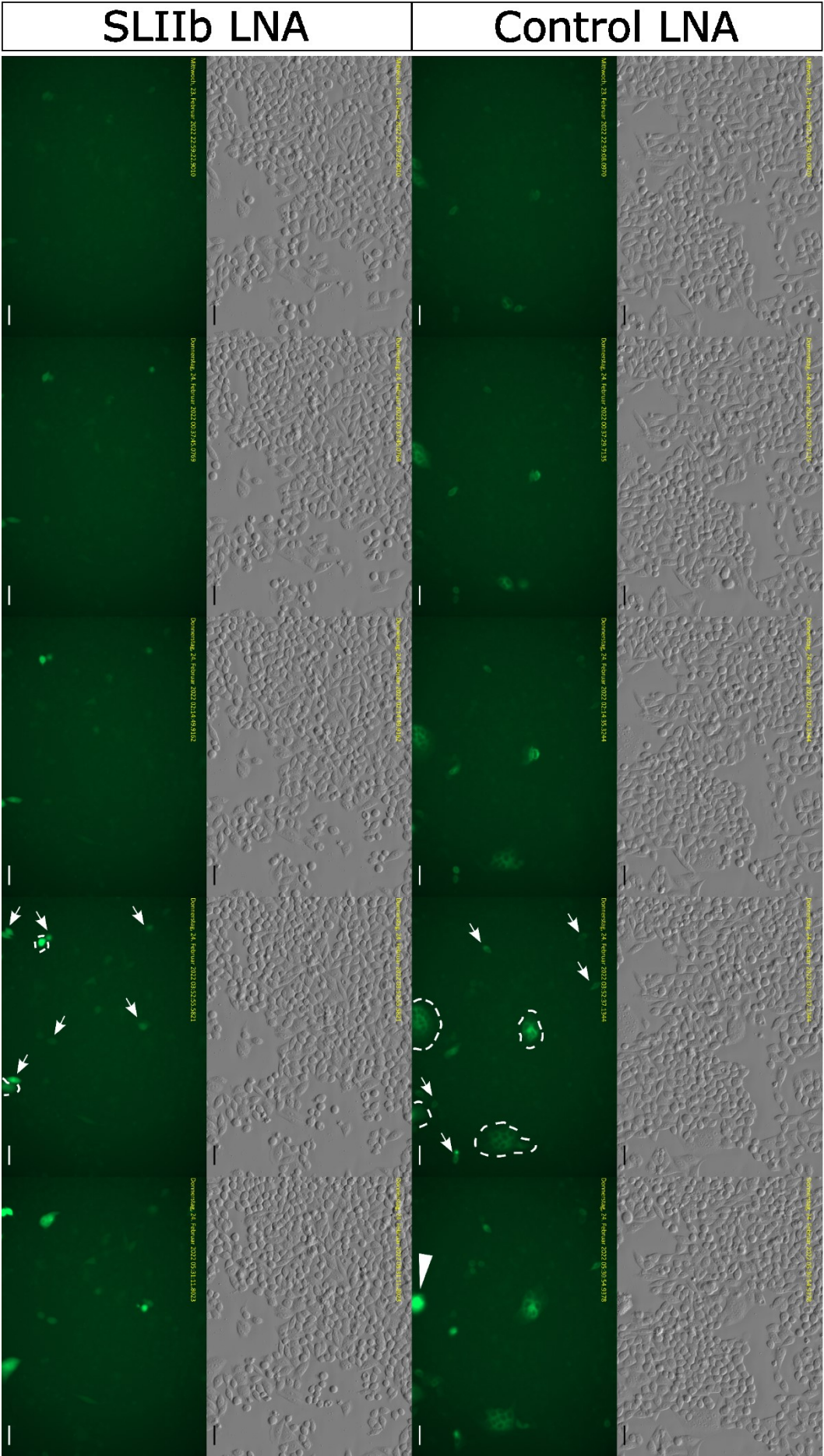
Fig. 3.26 Delayed HIV-1 Env-induced syncytia formation by SLIIb LNA mixmer co-transfection monitored by live cell imaging. Serial pictures of SLIIb or control LNA mixmer co-transfected TZM-bl cells taken between 13 to 19 hours post-transfection (hpt) in 1.5 hours intervals. TZM-bl cells were co-transfected with the HIV-1 Env-eGFP reporter and the HIV-1 Rev expression vector pcRev in addition to the respective LNA mixmer. Exemplary GFP-positive cells (white arrow) and syncytia at 17.5 hpt are indicated (white-dotted line). An already partially detached syncytium in the control LNA mixmer condition at 19 hpt is depicted (white arrowhead). Scale bars are 100 μm.

After having now shown the potential of the SLIIb LNA mixmer to interfere with HIV-1 RNA processing, its full antiviral potential should be investigated by unassisted delivery to HIV-1-infected cells. For this, PM1 T-cells were infected with the HIV-1 NL4-3 clone and subsequently treated with the SLIIb LNA mixmer as described before for the anti-HIV-1 G_{I3}-2 LNA mixmer. RT-qPCR analysis for total HIV-1 RNA at 2 dpi indicated an SLIIb LNA mixmer-induced inhibitory effect on HIV-1 replication after unassisted delivery (Fig. 3.27 **A**). Therefore, it could be assumed that besides viral SREs also viral RNA transport elements, like the HIV-1 RRE, display promising targets for potential LNA mixmer-based antiviral therapy approaches.

3.7.1 SLIIb LNA antiviral activity after unassisted delivery underlies the same T-cell specificity as observed for the G_{I3}-2 LNA mixmer

In a last experiment, monocyte-like THP-1 cells and TZM-bl cells were infected with NL-918 +g15 and NL4-3, respectively, and subsequently treated with the SLIIb LNA mixmer, to investigate the proposed T-cell specificity also with the SLIIb LNA mixmer as an additional example. As expected, RT-qPCR analysis at 3 dpi could not reveal any inhibitory effect on HIV-1 replication after unassisted SLIIb LNA mixmer to these cells, further approving the hypothesis on a T-cell specific effect (Fig. 3.27 **B**, **C**).

In summary, the work performed in this dissertation on the antiviral potential of LNA mixmers suggests that the previously observed non-detectability of HIV-1 transcripts following RT-PCR analyses after unassisted LNA mixmer delivery (1) was due to inhibition of PCR amplification rather than LNA-induced RNA degradation. Further, the data obtained here showed that LNA mixmer-induced splice switching most likely caused the observed inhibition of HIV-1 replication.

By using different HIV-1 permissive cell lines and a cellular control gene, this dissertation moreover suggests that T-cells exhibit a characteristic susceptibility to unassisted LNA mixmer delivery that sets them apart from the other cell types tested here
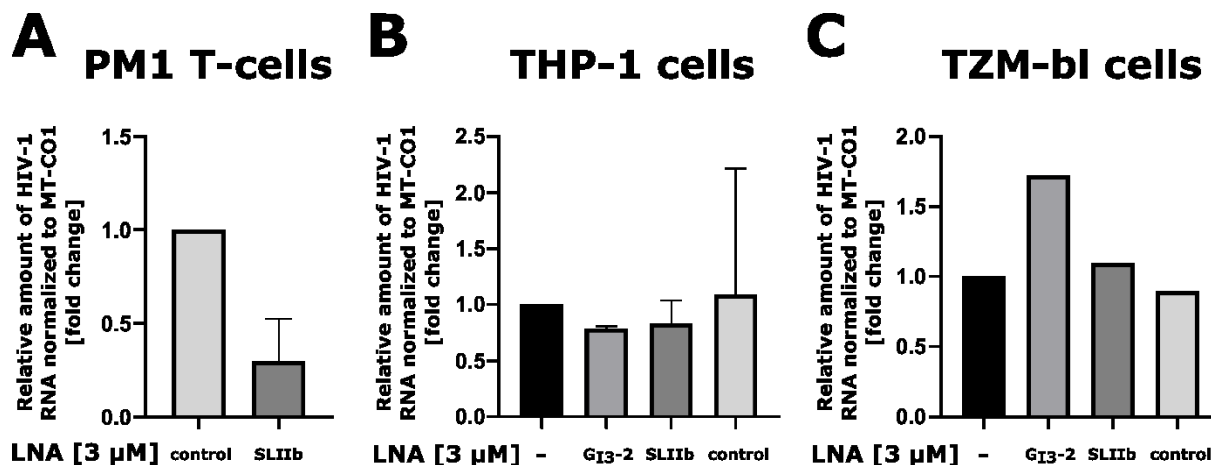
Fig. 3.27 Unassisted SLIIb LNA mixmer delivery achieves inhibition of HIV-1 replication only in T-cells. (**A** – **C**) Quantification of total HIV-1 RNA isolated from HIV-1 infected PM1 T-cells (**A**), monocyte-like THP-1 (**B**) and HeLa cell-derived TZM-bl cells (**C**) at two (PM1) or three days post-infection (THP-1 and TZM-bl) via RT-qPCR analysis using HIV-1 exon 7 specific primers #3387 and #3388 and normalized to cellular *MT-CO1* expression. PM1 (n = 2) and TZM-bl cells (n = 1) were infected with the HIV-1 laboratory strain NL4-3 at an MOI 0.005 and at 6 hours post-infection washed with PBS. PMA-stimulated THP-1 cells were infected with the M-tropic HIV-1 laboratory strain NL4-3-derivate NL-918 +g15 (139) at an MOI 0.005 and at 6 hours post-infection washed with PBS (n = 2). The depicted LNA mixmers were added to the new medium at a final conc. of 3 µM. Data presented as mean +SD.

.

4   Discussion

Due to improved chemical modifications and better characterization of their functions, more and more therapeutic ASOs are now being tested in clinical trials. Some ASOs have already been approved by the relevant health authorities. However, there are still major pitfalls in ASO technology that limit their success in the clinic. One of which is the very low rate of productive ASO uptake that leads to the desired ASO activity.

In this context, a previous study showed successful inhibition of HIV-1 replication in T-cell lines and primary T-cells by unassisted delivery of so-called LNA mixmer-modified ASOs designed to bind viral splicing regulatory elements (SREs) (1). Based on this promising work, the aim of this thesis was to investigate the potential of such LNA mixmers to inhibit replication also of other pathogenic viruses with respect to the diverse replication mechanisms of (+)ssRNA, (-)ssRNA and retroviruses as well as cytoplasmic and nuclear replicating viruses.

To be able to analyze the antiviral activity of LNA mixmers against the recently emerged SARS-CoV-2, a virus that became pandemic within only few months and continues to have enormous impact on society, SARS-CoV-2 was first isolated from a nasal/oropharyngeal swab taken from a SARS-CoV-2-infected individual.

The first evidence for successful inoculation of Vero cells was an increased amount of SARS-CoV-2 RNA within the cell culture supernatant already at 24 hpi. The amount of viral RNA continued to increase exponentially until 96 hpi (Fig. 3.1). The increased amount of SARS-CoV-2 RNA, which was observed already at 24 hpi, is in agreement with the short duration of the SARS-CoV-2 replication cycle that was determined to be less than 6 hours by Cortese and co-workers (95).

Besides analyzing viral replication by RT-qPCR after initial inoculation, the inoculated Vero cells were monitored for the appearance of potential virus-induced cytopathic effects (CPEs). Indeed, the inoculated Vero cells started to round-up and detach from the cell culture flask at 3 dpi. This hinted to the induction of a SARS-CoV-2-induced CPE in the applied setting (Fig. 3.2). Importantly, the same detachment of SARS-CoV-2-inoculated Vero cells at 3 dpi was observed by two independent research groups at around the same time (167, 168). Overall, this observation, therefore, not only supported the idea of successful inoculation with SARS-CoV-2 during this thesis, but also provided the foundation for different molecular methods like end-point dilution and diagnostic neutralization tests that can be evaluated on the appearance of virus-induced CPE (18, 66, 91, 184, 185).

Transfer of cell culture supernatant to newly seeded Vero cells demonstrated the presence of infectious material, which had to be released into the supernatant (Fig. 3.4). The presence of

intact viral particles intracellularly and extracellularly was eventually confirmed by transmission electron microscopic analysis performed in collaboration with the Dr. Ann-Kathrin Bergmann (Electron microscopy core facility, University Hospital Düsseldorf) (Fig. 3.5). Here, infected Vero cells harbored membranous structures, often referred to as double membrane vesicles (DMVs), throughout their cytoplasm. Such radical reshaping of subcellular morphologies was observed also by others (95), and most likely stems from viral interactions with the cellular autophagy machinery (96). Induction of these DMVs was suggested to assist SARS-CoV-2 replication and in this context, especially a role for SARS-CoV-2 ORF3a protein was shown (186, 187). Overall, the conducted transmission electron microscopic analysis, therefore, endorsed the suitability of the employed Vero cell-based cell culture system to investigate SARS-CoV-2 replication and concomitant drug-mediated interferences.

After this thesis contributed to the generation of an infectious SARS-CoV-2 isolate termed *NRW-42*, the viral 30 kb RNA genome of this isolate was sequenced by whole-genome sequencing in collaboration with Dr. Andreas Walker (Institute of Virology, University Hospital Düsseldorf). The NRW-42 isolate, obtained from a swab specimen taken during March 2020, was found to harbor only 6 nucleotide mutations compared to the Wuhan-Hu-1 reference genome isolated in late 2019 (NC_045512) (Tab 3.1).

This low number of nucleotide substitutions is in line with the first Korean SARS-CoV-2 isolate exhibiting 9 nucleotide exchanges as well as with an early isolate from the USA that exhibited only 3 nucleotide exchanges compared to Wuhan-Hu-1, both of which were generated in late January 2020 (167, 168). The low number of nucleotide exchanges of this RNA genome over the course of several months is most likely due to the proof-reading function of the coronavirus replicase complex, which sets coronaviruses apart from other RNA viruses (82).

From the mutations caused by these six nucleotide substitutions, the SARS-CoV-2 spike protein D614G mutation (g.23403A>G) is perhaps the most well-studied. This amino acid substitution was early on shown to increase infectivity of SARS-CoV-2, which was then suggested to be the reason why D614G viral strains quickly supplanted wild-type SARS-CoV-2 (170, 171). Hence, the appearance of this mutation in the here generated isolate was to be expected.

Besides this well-known g.23403A>G substitution, which causes the spike D614G mutation, the NRW-42 isolate harbored also nucleotide substitutions g.241C>T, g.1059C>T, g.3037C>T, g.14408C>T and g.25563G>T (Tab. 3.1). These substitutions were also not uncommon as they quickly spread globally at around the time of collecting the NRW-42 swab specimen (169, 188-191). This wide spread may indicate some sort of increased viral fitness mediated also by these lesser known mutations. Indeed, *in silico* analysis of the g.C241T mutation within the viral 5'UTR indicated a lower affinity of viral RNA to cellular proteins like Zinc finger CCHC domain- and RNA-binding motif-containing protein 1 (ZCRB1), which was suggested to reduce

replication efficiency (192). The g.14408C>T mutation, which leads to a Pro>Leu mutation in viral nsp12 on the other hand, was shown to increase activation of cellular receptor-interacting serine/Threonine Kinase 1 (RIPK1), which was suggested to facilitate viral propagation (193). Overall, it can be assumed that due to the widespread of its six individual nucleotide exchanges, the NRW-42 is a prototypic SARS-CoV-2 isolate that very well reflected the SARS-CoV-2 strains circulating at the time of the performed experiments. Hence, it was considered a suited model to investigate anti-SARS-CoV-2 compounds in cell culture.

With the NRW-42 isolate, it was analyzed whether unassisted LNA mixmer delivery can inhibit SARS-CoV-2 replication. However, unassisted delivery of two different LNA mixmers targeting sequences within the viral 5'UTR and 3'UTR, respectively, and which are essential for viral replication did not interfere with SARS-CoV-2 NRW-42- replication (Fig. 3.6). This was a surprising observation, because the previous study on anti-HIV-1 LNA mixmers suggested a predominant cytoplasmic activity of the applied LNA mixmers (1). Moreover, others likewise demonstrated profound cytoplasmic activity of their PS-modified ASOs, which is suggested to stem from ASOs escaping the endosomal pathway (41, 194).

No work was done to this point on the importance of the LNA mixmer-targeted sequences specifically for SARS-CoV-2 replication. However, given their fundamental role for the replication of other coronaviruses either by recruiting cellular proteins or by allowing template-switches during (-)ssRNA synthesis, it was strongly assumed that masking these sequences by the two designed anti-SARS-CoV-2 LNA mixmers would interfere with viral replication (82, 100-104).

Given this supposed importance of the targeted SARS-CoV-2 sequences, it was argued whether the drastic infection-induced reshaping of cellular morphologies observed also during this thesis (Fig. 3.5) and described by others (95, 96) may hamper LNA mixmer activity by restricting their access to viral target RNA. Interestingly, (+)ssRNA viruses in general are well-known to induce DMVs and it is suggested that this process protects the viral RNA from innate immunity and other restriction factors like RNase (195-198). For instance, another member of the coronavirus family, Mouse Hepatitis Virus was shown to synthesize its RNA within DMVs, where viral RNA is supposedly shielded from cellular factors (199). Thus, the inability of the two anti-SARS-CoV-2 LNA mixmers to inhibit viral replication may be explained by the inaccessibility of the viral target RNA.

In contrast to (+)ssRNA viruses like SARS-CoV-2, the (-)ssRNA bunyavirus Crimean-Congo hemorrhagic fever virus (CCHFV) and its close relative Hazara virus (HAZV) are not known to induce DMV formation. To test whether LNA mixmers exert antiviral activity in the absence of virus-induced DMVs, HAZV-infected cells were treated with an LNA mixmer targeting the conserved 5'end of the genomic S and L segment. However, unexpectedly, unassisted delivery to HAZV-infected CaCo-2 cells also did not affect viral replication (Fig. 3.7). The anti-HAZV LNA

mixmer was designed to interfere with the complementary binding between the 5' and 3' terminal ends of the genomic segments, which was previously shown to be essential for transcription of bunyaviral RNA (110-112). Hence, this data set could again not show any cytoplasmic ASO activity as indicated by preceding studies (1, 41, 194).

In the absence of any observable anti-HAZV LNA mixmer activity in CaCo-2 cells, a potential high suscebtibitly of viral SREs to LNA mixmer-mediated antiviral effects, which was previously suggested in the context of HIV-1 infection, was sought to be analyzed in the CaCo-2 cell model. To test this, Influenza A virus (IAV)-infected CaCo-2 cells were now treated with LNA mixmers. Even though Influenza A virus (IAV) is a (-)ssRNA virus, it replicates in the nuclear compartment and its RNA is processed by pre-mRNA splicing. The anti-IAV LNA mixmers were designed to mask viral SREs within the IAV M segment RNA and should therefore interfere with IAV replication either by disturbing the balanced splicing of its pre-mRNA or directed RNA degradation as at this point still hypothesized for the anti-HIV-1 LNA mixmers. Surprisingly, no antiviral activity was observed for the two designed LNA mixmers after unassisted delivery (Fig. 3.8).

One major pitfall of ASO activity is that their uptake is considered to lead to an either productive or a non-productive pathway. The non-productive is primarily due to the endosomal entrapment of ASOs and competes with the productive pathway (reviewed in (46)). Furthermore, the rate at which the productive pathway, or both, are taken depends on the cell line treated with some being more susceptible to ASO activity than others (35). Since neither HAZV (cytoplasmic) nor IAV (nuclear) replication was inhibited by unassisted LNA mixmer delivery to CaCo-2 cells, most likely endosomal entrapment within the experimental time period of 2 dpi restricts their supposed antiviral activity even in the absence of DMVs. Interestingly, Stein and co-workers found that ammonium ions in the form of ammonium chloride treatment could enhances cytoplasmic and nuclear ASO activity, most likely by facilitating endosomal ASO escape (200). In addition to that, arsenic trioxide treatment apparently promoted nuclear ASO import by inducing a so-called stress-induced response complex, which shuttles ASOs into the nucleus (36, 200). However, the SRE targeting anti-HIV-1 LNA mixmers exhibited profound antiviral activity even in the absence of such external facilitators of unassisted delivery (1). Hence, although it would be interesting to test the antiviral activity of the anti-HAZV and anti-IAV LNA mixmers in the presence of ammonium chloride and/or arsenic trioxide, there must be other most likely intrinsic cellular factors that contribute to this high anti-HIV-1 ASO activity and whose identification is key to unravel the complex productive ASO uptake.

In the preceding study, unassisted delivery of LNA mixmers targeting HIV-1 SREs completely abrogated HIV-1 replication in infected T-cell lines and primary T-cells in a low molecular range (1). In addition, LNA mixmer activity was thought to occur predominantly in the cytoplasm and

is observable as early as 24 hours post-delivery (1). In this thesis, unassisted LNA mixmer delivery failed to inhibit SARS-CoV-2, HAZV and IAV replication, which was especially intriguingly in the context of IAV, because its replication is also dependent on viral SREs like HIV-1. Thus, in a next step, this thesis aimed at understanding the particular pathway responsible for this complete abrogation of HIV-1 replication after unassisted LNA mixmer delivery (1).

Dose-depend treatment of HIV-1-infected Jurkat T-cells with the G_{I3}-2 LNA mixmer for 24 hours resulted in the same lack of G_{I3}-2 LNA mixmer-targeted HIV-1 Vpr3 transcript during RT-PCR analysis as observed during the previous study (Fig. 3.9) (1). This initial observation substantiated the conclusion that unassisted LNA mixmer delivery leads to a target-specific RNA degradation already at a low molecular range and at 24 hours post-delivery. Although ASOs in mixmer design are commonly not employed to achieve target RNA degradation, they were already shown to induce RNA degradation, for instance, through the cellular nonsense-mediated decay or no-go decay pathway and yet unknown, supposedly RNase H1-independent, pathways (194, 201).

Hence, to better characterize the underlying pathway that is responsible for complete abrogation of HIV-1 replication after unassisted G_{I3}-2 LNA mixmer delivery, first, the EC_{50} value of this suggested degradation was to be determined. Surprisingly, the performed experiments showed that the lack of G_{I3}-2 LNA mixmer-targeted HIV-1 transcripts after unassisted delivery to infected T-cells was due to an LNA mixmer-mediated interference with the conducted PCR. These experiments additionally indicated that this interference is likely caused by binding of the LNA mixmer to their target sequence on PCR products during elongation (Fig. 3.10, 3.11, 3.12). Such a specific inhibition of PCR product amplification by the G_{I3}-2 LNA mixmer is in line with a study by Hummelshoj et al, in which the authors successfully added intron-targeting LNA mixmers to their PCR mix with the intention to prevent amplification of unwanted genomic DNA during RT-PCR (202). This work on intron-targeting LNA mixmers does, however, not deal with the apparent co-extraction of LNA mixmers during RNA preparation, as observed during this thesis (202). Thus, to gather more evidence on such a co-extraction, this thesis showed that FAM-based TaqMan RT-qPCR is disturbed by prior unassisted FAM-conjugated LNA mixmer delivery (Fig. 3.14). Overall, therefore, the combined data ultimately calls for attention with regard to performing RT-(q)PCR analysis after ASO treatment due to an apparent co-extraction with cellular nucleic acid. Moreover, while revealing the presence of vpr and vif RNA even after unassisted G_{I3}-2 LNA mixmer delivery, it is arguable if LNA mixmer-mediated RNA degradation is the reason behind the profound anti-HIV-1 activity observed before (1). Indeed, northern blot analysis during the preceding study showed a lack of viral RNA after unassisted G_{I3}-2 LNA mixmer delivery. However, this analysis was performed at 6 dpi and even the 2 kb HIV-1 class, which is composed of mainly G_{I3}-2 LNA mixmer-untargeted viral transcripts, was completely absence. Hence, this lack of HIV-1 RNA after performed

northern blot analysis could also be due a different way of HIV-1 inhibition, which simply suppresses viral replication.

While investigating what else may cause the described HIV-1 inhibition, if not targeted RNA degradation, RT-qPCR analysis demonstrated that the level of HIV-1 RNA is for the first time significantly reduced three days after unassisted G_{I3}-2 LNA mixmer delivery (Fig. 3.15). Subsequent G_{I3}-2 LNA mixmer-unaffected RT-qPCR analysis on the HIV-1 Tat/Vpr RNA ratio indicated that induced splice switching by masking of the G_{I3}-2 SRE is causing the HIV-1 inhibition (Fig. 3.16). Importantly, mediated splice switching by ASOs in mixmer design is a well-known phenomenon that is, for instance, harnessed by the FDA-approved drug Nusinersen, which targets an SRE to influence splice site usage during *SMN2* pre-mRNA processing (45, 200). In addition, mutating the G_{I3}-2 SRE was shown to interfere with HIV-1 replication in the same way (44). Therefore, the G_{I3}-2 LNA mixmer most likely interferes with viral pre-mRNA splicing and this causes its inhibitory effect on HIV-1 replication after unassisted delivery.

Arguing that any inhibitory effect on HIV-1 replication may influence the ratio of HIV-1 RNA transcripts over the course of 3 dpi, a simplified model system was established based on replication-incompetent lentiviral vectors. However, by performing transcript-specific RT-qPCR analysis, it became evident that although overall G_{I3}-2 LNA mixmer-induced splice switching was suggested, unassisted G_{I3}-2 LNA mixmer delivery affected pre-mRNA splicing differently as compared to during HIV-1 infection (Fig. 3.18 and 3.20). Given the complex nature of HIV-1 pre-mRNA splicing, which is dependent on several splice sites concomitant many SREs (reviewed in (142), the aberrant landscape of HIV-1 splice sites and SREs in this simplified model system most likely is responsible that masking the HIV-1 G_{I3}-2 in this case presumably increased splice acceptor 3 usage while it seemed to decrease usage of splice acceptor 4a and 4b.

Interestingly, using this model system, the activity of the SFFV-U3 promoter was shown to be increased 2.3-fold by the expression of HIV-1-Tat (Fig. 3.19). HIV-1 Tat is known to upregulate different cellular genes by activation of host transcription factors, which might affect also SFFV U3 promoter activity (reviewed in (203)). On the other hand, SFFV U3 is a retroviral promoter element. Hence, the HIV-1 Tat-induced upregulation of SFFV U3 promoter activity may be also explained by HIV-1 Tat binding to a secondary structure similar to the HIV-1 TAR within the SFFV U3 promoter.

To this point, the used T-cell lines allowed efficient inhibition of viral replication by unassisted delivery of LNA mixmers targeting viral SREs, but the previously IAV-infected CaCo-2 cells did not. Hence, a T-cell type-specific effect on LNA mixmer activity was subsequently investigated by LNA mixmer treatment also of the HIV-1-infected monocyte-like THP-1 cells and the epithelial TZM-bl cells. Unlike the HIV-1-infected T-cell lines, neither of these two additional

cell lines allowed inhibition of HIV-1 replication over 3 dpi (Fig. 3.21). These observations strongly suggested some kind of T-cell specific susceptibility to unassisted LNA mixmer delivery. Such a conclusion is consistent with the assumption that the productive pathway of PS-modified ASOs uptake is more accessible in certain cell lines/types as described before (35). Interestingly, however, Zhang et al. could achieve LNA mixmer-induced splice switching in their HeLa cell-derived GFP-based reporter cell line after unassisted delivery (200). Although, at first sight, this may contradict the lack of HIV-1 inhibition observed after unassisted G_{I3}-2 LNA mixmer delivery to the HeLa cell-derived TZM-bl cells, it may be possible that the GFP-based reporter cell line used in the described study was simply more sensitive to LNA mixmer-induced splice switching.

To expand the analysis on the presumed high productive uptake of LNA mixmers by T-cells, cellular *CENPJ* was selected as HIV-1-independent reporter gene to test LNA mixmer activity. As expected, only in the employed Jurkat T-cells and not in the used RPE cells, unassisted LNA mixmer delivery mediated aberrant splicing of the *CENPJ* pre-mRNA (Fig. 3.23). In line with this, another study that tested the activity of LNA gapmers after unassisted delivery to primary T-cells and T-cell lines also found profound ASO activity in these cells (204). Unfortunately, the authors did not compare different cell types, but exclusively focused on LNA gapmer activity in T-cells (204).

Overall, different proteins and complexes like epidermal growth factor receptor (EGFR) Golgi-58K, M6PR, coat protein complex II were brought in connection with the productive ASO uptake in the past ((49, 51, 205, 206) and reviewed in (207)). How these proteins and complexes are differentially expressed between different cell types, however, was not yet elucidated. Based on the data obtained in this thesis, it may be possible that an increased expression of some of these host factors of the productive ASO uptake may contribute to the observed higher susceptibility of T-cells to unassisted ASO delivery. In addition, a perinuclear localization of endosomes was found to enhance PS-ASO activity (50). Hence, it may also be speculated that the intracellular arrangement of the endosome may favor the productive ASO pathway in T-cells.

Although not yet characterized, a high frequency of productive PS-ASO uptake in T-cells still may contribute to future therapeutics. For instance, higher rates of interleukin 7 receptor (*IL7R*) exon 6 exclusion in T-cells, which occurs more often in individuals harboring the SNP rs6897932 (SNP database (dbSNP) of NIH), is associated with multiple sclerosis and type 1 diabetes (208, 209). Very recently, SRE-targeting phosphorodiamidate morpholino-modified ASOs, which make up a different class of ASOs besides the PS- and 2'ribose-modified ASOs, were used to mediate *IL7R* exon 6 inclusion (210). This study, however, used very high concentrations of these so-called *morpholinos* and applied them either via transfection (HeLa cells) or nucleofection (primary CD4$^+$ T-cells) (210).

Interestingly, of the three anti-CENPJ LNA mixmer tested, only the CENPJ DownS LNA induced aberrant splicing of the *CENPJ* pre-mRNA after unassisted delivery (Fig. 3.23). The CENPJ DownS LNA does not target the *CENPJ* exon 12 splice acceptor dinucleotide or the upstream located polypyrimidine tract, which is also important for splice site usage, as opposed to the CENPJ SA and CENPJ UpS LNA, respectively. Hence, it was concluded that the CENPJ DownS LNA masks an SRE, which regulates usage of the *CENPJ* exon 12 splice acceptor, an observation, which is also consistent with the HEXplorer-predicted SRE landscape (Fig. S.1). Such a masking would also be according to the literature showing that due to position-dependent effects, SR protein binding downstream of splice acceptor sites supports splice acceptor site usage (211). Overall, therefore, the obtained data set on the CENPJ DownS LNA-induced splice switching during *CENPJ* pre-mRNA processing likely revealed a novel SRE within the *CENPJ* gene that stretches from *CENPJ* nucleotide positions 42,281 – 42,297.

Still, it remains puzzling why the CENPJ SA and CENPJ UpS LNA did not interfere with CENPJ splice site usage after unassisted delivery whereas the CENPJ DownS did (Fig. 3.23). Notably, it was shown that the ASO sequence alone constitutes an important factor for protein binding affinity (43). Hence, simply the sequence of nucleobases within the anti-CENPJ LNA mixmers may contribute to this discrepancy by preventing access to the LNA mixmer target RNA after unassisted delivery. However, unpublished data by Dr. Frank Hillebrand likewise showed a lack of ASO activity for an LNA mixmer targeting HIV-1 splice donor site 4, whereas LNA mixmers targeting viral SREs G_{I3}-2, ESE_{tat} and GAR-ESE exhibited profound antiviral activity after unassisted delivery to T-cells ((1) and unpublished data, Dr. Frank Hillebrand, Institute of Virology, University Hospital Düsseldorf). Therefore, the involvement of several helicases or other processes during splicing may render splice sites inaccessible or rather hard-to-target, because bound ASOs may be efficiently removed from the pre-mRNA (212). Consequently, SRE-targeting ASOs may be preferred over splice site-targeting ASOs when aiming at induced splice switching after unassisted delivery in the future. However, more data is necessary to confirm such an effect.

To this point, HIV-1 replication was inhibited only by LNA mixmers targeting viral SREs (Fig. 3.15 and (1)). With the aim to investigate the overall potential of LNA mixmers as antivirals, additional target sites within the HIV-1 genome were considered. Based on the conclusion that LNA mixmers exert their activity within the nucleus after unassisted delivery to T-cells, the HIV-1 Rev-dependent nuclear RNA export was targeted. In an HIV-1-based reporter system, transfection of TZM-bl cells with the SLIIb LNA mixmer, which masks the HIV-1 RRE SLIIb sequence, indicated successful interference with the Rev-dependent nuclear export of intron-containing RNA (Fig. 3.25, 3.26). Finally, unassisted delivery also of the SLIIb LNA mixmer to HIV-1 infected cells indicated antiviral activity in T-cells, but not in infected monocyte-like THP-1 and TZM-bl epithelial cells (Fig. 3.27). Overall, these experiments, again,

substantiate the idea that T-cells exhibit a characteristic high rate of productive LNA mixmer uptake (Fig. 4.1).
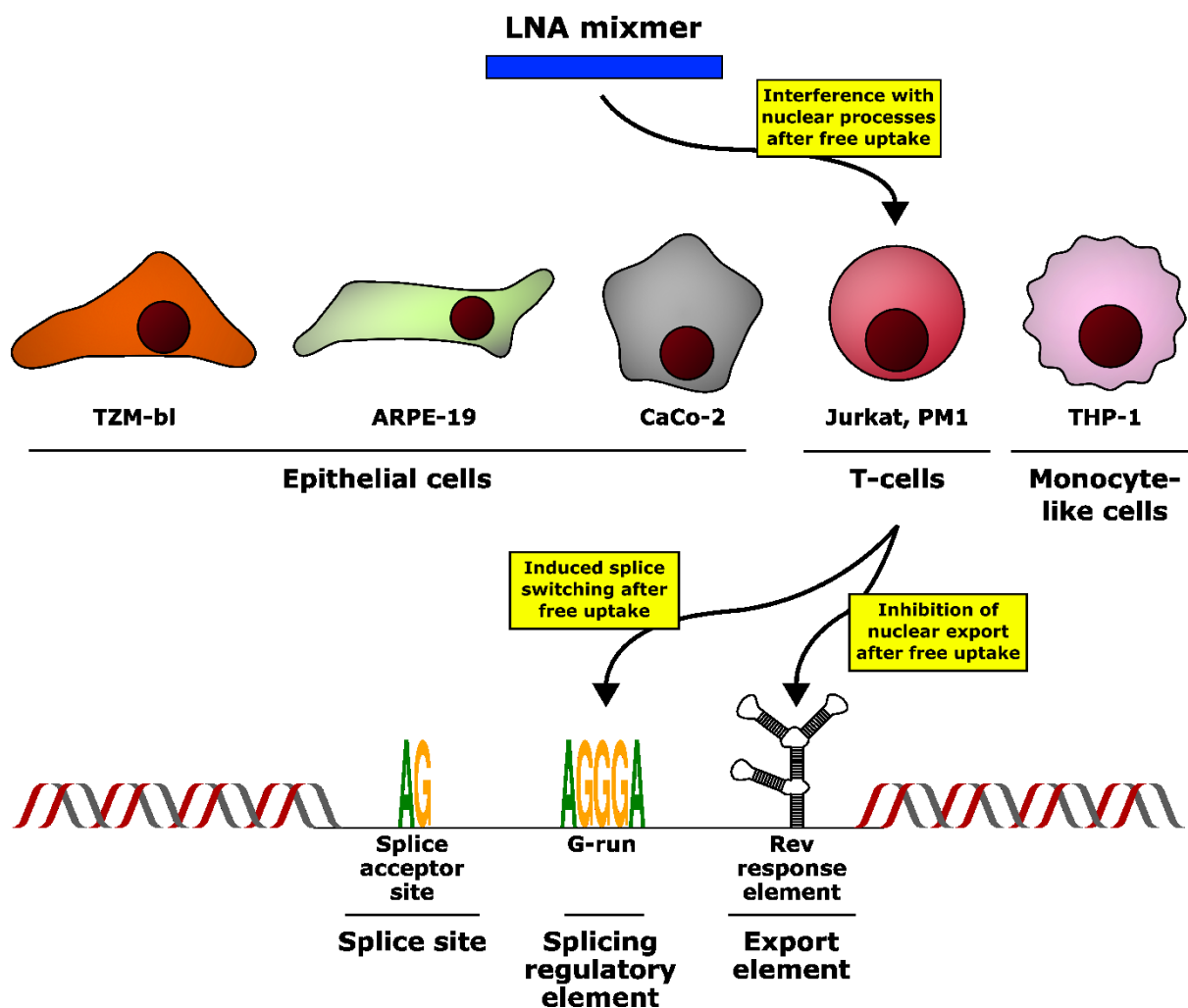
Fig. 4.1 Schematic summarizing the particular susceptibility of T-cells to unassisted LNA mixmer delivery revealed during this thesis. Interference with nuclear processes after unassisted LNA mixmer delivery was to this point only observed in T-cells indicating some sort of cell type specificity. In the context of nuclear processes, interference after unassisted LNA mixmer delivery was only indicated while targeting splicing regulatory elements or export elements, but not splice sites.

However, the performed transfection and infection experiments do not provide complete certainty that the applied SLIIb LNA mixmer interferes with HIV-1 Rev binding to the RRE within the nucleus. Other possibilities like steric hindrance of HIV-1 env translation may likewise cause the observed lower fusion rate of transfected TZM-bl cells and the decreased amount of viral RNA in infected T-cells at 2 dpi. Nevertheless, based on the preceding experiments on G_{I3}-2 LNA mixmer function and CENPJ splicing, SLIIb-mediated interference with the HIV-1 Rev-RRE-mediated nuclear RNA export is likely to occur. Yet, more experiments that may involve cellular fractionation assays are needed to gain certainty about an SLIIb LNA mixmer-induced inhibition of the HIV-1 Rev-dependent nuclear RNA export.

Although the HIV-1 RRE SLIIb offers a promising target for LNA mixmer-mediated inhibition of HIV-1 replication, its sequence is not well conserved among HIV-1 subtypes or even just within HIV-1 subtype B, to which the here used HIV-1 NL4-3 laboratory strain belongs (Tab 4.1). In addition, also the so far analyzed viral SREs are not well conserved, with the G_{I3}-2 LNA mixmer binding site exhibiting the highest conservation rate of about 20 % among the different HIV-1 subtypes.

Tab 4.1 Conservation rates of the different LNA mixmers that were shown to exhibit anti-HIV-1 activity after unassisted delivery to T-cells.

HIV-1 LNA Mixmer	Location of target site (HXB2 reference genome)	Conservation rate [%]	
		All HIV-1 subtypes[a]	HIV-1 subtype B[b]
ESE$_{tat}$ LNA[c]	5587 - 5602	9.55	27.26
G_{I3}-2 LNA	5815 - 5830	19.99	41.46
SLIIb LNA	7815 - 7830	5.81	15.87

[a]Total of 3666 sequences analyzed. [b]Total of 1071 sequences analyzed. All data from Los Alamos HIV sequence database (http://www.hiv.lanl.gov/). [c]LNA mixmer published in (1)

In summary, unassisted LNA mixmer delivery did not achieve inhibition of cytoplasmic (+)ssRNA virus SARS-CoV-2, cytoplasmic (-)ssRNA virus HAZV nor the nuclear replicating (-)ssRNA virus IAV, although anti-HIV-1 LNA mixmer activity was strongly suggested to occur within the nucleus. However, in this respect, T-cells were shown to exhibit a particular high rate of productive LNA mixmer uptake that enables efficient interference with pre-mRNA splicing, but perhaps only when targeting SREs but not splice sites directly. The obtained data from this thesis may therefore be used to on one hand improve antiretroviral therapy against T-cell-tropic viruses like HIV-1 or the also important viral pathogen HTLV-1 as well as to approach other diseases associated with aberrant splicing in T-cells like the described autoimmune conditions multiple sclerosis and type 1 diabetes (213, 214).

List of abbreviations

μl	Microliter
μM	Micromolar
2'-MOE	2'-Methoxyethyl
2'-OMe	2'-O-methyl
ACE2	Angiotensin-converting enzyme 2
AIDS	Acquired immunodeficiency syndrome
ART	Antiretroviral therapy
ASO	Antisense oligonucleotide
CA	Capsid protein
cART	Combined antiretroviral therapy
CCHF	Crimean-Congo hemorrhagic fever
CCHFV	Crimean-Congo hemorrhagic fever virus
CCR5	C-C chemokine receptor type 5
CD4	Cluster of Differentiation 4 protein
CDC	Centers for Disease Control and Prevention
CENPJ	Centromere Protein J
CMV	Cytomegalovirus
CNS	Central nervous system
COVID-19	Coronavirus disease 2019
CPE	Cytopathic effect
CRM1	Exportin 1 (XPO1)
CRS	*cis*-acting repressive sequence
CXCR4	C-X-C chemokine receptor type 4
DMV	Double membrane vesicle
Dpi	Days post-infection
eGFP	Enhanced greed fluorescent protein
Env	Envelope
ESCRT	Endosomal sorting complex required for transport
FDA	U.S. Food and Drug Administration
GalNAc	*N*-Acetylgalactosamine
Gc	Glycoprotein C
Gn	Glycoprotein N
GP	Glycoprotein

GPC	Glycoprotein precurser
HA	Hemagglutinin
HAART	Highly active antiretroviral therapy
HAZV	Hazara virus
HIV-1	Human immunodeficiency virus 1
Hpi	Hours post-infection
HSV	Herpes Simplex Virus
HTLV-1	Primate T-lymphotropic virus 1
IAV	Influenza A virus
IN	Integrase
Kb	Kilobase
LNA	Locked nucleic acid
LTR	Long terminal repeat
MA	Matrix protein
mAb	Monoclonal antibody
mRNA	messenger RNA
NA	Neuraminidase
NC	Nucleocapsid protein
NEP	Nuclear export protein
NLS	Nuclear localization signal
nm	Nanometer
Np	Nucleoprotein
Nsp	Non-structural protein
ORF	Open reading frame
PA	Polymerase acidic protein
PB1	Polymerase basic protein 1
PB2	Polymerase basic protein 2
PE	Promoter element
PFU	Plaque-forming units
PMO	Phosphorodiamidate morpholino oligonucleotide
Pol	Polymerase gene encoding RT, IN and Pro
Pr55^{Gag}	Gag precursor protein (55 kDa)
PS	Phosphorothioate
RdRp	RNA-dependent RNA polymerase
Rev	Regulator of expression of viral protein

RKI	Robert Koch Institut
RPE	Retina epithelial cells
RRE	Rev response element
RT	Reverse Transcriptase
RT-PCR	Reverse transcription PCR
RT-qPCR	Reverse transcription quantitative PCR
SA	Splice acceptor site
SARS-CoV-2	Severe acute respiratory syndrome coronavirus type 2
SD	Splice donor site
SFFV	Spleen focus-forming virus
siRNA	small interfering RNA
SLIIb	Stem loop IIb
SMN2	Survival of motor neuron 2
SRE	Splicing regulatory elements
SRP	Splicing regulatory protein
TAR	Transactivation response element
Tat	Transactivator of transcription
TEM	Transmission electron microscopy
TMRPSS2	Transmembrane serine protease 2
TRS-B	Transcription regulating sequence body
TRS-L	Transcription regulating sequence leader
UTR	Untranslated region
VOC	Variant of concern
WHO	World Health Organization

Literature

1. Hillebrand F, Ostermann PN, Müller L, Degrandi D, Erkelenz S, Widera M, Pfeffer K, Schaal H. 2019. Gymnotic Delivery of LNA Mixmers Targeting Viral SREs Induces HIV-1 mRNA Degradation. Int J Mol Sci 20.
2. Flint SJ, Racaniello VR, Rall GF, Skalka AM, Enquist LW. 2015. Principles of virology, 4th edition. ed. ASM Press, Washington, DC.
3. King DH. 1988. History, pharmacokinetics, and pharmacology of acyclovir. J Am Acad Dermatol 18:176-9.
4. Yarchoan R, Klecker RW, Weinhold KJ, Markham PD, Lyerly HK, Durack DT, Gelmann E, Lehrman SN, Blum RM, Barry DW. 1986. Administration of 3'-azido-3'-deoxythymidine, an inhibitor of HTLV-III/LAV replication, to patients with AIDS or AIDS-related complex. Lancet 1:575-80.
5. Di Marco L, La Mantia C, Di Marco V. 2022. Hepatitis C: Standard of Treatment and What to Do for Global Elimination. Viruses 14.
6. Guvenir M, Arikan A. 2020. Hepatitis B Virus: From Diagnosis to Treatment. Pol J Microbiol 69:391-399.
7. Pantaleo G, Correia B, Fenwick C, Joo VS, Perez L. 2022. Antibodies to combat viral infections: development strategies and progress. Nat Rev Drug Discov.
8. Rossignol E, Alter G, Julg B. 2021. Antibodies for Human Immunodeficiency Virus-1 Cure Strategies. J Infect Dis 223:22-31.
9. Frame JD, Verbrugge GP, Gill RG, Pinneo L. 1984. The use of Lassa fever convalescent plasma in Nigeria. Trans R Soc Trop Med Hyg 78:319-24.
10. Ruck T, Barman S, Schulte-Mecklenbeck A, Pfeuffer S, Steffen F, Nelke C, Schroeter CB, Willison A, Heming M, Müntefering T, Melzer N, Krämer J, Lindner M, Riepenhausen M, Gross CC, Klotz L, Bittner S, Muraro PA, Schneider-Hohendorf T, Schwab N, Meyer Zu Hörste G, Goebels N, Meuth SG, Wiendl H. 2022. Alemtuzumab-induced immune phenotype and repertoire changes: implications for secondary autoimmunity. Brain 145:1711-1725.
11. Beuerlein KG, Martin ED, Strowd LC. 2022. Interstitial Granulomatous Dermatitis as an Adverse Reaction to Vedolizumab. Cutis 109:167-169.
12. Jensen B, Luebke N, Feldt T, Keitel V, Brandenburger T, Kindgen-Milles D, Lutterbeck M, Freise NF, Schoeler D, Haas R, Dilthey A, Adams O, Walker A, Timm J, Luedde T. 2021. Emergence of the E484K mutation in SARS-COV-2-infected immunocompromised patients treated with bamlanivimab in Germany. Lancet Reg Health Eur 8:100164.
13. Ali MG, Zhang Z, Gao Q, Pan M, Rowan EG, Zhang J. 2020. Recent advances in therapeutic applications of neutralizing antibodies for virus infections: an overview. Immunol Res 68:325-339.
14. Renegar KB, Small PA. 1991. Passive transfer of local immunity to influenza virus infection by IgA antibody. J Immunol 146:1972-8.
15. Jahrling PB, Peters CJ. 1984. Passive antibody therapy of Lassa fever in cynomolgus monkeys: importance of neutralizing antibody and Lassa virus strain. Infect Immun 44:528-33.
16. Abeldaño Zuñiga RA, González-Villoria RAM, Elizondo MV, Osorio AYN, Martínez DG, Coca SM. 2021. Clinical effectiveness of convalescent plasma in hospitalized patients with COVID-19: a systematic review and meta-analysis. Ther Adv Respir Dis 15:17534666211028077.
17. Kirenga B, Byakika-Kibwika P, Muttamba W, Kayongo A, Loryndah NO, Mugenyi L, Kiwanuka N, Lusiba J, Atukunda A, Mugume R, Ssali F, Ddungu H, Katagira W, Sekibira R, Kityo C, Kyeyune D, Acana S, Aanyu-Tukamuhebwa H, Kabweru W, Nakwagala F, Bagaya BS, Kimuli I, Nantanda R, Buregyeya E, Byarugaba B, Olaro C, Mwebesa H, Joloba ML, Siddharthan T, Bazeyo W. 2021. Efficacy of convalescent plasma for treatment of COVID-19 in Uganda. BMJ Open Respir Res 8.

18. Keitel V, Bode JG, Feldt T, Walker A, Müller L, Kunstein A, Klindt C, Killer A, Senff T, Timm J, Ostermann P, Damagnez M, Lübke N, Adams O, Schaal H, Antoch G, Neubert J, Albrecht P, Meuth S, Elben S, Mohring A, Fischer JC, Bölke E, Hoenig M, Schulz AS, Luedde T, Jensen B. 2021. Case Report: Convalescent Plasma Achieves SARS-CoV-2 Viral Clearance in a Patient With Persistently High Viral Replication Over 8 Weeks Due to Severe Combined Immunodeficiency (SCID) and Graft Failure. Front Immunol 12:645989.

19. Marwick C. 1998. First "antisense" drug will treat CMV retinitis. JAMA 280:871.

20. Stein CA, Castanotto D. 2017. FDA-Approved Oligonucleotide Therapies in 2017. Mol Ther 25:1069-1075.

21. Zamecnik PC, Stephenson ML. 1978. Inhibition of Rous sarcoma virus replication and cell transformation by a specific oligodeoxynucleotide. Proc Natl Acad Sci U S A 75:280-4.

22. Crooke ST. 1999. Molecular mechanisms of action of antisense drugs. Biochim Biophys Acta 1489:31-44.

23. Radvánszka M, Paul ED, Hajdu R, Boršová K, Kováčová V, Putaj P, Bírová S, Čirková I, Čarnecký M, Buranovská K, Szobi A, Vojtaššáková N, Drobná D, Čabanová V, Sláviková M, Ličková M, Vaňová V, Fumačová Havlíková S, Lukáčiková Ľ, Kajanová I, Koči J, Rusňáková D, Sedláčková T, Max KEA, Tuschl T, Szemes T, Klempa B, Čekan P. 2022. Sequential development of several RT-qPCR tests using LNA nucleotides and dual probe technology to differentiate SARS-CoV-2 from influenza A and B. Microb Biotechnol.

24. Durand M, Thibault P, Lévesque S, Brault A, Carignan A, Valiquette L, Martin P, Labbé S. 2022. Detection of severe acute respiratory syndrome coronavirus 2 (SARS-CoV-2) and its first variants in fourplex real-time quantitative reverse transcription-PCR assays. Microb Cell 9:1-20.

25. Juliano RL. 2016. The delivery of therapeutic oligonucleotides. Nucleic Acids Res 44:6518-48.

26. Kurreck J. 2003. Antisense technologies. Improvement through novel chemical modifications. Eur J Biochem 270:1628-44.

27. Crooke ST, Witztum JL, Bennett CF, Baker BF. 2018. RNA-Targeted Therapeutics. Cell Metab 27:714-739.

28. Janssen HL, Reesink HW, Lawitz EJ, Zeuzem S, Rodriguez-Torres M, Patel K, van der Meer AJ, Patick AK, Chen A, Zhou Y, Persson R, King BD, Kauppinen S, Levin AA, Hodges MR. 2013. Treatment of HCV infection by targeting microRNA. N Engl J Med 368:1685-94.

29. Kinberger GA, Prakash TP, Yu J, Vasquez G, Low A, Chappell A, Schmidt K, Murray HM, Gaus H, Swayze EE, Seth PP. 2016. Conjugation of mono and di-GalNAc sugars enhances the potency of antisense oligonucleotides via ASGR mediated delivery to hepatocytes. Bioorg Med Chem Lett 26:3690-3.

30. Stockert RJ. 1995. The asialoglycoprotein receptor: relationships between structure, function, and expression. Physiol Rev 75:591-609.

31. Schmidt K, Prakash TP, Donner AJ, Kinberger GA, Gaus HJ, Low A, Østergaard ME, Bell M, Swayze EE, Seth PP. 2017. Characterizing the effect of GalNAc and phosphorothioate backbone on binding of antisense oligonucleotides to the asialoglycoprotein receptor. Nucleic Acids Res 45:2294-2306.

32. Prakash TP, Graham MJ, Yu J, Carty R, Low A, Chappell A, Schmidt K, Zhao C, Aghajan M, Murray HF, Riney S, Booten SL, Murray SF, Gaus H, Crosby J, Lima WF, Guo S, Monia BP, Swayze EE, Seth PP. 2014. Targeted delivery of antisense oligonucleotides to hepatocytes using triantennary N-acetyl galactosamine improves potency 10-fold in mice. Nucleic Acids Res 42:8796-807.

33. Heasman J. 2002. Morpholino oligos: making sense of antisense? Dev Biol 243:209-14.

34. Levin AA. 1999. A review of the issues in the pharmacokinetics and toxicology of phosphorothioate antisense oligonucleotides. Biochim Biophys Acta 1489:69-84.

35. Stein CA, Hansen JB, Lai J, Wu S, Voskresenskiy A, Høg A, Worm J, Hedtjärn M, Souleimanian N, Miller P, Soifer HS, Castanotto D, Benimetskaya L, Ørum H, Koch T. 2010. Efficient gene

silencing by delivery of locked nucleic acid antisense oligonucleotides, unassisted by transfection reagents. Nucleic Acids Res 38:e3.

36. Castanotto D, Zhang X, Alluin J, Rüger J, Armstrong B, Rossi J, Riggs A, Stein CA. 2018. A stress-induced response complex (SIRC) shuttles miRNAs, siRNAs, and oligonucleotides to the nucleus. Proc Natl Acad Sci U S A.

37. Scoles DR, Minikel EV, Pulst SM. 2019. Antisense oligonucleotides: A primer. Neurol Genet 5:e323.

38. Kurreck J, Wyszko E, Gillen C, Erdmann VA. 2002. Design of antisense oligonucleotides stabilized by locked nucleic acids. Nucleic Acids Res 30:1911-8.

39. Hagedorn PH, Persson R, Funder ED, Albæk N, Diemer SL, Hansen DJ, Møller MR, Papargyri N, Christiansen H, Hansen BR, Hansen HF, Jensen MA, Koch T. 2018. Locked nucleic acid: modality, diversity, and drug discovery. Drug Discov Today 23:101-114.

40. Grünweller A, Hartmann RK. 2007. Locked nucleic acid oligonucleotides: the next generation of antisense agents? BioDrugs 21:235-43.

41. Liang XH, Sun H, Nichols JG, Crooke ST. 2017. RNase H1-Dependent Antisense Oligonucleotides Are Robustly Active in Directing RNA Cleavage in Both the Cytoplasm and the Nucleus. Mol Ther 25:2075-2092.

42. Wahlestedt C, Salmi P, Good L, Kela J, Johnsson T, Hökfelt T, Broberger C, Porreca F, Lai J, Ren K, Ossipov M, Koshkin A, Jakobsen N, Skouv J, Oerum H, Jacobsen MH, Wengel J. 2000. Potent and nontoxic antisense oligonucleotides containing locked nucleic acids. Proc Natl Acad Sci U S A 97:5633-8.

43. Vickers TA, Crooke ST. 2016. Development of a Quantitative BRET Affinity Assay for Nucleic Acid-Protein Interactions. PLoS One 11:e0161930.

44. Widera M, Hillebrand F, Erkelenz S, Vasudevan AA, Münk C, Schaal H. 2014. A functional conserved intronic G run in HIV-1 intron 3 is critical to counteract APOBEC3G-mediated host restriction. Retrovirology 11:72.

45. Rigo F, Hua Y, Krainer AR, Bennett CF. 2012. Antisense-based therapy for the treatment of spinal muscular atrophy. J Cell Biol 199:21-5.

46. Khorkova O, Wahlestedt C. 2017. Oligonucleotide therapies for disorders of the nervous system. Nat Biotechnol 35:249-263.

47. Hua Y, Vickers TA, Okunola HL, Bennett CF, Krainer AR. 2008. Antisense masking of an hnRNP A1/A2 intronic splicing silencer corrects SMN2 splicing in transgenic mice. Am J Hum Genet 82:834-48.

48. Crooke ST, Wang S, Vickers TA, Shen W, Liang XH. 2017. Cellular uptake and trafficking of antisense oligonucleotides. Nat Biotechnol 35:230-237.

49. Liang XH, Nichols JG, De Hoyos CL, Sun H, Zhang L, Crooke ST. 2021. Golgi-58K can re-localize to late endosomes upon cellular uptake of PS-ASOs and facilitates endosomal release of ASOs. Nucleic Acids Res 49:8277-8293.

50. Liang XH, Nichols JG, Tejera D, Crooke ST. 2021. Perinuclear positioning of endosomes can affect PS-ASO activities. Nucleic Acids Res 49:12970-12985.

51. Liang XH, Sun H, Hsu CW, Nichols JG, Vickers TA, De Hoyos CL, Crooke ST. 2020. Golgi-endosome transport mediated by M6PR facilitates release of antisense oligonucleotides from endosomes. Nucleic Acids Res 48:1372-1391.

52. Liang XH, Sun H, Shen W, Crooke ST. 2015. Identification and characterization of intracellular proteins that bind oligonucleotides with phosphorothioate linkages. Nucleic Acids Res 43:2927-45.

53. Cui J, Li F, Shi ZL. 2019. Origin and evolution of pathogenic coronaviruses. Nat Rev Microbiol 17:181-192.

54. Wu F, Zhao S, Yu B, Chen YM, Wang W, Song ZG, Hu Y, Tao ZW, Tian JH, Pei YY, Yuan ML, Zhang YL, Dai FH, Liu Y, Wang QM, Zheng JJ, Xu L, Holmes EC, Zhang YZ. 2020. A new coronavirus associated with human respiratory disease in China. Nature 579:265-269.

55. Zhu N, Zhang D, Wang W, Li X, Yang B, Song J, Zhao X, Huang B, Shi W, Lu R, Niu P, Zhan F, Ma X, Wang D, Xu W, Wu G, Gao GF, Tan W, Team CNCIaR. 2020. A Novel Coronavirus from Patients with Pneumonia in China, 2019. N Engl J Med 382:727-733.

56. Dong E, Du H, Gardner L. 2020. An interactive web-based dashboard to track COVID-19 in real time. Lancet Infect Dis 20:533-534.

57. Dong E, Du H, Gardner L. 2020. An interactive web-based dashboard to track COVID-19 in real time. Lancet Infect Dis.

58. Müller L, Ostermann PN, Walker A, Wienemann T, Mertens A, Adams O, Andree M, Hauka S, Lübke N, Keitel V, Drexler I, Di Cristanziano V, Hermsen DF, Kaiser R, Boege F, Klein F, Schaal H, Timm J, Senff T. 2021. Sensitivity of anti-SARS-CoV-2 serological assays in a high-prevalence setting. Eur J Clin Microbiol Infect Dis.

59. Jackson LA, Anderson EJ, Rouphael NG, Roberts PC, Makhene M, Coler RN, McCullough MP, Chappell JD, Denison MR, Stevens LJ, Pruijssers AJ, McDermott A, Flach B, Doria-Rose NA, Corbett KS, Morabito KM, O'Dell S, Schmidt SD, Swanson PA, Padilla M, Mascola JR, Neuzil KM, Bennett H, Sun W, Peters E, Makowski M, Albert J, Cross K, Buchanan W, Pikaart-Tautges R, Ledgerwood JE, Graham BS, Beigel JH, Group m-S. 2020. An mRNA Vaccine against SARS-CoV-2 - Preliminary Report. N Engl J Med 383:1920-1931.

60. Polack FP, Thomas SJ, Kitchin N, Absalon J, Gurtman A, Lockhart S, Perez JL, Pérez Marc G, Moreira ED, Zerbini C, Bailey R, Swanson KA, Roychoudhury S, Koury K, Li P, Kalina WV, Cooper D, Frenck RW, Hammitt LL, Türeci Ö, Nell H, Schaefer A, Ünal S, Tresnan DB, Mather S, Dormitzer PR, Şahin U, Jansen KU, Gruber WC, Group CCT. 2020. Safety and Efficacy of the BNT162b2 mRNA Covid-19 Vaccine. N Engl J Med 383:2603-2615.

61. Voysey M, Clemens SAC, Madhi SA, Weckx LY, Folegatti PM, Aley PK, Angus B, Baillie VL, Barnabas SL, Bhorat QE, Bibi S, Briner C, Cicconi P, Collins AM, Colin-Jones R, Cutland CL, Darton TC, Dheda K, Duncan CJA, Emary KRW, Ewer KJ, Fairlie L, Faust SN, Feng S, Ferreira DM, Finn A, Goodman AL, Green CM, Green CA, Heath PT, Hill C, Hill H, Hirsch I, Hodgson SHC, Izu A, Jackson S, Jenkin D, Joe CCD, Kerridge S, Koen A, Kwatra G, Lazarus R, Lawrie AM, Lelliott A, Libri V, Lillie PJ, Mallory R, Mendes AVA, Milan EP, Minassian AM, et al. 2021. Safety and efficacy of the ChAdOx1 nCoV-19 vaccine (AZD1222) against SARS-CoV-2: an interim analysis of four randomised controlled trials in Brazil, South Africa, and the UK. Lancet 397:99-111.

62. Amanat F, Krammer F. 2020. SARS-CoV-2 Vaccines: Status Report. Immunity 52:583-589.

63. Liu Y, Liu J, Plante KS, Plante JA, Xie X, Zhang X, Ku Z, An Z, Scharton D, Schindewolf C, Widen SG, Menachery VD, Shi PY, Weaver SC. 2021. The N501Y spike substitution enhances SARS-CoV-2 infection and transmission. Nature.

64. Syed AM, Taha TY, Tabata T, Chen IP, Ciling A, Khalid MM, Sreekumar B, Chen PY, Hayashi JM, Soczek KM, Ott M, Doudna JA. 2021. Rapid assessment of SARS-CoV-2-evolved variants using virus-like particles. Science 374:1626-1632.

65. Ulrich L, Halwe NJ, Taddeo A, Ebert N, Schön J, Devisme C, Trüeb BS, Hoffmann B, Wider M, Fan X, Bekliz M, Essaidi-Laziosi M, Schmidt ML, Niemeyer D, Corman VM, Kraft A, Godel A, Laloli L, Kelly JN, Calderon BM, Breithaupt A, Wylezich C, Veiga IB, Gultom M, Osman S, Zhou B, Adea K, Meyer B, Eberhardt C, Thomann L, Gsell M, Labroussaa F, Jores J, Summerfield A, Drosten C, Eckerle IA, Wentworth DE, Dijkman R, Hoffmann D, Thiel V, Beer M, Benarafa C. 2021. Enhanced fitness of SARS-CoV-2 variant of concern Alpha but not Beta. Nature.

66. Müller L, Andrée M, Ostermann PN, Jazmati N, Flüh G, Fischer JC, Bölke E, Heger E, Vanshylla K, Klein F, Wisplinghoff H, Schaal H, Drexler I, Walker A, Adams O, Timm J. 2021. SARS-CoV-2 Infection in Fully Vaccinated Individuals of Old Age Strongly Boosts the Humoral Immune Response. Front Med (Lausanne) 8:746644.

67. Dejnirattisai W, Shaw RH, Supasa P, Liu C, Stuart AS, Pollard AJ, Liu X, Lambe T, Crook D, Stuart DI, Mongkolsapaya J, Nguyen-Van-Tam JS, Snape MD, Screaton GR. 2021. Reduced neutralisation of SARS-CoV-2 omicron B.1.1.529 variant by post-immunisation serum. Lancet.

68. Thorne LG, Bouhaddou M, Reuschl AK, Zuliani-Alvarez L, Polacco B, Pelin A, Batra J, Whelan MVX, Hosmillo M, Fossati A, Ragazzini R, Jungreis I, Ummadi M, Rojc A, Turner J, Bischof ML,

Obernier K, Braberg H, Soucheray M, Richards A, Chen KH, Harjai B, Memon D, Hiatt J, Rosales R, McGovern BL, Jahun A, Fabius JM, White K, Goodfellow IG, Takeuchi Y, Bonfanti P, Shokat K, Jura N, Verba K, Noursadeghi M, Beltrao P, Kellis M, Swaney DL, García-Sastre A, Jolly C, Towers GJ, Krogan NJ. 2021. Evolution of enhanced innate immune evasion by SARS-CoV-2. Nature.

69.   Müller L, Andrée M, Moskorz W, Drexler I, Walotka L, Grothmann R, Ptok J, Hillebrandt J, Ritchie A, Rabl D, Ostermann PN, Robitzsch R, Hauka S, Walker A, Menne C, Grutza R, Timm J, Adams O, Schaal H. 2021. Age-dependent immune response to the Biontech/Pfizer BNT162b2 COVID-19 vaccination. Clin Infect Dis.

70.   Kolb T, Fischer S, Müller L, Lübke N, Hillebrandt J, Andrée M, Schmitz M, Schmidt C, Küçükköylü S, Koster L, Kittel M, Weiland L, Dreyling KW, Hetzel G, Adams O, Schaal H, Ivens K, Rump LC, Timm J, Stegbauer J. 2021. Impaired Immune Response to SARS-CoV-2 Vaccination in Dialysis Patients and in Kidney Transplant Recipients. Kidney360 2:1491.

71.   Huang C, Wang Y, Li X, Ren L, Zhao J, Hu Y, Zhang L, Fan G, Xu J, Gu X, Cheng Z, Yu T, Xia J, Wei Y, Wu W, Xie X, Yin W, Li H, Liu M, Xiao Y, Gao H, Guo L, Xie J, Wang G, Jiang R, Gao Z, Jin Q, Wang J, Cao B. 2020. Clinical features of patients infected with 2019 novel coronavirus in Wuhan, China. Lancet 395:497-506.

72.   Liotta EM, Batra A, Clark JR, Shlobin NA, Hoffman SC, Orban ZS, Koralnik IJ. 2020. Frequent neurologic manifestations and encephalopathy-associated morbidity in Covid-19 patients. Ann Clin Transl Neurol 7:2221-2230.

73.   Kim J, Hu C, Moufawad El Achkar C, Black LE, Douville J, Larson A, Pendergast MK, Goldkind SF, Lee EA, Kuniholm A, Soucy A, Vaze J, Belur NR, Fredriksen K, Stojkovska I, Tsytsykova A, Armant M, DiDonato RL, Choi J, Cornelissen L, Pereira LM, Augustine EF, Genetti CA, Dies K, Barton B, Williams L, Goodlett BD, Riley BL, Pasternak A, Berry ER, Pflock KA, Chu S, Reed C, Tyndall K, Agrawal PB, Beggs AH, Grant PE, Urion DK, Snyder RO, Waisbren SE, Poduri A, Park PJ, Patterson A, Biffi A, Mazzulli JR, Bodamer O, Berde CB, Yu TW. 2019. Patient-Customized Oligonucleotide Therapy for a Rare Genetic Disease. N Engl J Med 381:1644-1652.

74.   Baig AM. 2020. Neurological manifestations in COVID-19 caused by SARS-CoV-2. CNS Neurosci Ther 26:499-501.

75.   Mao L, Jin H, Wang M, Hu Y, Chen S, He Q, Chang J, Hong C, Zhou Y, Wang D, Miao X, Li Y, Hu B. 2020. Neurologic Manifestations of Hospitalized Patients With Coronavirus Disease 2019 in Wuhan, China. JAMA Neurol 77:683-690.

76.   Helms J, Kremer S, Merdji H, Clere-Jehl R, Schenck M, Kummerlen C, Collange O, Boulay C, Fafi-Kremer S, Ohana M, Anheim M, Meziani F. 2020. Neurologic Features in Severe SARS-CoV-2 Infection. N Engl J Med 382:2268-2270.

77.   Taquet M, Dercon Q, Luciano S, Geddes JR, Husain M, Harrison PJ. 2021. Incidence, co-occurrence, and evolution of long-COVID features: A 6-month retrospective cohort study of 273,618 survivors of COVID-19. PLoS Med 18:e1003773.

78.   Ceban F, Ling S, Lui LMW, Lee Y, Gill H, Teopiz KM, Rodrigues NB, Subramaniapillai M, Di Vincenzo JD, Cao B, Lin K, Mansur RB, Ho RC, Rosenblat JD, Miskowiak KW, Vinberg M, Maletic V, McIntyre RS. 2021. Fatigue and Cognitive Impairment in Post-COVID-19 Syndrome: A Systematic Review and Meta-Analysis. Brain Behav Immun.

79.   Parker AM, Brigham E, Connolly B, McPeake J, Agranovich AV, Kenes MT, Casey K, Reynolds C, Schmidt KFR, Kim SY, Kaplin A, Sevin CM, Brodsky MB, Turnbull AE. 2021. Addressing the post-acute sequelae of SARS-CoV-2 infection: a multidisciplinary model of care. Lancet Respir Med 9:1328-1341.

80.   Taquet M, Geddes JR, Husain M, Luciano S, Harrison PJ. 2021. 6-month neurological and psychiatric outcomes in 236 379 survivors of COVID-19: a retrospective cohort study using electronic health records. Lancet Psychiatry 8:416-427.

81.   Bar-On YM, Flamholz A, Phillips R, Milo R. 2020. SARS-CoV-2 (COVID-19) by the numbers. Elife 9.

82.   Masters PS. 2006. The molecular biology of coronaviruses. Adv Virus Res 66:193-292.

83. Hopfer H, Herzig MC, Gosert R, Menter T, Hench J, Tzankov A, Hirsch HH, Miller SE. 2021. Hunting coronavirus by transmission electron microscopy - a guide to SARS-CoV-2-associated ultrastructural pathology in COVID-19 tissues. Histopathology 78:358-370.

84. Jackson CB, Farzan M, Chen B, Choe H. 2022. Mechanisms of SARS-CoV-2 entry into cells. Nat Rev Mol Cell Biol 23:3-20.

85. Hoffmann M, Kleine-Weber H, Schroeder S, Krüger N, Herrler T, Erichsen S, Schiergens TS, Herrler G, Wu NH, Nitsche A, Müller MA, Drosten C, Pöhlmann S. 2020. SARS-CoV-2 Cell Entry Depends on ACE2 and TMPRSS2 and Is Blocked by a Clinically Proven Protease Inhibitor. Cell 181:271-280.e8.

86. Gu Y, Cao J, Zhang X, Gao H, Wang Y, Wang J, He J, Jiang X, Zhang J, Shen G, Yang J, Zheng X, Hu G, Zhu Y, Du S, Zhang R, Xu J, Lan F, Qu D, Xu G, Zhao Y, Gao D, Xie Y, Luo M, Lu Z. 2022. Receptome profiling identifies KREMEN1 and ASGR1 as alternative functional receptors of SARS-CoV-2. Cell Res 32:24-37.

87. Bailey AL, Dmytrenko O, Greenberg L, Bredemeyer AL, Ma P, Liu J, Penna V, Winkler ES, Sviben S, Brooks E, Nair AP, Heck KA, Rali AS, Simpson L, Saririan M, Hobohm D, Stump WT, Fitzpatrick JA, Xie X, Zhang X, Shi PY, Hinson JT, Gi WT, Schmidt C, Leuschner F, Lin CY, Diamond MS, Greenberg MJ, Lavine KJ. 2021. SARS-CoV-2 Infects Human Engineered Heart Tissues and Models COVID-19 Myocarditis. JACC Basic Transl Sci 6:331-345.

88. Lamers MM, Beumer J, van der Vaart J, Knoops K, Puschhof J, Breugem TI, Ravelli RBG, Paul van Schayck J, Mykytyn AZ, Duimel HQ, van Donselaar E, Riesebosch S, Kuijpers HJH, Schippers D, van de Wetering WJ, de Graaf M, Koopmans M, Cuppen E, Peters PJ, Haagmans BL, Clevers H. 2020. SARS-CoV-2 productively infects human gut enterocytes. Science.

89. Monteil V, Kwon H, Prado P, Hagelkrüys A, Wimmer RA, Stahl M, Leopoldi A, Garreta E, Hurtado Del Pozo C, Prosper F, Romero JP, Wirnsberger G, Zhang H, Slutsky AS, Conder R, Montserrat N, Mirazimi A, Penninger JM. 2020. Inhibition of SARS-CoV-2 Infections in Engineered Human Tissues Using Clinical-Grade Soluble Human ACE2. Cell 181:905-913.e7.

90. Yi SA, Nam KH, Yun J, Gim D, Joe D, Kim YH, Kim HJ, Han JW, Lee J. 2020. Infection of Brain Organoids and 2D Cortical Neurons with SARS-CoV-2 Pseudovirus. Viruses 12.

91. Ramani A, Müller L, Ostermann PN, Gabriel E, Abida-Islam P, Müller-Schiffmann A, Mariappan A, Goureau O, Gruell H, Walker A, Andrée M, Hauka S, Houwaart T, Dilthey A, Wohlgemuth K, Omran H, Klein F, Wieczorek D, Adams O, Timm J, Korth C, Schaal H, Gopalakrishnan J. 2020. SARS-CoV-2 targets neurons of 3D human brain organoids. EMBO J:e106230.

92. Geary RS, Norris D, Yu R, Bennett CF. 2015. Pharmacokinetics, biodistribution and cell uptake of antisense oligonucleotides. Adv Drug Deliv Rev 87:46-51.

93. Ou X, Liu Y, Lei X, Li P, Mi D, Ren L, Guo L, Guo R, Chen T, Hu J, Xiang Z, Mu Z, Chen X, Chen J, Hu K, Jin Q, Wang J, Qian Z. 2020. Characterization of spike glycoprotein of SARS-CoV-2 on virus entry and its immune cross-reactivity with SARS-CoV. Nat Commun 11:1620.

94. Shang J, Wan Y, Luo C, Ye G, Geng Q, Auerbach A, Li F. 2020. Cell entry mechanisms of SARS-CoV-2. Proc Natl Acad Sci U S A 117:11727-11734.

95. Cortese M, Lee JY, Cerikan B, Neufeldt CJ, Oorschot VMJ, Köhrer S, Hennies J, Schieber NL, Ronchi P, Mizzon G, Romero-Brey I, Santarella-Mellwig R, Schorb M, Boermel M, Mocaer K, Beckwith MS, Templin RM, Gross V, Pape C, Tischer C, Frankish J, Horvat NK, Laketa V, Stanifer M, Boulant S, Ruggieri A, Chatel-Chaix L, Schwab Y, Bartenschlager R. 2020. Integrative Imaging Reveals SARS-CoV-2-Induced Reshaping of Subcellular Morphologies. Cell Host Microbe 28:853-866.e5.

96. Twu WI, Lee JY, Kim H, Prasad V, Cerikan B, Haselmann U, Tabata K, Bartenschlager R. 2021. Contribution of autophagy machinery factors to HCV and SARS-CoV-2 replication organelle formation. Cell Rep 37:110049.

97. Hartenian E, Nandakumar D, Lari A, Ly M, Tucker JM, Glaunsinger BA. 2020. The molecular virology of coronaviruses. J Biol Chem 295:12910-12934.

98. Eymieux S, Uzbekov R, Rouillé Y, Blanchard E, Hourioux C, Dubuisson J, Belouzard S, Roingeard P. 2021. Secretory Vesicles Are the Principal Means of SARS-CoV-2 Egress. Cells 10.

99. Mendonça L, Howe A, Gilchrist JB, Sheng Y, Sun D, Knight ML, Zanetti-Domingues LC, Bateman B, Krebs AS, Chen L, Radecke J, Li VD, Ni T, Kounatidis I, Koronfel MA, Szynkiewicz M, Harkiolaki M, Martin-Fernandez ML, James W, Zhang P. 2021. Correlative multi-scale cryo-imaging unveils SARS-CoV-2 assembly and egress. Nat Commun 12:4629.

100. Enjuanes L, Almazán F, Sola I, Zuñiga S. 2006. Biochemical aspects of coronavirus replication and virus-host interaction. Annu Rev Microbiol 60:211-30.

101. Shi ST, Yu GY, Lai MM. 2003. Multiple type A/B heterogeneous nuclear ribonucleoproteins (hnRNPs) can replace hnRNP A1 in mouse hepatitis virus RNA synthesis. J Virol 77:10584-93.

102. Shi ST, Huang P, Li HP, Lai MM. 2000. Heterogeneous nuclear ribonucleoprotein A1 regulates RNA synthesis of a cytoplasmic virus. EMBO J 19:4701-11.

103. Huang P, Lai MM. 2001. Heterogeneous nuclear ribonucleoprotein a1 binds to the 3'-untranslated region and mediates potential 5'-3'-end cross talks of mouse hepatitis virus RNA. J Virol 75:5009-17.

104. Li HP, Huang P, Park S, Lai MM. 1999. Polypyrimidine tract-binding protein binds to the leader RNA of mouse hepatitis virus and serves as a regulator of viral transcription. J Virol 73:772-7.

105. Li HP, Zhang X, Duncan R, Comai L, Lai MM. 1997. Heterogeneous nuclear ribonucleoprotein A1 binds to the transcription-regulatory region of mouse hepatitis virus RNA. Proc Natl Acad Sci U S A 94:9544-9.

106. Howley P, Knipe D. 2021. Fields: Virology, vol 1. Wolters Kluwer, Philadelphia, PA.

107. Mendoza EJ, Warner B, Safronetz D, Ranadheera C. 2018. Crimean-Congo haemorrhagic fever virus: Past, present and future insights for animal modelling and medical countermeasures. Zoonoses Public Health 65:465-480.

108. de la Fuente J, Antunes S, Bonnet S, Cabezas-Cruz A, Domingos AG, Estrada-Peña A, Johnson N, Kocan KM, Mansfield KL, Nijhof AM, Papa A, Rudenko N, Villar M, Alberdi P, Torina A, Ayllón N, Vancova M, Golovchenko M, Grubhoffer L, Caracappa S, Fooks AR, Gortazar C, Rego ROM. 2017. Tick-Pathogen Interactions and Vector Competence: Identification of Molecular Drivers for Tick-Borne Diseases. Front Cell Infect Microbiol 7:114.

109. Zivcec M, Scholte FE, Spiropoulou CF, Spengler JR, Bergeron É. 2016. Molecular Insights into Crimean-Congo Hemorrhagic Fever Virus. Viruses 8:106.

110. Barr JN, Wertz GW. 2005. Role of the conserved nucleotide mismatch within 3'- and 5'-terminal regions of Bunyamwera virus in signaling transcription. J Virol 79:3586-94.

111. Barr JN, Wertz GW. 2004. Bunyamwera bunyavirus RNA synthesis requires cooperation of 3'- and 5'-terminal sequences. J Virol 78:1129-38.

112. Matsumoto Y, Ohta K, Kolakofsky D, Nishio M. 2019. A Minigenome Study of Hazara Nairovirus Genomic Promoters. J Virol 93.

113. Modrow S, Truyen U, Schätzl H. 2022. Molekulare Virologie, vol 4. Springer-Verlag GmbH Deutschland, Berlin.

114. Suda Y, Fukushi S, Tani H, Murakami S, Saijo M, Horimoto T, Shimojima M. 2016. Analysis of the entry mechanism of Crimean-Congo hemorrhagic fever virus, using a vesicular stomatitis virus pseudotyping system. Arch Virol 161:1447-54.

115. Javanian M, Barary M, Ghebrehewet S, Koppolu V, Vasigala V, Ebrahimpour S. 2021. A brief review of influenza virus infection. J Med Virol 93:4638-4646.

116. Johnson KEE, Ghedin E. 2020. Quantifying between-Host Transmission in Influenza Virus Infections. Cold Spring Harb Perspect Med 10.

117. Kim H, Webster RG, Webby RJ. 2018. Influenza Virus: Dealing with a Drifting and Shifting Pathogen. Viral Immunol 31:174-183.

118. Fineberg HV. 2014. Pandemic preparedness and response--lessons from the H1N1 influenza of 2009. N Engl J Med 370:1335-42.

119. Kasowski EJ, Garten RJ, Bridges CB. 2011. Influenza pandemic epidemiologic and virologic diversity: reminding ourselves of the possibilities. Clin Infect Dis 52 Suppl 1:S44-9.

120. Duwe SC, Schmidt B, Gärtner BC, Timm J, Adams O, Fickenscher H, Schmidtke M. 2021. Prophylaxis and treatment of influenza: options, antiviral susceptibility, and existing recommendations. GMS Infect Dis 9:Doc02.

121. Szewczyk B, Bieńkowska-Szewczyk K, Król E. 2014. Introduction to molecular biology of influenza a viruses. Acta Biochim Pol 61:397-401.

122. Hu Y, Sneyd H, Dekant R, Wang J. 2017. Influenza A Virus Nucleoprotein: A Highly Conserved Multi-Functional Viral Protein as a Hot Antiviral Drug Target. Curr Top Med Chem 17:2271-2285.

123. Luo M. 2012. Influenza virus entry. Adv Exp Med Biol 726:201-21.

124. Vankadari N, Shepherd DC, Carter SD, Ghosal D. 2022. Three-dimensional insights into human enveloped viruses in vitro and in situ. Biochem Soc Trans 50:95-105.

125. Moreira EA, Yamauchi Y, Matthias P. 2021. How Influenza Virus Uses Host Cell Pathways during Uncoating. Cells 10.

126. Te Velthuis AJ, Fodor E. 2016. Influenza virus RNA polymerase: insights into the mechanisms of viral RNA synthesis. Nat Rev Microbiol 14:479-93.

127. Dubois J, Terrier O, Rosa-Calatrava M. 2014. Influenza viruses and mRNA splicing: doing more with less. mBio 5:e00070-14.

128. Gao Y, McKay PF, Mann JFS. 2018. Advances in HIV-1 Vaccine Development. Viruses 10.

129. Van Lint C, Bouchat S, Marcello A. 2013. HIV-1 transcription and latency: an update. Retrovirology 10:67.

130. Pau AK, George JM. 2014. Antiretroviral therapy: current drugs. Infect Dis Clin North Am 28:371-402.

131. Barré-Sinoussi F, Ross AL, Delfraissy JF. 2013. Past, present and future: 30 years of HIV research. Nat Rev Microbiol 11:877-83.

132. Siliciano JD, Kajdas J, Finzi D, Quinn TC, Chadwick K, Margolick JB, Kovacs C, Gange SJ, Siliciano RF. 2003. Long-term follow-up studies confirm the stability of the latent reservoir for HIV-1 in resting CD4+ T cells. Nat Med 9:727-8.

133. Izzedine H, Harris M, Perazella MA. 2009. The nephrotoxic effects of HAART. Nat Rev Nephrol 5:563-73.

134. Esser S, Helbig D, Hillen U, Dissemond J, Grabbe S. 2007. Side effects of HIV therapy. J Dtsch Dermatol Ges 5:745-54.

135. Lübke N, Jensen B, Hüttig F, Feldt T, Walker A, Thielen A, Däumer M, Obermeier M, Kaiser R, Knops E, Heger E, Sierra S, Oette M, Lengauer T, Timm J, Häussinger D. 2019. Failure of Dolutegravir First-Line ART with Selection of Virus Carrying R263K and G118R. N Engl J Med 381:887-889.

136. Costagliola D, Descamps D, Assoumou L, Morand-Joubert L, Marcelin AG, Brodard V, Delaugerre C, Mackiewicz V, Ruffault A, Izopet J, Plantier JC, Tamalet C, Yerly S, Saidi S, Brun-Vezinet F, Masquelier B, Group ANdRslSelHVAARS. 2007. Prevalence of HIV-1 drug resistance in treated patients: a French nationwide study. J Acquir Immune Defic Syndr 46:12-8.

137. Joshi S, Joshi RL. 1996. Molecular biology of human immunodeficiency virus type-1. Transfus Sci 17:351-78.

138. Xiao T, Cai Y, Chen B. 2021. HIV-1 Entry and Membrane Fusion Inhibitors. Viruses 13.

139. Polzer S, Dittmar MT, Schmitz H, Schreiber M. 2002. The N-linked glycan g15 within the V3 loop of the HIV-1 external glycoprotein gp120 affects coreceptor usage, cellular tropism, and neutralization. Virology 304:70-80.

140. Naghavi MH. 2021. HIV-1 capsid exploitation of the host microtubule cytoskeleton during early infection. Retrovirology 18:19.

141. Zila V, Margiotta E, Turoňová B, Müller TG, Zimmerli CE, Mattei S, Allegretti M, Börner K, Rada J, Müller B, Lusic M, Kräusslich HG, Beck M. 2021. Cone-shaped HIV-1 capsids are transported through intact nuclear pores. Cell 184:1032-1046.e18.

142. Sertznig H, Hillebrand F, Erkelenz S, Schaal H, Widera M. 2018. Behind the scenes of HIV-1 replication: Alternative splicing as the dependency factor on the quiet. Virology 516:176-188.

143. Fernandes J, Jayaraman B, Frankel A. 2012. The HIV-1 Rev response element: an RNA scaffold that directs the cooperative assembly of a homo-oligomeric ribonucleoprotein complex. RNA Biol 9:6-11.
144. Frankel AD, Young JA. 1998. HIV-1: fifteen proteins and an RNA. Annu Rev Biochem 67:1-25.
145. Jones KA. 1993. Tat and the HIV-1 promoter. Curr Opin Cell Biol 5:461-8.
146. Freed EO. 2015. HIV-1 assembly, release and maturation. Nat Rev Microbiol 13:484-96.
147. Prescher J, Baumgärtel V, Ivanchenko S, Torrano AA, Bräuchle C, Müller B, Lamb DC. 2015. Super-resolution imaging of ESCRT-proteins at HIV-1 assembly sites. PLoS Pathog 11:e1004677.
148. Ocwieja KE, Sherrill-Mix S, Mukherjee R, Custers-Allen R, David P, Brown M, Wang S, Link DR, Olson J, Travers K, Schadt E, Bushman FD. 2012. Dynamic regulation of HIV-1 mRNA populations analyzed by single-molecule enrichment and long-read sequencing. Nucleic Acids Res 40:10345-55.
149. Schwartz S, Felber BK, Pavlakis GN. 1992. Mechanism of translation of monocistronic and multicistronic human immunodeficiency virus type 1 mRNAs. Mol Cell Biol 12:207-19.
150. Moorlag SJCF, Taks E, Ten Doesschate T, van der Vaart TW, Janssen AB, Müller L, Ostermann P, Dijkstra H, Lemmers H, Simonetti E, Mazur M, Schaal H, Ter Heine R, van de Veerdonk FL, Bleeker-Rovers CP, van Crevel R, Ten Oever J, de Jonge MI, Bonten MJ, van Werkhoven CH, Netea MG. 2022. Efficacy of Bacillus Calmette-Guérin vaccination against respiratory tract infections in the elderly during the Covid-19 pandemic. Clin Infect Dis.
151. Ptok J, Müller L, Theiss S, Schaal H. 2019. Context matters: Regulation of splice donor usage. Biochim Biophys Acta Gene Regul Mech 1862:194391.
152. Brillen AL, Walotka L, Hillebrand F, Müller L, Widera M, Theiss S, Schaal H. 2017. Analysis of Competing HIV-1 Splice Donor Sites Uncovers a Tight Cluster of Splicing Regulatory Elements within Exon 2/2b. J Virol 91.
153. Widera M, Erkelenz S, Hillebrand F, Krikoni A, Widera D, Kaisers W, Deenen R, Gombert M, Dellen R, Pfeiffer T, Kaltschmidt B, Münk C, Bosch V, Köhrer K, Schaal H. 2013. An intronic G run within HIV-1 intron 2 is critical for splicing regulation of vif mRNA. J Virol 87:2707-20.
154. Asang C, Hauber I, Schaal H. 2008. Insights into the selective activation of alternatively used splice acceptors by the human immunodeficiency virus type-1 bidirectional splicing enhancer. Nucleic Acids Res 36:1450-63.
155. Caputi M, Freund M, Kammler S, Asang C, Schaal H. 2004. A bidirectional SF2/ASF- and SRp40-dependent splicing enhancer regulates human immunodeficiency virus type 1 rev, env, vpu, and nef gene expression. J Virol 78:6517-26.
156. Stoltzfus CM. 2009. Chapter 1. Regulation of HIV-1 alternative RNA splicing and its role in virus replication. Adv Virus Res 74:1-40.
157. Madsen JM, Stoltzfus CM. 2005. An exonic splicing silencer downstream of the 3' splice site A2 is required for efficient human immunodeficiency virus type 1 replication. J Virol 79:10478-86.
158. Domsic JK, Wang Y, Mayeda A, Krainer AR, Stoltzfus CM. 2003. Human immunodeficiency virus type 1 hnRNP A/B-dependent exonic splicing silencer ESSV antagonizes binding of U2AF65 to viral polypyrimidine tracts. Mol Cell Biol 23:8762-72.
159. Bilodeau PS, Domsic JK, Mayeda A, Krainer AR, Stoltzfus CM. 2001. RNA splicing at human immunodeficiency virus type 1 3' splice site A2 is regulated by binding of hnRNP A/B proteins to an exonic splicing silencer element. J Virol 75:8487-97.
160. Schaub MC, Lopez SR, Caputi M. 2007. Members of the heterogeneous nuclear ribonucleoprotein H family activate splicing of an HIV-1 splicing substrate by promoting formation of ATP-dependent spliceosomal complexes. J Biol Chem 282:13617-26.
161. Mann DA, Mikaélian I, Zemmel RW, Green SM, Lowe AD, Kimura T, Singh M, Butler PJ, Gait MJ, Karn J. 1994. A molecular rheostat. Co-operative rev binding to stem I of the rev-response element modulates human immunodeficiency virus type-1 late gene expression. J Mol Biol 241:193-207.
162. Ostermann PN, Ritchie A, Ptok J, Schaal H. 2021. Let it go: HIV-1. J Virol.

163. Pollard VW, Malim MH. 1998. The HIV-1 Rev protein. Annu Rev Microbiol 52:491-532.

164. Adachi A, Gendelman HE, Koenig S, Folks T, Willey R, Rabson A, Martin MA. 1986. Production of acquired immunodeficiency syndrome-associated retrovirus in human and nonhuman cells transfected with an infectious molecular clone. J Virol 59:284-91.

165. Corman VM, Landt O, Kaiser M, Molenkamp R, Meijer A, Chu DK, Bleicker T, Brünink S, Schneider J, Schmidt ML, Mulders DG, Haagmans BL, van der Veer B, van den Brink S, Wijsman L, Goderski G, Romette JL, Ellis J, Zambon M, Peiris M, Goossens H, Reusken C, Koopmans MP, Drosten C. 2020. Detection of 2019 novel coronavirus (2019-nCoV) by real-time RT-PCR. Euro Surveill 25.

166. Schmittgen TD, Livak KJ. 2008. Analyzing real-time PCR data by the comparative C(T) method. Nat Protoc 3:1101-8.

167. Harcourt J, Tamin A, Lu X, Kamili S, Sakthivel SK, Murray J, Queen K, Tao Y, Paden CR, Zhang J, Li Y, Uehara A, Wang H, Goldsmith C, Bullock HA, Wang L, Whitaker B, Lynch B, Gautam R, Schindewolf C, Lokugamage KG, Scharton D, Plante JA, Mirchandani D, Widen SG, Narayanan K, Makino S, Ksiazek TG, Plante KS, Weaver SC, Lindstrom S, Tong S, Menachery VD, Thornburg NJ. 2020. Severe Acute Respiratory Syndrome Coronavirus 2 from Patient with 2019 Novel Coronavirus Disease, United States. Emerg Infect Dis 26.

168. Park WB, Kwon NJ, Choi SJ, Kang CK, Choe PG, Kim JY, Yun J, Lee GW, Seong MW, Kim NJ, Seo JS, Oh MD. 2020. Virus Isolation from the First Patient with SARS-CoV-2 in Korea. J Korean Med Sci 35:e84.

169. Walker A, Houwaart T, Wienemann T, Vasconcelos MK, Strelow D, Senff T, Hülse L, Adams O, Andree M, Hauka S, Feldt T, Jensen BE, Keitel V, Kindgen-Milles D, Timm J, Pfeffer K, Dilthey AT. 2020. Genetic structure of SARS-CoV-2 reflects clonal superspreading and multiple independent introduction events, North-Rhine Westphalia, Germany, February and March 2020. Euro Surveill 25.

170. Yurkovetskiy L, Wang X, Pascal KE, Tomkins-Tinch C, Nyalile TP, Wang Y, Baum A, Diehl WE, Dauphin A, Carbone C, Veinotte K, Egri SB, Schaffner SF, Lemieux JE, Munro JB, Rafique A, Barve A, Sabeti PC, Kyratsous CA, Dudkina NV, Shen K, Luban J. 2020. Structural and Functional Analysis of the D614G SARS-CoV-2 Spike Protein Variant. Cell 183:739-751.e8.

171. Korber B, Fischer WM, Gnanakaran S, Yoon H, Theiler J, Abfalterer W, Hengartner N, Giorgi EE, Bhattacharya T, Foley B, Hastie KM, Parker MD, Partridge DG, Evans CM, Freeman TM, de Silva TI, McDanal C, Perez LG, Tang H, Moon-Walker A, Whelan SP, LaBranche CC, Saphire EO, Montefiori DC, Group SC-G. 2020. Tracking Changes in SARS-CoV-2 Spike: Evidence that D614G Increases Infectivity of the COVID-19 Virus. Cell 182:812-827.e19.

172. Van Nostrand EL, Freese P, Pratt GA, Wang X, Wei X, Xiao R, Blue SM, Chen JY, Cody NAL, Dominguez D, Olson S, Sundararaman B, Zhan L, Bazile C, Bouvrette LPB, Bergalet J, Duff MO, Garcia KE, Gelboin-Burkhart C, Hochman M, Lambert NJ, Li H, McGurk MP, Nguyen TB, Palden T, Rabano I, Sathe S, Stanton R, Su A, Wang R, Yee BA, Zhou B, Louie AL, Aigner S, Fu XD, Lécuyer E, Burge CB, Graveley BR, Yeo GW. 2020. A large-scale binding and functional map of human RNA-binding proteins. Nature 583:711-719.

173. Piñol-Roma S. 1997. HnRNP proteins and the nuclear export of mRNA. Semin Cell Dev Biol 8:57-63.

174. Chiang C, Chen GW, Shih SR. 2008. Mutations at alternative 5' splice sites of M1 mRNA negatively affect influenza A virus viability and growth rate. J Virol 82:10873-86.

175. Cheung TKW, Guan Y, Ng SSF, Chen H, Wong CHK, Peiris JSM, Poon LLM. 2005. Generation of recombinant influenza A virus without M2 ion-channel protein by introduction of a point mutation at the 5' end of the viral intron. J Gen Virol 86:1447-1454.

176. Chiang MJ, Musayev FN, Kosikova M, Lin Z, Gao Y, Mosier PD, Althufairi B, Ye Z, Zhou Q, Desai UR, Xie H, Safo MK. 2017. Maintaining pH-dependent conformational flexibility of M1 is critical for efficient influenza A virus replication. Emerg Microbes Infect 6:e108.

177. Zhirnov OP, Manykin AA, Rossman JS, Klenk HD. 2016. Intravirion cohesion of matrix protein M1 with ribonucleocapsid is a prerequisite of influenza virus infectivity. Virology 492:187-96.

178. Gómez-Puertas P, Albo C, Pérez-Pastrana E, Vivo A, Portela A. 2000. Influenza virus matrix protein is the major driving force in virus budding. J Virol 74:11538-47.

179. Shih SR, Krug RM. 1996. Novel exploitation of a nuclear function by influenza virus: the cellular SF2/ASF splicing factor controls the amount of the essential viral M2 ion channel protein in infected cells. EMBO J 15:5415-27.

180. Erkelenz S, Theiss S, Otte M, Widera M, Peter JO, Schaal H. 2014. Genomic HEXploring allows landscaping of novel potential splicing regulatory elements. Nucleic Acids Res 42:10681-97.

181. Bao Y, Bolotov P, Dernovoy D, Kiryutin B, Zaslavsky L, Tatusova T, Ostell J, Lipman D. 2008. The influenza virus resource at the National Center for Biotechnology Information. J Virol 82:596-601.

182. Crooks GE, Hon G, Chandonia JM, Brenner SE. 2004. WebLogo: a sequence logo generator. Genome Res 14:1188-90.

183. Al-Dosari MS, Shaheen R, Colak D, Alkuraya FS. 2010. Novel CENPJ mutation causes Seckel syndrome. J Med Genet 47:411-4.

184. Adams O, Andrée M, Rabl D, Ostermann PN, Schaal H, Lehnert E, Ackerstaff S, Müller L, Fischer JC. 2021. Humoral response to SARS-CoV-2 and seasonal coronaviruses in COVID-19 patients. J Med Virol.

185. Mueller L, Ostermann PN, Walker A, Wienemann T, Mertens A, Adams O, Andree M, Hauka S, Luebke N, Keitel V, Drexler I, Di Cristanziano V, Hermsen DF, Kaiser R, Boege F, Klein F, Schaal H, Timm J, Senff T. 2020. Sensitivity of commercial Anti-SARS-CoV-2 serological assays in a high-prevalence setting. medRxiv:2020.06.11.20128686.

186. Zhang Y, Sun H, Pei R, Mao B, Zhao Z, Li H, Lin Y, Lu K. 2021. The SARS-CoV-2 protein ORF3a inhibits fusion of autophagosomes with lysosomes. Cell Discov 7:31.

187. Qu Y, Wang X, Zhu Y, Wang W, Wang Y, Hu G, Liu C, Li J, Ren S, Xiao MZX, Liu Z, Wang C, Fu J, Zhang Y, Li P, Zhang R, Liang Q. 2021. ORF3a-Mediated Incomplete Autophagy Facilitates Severe Acute Respiratory Syndrome Coronavirus-2 Replication. Front Cell Dev Biol 9:716208.

188. Ruan Y, Wen H, Hou M, He Z, Lu X, Xue Y, He X, Zhang YP, Wu CI. 2022. The twin-beginnings of COVID-19 in Asia and Europe-one prevails quickly. Natl Sci Rev 9:nwab223.

189. Fang S, Liu S, Shen J, Lu AZ, Wang AKY, Zhang Y, Li K, Liu J, Yang L, Hu CD, Wan J. 2021. Updated SARS-CoV-2 single nucleotide variants and mortality association. J Med Virol 93:6525-6534.

190. Cheng L, Han X, Zhu Z, Qi C, Wang P, Zhang X. 2021. Functional alterations caused by mutations reflect evolutionary trends of SARS-CoV-2. Brief Bioinform 22:1442-1450.

191. Pachetti M, Marini B, Benedetti F, Giudici F, Mauro E, Storici P, Masciovecchio C, Angeletti S, Ciccozzi M, Gallo RC, Zella D, Ippodrino R. 2020. Emerging SARS-CoV-2 mutation hot spots include a novel RNA-dependent-RNA polymerase variant. J Transl Med 18:179.

192. Chaudhari A, Chaudhari M, Mahera S, Saiyed Z, Nathani NM, Shukla S, Patel D, Patel C, Joshi M, Joshi CG. 2021. In-Silico analysis reveals lower transcription efficiency of C241T variant of SARS-CoV-2 with host replication factors MADP1 and hnRNP-1. Inform Med Unlocked 25:100670.

193. Xu G, Li Y, Zhang S, Peng H, Wang Y, Li D, Jin T, He Z, Tong Y, Qi C, Wu G, Dong K, Gou J, Liu Y, Xiao T, Qu J, Li L, Liu L, Zhao P, Zhang Z, Yuan J. 2021. SARS-CoV-2 promotes RIPK1 activation to facilitate viral propagation. Cell Res 31:1230-1243.

194. Castanotto D, Lin M, Kowolik C, Wang L, Ren XQ, Soifer HS, Koch T, Hansen BR, Oerum H, Armstrong B, Wang Z, Bauer P, Rossi J, Stein CA. 2015. A cytoplasmic pathway for gapmer antisense oligonucleotide-mediated gene silencing in mammalian cells. Nucleic Acids Res 43:9350-61.

195. Liang H, Luo D, Liao H, Li S. 2022. Coronavirus Usurps the Autophagy-Lysosome Pathway and Induces Membranes Rearrangement for Infection and Pathogenesis. Front Microbiol 13:846543.

196. Wolff G, Melia CE, Snijder EJ, Bárcena M. 2020. Double-Membrane Vesicles as Platforms for Viral Replication. Trends Microbiol 28:1022-1033.

197. Du X, Zhang Y, Zou J, Yuan Z, Yi Z. 2018. Replicase-mediated shielding of the poliovirus replicative double-stranded RNA to avoid recognition by MDA5. J Gen Virol 99:1199-1209.

198. Knoops K, Kikkert M, Worm SH, Zevenhoven-Dobbe JC, van der Meer Y, Koster AJ, Mommaas AM, Snijder EJ. 2008. SARS-coronavirus replication is supported by a reticulovesicular network of modified endoplasmic reticulum. PLoS Biol 6:e226.

199. Gosert R, Kanjanahaluethai A, Egger D, Bienz K, Baker SC. 2002. RNA replication of mouse hepatitis virus takes place at double-membrane vesicles. J Virol 76:3697-708.

200. Zhang X, Castanotto D, Liu X, Shemi A, Stein CA. 2018. Ammonium and arsenic trioxide are potent facilitators of oligonucleotide function when delivered by gymnosis. Nucleic Acids Res.

201. Liang XH, Nichols JG, Hsu CW, Vickers TA, Crooke ST. 2019. mRNA levels can be reduced by antisense oligonucleotides via no-go decay pathway. Nucleic Acids Res 47:6900-6916.

202. Hummelshoj L, Ryder LP, Madsen HO, Poulsen LK. 2005. Locked nucleic acid inhibits amplification of contaminating DNA in real-time PCR. Biotechniques 38:605-10.

203. Ajasin D, Eugenin EA. 2020. HIV-1 Tat: Role in Bystander Toxicity. Front Cell Infect Microbiol 10:61.

204. Fazil MH, Ong ST, Chalasani ML, Low JH, Kizhakeyil A, Mamidi A, Lim CF, Wright GD, Lakshminarayanan R, Kelleher D, Verma NK. 2016. GapmeR cellular internalization by macropinocytosis induces sequence-specific gene silencing in human primary T-cells. Sci Rep 6:37721.

205. Liang XH, Sun H, Nichols JG, Allen N, Wang S, Vickers TA, Shen W, Hsu CW, Crooke ST. 2018. COPII vesicles can affect the activity of antisense oligonucleotides by facilitating the release of oligonucleotides from endocytic pathways. Nucleic Acids Res.

206. Wang S, Allen N, Vickers TA, Revenko AS, Sun H, Liang XH, Crooke ST. 2018. Cellular uptake mediated by epidermal growth factor receptor facilitates the intracellular activity of phosphorothioate-modified antisense oligonucleotides. Nucleic Acids Res.

207. Crooke ST, Vickers TA, Liang XH. 2020. Phosphorothioate modified oligonucleotide-protein interactions. Nucleic Acids Res 48:5235-5253.

208. Hoffmann M, Enczmann J, Balz V, Kummer S, Reinauer C, Döing C, Förtsch K, Welters A, Kohns Vasconcelos M, Mayatepek E, Meissner T, Jacobsen M, Seyfarth J. 2022. Interleukin-7 and soluble Interleukin-7 receptor levels in type 1 diabetes - Impact of IL7RA polymorphisms, HLA risk genotypes and clinical features. Clin Immunol 235:108928.

209. Gregory SG, Schmidt S, Seth P, Oksenberg JR, Hart J, Prokop A, Caillier SJ, Ban M, Goris A, Barcellos LF, Lincoln R, McCauley JL, Sawcer SJ, Compston DA, Dubois B, Hauser SL, Garcia-Blanco MA, Pericak-Vance MA, Haines JL, Group MSG. 2007. Interleukin 7 receptor alpha chain (IL7R) shows allelic and functional association with multiple sclerosis. Nat Genet 39:1083-91.

210. Galarza-Munoz G, Kennedy-Boone D, Schott G, Bradrick SS, Garcia-Blanco MA. 2022. Antisense modulation of IL7R splicing to control sIL7R expression in human CD4 T cells. RNA.

211. Erkelenz S, Mueller WF, Evans MS, Busch A, Schöneweis K, Hertel KJ, Schaal H. 2013. Position-dependent splicing activation and repression by SR and hnRNP proteins rely on common mechanisms. RNA 19:96-102.

212. De Bortoli F, Espinosa S, Zhao R. 2021. DEAH-Box RNA Helicases in Pre-mRNA Splicing. Trends Biochem Sci 46:225-238.

213. Hirons A, Khoury G, Purcell DFJ. 2021. Human T-cell lymphotropic virus type-1: a lifelong persistent infection, yet never truly silent. Lancet Infect Dis 21:e2-e10.

214. Marino-Merlo F, Balestrieri E, Matteucci C, Mastino A, Grelli S, Macchi B. 2020. Antiretroviral Therapy in HTLV-1 Infection: An Updated Overview. Pathogens 9.

Supplementary material

Centromere protein J (CENPJ)

NCBI RefSeq: NG_009165
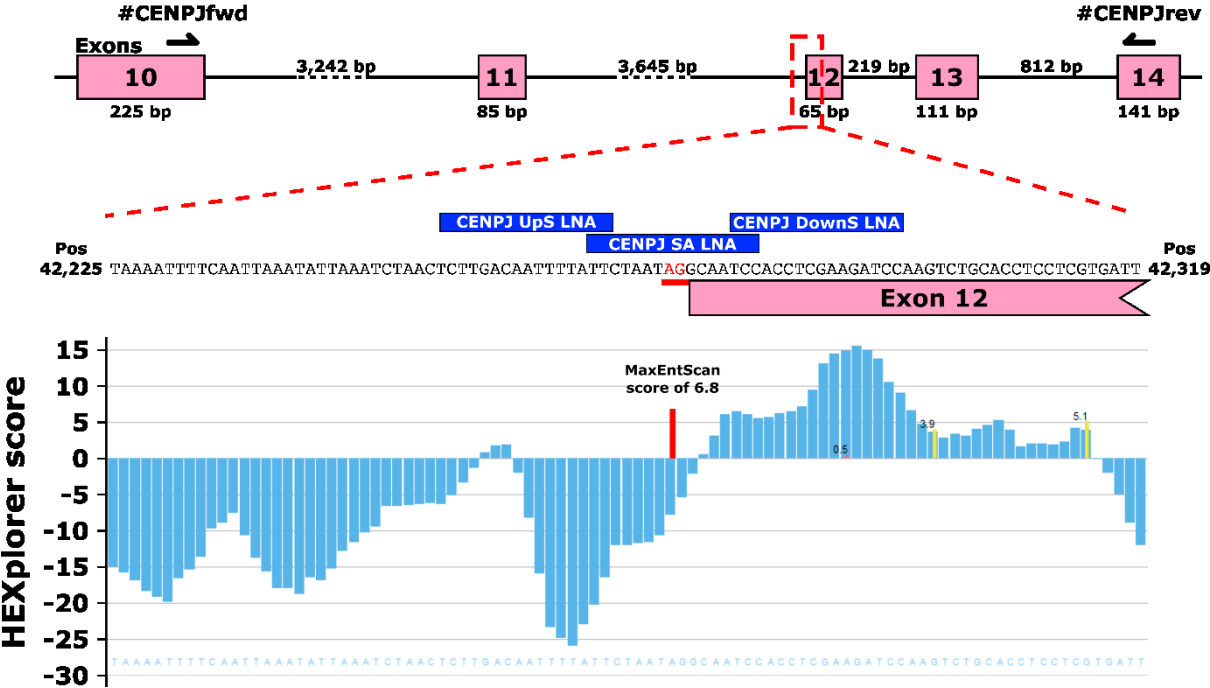ENSEMBL: ENSG00000151849

Fig. S.1 Schematic showing the *CENPJ* region targeted by the three anti-CENPJ LNA mixmers. Overview of the region spanning exon 11 to 14 of the Centromere protein J (*CENPJ*) gene. Primer binding sites are indicated with black arrows. Sequence between nucleotide positions (pos) 42,225 and 42,319 is depicted with the splice acceptor site of exon 12 (red) and LNA mixmer binding sites (blue bars). HEXplorer profile predicting the splicing regulatory element (SRE) landscape in the depicted CENPJ region (180). Indicated are the positions and MaxEntScan scores of the annotated *CENPJ* exon 12 splice acceptor site and an additional AG dinucleotide (red bars) and positions and HBond scores of putative GT dinucleotide containing splice donor sites (yellow bars).

Declaration

Ich versichere an Eides Statt, dass die Dissertation von mir selbständig und ohne unzulässige fremde Hilfe unter Beachtung der „Grundsätze zur Sicherung guter wissenschaftlicher Praxis an der Heinrich-Heine-Universität Düsseldorf" erstellt worden ist. Ich habe diese Dissertation bei keiner anderen Fakultät vorgelegt und ich habe bisher keine erfolglosen oder erfolgreichen Promotionsversuche unternommen.

Philipp Niklas Ostermann

Düsseldorf, den